



저작자표시-비영리-변경금지 2.0 대한민국

이용자는 아래의 조건을 따르는 경우에 한하여 자유롭게

- 이 저작물을 복제, 배포, 전송, 전시, 공연 및 방송할 수 있습니다.

다음과 같은 조건을 따라야 합니다:



저작자표시. 귀하는 원저작자를 표시하여야 합니다.



비영리. 귀하는 이 저작물을 영리 목적으로 이용할 수 없습니다.



변경금지. 귀하는 이 저작물을 개작, 변형 또는 가공할 수 없습니다.

- 귀하는, 이 저작물의 재이용이나 배포의 경우, 이 저작물에 적용된 이용허락조건을 명확하게 나타내어야 합니다.
- 저작권자로부터 별도의 허가를 받으면 이러한 조건들은 적용되지 않습니다.

저작권법에 따른 이용자의 권리는 위의 내용에 의하여 영향을 받지 않습니다.

이것은 [이용허락규약\(Legal Code\)](#)을 이해하기 쉽게 요약한 것입니다.

[Disclaimer](#)

이학박사 학위논문

**Nature of polymerization, structural disorder, and
properties of iron-bearing silicate and aluminosilicate
glasses and melts: Insights from high-resolution
 ^{29}Si , ^{27}Al and ^{17}O solid-state NMR**

함철 규산염 및 알루미늄규산염 비정질의 중합도와 무질서도
규명을 통한 용융체 물성의 이해: 고분해능 고상 핵자기공명
분광분석 연구

A dissertation in partial fulfillment of the requirements
for the degree of Doctor of Philosophy

2019 년 8 월

서울대학교 대학원
지구환경과학부

김 효 임

ABSTRACT

Nature of polymerization, structural disorder, and properties of iron-bearing silicate and aluminosilicate glasses and melts: Insights from high-resolution ^{29}Si , ^{27}Al and ^{17}O solid-state NMR

Hyo-Im Kim

School of Earth and Environmental Sciences

The Graduate School

Seoul National University

Iron is one of the most abundant transition metals in the natural magmatic melts of the Earth and other terrestrial planets. In the silicate melts and glasses, iron can be found in variable content and multiple valence states. The physical and chemical properties of silicate melts and glasses (e.g., viscosity, density, and element partitioning) are strongly dependent on iron content and the redox state. The key to fundamental understanding of the properties of iron-bearing silicate glasses and their corresponding melts is the determination of detailed structure and disorder among constituent cations and anions. Despite the importance, the detailed structure and disorder of iron-bearing glasses is largely unknown, because the solid-state NMR, one of the most effective experimental methods to probe the structure of oxide glasses, cannot be fully utilized for exploring the structural details of iron-bearing glasses as the unpaired electrons in Fe induce strong local magnetic fields that mask the original spectroscopic features.

The main objective of the dissertation is to reveal the effect of iron content and redox state on the atomic structure and extent of structural disorder of iron-bearing silicate and aluminosilicate glasses and to provide insights into the systematic relationships between atomic structure and macroscopic properties. To systematically investigate the effect of iron content and redox state on structure and disorder of iron-bearing glasses, solid-state NMR techniques have been mainly utilized, despite the inherent difficulties.

First, I have demonstrated that high-resolution solid-state NMR techniques can be effectively applied to study the effect of iron content on the atomic configurations around Si and O sites in $\text{Na}_2\text{O}-\text{Fe}_2\text{O}_3-\text{SiO}_2$ glasses [up to 22.9 wt% Fe_2O_3 ($\text{Fe}^{3+}/\Sigma\text{Fe} = 0.89$)]. The NMR results show that changes in NMR peaks and relevant parameters reflect iron-induced structural changes, such as degree of polymerization, topological disorder, and iron distribution around silicon and oxygen sites. This study also yields the first glimpse of the iron distribution in the silicate networks. Second, the NMR results provided the structural details of the geologically vital Fe^{2+} -dominant $(\text{Mg,Fe})\text{SiO}_3$ glasses ($\text{Fe}^{3+}/\Sigma\text{Fe} = 0.2$) with varying iron content, despite severe overlap among spectral features. In conjunction with the NMR results of Fe^{3+} -dominant sodium silicate glasses, the effect of valence state of iron on the short- (i.e., Q species, NBO/BO) and medium-range (i.e., spatial proximity between iron and nuclear spins) of atomic structure was explored. These results show that an increase in Fe^{3+} in silicate glasses leads to an increase in the extent of polymerization. The type of oxygen site that preferentially interacts with iron depends on the valence state of the iron: specifically, the ^{17}O NMR results indicate the presence of a moderate degree of preferential interaction between Fe^{2+} and non-bridging oxygen (NBO), as well as that

between Fe^{3+} and bridging oxygen (BO) in the iron-bearing silicate glasses. The unique NMR results of $(\text{Mg,Fe})\text{SiO}_3$ glasses provide atomistic insights into the viscous flow of mafic silicate melts.

Beyond the binary silicate glasses, the detailed structure and disorder of iron-bearing Na- and Ca-aluminosilicate glasses can be obtained using high-resolution solid-state NMR and Mössbauer spectroscopy. The iron-bearing aluminosilicate glasses used in this study are simplified model rhyolitic charge-balanced glasses, which corresponds to the tectosilicate composition. High-resolution solid-state NMR techniques can determine the effect of iron content on the atomic configurations around Si, Al, and O sites in $\text{Na}(\text{Al}_{1-x}\text{Fe}_x)\text{Si}_3\text{O}_8$ ($\text{Fe}^{3+}/\Sigma\text{Fe} = \sim 0.8$), $\text{NaAlSi}_3\text{O}_8 + \text{Fe}_2\text{O}_3$ ($\text{Fe}^{3+}/\Sigma\text{Fe} = \sim 0.5$), and $\text{CaAl}_2\text{Si}_2\text{O}_8 + \text{Fe}_2\text{O}_3$ ($\text{Fe}^{3+}/\Sigma\text{Fe} = \sim 0.3$) glasses. The noble NMR results for iron-bearing aluminosilicate glasses revealed the nature of diverse aspect of iron-induced structural disorder, mainly characterized by the intermixing between Si and Fe^{3+} , preferential interaction between Al and Fe^{2+} , and formation of highly coordinated $^{55}\text{Fe}^{3+}$. The observed increase in the extent of structural disorder in charge-balanced Na- and Ca-aluminosilicate glasses with increasing Fe^{2+} and Fe^{3+} can account for the iron-induced decrease in viscosity of the corresponding iron-bearing aluminosilicate melts. Though qualitative, these structural findings with increasing iron content can provide unique constraints on the atomistic origins of the properties of natural silicate melts.

Keywords: Iron-bearing silicate/aluminosilicate glasses and melts, structure and disorder, solid-state nuclear magnetic resonance, paramagnetic effect

Student Number: 2011-30916

Table of Contents

ABSTRACT	i
Table of Contents	v
List of Figures	ix
List of Tables.....	xxi
Chapter 1. Introduction.....	1
1.1. Geological importance of the study for atomic configurations of iron-bearing silicate glasses and melts	1
1.2. Contents of thesis	9
Chapter 2. Solid-state NMR study of paramagnetic cation-bearing materials.....	15
Chapter 3. Effect of iron content of the structure and disorder of iron-bearing sodium silicate glasses: A high-resolution ²⁹Si and ¹⁷O solid-state NMR study.....	31
ABSTRACT	31
3.1. Introduction	33
3.2. Experimental Methods	38
3.3. Results.....	44
3.3.1. Effect of iron content on Q species distribution in iron-bearing sodium silicate glasses: ²⁹ Si MAS NMR results	44
3.3.2. Iron distribution in the silicate glass networks: Insights from ²⁹ Si spin-lattice (<i>T</i> ₁) relaxation results and analyses	47
3.3.3. Effect of iron content on oxygen configurations in iron-bearing sodium silicate glasses: ¹⁷ O MAS and 3QMAS NMR results.....	51
3.3.4. Variation of structurally relevant ¹⁷ O NMR parameters and oxygen site population in iron-bearing sodium silicate glasses...	61
3.4. Discussion	67

3.4.1. Si environments in iron-bearing glasses based on ^{29}Si MAS NMR results	67
3.4.2. Homogeneous distribution of Fe in the iron-bearing silicate glasses	68
3.4.3. Hidden oxygen species in ^{17}O NMR spectra	69
3.4.4. Insights into iron distribution, the degree of polymerization, and the extent of chemical disorder in iron-bearing sodium silicate glasses	70
3.4.5. Implications and limitation of the current analysis	73
3.5. Conclusion.....	75
APPENDIX.....	77
REFERENCES.....	82

Chapter 4. The degree of polymerization and structural disorder in

(Mg,Fe)SiO₃ glasses and melts: Insights from high-resolution ^{29}Si and

^{17}O solid-state NMR..... 95

ABSTRACT	95
4.1. Introduction	96
4.2. Experimental methods	105
4.3. Results.....	110
4.3.1. Effect of iron content on Si coordination environments in (Mg,Fe)SiO ₃ glasses: ^{29}Si MAS NMR results.....	110
4.3.2. Distribution of iron in iron-bearing Mg-silicate glasses: A view from ^{29}Si T ₁ relaxation time measurement.....	117
4.3.3. Changes in the oxygen configurations with increasing X _{Fe} : ^{17}O MAS and 3QMAS NMR results	122
4.4. Discussion	128
4.4.1. Nature of paramagnetic interactions between Fe and melt networks with varying length scale	128

4.4.2. Variation in structure and extent of disorder of (Mg,Fe)SiO ₃ glasses with iron concentration.....	132
4.4.3. Effect of the valence state of iron on the paramagnetic effect and the structure of iron-bearing silicate glasses: Insights from the comparison with iron-bearing sodium silicate glasses.....	135
4.4.4. Nature of hidden NBO sites in iron-bearing Mg-silicate glasses: Insights from quantum chemical calculations of ¹⁷ O NMR chemical shift.....	138
4.4.5. Limitations of the current study	140
4.5. Implications.....	142
4.6. Conclusion.....	147
APPENDIX.....	149
REFERENCES.....	171

Chapter 5. Extent of disorder in iron-bearing albite and anorthite melts: Insights from multi-nuclear (²⁹Si, ²⁷Al, and ¹⁷O) solid-state NMR study of iron-bearing NaAlSi₃O₈ and CaAl₂Si₂O₈ glasses.....	189
ABSTRACT	189
5.1. Introduction	191
5.2. Experimental Methods	198
5.3. Results.....	203
5.3.1. Iron redox ratio and hyperfine parameters of Na(Al _{1-x} Fe _x)Si ₃ O ₈ , NaAlSi ₃ O ₈ + Fe ₂ O ₃ , and CaAl ₂ Si ₂ O ₈ + Fe ₂ O ₃ glasses with varying iron contents: Mössbauer results	203
5.3.2. The Si and Al environments and extent of intermixing among framework cations in Na(Al _{1-x} Fe _x)Si ₃ O ₈ glasses with varying X [=Fe/(Al+Fe)]: ²⁹ Si and ²⁷ Al NMR results.....	206
5.3.3. The changes in the local configurations around framework cations and oxygen sites with increasing excess Fe ₂ O ₃ in the	

NaAlSi ₃ O ₈ glasses (NaAlSi ₃ O ₈ + Fe ₂ O ₃): ²⁹ Si, ²⁷ Al, and ¹⁷ O NMR results.....	215
5.3.4. The changes in the local configurations around framework cations and oxygen sites with increasing excess Fe ₂ O ₃ in the CaAl ₂ Si ₂ O ₈ glasses (CaAl ₂ Si ₂ O ₈ + Fe ₂ O ₃): ²⁹ Si, ²⁷ Al, and ¹⁷ O NMR results.....	223
5.4. Discussion	233
5.4.1. Effect of iron on the extent of structural disorder in iron-bearing albite and anorthite glasses.....	234
5.4.2. The mixing among non-framework cations and selective partitioning of Na ⁺ , Ca ²⁺ , and Fe ²⁺ into NBO and BOs	237
5.4.3. Iron-induced changes in NMR peak intensities.....	238
5.4.4. Implications.....	241
5.5. Conclusion.....	243
APPENDIX.....	245
REFERENCES.....	264
APPENDIX I. The determination of iron redox ratios (Fe³⁺/ΣFe) of iron-bearing silicate and aluminosilicate glasses: Preliminary electron microprobe (EPMA) study.....	279
APPENDIX II. Effect of spinning speed on ²⁹Si and ²⁷Al solid-state MAS NMR spectra for iron-bearing silicate glasses.....	287
APPENDIX III. Publication list.....	293
A1. Publication list	293
A2. Conference List.....	294
요약 (국문초록)	297

List of Figures

Chapter 3

Figure 3-1. ^{29}Si MAS NMR spectra of iron-bearing sodium silicate glasses $[(\text{Na}_2\text{O})_{1-x} \cdot (\text{Fe}_2\text{O}_3)_x \cdot 2\text{SiO}_2]$ at 9.4 T with varying $X_{\text{Fe}_2\text{O}_3}$ $[= \text{Fe}_2\text{O}_3/(\text{Na}_2\text{O} + \text{Fe}_2\text{O}_3)]$, as labeled. (A) The spectra are plotted on a vertical scale reflecting signal intensity reduction corresponding to the changes in iron content, and (B) a normalized vertical scale. (C) Comparison of ^{29}Si MAS NMR spectra for glasses with $X_{\text{Fe}_2\text{O}_3}$ of 0.05 (black) and 0.3 (red). (D) Variation of peak maxima (open circles) and FWHM (closed circles) of the peak in ^{29}Si MAS NMR spectra with varying iron content $X_{\text{Fe}_2\text{O}_3}$ $[= \text{Fe}_2\text{O}_3/(\text{Na}_2\text{O} + \text{Fe}_2\text{O}_3)]$.

Figure 3-2. (A) Evolution of the ^{29}Si NMR spectra of iron-bearing sodium silicate glasses with $X_{\text{Fe}_2\text{O}_3}$ $[= \text{Fe}_2\text{O}_3/(\text{Na}_2\text{O} + \text{Fe}_2\text{O}_3)]$ and increasing delay time (τ), after saturation of magnetization at 9.4 T. (B) Variation of the integrated peak area of the recovered ^{29}Si NMR signal (normalized with respect to the total peak area of a fully relaxed spectrum (M/M_0)) on the delay time (τ), for (A) iron-free sodium disilicate glass (open circle) and (B) iron-bearing sodium silicate glasses (closed symbols), with varying $X_{\text{Fe}_2\text{O}_3}$ $[= \text{Fe}_2\text{O}_3/(\text{Na}_2\text{O} + \text{Fe}_2\text{O}_3)]$. Circles, triangles, and squares correspond to $X_{\text{Fe}_2\text{O}_3}$ of 0.03, 0.05, and 0.1, respectively.

Figure 3-3. ^{29}Si MAS NMR signal intensity of iron-bearing sodium silicate glasses with varying iron contents. The signal is normalized with respect to that of the iron-free sodium disilicate glasses.

Figure 3-4. ^{17}O MAS NMR spectra of iron-bearing sodium silicate glasses at 9.4 T with varying $X_{\text{Fe}_2\text{O}_3}$ $[= \text{Fe}_2\text{O}_3/(\text{Na}_2\text{O} + \text{Fe}_2\text{O}_3)]$, as labeled.

Figure 3-5. 2D ^{17}O 3QMAS NMR spectra of iron-bearing sodium silicate glasses at 9.4 T with varying $X_{\text{Fe}_2\text{O}_3}$ $[= \text{Fe}_2\text{O}_3/(\text{Na}_2\text{O} + \text{Fe}_2\text{O}_3)]$, as labeled. Contour lines are drawn from 13% to 98% relative intensity with a 5% increment and two

additional lines at 6% and 9.5% levels, for better presentation of low-intensity peaks.

Figure 3-6. (A) Total isotropic projection of ^{17}O 3QMAS NMR spectra of iron-bearing sodium silicate glasses with varying $X_{\text{Fe}_2\text{O}_3}$ [$= \text{Fe}_2\text{O}_3 / (\text{Na}_2\text{O} + \text{Fe}_2\text{O}_3)$], as labeled. (B) Results of fitting the isotropic projection of ^{17}O 3QMAS NMR spectra for iron-bearing sodium silicate glasses with varying $X_{\text{Fe}_2\text{O}_3}$ (fits were performed using 2 Gaussian and 2 Lorentzian functions representing Na-O-Si and Si-O-Si), as labeled. Thick solid lines are the experimental spectra and thin solid lines show the fitted curves and each component.

Figure 3-7. Variation of (A) full width at half maximum (FWHM) and (B) peak maximum in isotropic dimension of Na-O-Si (closed circle) and Si-O-Si (open triangle) peaks in the isotropic projection of ^{17}O 3QMAS NMR spectra of iron-bearing sodium silicate glasses with a varying Fe_2O_3 content ($X_{\text{Fe}_2\text{O}_3}$).

Figure 3-8. Schematic structures describing the potential (visible and hidden in NMR spectra) oxygen clusters in the iron-bearing silicate glasses.

Figure 3-9. Variation of (A) ^{17}O isotropic chemical shifts (δ_{iso}) and (B) quadrupolar coupling products (P_q) of the Na-O-Si (closed circles) and Si-O-Si (open triangles) peaks in ^{17}O 3QMAS NMR spectra of iron-bearing sodium silicate glasses, for different with varying Fe_2O_3 content ($X_{\text{Fe}_2\text{O}_3}$).

Figure 3-10. Variation of Na-O-Si fraction in iron-bearing sodium silicate glasses with varying Fe_2O_3 content ($X_{\text{Fe}_2\text{O}_3}$). The fractions were obtained from ^{17}O isotropic projections of the spectra at 9.4 T (closed circles). The dotted line represents the hypothetical Na-O-Si fraction values (see text), calculated by considering the Fe^{3+} as a network-forming cation and Fe^{2+} as a network-modifying cation. The assumed iron redox ratio ($\text{Fe}^{3+} / \Sigma\text{Fe}$) values are shown on the dotted lines.

Figure 3-A1. Mössbauer spectra of ^{57}Fe in iron-bearing sodium silicate glasses $[(\text{Na}_2\text{O})_{1-x} \cdot (\text{Fe}_2\text{O}_3)_x \cdot 2\text{SiO}_2]$ at 298 K with varying $X_{\text{Fe}_2\text{O}_3}$ [$= \text{Fe}_2\text{O}_3 / (\text{Na}_2\text{O} + \text{Fe}_2\text{O}_3)$], as labeled.

Figure 3-A2. The iron redox ratios ($\text{Fe}^{3+}/\Sigma\text{Fe}$) in the ternary Na-Fe silicate glasses with varying oxygen fugacity (A), SiO_2 content (B), and $\text{Fe}/(\text{Na}+\text{Fe})$ (C and D). Note that (D) shows the $\text{Fe}^{3+}/\Sigma\text{Fe}$ with varying $\text{Fe}/(\text{Na}+\text{Fe})$ for the glasses synthesized in air ($\log f_{\text{O}_2} = -0.68$). The shaded area in Figure (A) corresponds to the assumed oxygen fugacity of an Ar environment in the furnace studied here ($1/20 \sim 1/100 f_{\text{O}_2}^{\text{air}}$). Note also that grey solid and dashed lines in (A) are guides to the eye. The shaded areas in (B) and (C) correspond to the composition of the currently studied glasses (see Table 2-A1 for details and references).

Chapter 4

Figure 4-1. ^{29}Si MAS NMR spectra of iron-bearing magnesium silicate glasses $[(\text{Mg}_{1-x}\text{Fe}_x)\text{SiO}_3]$ with varying $X_{\text{Fe}} [= \text{Fe}/(\text{Mg} + \text{Fe})]$ at 9.4 T, as labeled. (A) The spectra are plotted on a vertical scale reflecting signal intensity reduction corresponding to the changes in iron content, and (B) a normalized vertical scale. Comparison of ^{29}Si MAS NMR spectra for glasses with X_{Fe} of 0.05 (black) and 0.2 (red) is also shown. (C) Variation of peak maxima (open circles) and FWHM (closed circles) of the peak in ^{29}Si MAS NMR spectra with varying iron content X_{Fe} . (D) The previously reported ^{29}Si MAS NMR spectra of iron-bearing sodium silicate glasses $[(\text{Na}_2\text{O})_{1-x} \cdot (\text{Fe}_2\text{O}_3)_x \cdot 2\text{SiO}_2]$ with X_{Fe} of 0.05 (black) and 0.2 (red) is also shown (Kim et al., 2016).

Figure 4-2. ^{29}Si (black closed circles) and ^{17}O (red closed triangles) NMR signal intensities of iron-bearing silicate glasses with varying iron content in atoms per formula unit (*afu*) of $(\text{Mg}_{1-x}\text{Fe}_x)\text{SiO}_3$ glasses. Black open circles represent the ^{29}Si NMR signal intensities for $(\text{Na}_2\text{O})_{1-x} \cdot (\text{Fe}_2\text{O}_3)_x \cdot 2\text{SiO}_2$ glasses (Kim et al., 2016). Note that the line width of the gray dotted line corresponds to the 95% confidence interval centered on the average values of the 20 iterations of simulations for each composition (see Section 4.4.1).

Figure 4-3. Evolution of the ^{29}Si NMR spectra of $(\text{Mg}_{1-x}\text{Fe}_x)\text{SiO}_3$ glasses with $X_{\text{Fe}} [= \text{Fe}/(\text{Mg} + \text{Fe})]$ and increasing delay time (τ , in s), after saturation of magnetization at 9.4 T.

Figure 4-4. Variation in the integrated peak area of the recovered ^{29}Si NMR signal [normalized with respect to the total peak area of a fully relaxed spectrum (M/M_0)] on the delay time (τ) for iron-free MgSiO_3 glass (closed red circles) and iron-bearing magnesium silicate glasses (closed black circles) with varying $X_{\text{Fe}} [= \text{Fe}/(\text{Mg} + \text{Fe})]$. The M/M_0 values for iron-free sodium disilicate glass (open red circles) and iron-bearing sodium silicate glasses (open black circles) with iron concentration are also shown for comparison. The solid and dash lines refer to the relaxation trend described using the stretched exponential equation for the iron-bearing magnesium and sodium silicate glasses, respectively.

Figure 4-5. Variation in the normalized time constant for the recovery of magnetization (T'/T_0 , refers to T' for iron-bearing glasses divided by the T_0 for iron-free glass) in the stretched exponential equation for the iron-bearing magnesium (closed circles) and sodium (open circles) silicate glasses with varying iron concentration (atoms in a formula unit). The solid and dashed lines are guides for the eye.

Figure 4-6. ^{17}O MAS NMR spectra of iron-bearing magnesium silicate glasses $[(\text{Mg}_{1-x}\text{Fe}_x)\text{SiO}_3]$ at 9.4 T with varying $X_{\text{Fe}} [= \text{Fe}/(\text{Mg} + \text{Fe})]$, as labeled.

Figure 4-7. 2D ^{17}O 3QMAS NMR spectra of iron-bearing magnesium silicate glasses at 9.4 T with varying $X_{\text{Fe}} [= \text{Fe}/(\text{Mg} + \text{Fe})]$, as labeled. Contour lines are drawn from 8% to 98% relative intensity with a 6% increment and four additional lines at 4, 6, 11, and 17% levels, for better presentation of the low-intensity peaks.

Figure 4-8. Total isotropic projection of ^{17}O 3QMAS NMR spectra of iron-bearing magnesium silicate glasses at 9.4 T with varying $X_{\text{Fe}} [= \text{Fe}/(\text{Mg} + \text{Fe})]$, as labeled.

Figure 4-9. Schematic diagram of the variation in the paramagnetic effect depending on the distance between paramagnetic center and nuclear spins.

Figure 4-10. The optimized geometry of the non-bridging oxygen cluster in alkaline-earth silicate glasses with (A) Fe²⁺-NBO (Fe²⁺Si₃O₂^{BO}O₂^{Fe-NBO}(OH)₆), (B) Mg²⁺-NBO (Mg²⁺Si₃O₂^{BO}O₂^{Fe-NBO}(OH)₆), and (C) Ca²⁺-NBO (Ca²⁺Si₃O₂^{BO}O₂^{Fe-NBO}(OH)₆).

Figure 4A-1. Mössbauer spectra (dots) and fitting results (gray thick line) of ⁵⁷Fe in (Mg_{1-X}Fe_X)SiO₃ glasses with X = 0.1 (left) and 0.2 (right) at 298 K. The spectra were fitted with two doublets, corresponding to Fe³⁺ (red line) and Fe²⁺ (blue line).

Figure 4-A2. Iron redox ratios (Fe³⁺/ΣFe) in iron-bearing magnesium silicate and alumino-silicate glasses with varying oxygen fugacities [closed symbols; black circles and triangles represent MgO-FeO-SiO₂ glasses (Mysen et al., 1984), black diamonds represent the (Mg_{0.95}Fe_{0.05})SiO₃ glasses, and blue circles represent MgO-Al₂O₃-Fe₂O₃-SiO₂ glasses (Mysen et al., 1985), as reported in previous Mössbauer studies. The Fe³⁺/ΣFe values of (Mg_{0.5}Fe_{0.5})SiO₃ glasses from X-ray absorption spectroscopy are also shown (red closed triangles)(Alderman et al., 2017). Open circles represent the directly measured Fe³⁺/ΣFe values using Mössbauer spectroscopy for the glasses studied here (X = 0.1 and 0.2). The yellow shaded area corresponds to the measured oxygen fugacity of an Ar environment in the furnace studied here. The blue line is a guide to the eye.

Figure 4A-3. ²⁹Si MAS NMR spectra and simulation results for (Mg,Fe)SiO₃ glasses with varying X_{Fe}. Upon simulation peak positions of each Q species are allowed to vary with increasing X_{Fe}. The thick lines represent the observed spectra and thin lines refer to simulation results using the combination of the Gaussian and Lorentzian functions.

Figure 4-A4. ²⁹Si MAS NMR spectra and simulation results for (Mg,Fe)SiO₃ glasses with X_{Fe} = 0 and 0.2. The simulation was based on the scheme 2.

Figure 4-A5. ²⁹Si MAS NMR spectra and simulation results for (Mg,Fe)SiO₃ glasses with varying X_{Fe}. The simulation was performed with the constant peak position for Q species. The thick lines represent the observed spectra and thin lines refer to results fitted using the combination of the Gaussian and Lorentzian functions.

Figure 4-A6. “Sheared” 2D ^{17}O 3QMAS NMR spectra of iron-bearing magnesium silicate glasses with varying X_{Fe} [= Fe/(Mg + Fe)], as labeled. To obtain better resolution of oxygen sites in the spectra, the 2D spectra were sheared with shearing factor of $\sim 15 \mu\text{s}$.

Figure 4-A7. Total isotropic projection of ‘sheared’ ^{17}O 3QMAS NMR spectra with varying X_{Fe} . Comparison of total isotropic projection for ‘sheared’ ^{17}O 3QMAS NMR spectra for $X_{\text{Fe}} = 0$ (black) and $X_{\text{Fe}} = 0.2$ (red) is also shown. Note that the spectrum at $X_{\text{Fe}} = 0.2$ was moved to align the spectra horizontally. The simulation was performed using the 2 Gaussian and 2 Lorentzian functions representing Mg-O-Si (red thin lines) and Si-O-Si (blue thin lines) (Right).

Chapter 5.

Figure 5-1. A ternary phase diagram showing the glass compositions in this study [Black symbols: $\text{Na}(\text{Al}_{1-x}\text{Fe}_x)\text{Si}_3\text{O}_8$, Red symbols: $\text{NaAlSi}_3\text{O}_8 + \text{Fe}_2\text{O}_3$, and Blue symbols: $\text{CaAl}_2\text{Si}_2\text{O}_8 + \text{Fe}_2\text{O}_3$]. M refers to non-framework cation (Na^+ , Ca^{2+} , and Fe^{2+}) and Z refers to framework cation (Al^{3+} and Fe^{3+}). The directions of the arrow for each glass composition refer to the increase in the iron contents.

Figure 5-2. Mössbauer spectra obtained at 298 K (dots) and fitting results (gray thick line) of $\text{Na}(\text{Al}_{0.5}\text{Fe}_{0.5})\text{Si}_3\text{O}_8$ glass, $\text{NaAlSi}_3\text{O}_8 + 5$ and 10 wt% Fe_2O_3 glasses, and $\text{CaAl}_2\text{Si}_2\text{O}_8 + 5$ and 10 wt% Fe_2O_3 glasses, respectively (as labeled). The spectra were fitted with two doublets corresponding to Fe^{3+} (red line) and Fe^{2+} (blue line).

Figure 5-3. ^{29}Si MAS NMR spectra for $\text{Na}(\text{Al}_{1-x}\text{Fe}_x)\text{Si}_3\text{O}_8$ glasses with varying X [i.e., Fe/(Fe+Al)], as labeled. The spectra are plotted on a normalized vertical scale. A comparison of the ^{29}Si MAS NMR spectra for the iron-free (thick grey line) and iron-bearing (thick red line) is also shown. The shaded area with black arrow

shows the preferential broadening of $Q_{Si}^4(mAl)$ species with smaller m number by replacing Al with Fe.

Figure 5-4. ^{27}Al MAS NMR spectra for $Na(Al_{1-x}Fe_x)Si_3O_8$ glasses with varying X [i.e., $Fe/(Fe+Al)$], as labeled. The spectra are plotted on a normalized vertical scale. The rotor backgrounds were subtracted from the spectra (see Section 5A-5). A comparison of the ^{27}Al MAS NMR spectra for the iron-free (thick grey line) and iron-bearing (thick red line) is also shown.

Figure 5-5. (A) 2D ^{27}Al 3QMAS NMR spectra (at 9.4 T) for $Na(Al_{1-x}Fe_x)Si_3O_8$ glasses with varying X [i.e., $Fe/(Fe+Al)$], as labeled. Contour lines are drawn from 8% to 98% relative intensity with a 5% increment and an additional line at 6% levels. The red square in the spectra refers to the expected position of ^{51}Al . (B) Total isotropic projection of ^{27}Al 3QMAS NMR spectra. A comparison of spectrum for the iron-free (thick grey line) and iron-bearing (thick red line) is also shown. The shaded area correspond to the ^{51}Al .

Figure 5-6. ^{29}Si MAS NMR spectra for $NaAlSi_3O_8$ glasses with varying additional Fe_2O_3 (0, 5, and 10 wt% Fe_2O_3). The spectra are plotted on a normalized vertical scale. A comparison of the ^{29}Si MAS NMR spectra for the iron-free (thick grey line) and iron-bearing (thick red line) is also shown.

Figure 5-7. ^{27}Al MAS NMR spectra for $NaAlSi_3O_8$ glasses with varying additional Fe_2O_3 (0, 5, and 10 wt% Fe_2O_3) at 9.4 T. The spectra are plotted on a normalized vertical scale. The rotor backgrounds were subtracted from the spectra (see Section 5A-5). A comparison of the ^{27}Al MAS NMR spectra for the iron-free (thick grey line) and iron-bearing (thick red line) is also shown.

Figure 5-8. (A) 2D ^{27}Al 3QMAS NMR spectra for $NaAlSi_3O_8$ glasses with varying additional Fe_2O_3 (0, 5, and 10 wt% Fe_2O_3) at 9.4 T and 14.1 T, as labeled. Contour lines are drawn from 8% to 98% relative intensity with a 5% increment and an additional line at 6% levels. (B) Total isotropic projection of ^{27}Al 3QMAS NMR

spectra. A comparison of spectrum for the iron-free (thick grey line) and iron-bearing (thick red line) is also shown.

Figure 5-9. (A) ^{17}O 3QMAS NMR spectra for $\text{NaAlSi}_3\text{O}_8$ glasses with varying Fe_2O_3 contents (0, 5, and 10 wt% Fe_2O_3) at 9.4 T, as labeled. Contour lines are drawn from 13% to 93% relative intensity with a 5% increment and three additional lines at 5.5%, 7.5%, and 10% levels. The red square in the spectra refers to the expected position of Na-O-Si (Na-NBO). (B) Total isotropic projection of ^{17}O 3QMAS NMR spectra. A comparison of spectrum for the iron-free (thick grey line) and iron-bearing (thick red line) is also shown.

Figure 5-10. ^{29}Si MAS NMR spectra for $\text{CaAl}_2\text{Si}_2\text{O}_8$ glasses with varying additional Fe_2O_3 (0, 5, and 10 wt% Fe_2O_3). The spectra are plotted on a normalized vertical scale. A comparison of the ^{29}Si MAS NMR spectra for the iron-free (thick grey line) and iron-bearing (thick red line) is also shown.

Figure 5-11. ^{27}Al MAS NMR spectra for $\text{CaAl}_2\text{Si}_2\text{O}_8$ glasses with varying additional Fe_2O_3 (0, 5, and 10 wt% Fe_2O_3) at 9.4 T. The spectra are plotted on a normalized vertical scale. The rotor backgrounds were subtracted from the spectra (see Section 5A-5). A comparison of the ^{27}Al MAS NMR spectra for the iron-free (thick grey line) and iron-bearing (thick red line) is also shown.

Figure 5-12. (A) 2D ^{27}Al 3QMAS NMR spectra for $\text{CaAl}_2\text{Si}_2\text{O}_8$ glasses with varying additional Fe_2O_3 (0, 5, and 10 wt% Fe_2O_3) at 9.4 T (top) and 14.1 T (bottom), as labeled. Contour lines are drawn from 8% to 93% relative intensity with a 5% increment and two additional lines at 4 and 6% levels. The red square in the spectra refers to the expected position of ^{51}Al . (B) Total isotropic projection of ^{27}Al 3QMAS NMR spectra. A comparison of spectrum for the iron-free (thick grey line) and iron-bearing (thick red line) is also shown.

Figure 5-13. (A) ^{17}O 3QMAS NMR spectra for $\text{CaAl}_2\text{Si}_2\text{O}_8$ glasses with varying Fe_2O_3 contents (0, 5, and 10 wt% Fe_2O_3) at 9.4 T, as labeled. Contour lines are drawn from 13% to 98% relative intensity with a 5% increment and two additional lines

at 5.5% and 9% levels. (B) Total isotropic projection of ^{17}O 3QMAS NMR spectra. A comparison of spectrum for the iron-free (thick grey line) and iron-bearing (thick red line) is also shown.

Figure 5-14. Variations in the (A) ^{29}Si , (B) ^{27}Al , and (C) ^{17}O MAS NMR signal intensities of $\text{Na}(\text{Al}_{1-x}\text{Fe}_x)\text{Si}_3\text{O}_8$ (red circles), $\text{NaAlSi}_3\text{O}_8 + \text{Fe}_2\text{O}_3$ glasses (black triangles), and $\text{CaAl}_2\text{Si}_2\text{O}_8 + \text{Fe}_2\text{O}_3$ glasses with varying iron content (atom%). The lines are to guide the eye.

Figure 5A-1. ^{29}Si MAS NMR spectra of $\text{Na}(\text{Al}_{1-x}\text{Fe}_x)\text{Si}_3\text{O}_8$ (left), $\text{NaAlSi}_3\text{O}_8 + \text{Fe}_2\text{O}_3$ (middle), and $\text{CaAl}_2\text{Si}_2\text{O}_8 + \text{Fe}_2\text{O}_3$ (right) glasses with varying iron content, as labeled. The spectra are plotted on a vertical scale reflecting signal intensity reduction corresponding in iron content.

Figure 5A-2. ^{27}Al MAS NMR spectra (obtained at 9.4 T) of $\text{Na}(\text{Al}_{1-x}\text{Fe}_x)\text{Si}_3\text{O}_8$ (left), $\text{NaAlSi}_3\text{O}_8 + \text{Fe}_2\text{O}_3$ (middle), and $\text{CaAl}_2\text{Si}_2\text{O}_8 + \text{Fe}_2\text{O}_3$ (right) glasses with varying iron content, as labeled. The spectra are plotted on a vertical scale reflecting signal intensity reduction corresponding in iron content.

Figure 5A-3. ^{27}Al NMR spectra at 9.4 T with 17 kHz of spinning speed for $\text{Na}(\text{Al}_{1-x}\text{Fe}_x)\text{Si}_3\text{O}_8$ (top), $\text{NaAlSi}_3\text{O}_8 + \text{Fe}_2\text{O}_3$ (middle), and $\text{CaAl}_2\text{Si}_2\text{O}_8 + \text{Fe}_2\text{O}_3$ (bottom) glasses with varying iron content, showing the spinning side band (*).

Figure 5A-4. The ^{27}Al MAS NMR spectra at 9.4 T with 17 kHz of spinning speed for background-subtracted iron-bearing aluminosilicate glasses [black, $\text{Na}(\text{Al}_{0.5}\text{Fe}_{0.5})\text{Si}_3\text{O}_8$ (left), $\text{NaAlSi}_3\text{O}_8 + 10 \text{ wt}\% \text{Fe}_2\text{O}_3$ (center), and $\text{CaAl}_2\text{Si}_2\text{O}_8 + \text{Fe}_2\text{O}_3$ (right) glasses] and rotor background (blue).

Figure 5A-5(1). ^{27}Al 3QMAS NMR spectra at 9.4 T for $\text{Na}(\text{Al}_{1-x}\text{Fe}_x)\text{Si}_3\text{O}_8$ glasses with varying iron content, showing the spinning side band (*). Contour lines are drawn from 8% to 98% relative intensity with a 5% increment and an additional line at 6% levels.

Figure 5A-5(2). ^{27}Al 3QMAS NMR spectra at 9.4 T for $\text{NaAlSi}_3\text{O}_8 + \text{Fe}_2\text{O}_3$ glasses with varying iron content, showing the spinning side band (*). Contour lines are

drawn from 13% to 93% relative intensity with a 5% increment and three additional lines at 5.5%, 7.5%, and 10% levels.

Figure 5A-6. ^{17}O MAS NMR spectra for $\text{NaAlSi}_3\text{O}_8 + \text{Fe}_2\text{O}_3$ (left) and $\text{CaAl}_2\text{Si}_2\text{O}_8 + \text{Fe}_2\text{O}_3$ (right) glasses with varying Fe_2O_3 (wt%) content, as labeled.

Figure 5A-7. ^{29}Si MAS NMR spectra and simulation results for $\text{NaAlSi}_3\text{O}_8$ (top), $\text{Na}(\text{Al}_{0.5}\text{Fe}_{0.5})\text{Si}_3\text{O}_8$ (with $\text{Fe}^{3+}/\Sigma\text{Fe} \sim 0.8$, middle), and $\text{NaAlSi}_3\text{O}_8 + 10 \text{ wt}\% \text{Fe}_2\text{O}_3$ (with $\text{Fe}^{3+}/\Sigma\text{Fe} \sim 0.5$, bottom) glasses. The simulation was performed with the constant peak position and relative fractions for $\text{Q}^4_{\text{Si}}(m\text{Al})$ species. The thick lines represent the observed spectra and thin lines refer to results fitted using the Gaussian functions for iron-free glass and combination of the Gaussian and Lorentzian functions for iron-bearing glasses.

Figure 5A-8. ^{29}Si MAS NMR spectra and simulation results for $\text{CaAl}_2\text{Si}_2\text{O}_8$ (top) and $\text{CaAl}_2\text{Si}_2\text{O}_8 + 10 \text{ wt}\% \text{Fe}_2\text{O}_3$ (with $\text{Fe}^{3+}/\Sigma\text{Fe} \sim 0.3$, bottom) glasses. The simulation was performed with the constant peak position and relative fractions for $\text{Q}^4_{\text{Si}}(m\text{Al})$ species. The thick lines represent the observed spectra and thin lines refer to results fitted using the Gaussian functions for iron-free glass and combination of the Gaussian and Lorentzian functions for iron-bearing glasses.

APPENDIX I.

Figure A1-1. (A) Fe *L*-edge emission spectra (operating with 10 keV) of crystalline iron oxides (FeO and Fe_2O_3). The enlarged spectra (B) are also shown to manifest the $\text{Fe}L\alpha$ peaks.

Figure A1-2. Variations of the $\text{Fe}L\alpha$ peak positions as a function of the total Fe concentration for a series of pure Fe^{2+} -bearing (black open symbols) and Fe^{3+} -bearing (black closed symbols) minerals and iron-bearing silicate glasses in the current study (colored closed symbols).

APPENDIX II.

Figure A2-1. ^{29}Si MAS NMR spectra for $(\text{Mg}_{0.95}\text{Fe}_{0.05})\text{SiO}_3$ glass with varying spinning speed (6, 10, and 14 kHz) at 9.4 T. The asterisks (*) denote spinning side band.

Figure A2-2. The normalized ^{27}Al MAS NMR spectra for Fe_2O_3 -bearing $\text{CaAl}_2\text{Si}_2\text{O}_8$ glasses with varying Fe_2O_3 at spinning speed of (A) 20 kHz and (B) 30 kHz. The asterisks (*) refer the spinning side band.

Figure A2-3. ^{27}Al MAS NMR spectra for $\text{CaAl}_2\text{Si}_2\text{O}_8$ glasses with 5 wt% Fe_2O_3 (left) and 10 wt% Fe_2O_3 (right) with varying spinning speed (15 to 30 kHz). The spectra are plotted on a vertical scale reflecting the variation of signal intensity with the changes in spinning speed.

Figure A2-4. The normalized ^{27}Al NMR signal intensities of Fe_2O_3 -bearing $\text{CaAl}_2\text{Si}_2\text{O}_8$ glasses with respect to the signal intensity of Fe-free glass with varying spinning speed. Closed circles, open squares, open circles, and closed triangles refer the 17, 20, 25, and 30 kHz of spinning speed, respectively. Grey line is guide to eye.

List of Tables

Chapter 2.

Table 2-1. List of the solid-state NMR studies for minerals and glasses containing para-magnetic cation

Chapter 3.

Table 3-1. Nominal compositions and ICP analyses of iron-bearing sodium silicate glasses ($\text{Na}_2\text{O}-\text{Fe}_2\text{O}_3-\text{SiO}_2$) with varying $X_{\text{Fe}_2\text{O}_3}$ [$= \text{Fe}_2\text{O}_3 / (\text{Na}_2\text{O} + \text{Fe}_2\text{O}_3)$].

Table 3-2. NMR experimental conditions (at 9.4 T, 14 kHz) used in this study.

Table 3-3. NMR parameters (^{17}O δ_{iso} and P_Q) of oxygen sites in iron-bearing sodium silicate glasses with varying iron content ($X_{\text{Fe}_2\text{O}_3}$)^a.

Table 3-A1. Iron redox ratios ($\text{Fe}^{3+} / \Sigma\text{Fe}$) for $\text{Na}_2\text{O}-\text{Fe}_2\text{O}_3-\text{SiO}_2$ glasses, as reported in previous studies that used Mössbauer spectroscopy at 298 K.

Chapter 4.

Table 4-1. Nominal compositions and ICP analyses for $\text{MgO}-\text{FeO}-\text{SiO}_2$ glasses with varying X_{Fe} [$=\text{Fe} / (\text{Mg} + \text{Fe})$].

Table 4-2. NMR experimental conditions used in this study (at 9.4 T).

Table 4-3. Summary of fitting parameters [stretched exponent (β) and time constant for the recovery of magnetization (T')] for spin-lattice relaxation curves for $\text{MgO}-\text{FeO}-\text{SiO}_2$ glasses with varying X_{Fe} [$=\text{Fe} / (\text{Mg} + \text{Fe})$], based on the stretched-exponential equation.

Table 4-A1. The previous studies for iron-bearing Mg-silicate glasses and melts at ambient and high pressures

Table 4-A2. Cation-oxygen distances [d(T-O)] and coordination number in iron-bearing silicate glasses and melts from X-ray and neutron scattering studies.

Table 4-A3. NMR parameters of silicon sites (^{29}Si chemical shielding) in model clusters calculated from quantum chemical calculations.

Table 4-A4. Equilibrium geometries and NMR parameters of non-bridging oxygen sites (NBO, up) and bridging oxygen sites (BO, bottom) in model clusters calculated from quantum chemical calculations.

Chapter 5.

Table 5-1. Nominal compositions for iron-bearing Na- and Ca-aluminosilicate glasses with varying iron content.

Table 5-2. Fitting parameters [isomer shift (δ , mm/s) and quadrupole splitting (Δ , mm/s)] and iron redox ratio ($\text{Fe}^{3+}/\Sigma\text{Fe}$) of room-temperature ^{57}Fe Mössbauer spectra for iron-bearing Na- and Ca-aluminosilicate glasses.

Table 5A-1(1). ^{27}Al NMR experimental conditions at 9.4 T used in this study.

Table 5A-1(2). ^{27}Al NMR experimental conditions at 14.1 T used in this study.

Table 5A-1(3). ^{17}O NMR experimental conditions at 9.4 T used in this study.

Table 5A-1(4). ^{29}Si NMR experimental conditions at 9.4 T used in this study.

Table 5A-2. The center of gravity (obtained from MAS and isotropic dimension) and NMR parameters for iron-bearing Na-aluminosilicate glasses (obtained at 9.4 T and 14.1 T)

APPENDIX I.

Table A1-1. Measured $\text{Fe}L\alpha$ peak positions and calculated $\text{Fe}^{3+}/\Sigma\text{Fe}$ for various silicate glasses

Chapter 1. Introduction

Iron is one of the most abundant transition metals in the natural magmatic melts of the Earth and other terrestrial planets. In the silicate melts, iron can be found in variable concentrations and multiple valence states (e.g., Baratoux et al., 2011; Berry et al., 2008; McDonough and Sun, 1995). The physical and chemical properties of silicate melts (e.g., viscosity, density, and element partitioning) are strongly dependent on iron concentration and the redox state (e.g., Dingwell et al., 1988; Dingwell and Virgo, 1988; Mysen and Richet, 2018; Mysen et al., 1985) (see Sections 3.1 and 4.1 for details). Changes in the macroscopic properties with varying iron content and oxidation state would affect the geochemical processes (i.e., magma migration) and chemical evolution of the early Earth. For example, the increase in melt density and the decrease in the viscosity with increasing iron content in silicate melts, facilitating the rapid descent of the iron-rich silicate melts, promotes the compilation of dense silicate melts at the core-mantle boundary (e.g., Labrosse et al., 2007; Lee et al., 2010; Williams, 1998). The changes in iron partitioning between silicate melts and minerals with varying iron contents and redox state in silicate melts may have implication for the O₂ release in the Great Oxygenation Event of Archean to Proterozoic Transition (Andrault et al., 2017). The detailed descriptions of the geological importance for my study in this thesis are given below.

1.1. Geological importance of the study for atomic configurations of iron-bearing silicate glasses and melts

1.1.1. Iron in the magmatic melts

The iron concentration in natural magmatic melts ranges from ~ 0.5 wt% in rhyolitic melts to ~ 20 wt% in basaltic melts (Philpotts, 1982; Wright and Fiske, 1971). The iron content in silicate melts is significantly related to the composition of the melts (e.g., SiO_2 content), which depends on the tectonic setting of magma generation and their host rock. The melt composition also has an influence on the iron redox state ($\text{Fe}^{3+}/\Sigma\text{Fe}$) in the magmatic melts. In particular, the $\text{Fe}^{3+}/\Sigma\text{Fe}$ in silicate melts generally decreases with increasing the average cation field strength (i.e., charge/ionic radii) of non-framework cations (e.g., Na^+ , Ca^{2+} , and Mg^{2+}) (Mysen and Richet, 2018; Paul and Douglas, 1965). The variations in the iron content and redox state can cause the changes in the viscous flow of silicate melts, which attribute to the transition of eruption style of the volcanoes.

Previous studies of viscosity measurement for silicate melts have shown that the iron content and redox state affect the melt viscosity. The viscosity of iron-bearing sodium silicate melts along the $\text{Na}_2\text{Si}_2\text{O}_5$ - $\text{NaFe}^{3+}\text{Si}_2\text{O}_6$ (acmite) join at ~ 1300 °C increases with increasing iron content from $10^{1.47}$ Pa s ($\text{Na}_2\text{O}:\text{Fe}_2\text{O}_3:\text{SiO}_2 = 0.8:0.2:2$) to $10^{1.73}$ Pa s ($\text{Na}_2\text{O}:\text{Fe}_2\text{O}_3:\text{SiO}_2 = 0.5:0.5:2$) at constant $\text{Fe}^{3+}/\Sigma\text{Fe}$. The viscosity of MgO-FeO-SiO_2 melts at a constant SiO_2 of 55 wt% also slightly decreases with increasing Fe^{2+}/Mg ratio, from $10^{1.66}$ (for $\text{Fe}^{2+}/\text{Mg} = 0.45$) to $10^{1.32}$ (for $\text{Fe}^{2+}/\text{Mg} = 4.5$) at constant $\text{Fe}^{3+}/\text{Fe} < 0.02$. For the melts with composition similar to the magma of Mars (i.e., tholeiitic and alkaline Fe-rich silicate melts), the viscosity of the Martian basaltic melts with 20 wt% FeO_{tot} is about $10^{0.5}$ lower than that with 14 wt% FeO_{tot} .

Based on the previous study of correlation between the composition, viscosity and eruptive style of rhyolitic magma, the small changes in viscosity can affect the volcanic eruption style (Di Genova et al., 2017). Particularly, the

recent studies showed that the slight changes in the ratio between network-modifying cations (i.e., Na^+ , Ca^{2+} , Mg^{2+} , and Fe^{2+}) and network-forming cation except SiO_2 (i.e., Al^{3+} and Fe^{3+}) can lead to a drastic changes in the viscosity of rhyolitic melts, which resulting in a drastic rheological transition. Therefore, the iron-induced decrease in viscosity can trigger the transition of the volcanic eruption style from explosive to effusive.

Taking into consideration the structural role of constituent cations, the drastic transition of the eruption style is attributed to changes in the degree of polymerization. The changes in the viscosity with increasing iron content and redox ratio, mentioned above, imply that the Fe^{3+} is mainly a network-former and Fe^{2+} is a network-modifier. However, the structural role of iron is still debated, and the changes in viscosity with iron content, which are difficult to understand intuitively, have been observed. For example, although Si^{4+} and Fe^{3+} are both network-forming cations, there is a trend that viscosity decreases as Si^{4+} substitutes Fe^{3+} . This is because the viscosity of silicate melts is affected both by the degree of polymerization (which can be estimated from the composition and structural role of iron) and the degree of disorder among framework cations (i.e., Si, Al, and Fe^{3+}). Thus, the key to understanding the variations of macroscopic properties with iron contents and oxidation states of iron-bearing silicate glasses and melts is the probing the atomic structures and extent of disorder. In this thesis, my efforts to reveal the atomic structures of iron-bearing silicate glasses for understanding the transport properties of silicate melts are shown in Chapters 3.4.5, 4.5, and 5.4.7.

1.1.2. Iron in natural silicate glasses

Iron content and iron oxidation state in natural silicate glasses (such as basaltic glasses, melt inclusion in minerals, submarine pillow rim glasses, and obsidian) are significantly affected by the oxygen fugacity, composition of source magma, temperature, and pressure. Particularly, the oxidation state of iron is one of the important factor revealing the oxidation conditions in Earth's interior. In general, it is relatively well known that the oxygen fugacity is one of the main factor controlling the iron oxidation state in silicate melts and glasses: the $\text{Fe}^{3+}/\Sigma\text{Fe}$ decreases with decreasing oxygen fugacity (i.e., $\log f_{\text{O}_2}$), and the trends of decreasing $\text{Fe}^{3+}/\Sigma\text{Fe}$ with decreasing $\log f_{\text{O}_2}$ are heavily dependent on the composition of melts and glasses. The composition of glasses and melts is also important factor affecting the iron oxidation state. To understand the changes in oxidation state with varying composition, the revealing the structural role of iron in silicate glasses are necessary.

In addition, the probing the structure and disorder of silicate glasses provides the opportunity to understand the formation of amorphous SiO_2 -rich phases in basaltic glasses. Recent studies have revealed the formation of amorphous SiO_2 -rich phases in a Hawaiian basaltic glasses in contact with aqueous fluids (Chemtob et al., 2010; Chemtob et al., 2012; Zhu et al., 2006). The phase is somewhat similar to those observed on the surface of the Mars (covered by basaltic glasses) (Squyres et al., 2008). The similarity implies the potential interaction between basaltic glasses and aqueous solutions. Although the dissolution may play an important role in the formation of the deposits, the origin of SiO_2 -rich deposits remains to be explored. Atomic structures of silicate glasses may allow us to reveal the structural insights into the formation of SiO_2 -rich phases from basaltic glasses.

1.1.3. Iron in the Earth's deep interior from lower mantle to core-mantle boundary

Seismic heterogeneities in the lower mantle and core-mantle boundary have been attributed to thermal and/or chemical variations in the Earth's interior. Of particular interest in chemical variations is the effect of iron on the density and seismic velocity for crystalline and melts with $(\text{Mg,Fe})\text{SiO}_3$ composition. Previous studies for the Fe-bearing bridgmanite (the most abundant mineral phase in the lower mantle) have suggested that the spin transition of the octahedrally-coordinated Fe^{3+} in bridgmanite is responsible for the changes in seismic velocity in the lower mantle (Fu et al., 2018). Note that earlier synchrotron X-ray emission spectroscopy (XES) studies of Fe spin transition in silicate glasses under compression have provided irreconcilable interpretations that vary from complete transitions to low spin states at high pressure to a prevalence of high spin states.

It has been also suggested that the seismic heterogeneity in core-mantle boundary (V_p and V_s decrease up to around 10% and 30%, respectively), which is named ultra-low velocity zone (ULVZ), stems from the chemical variation. The estimated sources for chemical heterogeneity in ULVZ are the iron-rich crystalline [e.g., iron-enriched $(\text{Mg,Fe})\text{O}$ (Wicks et al., 2010), iron-enriched post-perovskite (Mao et al., 2006), and subducted banded iron formation (Dobson and Brodholt, 2005), etc.] and/or Fe-rich partial melts associated with mantle-core interaction and ultra-dense remnants of subduction (Rost et al., 2005; Williams, 1998). While the origin of ULVZ in core-mantle boundary has been still controversial, the rheological characteristics of Fe^{2+} -rich partial melts may explain the evolution and morphology of ULVZ. As mentioned in Section 1.1.1, the viscosity of iron-bearing silicate melts is lower than that of iron-poor silicate melts. Thus, the

dense and less viscous Fe-rich melts facilitate the rapid descent into the Earth's deep interior and accumulation on the core-mantle boundary. The thin-patch shape of ULVZ (5~40 km thickness) can be also explained by the viscosity of Fe²⁺-partial melts. Based on the previous dynamic simulation studies, the thin layer of ULVZ can be attributed to the low viscosity of Fe²⁺-partial melts, and the localization of ULVZ without spreading is caused by the stirring of partial melts due to the low viscosity (Hernlund and Jellinek, 2010; McNamara et al., 2010). Thus, the high-resolution solid-state NMR study for (Mg,Fe)SiO₃ glasses was performed to investigate the microscopic origins of changes in viscosity of mafic silicate melts (Chapter 4).

1.1.4. Iron as the source of the Great Oxidation Event in the early Earth

The Great Oxidation Event, occurring around 2.35 billion years ago, switches the Earth's atmosphere from being oxygen free to having a small percentage of oxygen. To explain this event, the different scenarios were proposed, including the emergence of oxygenic cyanobacteria and changes in the oxidation state of sulfur in volcanic gases. The iron oxidation and disproportionation of iron [i.e., Fe²⁺ → Fe³⁺ + metallic iron (Fe⁰)] in the silicate minerals are also proposed as one of the scenarios of Great Oxidation Event. Because the Fe³⁺ can easily incorporate with Al³⁺ in bridgmanite (a dominant mineral in the lower mantle), the disproportionation of iron may be enhanced in lower mantle when the crystallization occurs in the magma ocean. Thus, the Fe metal segregation into the core and the excess of Fe³⁺ in the lower mantle may prevail in the primitive lower mantle. The recent study of X-ray absorption spectroscopy (XANES) has suggested that the Fe³⁺ in the bridgmanite with a primitive mantle composition increases with increasing pressure up to ~ 40% (~ 120 GPa). This corresponds to ~ 2 × 10²³ mol of Fe³⁺

in the lower mantle and an excess of $\sim 10^{23}$ mol of oxygen compared to a predominantly Fe^{2+} -bearing silicate mantle (Andrault et al., 2017). The excess O_2 would release in the atmosphere with the transition of tectonic regime from upper mantle convection to whole mantle convection in the Archean to Proterozoic Transition. Here, the partitioning of Fe^{3+} and Fe^{2+} between minerals and silicate melts would be another key factor to controlling the disproportionation reaction of iron in the primitive mantle. As the crystallization of melts in a Hadean Magma Ocean occurs, the residual partial melts are greatly enriched with iron because the iron tends to be preferentially partitioned into liquid at ambient and high pressure (Andrault et al., 2012; Mysen, 1975). If the incorporation of Fe^{2+} and Mg^{2+} is preferred in the residual melts, the Fe^{3+} excess in bridgmanite would be enhanced. On the other hand, if the incorporation of Fe^{3+} and Al^{3+} prevails in the melts, the excess Fe^{3+} would be drained to the basement of mantle because Fe-enriched melts would be heavier than the Fe-depleted mantle. Thus, the further studies of unveiling atomic structure and disorder of iron-bearing silicate melts are needed to investigate the incorporation of iron and constituent cations in silicate melts. The high-resolution solid-state NMR studies in this thesis would provide the opportunity to obtain the information of preferential interaction between Fe and nuclear spins.

1.1.5. Iron in meteorites

The iron is the abundant element in the entire solar system as well as the Earth. The iron concentrations in the CI chondrite (~ 20 wt% FeO) is much higher than that in the bulk silicate earth (~ 8 wt% FeO), indicating that the iron content of the silicate melts in the early Earth (before the differentiation) is presumably higher than that in present Earth. The previous studies for

chemical composition of Martian meteorite have suggested that the Fe content in bulk silicate Mars (~ 18 wt%) is higher than that in Earth (Tuff et al., 2013), implying that the evolution of the Mars is different from that of the Earth. To understand the thermal history (i.e., evolution and differentiation) of parent body including asteroid and Mars, the detailed knowledge of mobility and diffusion of iron in chondrite is necessary. While the experimental studies have reported with detailed description of the chemical characteristics and analysis of Fe isotope (Chernonozhkin et al., 2017; Leroux et al., 2000), the fundamental questions on the Fe partitioning and diffusion in the minerals and glasses of meteorites still remains to be explored. Previous studies have shown that quantifying the atomic disorder in iron-bearing silicate glasses has strong implications for the Fe diffusion in the silicate melts (Lee et al., 2004; Park and Lee, 2016). Therefore, the probing the atomic disorder in iron-bearing silicate minerals and glasses is essential to understand the Fe diffusion and differentiation in the chondrite. Although the solid-state NMR is limited to the analysis of bulk sample (making it difficult to obtain the structural information with a spatial resolution), the NMR studies of synthetic model system, together with other spectroscopic method such as Raman spectroscopy, would provide the detailed information of the atomic structure and disorder of minerals and glasses in the chondrites.

I note that my study for iron-bearing silicate glasses was initially motivated by the interest in the high content of iron in the meteorites. Although it was challenged to solve during my Ph. D. course, I would like to introduce the research topics with respect to the atomic structure of iron-bearing minerals and glasses in the meteorites.

1.2. Contents of thesis

During my Ph. D. course, I performed extensive solid-state NMR studies on various compositions of iron-bearing silicate and aluminosilicate glasses in order to systematically explore the effect of iron content on structure and disorder of iron-bearing silicate and aluminosilicate glasses. Knowledge of structural changes induced by the variations of iron content is essential to understand the macroscopic properties of corresponding silicate melts such as transport and thermodynamic properties. Notwithstanding, the detailed structure and disorder of iron-bearing glasses is largely unknown, because the solid-state NMR, one of the most versatile experimental methods to probe the structure of oxide glasses, cannot be fully utilized for exploring the structural details of iron-bearing glasses as the unpaired electrons in Fe induce strong local magnetic fields that mask the original spectroscopic features (i.e., paramagnetic effect). In Chapter 2, the difficulties of the probing structure of silicate glasses containing paramagnetic cation using solid-state NMR and technical motivation of this study are described.

In Chapter 3, the novel structural insights into the silicon and oxygen configurations in the iron-bearing sodium disilicate glasses with iron content reaching 22.9 wt% Fe₂O₃ ($Fe^{3+}/\Sigma Fe = 0.89$) are provided with the quantitative analysis of ²⁹Si and ¹⁷O NMR results. Because of the clear resolution of multiple structural sites in the NMR spectra, sodium disilicate glasses (an archetypal model system for complex silicate glasses) are suitable to initially study the effect of iron on each structural site, even with the spectral broadening. Despite the inherent difficulties due to the paramagnetic effect, these results demonstrated that the solid-state NMR techniques can be effectively applied to the study of iron-bearing silicate glasses.

Although it has been challenging to probe the atomic structure and disorder of the geologically vital (Mg,Fe)SiO₃ glasses due to severe overlap among spectral features, the results of high-resolution solid-state NMR have unveiled structural details in Fe²⁺-dominant (Mg,Fe)SiO₃ glasses (Fe³⁺/ΣFe = 0.2, Chapter 4). In conjunction with the NMR results of Fe³⁺-dominant sodium silicate glasses in Chapter 3, the effect of valence state of iron on the short- (i.e., Q species, NBO/BO) and medium-range (i.e., spatial proximity between iron and nuclear spins) of atomic structure was explored. Based on these results, the schemes to account for the paramagnetic effect depending on the distance between paramagnetic center and nuclear spins are also proposed. The unique NMR results of (Mg,Fe)SiO₃ glasses provide atomistic insights into the viscous flow of mafic silicate melts and the morphology of ultra-low velocity zone.

Beyond the binary silicate glasses, the detailed structure and disorder of iron-bearing Na- and Ca-aluminosilicate glasses can be obtained using high-resolution solid-state NMR in (Chapter 5). While it is too difficult to observe the atomic configurations in iron-bearing aluminosilicate glasses because the peaks are considerably overlapped due to the increase in number of species (and the types of chemical bonding), the multi-nuclear (²⁹Si, ¹⁷O and ²⁷Al) NMR would provide the opportunity to probe the coordination environments of two types of framework cations (²⁹Si and ²⁷Al), connectivity, and proximity of each atomic species. Thus, the local atomic configurations around aluminum, silicon, and oxygen of fully-polymerized Na- and Ca-aluminosilicate glasses (which correspond to the rhyolitic melts) with varying iron content were investigated from the results of solid-state NMR, showing that the changes in atomic configuration with Fe and constituent species (i.e., Al framework) depend on the cation field strength of non-framework cation

(e.g., Na⁺, Ca²⁺, and Fe²⁺). The changes in signal intensities of ²⁷Al and ²⁹Si NMR spectra provided the information of the preferential spatial proximity between Fe and framework cations (Al and Si).

Together with the aforementioned progress in solid-state NMR studies of iron-bearing and aluminosilicate glasses, my efforts to reveal the iron redox state of silicate glasses using electron microprobe are also shown in this dissertation (APPENDIX I). In addition, the preliminary NMR results for the effect of spinning speed on NMR signal intensity of iron-bearing silicate glasses are described in APPENDIX II.

REFERENCES

- Andrault, D., Munoz, M., Pesce, G., Cerantola, V., Chumakov, A., Kantor, I., Pascarelli, S., Ruffer, R. and Hennet, L. (2017) Large oxygen excess in the primitive mantle could be the source of the Great Oxygenation Event. *Geochemical Perspectives Letters* 6, 5-10.
- Andrault, D., Petitgirard, S., Lo Nigro, G., Devidal, J.L., Veronesi, G., Garbarino, G. and Mezouar, M. (2012) Solid-liquid iron partitioning in Earth's deep mantle. *Nature* 487, 354-357.
- Baratoux, D., Toplis, M.J., Monnereau, M. and Gasnault, O. (2011) Thermal history of Mars inferred from orbital geochemistry of volcanic provinces. *Nature* 472, 338-341.
- Berry, A.J., Danyushevsky, L.V., St C. O'Neill, H., Newville, M. and Sutton, S.R. (2008) Oxidation state of iron in komatiitic melt inclusions indicates hot Archaean mantle. *Nature* 455, 960-963.
- Chemtob, S.M., Jolliff, B.L., Rossman, G.R., Eiler, J.M. and Arvidson, R.E. (2010) Silica coatings in the Ka'u Desert, Hawaii, a Mars analog terrain: A micromorphological, spectral, chemical, and isotopic study. *Journal of Geophysical Research-Planets* 115.

- Chemtob, S.M., Rossman, G.R. and Stebbins, J.F. (2012) Natural hydrous amorphous silica: Quantitation of network speciation and hydroxyl content by ^{29}Si MAS NMR and vibrational spectroscopy. *Am. Mineral.* 97, 203-211.
- Chernonozhkin, S.M., Weyrauch, M., Goderis, S., Oeser, M., McKibbin, S.J., Horn, I., Hecht, L., Weyer, S., Claeys, P. and Vanhaecke, F. (2017) Thermal equilibration of iron meteorite and pallasite parent bodies recorded at the mineral scale by Fe and Ni isotope systematics. *Geochim. Cosmochim. Acta* 217, 95-111.
- Di Genova, D., Kolzenburg, S., Wiesmaier, S., Dallanave, E., Neuville, D.R., Hess, K.U. and Dingwell, D.B. (2017) A compositional tipping point governing the mobilization and eruption style of rhyolitic magma. *Nature* 552, 235-238.
- Dingwell, D.B., Brearley, M. and Dickinson, J.E. (1988) Melt densities in the Na_2O - FeO - Fe_2O_3 - SiO_2 system and the partial molar volume of tetrahedrally-coordinated ferric iron in silicate melts. *Geochim. Cosmochim. Acta* 52, 2467-2475.
- Dingwell, D.B. and Virgo, D. (1988) Viscosities of melts in the Na_2O - FeO - Fe_2O_3 - SiO_2 system and factors controlling relative viscosities of fully polymerized silicate melts. *Geochim. Cosmochim. Acta* 52, 395-403.
- Dobson, D.P. and Brodholt, J.P. (2005) Subducted banded iron formations as a source of ultralow-velocity zones at the core-mantle boundary. *Nature* 434, 371-374.
- Fu, S., Yang, J., Zhang, Y., Liu, J., Okuchi, T., McCammon, C., Kim, H.-I., Lee, S.K. and Lin, J.-F. (2018) Effects of Fe^{3+} spin transition on the elasticity of Fe-bearing bridgmanite in the Earth's lower mantle. *Geophysical Research Letters*, submitted.
- Hernlund, J.W. and Jellinek, A.M. (2010) Dynamics and structure of a stirred partially molten ultralow-velocity zone. *Earth Planet. Sci. Lett.* 296, 1-8.
- Labrosse, S., Hernlund, J.W. and Coltice, N. (2007) A crystallizing dense magma ocean at the base of the Earth's mantle. *Nature* 450, 866-869.
- Lee, C.T., Luffi, P., Hoink, T., Li, J., Dasgupta, R. and Hernlund, J. (2010) Upside-down differentiation and generation of a 'primordial' lower mantle. *Nature* 463, 930-933.

- Lee, S.K., Cody, G.D., Fei, Y.W. and Mysen, B.O. (2004) Nature of polymerization and properties of silicate melts and glasses at high pressure. *Geochim. Cosmochim. Acta* 68, 4189-4200.
- Leroux, H., Doukhan, J.C. and Perron, C. (2000) Microstructures of metal grains in ordinary chondrites: Implications for their thermal histories. *Meteoritics & Planetary Science* 35, 569-580.
- Mao, W.L., Mao, H.K., Sturhahn, W., Zhao, J., Prakapenka, V.B., Meng, Y., Shu, J., Fei, Y. and Hemley, R.J. (2006) Iron-rich post-perovskite and the origin of ultralow-velocity zones. *Science* 312, 564-565.
- McDonough, W.F. and Sun, S.S. (1995) The composition of the Earth. *Chem. Geol.* 120, 223-253.
- McNamara, A.K., Garnero, E.J. and Rost, S. (2010) Tracking deep mantle reservoirs with ultra-low velocity zones. *Earth Planet. Sci. Lett.* 299, 1-9.
- Mysen, B. (1975) Partitioning of iron and magnesium between crystals and partial melts in peridotite upper mantle. *Contrib. Mineral. Petrol.* 52, 69-76.
- Mysen, B.O. and Richet, P. (2018) *Silicate glasses and melts: Properties and structure*, 2nd ed. Elsevier, Amsterdam.
- Mysen, B.O., Virgo, D., Scarfe, C.M. and Cronin, D.J. (1985) Viscosity and structure of iron-bearing and aluminum-bearing calcium silicate melts at 1 atm. *Am. Mineral.* 70, 487-498.
- Park, S.Y. and Lee, S.K. (2016) Effects of difference in ionic radii on chemical ordering in mixed-cation silicate glasses: Insights from solid-state ^{17}O and ^6Li NMR of Li-Ba silicate glasses. *J. Am. Ceram. Soc.* 99, 3948-3956.
- Paul, A. and Douglas, R.W. (1965) Ferrous-ferric equilibrium in binary alkali silicate glasses. *Phys. Chem. Glasses* 6, 207-211.
- Philpotts, A.R. (1982) Compositions of immiscible liquids in volcanic-rocks. *Contrib. Mineral. Petrol.* 80, 201-218.
- Rost, S., Garnero, E.J., Williams, Q. and Manga, M. (2005) Seismological constraints on a possible plume root at the core-mantle boundary. *Nature* 435, 666-669.
- Squyres, S.W., Arvidson, R.E., Ruff, S., Gellert, R., Morris, R.V., Ming, D.W., Crumpler, L., Farmer, J.D., Des Marais, D.J., Yen, A., McLennan, S.M., Calvin,

- W., Bell, J.F., Clark, B.C., Wang, A., McCoy, T.J., Schmidt, M.E. and de Souza, P.A. (2008) Detection of silica-rich deposits on Mars. *Science* 320, 1063-1067.
- Tuff, J., Wade, J. and Wood, B.J. (2013) Volcanism on Mars controlled by early oxidation of the upper mantle. *Nature* 498, 342-345.
- Wicks, J.K., Jackson, J.M. and Sturhahn, W. (2010) Very low sound velocities in iron-rich (Mg,Fe)O: Implications for the core-mantle boundary region. *Geophysical Research Letters* 37.
- Williams, Q. (1998) A correlation between ultra-low basal velocities in the mantle and hot spots. *Science* 281, 546-549.
- Wright, T.L. and Fiske, R.S. (1971) Origin of differentiated and hybrid lavas of Kilauea volcano, Hawaii. *J. Petrol.* 12, 1-65.
- Zhu, C., Veblen, D.R., Blum, A.E. and Chipera, S.J. (2006) Naturally weathered feldspar surfaces in the Navajo Sandstone aquifer, Black Mesa, Arizona: Electron microscopic characterization. *Geochim. Cosmochim. Acta* 70, 4600-4616.

Chapter 2. Solid-state NMR study of paramagnetic cation-bearing materials

High-resolution solid-state NMR provides detailed information on the element-specific atomic arrangement around nuclides of interest in the diverse oxides and silicate glasses (e.g., Allwardt and Stebbins, 2004; Florian et al., 2007; Le Losq et al., 2014; Lee and Ryu, 2018; Neuville et al., 2007; Sen et al., 2009; Stebbins, 2017a), including the complex multi-component silicate glasses corresponding to natural magma (Kelsey et al., 2008a; Lee et al., 2016; Lee et al., 2012a; Malfait et al., 2012; Neuville et al., 2008; Park and Lee, 2012; Park and Lee, 2014, 2018), high-pressure oxide/silicate glasses (Allwardt et al., 2005; Allwardt et al., 2007; Kelsey et al., 2009; Lee, 2010; Lee et al., 2012b), and glasses with volatile components (Kim et al., 2018; Kim et al., 2016; Morizet et al., 2010; Mysen, 2013; Xue, 2009).

Particularly, ^{29}Si MAS NMR allows evaluating the environment around the Si atom and thus the Q^n speciation (Kirkpatrick et al., 1986; Mysen and Richet, 2018; e.g., Schramm et al., 1984; Stebbins, 1995; Stebbins and Xue, 2014). In addition, ^{17}O MAS and 3Q (triple quantum) MAS NMR of oxide glasses have resolved distinct non-bridging oxygen (NBO, e.g., Na-O-Si and Ca-O-Si) and bridging oxygen (BO, e.g., Si-O-Si and Al-O-Si) environments (Allwardt et al., 2003; Angeli et al., 2001; Ashbrook and Smith, 2006; Dirken et al., 1997; Kelsey et al., 2008a; Lee, 2011; Lee and Kim, 2015; Lee and Stebbins, 2006; e.g., Schramm and Oldfield, 1984; Stebbins et al., 1999; Stebbins et al., 2001; Thompson and Stebbins, 2013; Xue et al., 1994). The NMR parameters of NBO and BO including isotropic chemical shift (^{17}O δ_{iso}) and quadrupolar coupling product [$P_q = C_q(1 + \eta^2/3)^{1/2}$, where C_q is the quadrupolar coupling constant and η is the quadrupolar asymmetry parameter] are also sensitive

to bond angle and bond length distribution in the networks (Clark and Grandinetti, 2005; Clark et al., 2004; Farnan et al., 1992; Lee and Stebbins, 2009; Vermillion et al., 1998). The ^{17}O NMR thus directly allows estimating the degree of poly-merization and a variation in topological disorder in diverse oxide glasses and provides atomistic insights into viscosity of the corresponding melts (e.g., Lee, 2011 and references therein). The ^{27}Al NMR provides the information about the local configurations around Al polyhedra, such as Al coordination number and distortion of Al network.

Despite the utility of solid-state NMR, NMR studies of glasses containing paramagnetic cations (e.g., iron, nickel, and cobalt) remain a challenge due to the well-known effect of paramagnetic cation (i.e., Fe, Ni, and Mn) on NMR spectra. Paramagnetic cations, which possess unpaired electrons, induce strong local magnetic fields that cause the rapid spin-lattice relaxation of nuclear spins around paramagnetic cations, thereby leading to a severe loss of sensitivity and resolution of the NMR signal (e.g., Geiger et al., 1992; Grimmer et al., 1983; Murdoch et al., 1985; Oldfield et al., 1983; Stebbins and Kelsey, 2009). Earlier ^{29}Si MAS NMR showed that the presence of iron in the olivine broadens the peaks, accompanied by the loss of the observable signal (e.g., Grimmer et al., 1983; Smith et al., 1983; Stebbins et al., 2009). A similar trend has been observed for the ^{29}Si NMR spectra of naturally occurring layer silicates (e.g., kaolinite and pyrophyllite) and natural feldspar (e.g., plagioclase and alkali-feldspar) (Barron et al., 1983; Sherriff and Hartman, 1985; Watanabe et al., 1983) and for the ^{27}Al and ^{11}B NMR spectra of tourmaline (Lussier et al., 2009). Previous NMR studies of synthetic and natural pyrope garnets with ~ 3.5 wt% FeO demonstrated that there is a significant effect on both the ^{29}Si and ^{27}Al NMR peak intensities and widths; doping with as low as 1 wt% FeO degraded the resolution of the ^{29}Si spectra

of synthetic garnet solid solutions (Geiger et al., 1992; Kelsey et al., 2008b; Stebbins and Kelsey, 2009). The ^{29}Si NMR spectra of aluminosilicate glasses, although already quite broad due to disorder, are further broadened as the iron oxide content increases to greater than a few wt% FeO (Murdoch et al., 1985).

Notwithstanding the inherent difficulties, recent NMR studies of crystals and glasses comprising paramagnetic cations have shown that solid-state NMR can be successfully applied to obtain useful information on specific structural configurations, such as the site occupancy of iron in a crystalline lattice (Lussier et al., 2009; McCarty et al., 2015; Palke and Stebbins, 2011; Palke et al., 2012; Palke et al., 2015; Stebbins and Kelsey, 2009). Clearly resolved paramagnetic interactions, such as Fermi and pseudo-contact shifted NMR peaks, have been reported in ^{27}Al and ^{29}Si spectra for the crystalline silicates (e.g., olivine, ringwoodite, and garnet) with paramagnetic impurity reaching 3.5 wt% FeO (Palke and Stebbins, 2011; Palke et al., 2012; Stebbins and Kelsey, 2009). The resolution of the peaks corresponding to different Al coordination environments for aluminosilicate glasses (up to ~5 wt% FeO) quenched from melts at high pressure was also reported in high-field ^{27}Al NMR study (Kelsey et al., 2009). These advances yield prospects for investigating the structure of silicate glasses with relatively high iron content (up to 20-23 wt% Fe_2O_3 in the current study) using high-resolution solid-state NMR. Recently, local symmetry at the site of a paramagnetic cation has been explored for transition metal minerals (e.g., Fe_2SiO_4 and FeOOH) and compounds (e.g., Li-Mn oxide and NaFePO_4F) by observing the hyperfine shift in an expanded range of frequencies up to thousands ppm (Grey et al., 1989; Lee et al., 2017; Lee and Grey, 2002; Li et al., 2018; Nielsen et al., 2005; Stebbins, 2017b, c). Previous detailed studies on crystals and glasses

containing paramagnetic cations using solid-state NMR are summarized in Table 2-1.

Despite its being considered impossible to explore the structural details of iron-bearing glasses using solid-state NMR, I report the first high-resolution solid-state NMR spectra for iron-bearing silicate and aluminosilicate glasses containing up to ~23 wt% iron oxide. To provide the valuable structural information from the obtained NMR spectra, the careful and robust analysis considering the paramagnetic effect should be accompanied. As mentioned above, the presence of paramagnetic cation results in the signal loss and peak broadening of NMR spectra, stemming from the rapid spin-lattice relaxation behavior of nuclear spins around paramagnetic cations. Thus, observed NMR spectra in the current studies show only the information of 'survived' nuclear spins. Meanwhile, the spin-lattice relaxation behavior is dependent on the distance between the paramagnetic center and nuclear spins (Bakhmutov et al., 2009; Bertini et al., 2002; Bertini et al., 2005). Thus, the systematic protocol to interpret the changes in NMR spectra with increasing Fe (i.e., paramagnetic cation) in silicate and aluminosilicate glasses is necessary.

In the current studies, I conceptualized the scheme to account for paramagnetic interaction between iron and nuclear spins. Taking into consideration the signal loss, it is expected that there is a blind zone, where the nuclear spins within a certain distance from the paramagnetic cation would not be observed. Here, I define the size of the region where signal loss occurs as the cutoff radius. Based on the current quantification results of the extent of NMR signal loss, the cutoff radius is expected to be ~3.5 Å. Therefore, the NMR spins within the distance of the next nearest neighbors between paramagnetic center and nuclear spins are removed. Beyond the distance of

cutoff radius, the nuclear spins are still affected by the paramagnetic cation, while these spins are not fully removed in the spectra. The detectable NMR spins can provide the opportunity to explore the nature of interaction between paramagnetic cation and nuclear spins. The hypothetical distance in which the paramagnetic cation affects the nuclear spins without the overall signal loss is defined as effective paramagnetic radius. The effective paramagnetic radius is qualitatively expected to be ~1 nm, based on the previous NMR results on crystalline oxides. While more precise and robust efforts are necessary, this may help in the interpretation of the obtained NMR spectra for iron-bearing silicate and aluminosilicate glasses taking into account the distribution of para-magnetic cations in the glass network. Note that the detailed description on the scheme to account paramagnetic cation and nuclear spins are present in Chapter 4.4.1 and Figure 4.9 below. Based on the above considerations, I provide the detailed structural information (i.e., extent of polymerization, the topological disorder, and spatial distribution of Fe) of iron-bearing silicate and aluminosilicate glasses with varying composition using multi-nuclear (^{29}Si , ^{17}O , and ^{27}Al) solid-state NMR in this thesis.

Table 2-1. List of the solid-state NMR studies for minerals and glasses containing paramagnetic cation

Composition	Paramagnetic cation	Total amount ¹⁾ (wt%)	Target nuclide	Reference
<i>Paramagnetic cation-bearing minerals</i>				
Kaolinite, Dickite, Nacrite, Pyrophyllite	Fe	~ 0.23	²⁹ Si	Barron et al. (1983)
Natural Halloysites and Kaolinite	Fe	~ 2	²⁹ Si	Watanabe et al. (1983)
Plagioclase and alkali feldspar	Fe	~ 5	²⁹ Si	Sherriff and Hartman (1985)
Pyrope	Fe	~ 2	²⁹ Si and ²⁷ Al	Geiger et al. (1992)
Kaolinite	Fe	~ 1.8	²⁹ Si and ²⁷ Al	Schroeder and Pruett (1996)
Natural pyrope	Fe	~ 3.5	²⁹ Si and ²⁷ Al	Stebbins and Kelsey (2009)
SiO ₂ -Al ₂ O ₃ -MnO	Mn	~ 19	²⁹ Si T ₁	Bakhmutov et al. (2009)
Tourmaline group	Fe and Co	~ 1	¹¹ B and ²⁷ Al	Lussier et al. (2009)
Natural pyrope	Fe	~ 3.5	²⁹ Si and ²⁷ Al	Palke and Stebbins (2011)
MgSiO ₃ bridgmanite	Fe	~ 2.8	²⁹ Si and ²⁷ Al	Palke et al. (2012)
Pyroxene and Kaolinite+magnetite	Fe	~ 6.6	¹ H, ²⁹ Si, and ²⁷ Al	Begaudau et al. (2012)
Natural and synthetic garnet	Fe	~ 9.3	²⁹ Si and ²⁷ Al	Palke et al. (2015)
Forsterite	Fe, Ni, Co, and Mn	~ 1	²⁹ Si	McCarty et al. (2015)
MgO and CaO	Ni and Co	~ 2.2	¹⁷ O, ²⁵ Mg, and ⁴³ Ca	McCarty and Stebbins (2016)
<i>Transition metal minerals and compounds</i>				
La ₂ Sn ₂ O ₇	Sn		¹¹⁹ Sn	Grey et al. (1989)
LiZn _{0.5} Mn _{1.5} O ₄ and Li ₂ MnO ₃	Mn		⁶ Li	Lee and Grey (2002)
α-FeOOH	Fe		² H and ⁶ Li	Nielsen et al. (2005)
Mg ₆ MnO ₈ and MgCr ₂ O ₄	Mn and Cr		²⁵ Mg	Lee et al. (2017)
Cu-silicate minerals	Cu		²⁹ Si	Stebbins (2017)
M ₂ SiO ₄ and MCaSi ₂ O ₆ (M=Fe, Co, and Ni)	Fe, Co, and Ni		²⁹ Si	Stebbins (2018)
Na ₂ FePO ₄ F	Fe		²³ Na	Li et al. (2018)

Paramagnetic cation-bearing silicate glasses

Natural volcanic glass	Fe	~ 4	²⁹ Si	Murdoch et al. (1985)
Fe-doped Ca-Na aluminosilicate glass	Fe	~ 5	²⁷ Al	Kelsey et al. (2009)
Na ₂ O-Fe ₂ O ₃ -SiO ₂	Fe	~ 23	²⁹ Si and ¹⁷ O	Kim et al. (2016)
MgO-FeO-SiO ₂	Fe	~ 13.5	²⁹ Si and ¹⁷ O	Kim and Lee (2019)
NiCaSi ₂ O ₆ and CoCaSi ₂ O ₆	Ni and Co		²⁹ Si	Stebbins (2018)
Fe-bearing NaAlSi ₃ O ₈ and CaAl ₂ Si ₂ O ₈	Fe	~ 14.4	²⁹ Si, ¹⁷ O, and ²⁷ Al	This study

¹⁾The maximum amount of paramagnetic cation oxides in the samples of each experiment (e.g., FeO, Fe₂O₃, and NiO)

REFERENCES

- Allwardt, J.R., Lee, S.K. and Stebbins, J.F. (2003) Bonding preferences of non-bridging O atoms: Evidence from ^{17}O MAS and 3QMAS NMR on calcium aluminate and low-silica Ca-aluminosilicate glasses. *Am. Mineral.* 88, 949-954.
- Allwardt, J.R. and Stebbins, J.F. (2004) Ca-Mg and K-Mg mixing around non-bridging O atoms in silicate glasses: An investigation using ^{17}O MAS and 3QMAS NMR. *Am. Mineral.* 89, 777-784.
- Allwardt, J.R., Stebbins, J.F., Schmidt, B.C., Frost, D.J., Withers, A.C. and Hirschmann, M.M. (2005) Aluminum coordination and the densification of high-pressure aluminosilicate glasses. *Am. Mineral.* 90, 1218-1222.
- Allwardt, J.R., Stebbins, J.F., Terasaki, H., Du, L.-S., Frost, D.J., Withers, A.C., Hirschmann, M.M., Suzuki, A. and Ohtani, E. (2007) Effect of structural transitions on properties of high-pressure silicate melts: ^{27}Al NMR, glass densities, and melt viscosities. *Am. Mineral.* 92, 1093-1104.
- Angeli, F., Charpentier, T., Gin, S. and Petit, J.C. (2001) ^{17}O 3Q-MAS NMR characterization of a sodium aluminoborosilicate glass and its alteration gel. *Chem. Phys. Lett.* 341, 23-28.
- Ashbrook, S.E. and Smith, M.E. (2006) Solid state ^{17}O NMR - an introduction to the background principles and applications to inorganic materials. *Chemical Society Reviews* 35, 718-735.
- Bakmutov, V.I., Shpeizer, B.G., Prosvirin, A.V., Dunbar, K.R. and Clearfield, A. (2009) On ^{29}Si NMR relaxation as a structural criterion for studying paramagnetic supermicroporous silica-based materials: silica-based materials incorporating Mn^{2+} ions into the silica matrix of $\text{SiO}_2\text{-Al}_2\text{O}_3\text{-MnO}$. *Solid State Nucl. Magn. Reson.* 36, 129-136.
- Barron, P.F., Frost, R.L. and Skjemstad, J.O. (1983) ^{29}Si spin-lattice relaxation in aluminosilicates. *J. Chem. Soc. Chem. Comm.*, 581-583.
- Bertini, I., Luchinat, C. and Parigi, G. (2002) Magnetic susceptibility in paramagnetic NMR. *Prog. Nucl. Magn. Reson. Spectrosc.* 40, 249-273.
- Bertini, I., Luchinat, C., Parigi, G. and Pierattelli, R. (2005) NMR spectroscopy of paramagnetic metalloproteins. *Chembiochem* 6, 1536-1549.

- Clark, T.M. and Grandinetti, P.J. (2005) Calculation of bridging oxygen ^{17}O quadrupolar coupling parameters in alkali silicates: A combined *ab initio* investigation. *Solid State Nucl. Magn. Reson.* 27, 233-241.
- Clark, T.M., Grandinetti, P.J., Florian, P. and Stebbins, J.F. (2004) Correlated structural distributions in silica glass. *Phys. Rev. B* 70, 064202.
- Dirken, P.J., Kohn, S.C., Smith, M.E. and vanEck, E.R.H. (1997) Complete resolution of Si-O-Si and Si-O-Al fragments in an aluminosilicate glass by ^{17}O multiple quantum magic angle spinning NMR spectroscopy. *Chem. Phys. Lett.* 266, 568-574.
- Farnan, I., Grandinetti, P.J., Baltisberger, J.H., Stebbins, J.F., Werner, U., Eastman, M.A. and Pines, A. (1992) Quantification of the disorder in network-modified silicate glasses. *Nature* 358, 31-35.
- Florian, P., Sadiki, N., Massiot, D. and Coutures, J.P. (2007) Al-27 NMR study of the structure of lanthanum- and yttrium-based aluminosilicate glasses and melts. *J. Phys. Chem. B* 111, 9747-9757.
- Geiger, C.A., Merwin, L. and Sebald, A. (1992) Structural investigation of pyrope garnet using temperature-dependent FTIR and ^{29}Si and ^{27}Al MAS NMR spectroscopy. *Am. Mineral.* 77, 713-717.
- Grey, C.P., Dobson, C.M., Cheetham, A.K. and Jakeman, R.J.B. (1989) Studies of rare-earth stannates by ^{119}Sn MAS NMR: The use of paramagnetic shift probes in the solid-state. *J. Am. Chem. Soc.* 111, 505-511.
- Grimmer, A.R., Vonlampe, F., Magi, M. and Lippmaa, E. (1983) Solid-state high-resolution ^{29}Si NMR of silicates: Influence of Fe^{2+} in olivines. *Z. Chem.* 23, 343-344.
- Kelsey, K.E., Allwardt, J.R. and Stebbins, J.F. (2008a) Ca-Mg mixing in aluminosilicate glasses: An investigation using ^{17}O MAS and 3QMAS and ^{37}Al MAS NMR. *J. Non-Cryst. Solids* 354, 4644-4653.
- Kelsey, K.E., Stebbins, J.F., Du, L.-S., Mosenfelder, J.L., Asimow, P.D. and Geiger, C.A. (2008b) Cation order/disorder behavior and crystal chemistry of pyrope-grossular garnets: An ^{17}O 3QMAS and ^{27}Al MAS NMR spectroscopic study. *Am. Mineral.* 93, 134-143.

- Kelsey, K.E., Stebbins, J.F., Singer, D.M., Brown, G.E., Mosenfelder, J.L. and Asimow, P.D. (2009) Cation field strength effects on high pressure aluminosilicate glass structure: Multinuclear NMR and La XAFS results. *Geochim. Cosmochim. Acta* 73, 3914-3933.
- Kim, E.J., Fei, Y. and Lee, S.K. (2018) Effect of pressure on the short-range structure and speciation of carbon in alkali silicate and aluminosilicate glasses and melts at high pressure up to 8 GPa: ^{13}C , ^{27}Al , ^{17}O and ^{29}Si solid-state NMR study. *Geochim. Cosmochim. Acta* 224, 327-343.
- Kim, E.J., Fei, Y.W. and Lee, S.K. (2016) Probing carbon-bearing species and CO_2 inclusions in amorphous carbon-MgSiO₃ enstatite reaction products at 1.5 GPa: Insights from ^{13}C high-resolution solid-state NMR. *Am. Mineral.* 101, 1113-1124.
- Kirkpatrick, R.J., Dunn, T., Schramm, S., Smith, K.A., Oestrike, R. and Turner, G. (1986) Magic-angle sample-spinning nuclear magnetic resonance spectroscopy of silicate glasses: A review, in: Walrafen, G.E., Revesz, A.G. (Eds.), *Structure and Bonding in Noncrystalline Solids*. Plenum Press, New York, pp. 302-327.
- Le Losq, C., Neuville, D.R., Florian, P., Henderson, G.S. and Massiot, D. (2014) The role of Al^{3+} on rheology and structural changes in sodium silicate and aluminosilicate glasses and melts. *Geochim. Cosmochim. Acta* 126, 495-517.
- Lee, J., Seymour, L.D., Pell, A.J., Dutton, S.E. and Grey, C.P. (2017) A systematic study of Mg-25 NMR in paramagnetic transition metal oxides: applications to Mg-ion battery materials. *Phys. Chem. Chem. Phys.* 19, 613-625.
- Lee, S.K. (2010) Effect of pressure on structure of oxide glasses at high pressure: Insights from solid-state NMR of quadrupolar nuclides. *Solid State Nucl. Magn. Reson.* 38, 45-57.
- Lee, S.K. (2011) Simplicity in melt densification in multicomponent magmatic reservoirs in Earth's interior revealed by multinuclear magnetic resonance. *P. Natl. Acad. Sci. USA* 108, 6847-6852.
- Lee, S.K. and Kim, E.J. (2015) Probing metal-bridging oxygen and configurational disorder in amorphous lead silicates: Insights from ^{17}O solid-state nuclear magnetic resonance. *J. Phys. Chem. C* 119, 748-756.

- Lee, S.K., Kim, H.-I., Kim, E.J., Mun, K.Y. and Ryu, S. (2016) Extent of disorder in magnesium aluminosilicate glasses: Insights from ^{27}Al and ^{17}O NMR. *J. Phys. Chem. C* 120, 737-749.
- Lee, S.K., Park, S.Y., Kim, H.-I., Tschauner, O., Asimow, P., Bai, L., Xiao, Y. and Chow, P. (2012a) Structure of shock compressed model basaltic glass: Insights from O K-edge X-ray Raman scattering and high-resolution ^{27}Al NMR spectroscopy. *Geophysical Research Letters* 39.
- Lee, S.K. and Ryu, S. (2018) Probing of triply coordinated oxygen in amorphous Al_2O_3 . *Journal of Physical Chemistry Letters* 9, 150-156.
- Lee, S.K. and Stebbins, J.F. (2006) Disorder and the extent of polymerization in calcium silicate and aluminosilicate glasses: O-17 NMR results and quantum chemical molecular orbital calculations. *Geochim. Cosmochim. Acta* 70, 4275-4286.
- Lee, S.K. and Stebbins, J.F. (2009) Effects of the degree of polymerization on the structure of sodium silicate and aluminosilicate glasses and melts: An ^{17}O NMR study. *Geochim. Cosmochim. Acta* 73, 1109-1119.
- Lee, S.K., Yi, Y.S., Cody, G.D., Mibe, K., Fei, Y. and Mysen, B.O. (2012b) Effect of network polymerization on the pressure-induced structural changes in sodium aluminosilicate glasses and melts: ^{27}Al and ^{17}O solid-state NMR study. *J. Phys. Chem. C* 116, 2183-2191.
- Lee, Y.J. and Grey, C.P. (2002) Determining the lithium local environments in the lithium manganates $\text{LiZn}_{0.5}\text{Mn}_{1.5}\text{O}_4$ and Li_2MnO_3 by analysis of the Li-6 MAS NMR spinning sideband manifolds. *J. Phys. Chem. B* 106, 3576-3582.
- Li, Q., Liu, Z.G., Zheng, F., Liu, R., Lee, J., Xu, G.L., Zhong, G.M., Hou, X., Fu, R.Q., Chen, Z.H., Amine, K., Mi, J.X., Wu, S.Q., Grey, C.P. and Yang, Y. (2018) Identifying the Structural Evolution of the Sodium Ion Battery $\text{Na}_2\text{FePO}_4\text{F}$ Cathode. *Angewandte Chemie-International Edition* 57, 11918-11923.
- Lussier, A.J., Aguiar, P.M., Michaelis, V.K., Kroeker, S. and Hawthorne, F.C. (2009) The occurrence of tetrahedrally coordinated Al and B in tourmaline: An ^{11}B and ^{27}Al MAS NMR study. *Am. Mineral.* 94, 785-792.

- Malfait, W.J., Verel, R., Ardia, P. and Sanchez-Valle, C. (2012) Aluminum coordination in rhyolite and andesite glasses and melts: Effect of temperature, pressure, composition and water content. *Geochim. Cosmochim. Acta* 77, 11-26.
- McCarty, R.J., Palke, A.C., Stebbins, J.F. and Hartman, J.S. (2015) Transition metal cation site preferences in forsterite (Mg_2SiO_4) determined from paramagnetically shifted NMR resonances. *Am. Mineral.* 100, 1265-1276.
- Morizet, Y., Paris, M., Gaillard, F. and Scaillet, B. (2010) C-O-H fluid solubility in haplobasalt under reducing conditions: An experimental study. *Chem. Geol.* 279, 1-16.
- Murdoch, J.B., Stebbins, J.F. and Carmichael, I.S.E. (1985) High-resolution ^{29}Si NMR study of silicate and aluminosilicate glasses: The effect of network-modifying cations. *Am. Mineral.* 70, 332-343.
- Mysen, B. (2013) Structure-property relationships of COHN-saturated silicate melt coexisting with COHN fluid: A review of in-situ, high-temperature, high-pressure experiments. *Chem. Geol.* 346, 113-124.
- Mysen, B.O. and Richet, P. (2018) *Silicate glasses and melts: Properties and structure*, 2nd ed. Elsevier, Amsterdam.
- Neuville, D.R., Cormier, L., Montouillout, V., Florian, P., Millot, F., Rifflet, J.-C. and Massiot, D. (2008) Structure of Mg- and Mg/Ca aluminosilicate glasses: ^{27}Al NMR and Raman spectroscopy investigations. *Am. Mineral.* 93, 1721-1731.
- Neuville, D.R., Cormier, L., Montouillout, V. and Massiot, D. (2007) Local Al site distribution in aluminosilicate glasses by Al-27 MQMAS NMR. *J. Non-Cryst. Solids* 353, 180-184.
- Nielsen, U.G., Paik, Y., Julmis, K., Schoonen, M.A.A., Reeder, R.J. and Grey, C.P. (2005) Investigating sorption on iron-oxyhydroxide soil minerals by solid-state NMR spectroscopy: A 6Li MAS NMR study of adsorption and absorption on goethite. *J. Phys. Chem. B* 109, 18310-18315.
- Oldfield, E., Kinsey, R.A., Smith, K.A., Nichols, J.A. and Kirkpatrick, R.J. (1983) High-resolution NMR of inorganic solids - influence of magnetic centers on magic-angle sample-spinning lineshapes in some natural aluminosilicates. *J. Magn. Reson.* 51, 325-329.

- Palke, A.C. and Stebbins, J.F. (2011) Variable-temperature ^{27}Al and ^{29}Si NMR studies of synthetic forsterite and Fe-bearing Dora Maira pyrope garnet: Temperature dependence and mechanisms of paramagnetically shifted peaks. *Am. Mineral.* 96, 1090-1099.
- Palke, A.C., Stebbins, J.F., Frost, D.J. and McCammon, C.A. (2012) Incorporation of Fe and Al in MgSiO_3 perovskite: An investigation by ^{27}Al and ^{29}Si NMR spectroscopy. *Am. Mineral.* 97, 1955-1964.
- Palke, A.C., Stebbins, J.F., Geiger, C.A. and Tippelt, G. (2015) Cation order-disorder in Fe-bearing pyrope and grossular garnets: A ^{27}Al and ^{29}Si MAS NMR and ^{57}Fe Mössbauer spectroscopy study. *Am. Mineral.* 100, 536-547.
- Park, S.Y. and Lee, S.K. (2012) Structure and disorder in basaltic glasses and melts: Insights from high-resolution solid-state NMR study of glasses in diopside-Ca-tschermakite join and diopside-anorthite eutectic composition. *Geochim. Cosmochim. Acta* 80, 125-142.
- Park, S.Y. and Lee, S.K. (2014) High-resolution solid-state NMR study of the effect of composition on network connectivity and structural disorder in multi-component glasses in the diopside and jadeite join: Implications for structure of andesitic melts. *Geochim. Cosmochim. Acta* 147, 26-42.
- Park, S.Y. and Lee, S.K. (2018) Probing the structure of Fe-free model basaltic glasses: A view from a solid-state ^{27}Al and ^{17}O NMR study of Na-Mg silicate glasses, $\text{Na}_2\text{O-MgO-Al}_2\text{O}_3\text{-SiO}_2$ glasses, and synthetic Fe-free KLB-1 basaltic glasses. *Geochim. Cosmochim. Acta* 238, 563-579.
- Schramm, C.M., Dejong, B. and Parziale, V.E. (1984) ^{29}Si magic angle spinning NMR-study on local silicon environments in amorphous and crystalline lithium silicates. *J. Am. Chem. Soc.* 106, 4396-4402.
- Schramm, S. and Oldfield, E. (1984) High-resolution oxygen-17 NMR of solids. *J. Am. Chem. Soc.* 106, 2502-2506.
- Sen, S., Maekawa, H. and Papatheodorou, G.N. (2009) Short-range structure of invert glasses along the pseudo-binary join $\text{MgSiO}_3\text{-Mg}_2\text{SiO}_4$: Results from ^{29}Si and ^{25}Mg MAS NMR spectroscopy. *J. Phys. Chem. B* 113, 15243-15248.

- Sherriff, B.L. and Hartman, J.S. (1985) Solid-state high-resolution ^{29}Si NMR of feldspars: Al-Si disorder and the effects of paramagnetic centers. *Can. Mineral.* 23, 205-212.
- Smith, K.A., Kirkpatrick, R.J., Oldfield, E. and Henderson, D.M. (1983) High-resolution silicon-29 nuclear magnetic resonance spectroscopic study of rock-forming silicates. *Am. Mineral.* 68, 1206-1215.
- Stebbins, J.F. (1995) Dynamics and structure of silicate and oxide melts: Nuclear magnetic resonance studies, in: Stebbins, J.F., McMillan, P.F., Dingwell, D.B. (Eds.), *Reviews in Mineralogy*. Mineralogical Society of America, Washington, D.C., pp. 191-246.
- Stebbins, J.F. (2017a) "Free" oxide ions in silicate melts: Thermodynamic considerations and probable effects of temperature. *Chem. Geol.* 461, 2-12.
- Stebbins, J.F. (2017b) Toward the wider application of ^{29}Si NMR spectroscopy to paramagnetic transition metal silicate minerals: Copper(II) silicates. *Am. Mineral.* 102, 2406-2414.
- Stebbins, J.F. (2017c) Toward the wider application of Si-29 NMR spectroscopy to paramagnetic transition metal silicate minerals: Copper(II) silicates. *Am. Mineral.* 102, 2406-2414.
- Stebbins, J.F. and Kelsey, K.E. (2009) Anomalous resonances in ^{29}Si and ^{27}Al NMR spectra of pyrope ($[\text{Mg,Fe}]_3\text{Al}_2\text{Si}_3\text{O}_{12}$) garnets: Effects of paramagnetic cations. *Phys. Chem. Chem. Phys.* 11, 6906-6917.
- Stebbins, J.F., Lee, S.K. and Oglesby, J.V. (1999) Al-O-Al oxygen sites in crystalline aluminates and aluminosilicate glasses: High-resolution oxygen-17 NMR results. *Am. Mineral.* 84, 983-986.
- Stebbins, J.F., Panero, W.R., Smyth, J.R. and Frost, D.J. (2009) Forsterite, wadsleyite, and ringwoodite (Mg_2SiO_4): ^{29}Si NMR constraints on structural disorder and effects of paramagnetic impurity ions. *Am. Mineral.* 94, 626-629.
- Stebbins, J.F. and Xue, X. (2014) NMR spectroscopy of inorganic Earth materials, in: Henderson, G.S., Neuville, D.R., Downs, R.T. (Eds.), *Reviews in Mineralogy and Geochemistry*. Mineralogical Society of America, Chantilly, Virginia, pp. 605-653.
- Stebbins, J.F., Zhao, P.D., Lee, S.K. and Oglesby, J.V. (2001) Direct observation of multiple oxygen sites in oxide glasses: Recent advances from triple-quantum

- magic-angle spinning nuclear magnetic resonance. *J. Non-Cryst. Solids* 293, 67-73.
- Thompson, L.M. and Stebbins, J.F. (2013) Interaction between composition and temperature effects on non-bridging oxygen and high-coordinated aluminum in calcium aluminosilicate glasses. *Am. Mineral.* 98, 1980-1987.
- Vermillion, K.E., Florian, P. and Grandinetti, P.J. (1998) Relationships between bridging oxygen ^{17}O quadrupolar coupling parameters and structure in alkali silicates. *J. Chem. Phys.* 108, 7274-7285.
- Watanabe, T., Shimizu, H., Masuda, A. and Saito, H. (1983) Studies of ^{29}Si spin-lattice relaxation-times and paramagnetic impurities in clay minerals by magic-angle spinning ^{29}Si NMR and EPR. *Chem. Lett.*, 1293-1296.
- Xue, X. (2009) Water speciation in hydrous silicate and aluminosilicate glasses: Direct evidence from ^{29}Si - ^1H and ^{27}Al - ^1H double-resonance NMR. *Am. Mineral.* 94, 395-398.
- Xue, X.Y., Stebbins, J.F. and Kanzaki, M. (1994) Correlations between ^{17}O NMR parameters and local-structure around oxygen in high-pressure silicates: Implications for the structure of silicate melts at high pressure. *Am. Mineral.* 79, 31-42.

Chapter 3. Effect of iron content of the structure and disorder of iron-bearing sodium silicate glasses: A high-resolution ^{29}Si and ^{17}O solid-state NMR study

Hyo-Im Kim, Jung Chul Sur, Sung Keun Lee

Published in *Geochimica et Cosmochimica Acta* (2016) **173** 160-180

Some parts of this study include my previous thesis of Master of Science (M. Sc.) and therefore the part overlapped with M. Sc. was not included here. The results of this study were published in *Geochimica et Cosmochimica Acta* in 2016.

ABSTRACT

Despite its geochemical importance and implications for the properties of natural magmatic melts, understanding the detailed structure of iron-bearing silicate glasses remains among the outstanding problems in geochemistry. This is mainly because solid-state NMR techniques, one of the most versatile experimental methods to probe the structure of oxide glasses, cannot be fully utilized for exploring the structural details of iron-bearing glasses as the unpaired electrons in Fe induce strong local magnetic fields that mask the original spectroscopic features (i.e., paramagnetic effect). Here, we report high-resolution ^{29}Si and ^{17}O solid-state NMR spectra of iron-bearing sodium silicate glasses ($\text{Na}_2\text{O}-\text{Fe}_2\text{O}_3-\text{SiO}_2$, $\text{Fe}^{3+}/\Sigma\text{Fe} = 0.89 \pm 0.04$, thus

containing both ferric and ferrous iron) with varying $X_{\text{Fe}_2\text{O}_3}$ [$=\text{Fe}_2\text{O}_3/(\text{Na}_2\text{O} + \text{Fe}_2\text{O}_3)$], containing up to 22.9 wt% Fe_2O_3 . This compositional series involves Fe–Na substitution at constant SiO_2 contents of 66.7 mol% in the glasses. For both nuclides, the NMR spectra exhibit a decrease in the signal intensities and an increase in the peak widths with increasing iron concentration partly because of the paramagnetic effect. Despite the intrinsic difficulties that result from the pronounced paramagnetic effect, the ^{29}Si and ^{17}O NMR results yield structural details regarding the effect of iron content on Q speciation, spatial distribution of iron, and the extent of polymerization in the iron-bearing silicate glasses. The ^{29}Si NMR spectra show an apparent increase in highly polymerized Q species with increasing $X_{\text{Fe}_2\text{O}_3}$, suggesting an increase in the degree of melt polymerization. The ^{17}O 3QMAS NMR spectra exhibit well-resolved non-bridging oxygen (NBO, Na–O–Si) and bridging oxygen (BO, Si–O–Si) peaks with varying iron concentration. By replacing Na_2O with Fe_2O_3 (and thus with increasing iron content), the fraction of Na–O–Si decreases. Quantitative consideration of this effect confirms that the degree of polymerization is likely to increase with iron content and that Fe^{3+} is predominantly a network-former. The ^{17}O NMR spectra suggest a moderate degree of preferential partitioning of iron between NBO and BO clusters. The present results bear strong promise for studying iron-bearing silicate glasses using solid-state NMR techniques, constraining the effect of iron content on the degree of polymerization. The observed changes in atomic structures of iron-bearing sodium silicate glasses will be helpful for unraveling atomic origins of the properties of natural silicate melts.

3.1. Introduction

Iron is one of the essential components of silicate melts in the Earth and other terrestrial planets. The overall concentration of iron oxide in natural magmatic melts ranges from approximately 0.5 wt% (in rhyolitic melts) to ~20 wt% (in basalts) (e.g., Mysen and Richet, 2018; Philpotts, 1982; Wright and Fiske, 1971). The two oxidation states of iron, ferrous (Fe^{2+}) and ferric (Fe^{3+}) states, coexist in silicate melts, and the iron redox ratio ($\text{Fe}^{3+}/\Sigma\text{Fe}$) also varies with composition, temperature, pressure, and oxygen fugacity (Borisov and McCammon, 2010; Cottrell and Kelley, 2011; e.g., Fudali, 1965; Jayasuriya et al., 2004; Kilinc et al., 1983; Mysen and Virgo, 1978, 1985; Mysen et al., 1985a; Mysen et al., 1984). The iron content and its redox ratio affect the melt density and viscosity, controlling magmatic and volcanic processes (Bell and Simon, 2011; Bezos and Humler, 2005; Chevrel et al., 2013; Dingwell, 1991; Dingwell et al., 1988; Hara et al., 1988; Lange and Carmichael, 1989; Liu and Lange, 2006; Mysen et al., 1985b). Determining the structure of iron-bearing silicate glasses and melts is necessary for better understanding how the corresponding melt properties depend on the iron content. The objective of this study is thus, to determine the atomic configurations and the degree of melt polymerization in iron-bearing silicate glasses with varying iron content (at constant $\text{Fe}^{3+}/\Sigma\text{Fe}$ ratio), and to provide better insight into the relationship between the atomic structures and their macroscopic properties, particularly viscosity.

The structure of iron-bearing silicate melts and glasses (e.g., the coordination number, the bond length, and the angle) has been extensively studied by using various scattering and spectroscopic methods, including Raman, X-ray absorption, and Mössbauer spectroscopy. These studies suggested that Fe^{3+} should be considered to be primarily a network-forming

cation, similar to Al^{3+} (Alberto et al., 1996; Burkhard, 2000; Cochain et al., 2012; Farges et al., 2004; Hannoyer et al., 1992; Holland et al., 1999; Mysen, 2006; Mysen et al., 1980; Mysen and Virgo, 1989; Mysen et al., 1985a). While network-forming Fe^{3+} is often suggested to be 4-coordinated, a highly coordinated Fe^{3+} (5- and 6-coordinated Fe^{3+}) has been reported for iron-bearing silicate glasses, in particular at low Fe^{3+} contents (Farges et al., 2004; Hannoyer et al., 1992; Liu and Lange, 2006; Mysen et al., 1980; Mysen and Virgo, 1989; Mysen et al., 1984). On the other hand, Fe^{2+} is proposed to play the role of a network-modifying cation, similar to Mg^{2+} in silicate glasses and melts (Mao et al., 1973; Mysen et al., 1980; Mysen and Virgo, 1978; Nolet, 1980; Seifert and Olesch, 1977). The reported coordination number of Fe^{2+} ranges from 4 to 6: the optical absorption studies of diverse Fe^{2+} -bearing silicate glasses (e.g., $\text{Na}_2\text{O-SiO}_2$, CaO-SiO_2 , $\text{CaO-Al}_2\text{O}_3\text{-SiO}_2$, $\text{CaO-Al}_2\text{O}_3\text{-B}_2\text{O}_3\text{-SiO}_2$, etc.) have suggested that 6-coordinated Fe^{2+} is dominant (Bell et al., 1976; Boon and Fyfe, 1972; Fox et al., 1982; Goldman and Berg, 1980; Nolet, 1980). Earlier Mössbauer spectroscopy studies of ternary peralkaline Na-, Ca-, and Mg-aluminosilicate glasses also concluded that Fe^{2+} is predominantly 6-fold coordinated (Virgo and Mysen, 1985). On the basis of Mössbauer studies of $\text{CaO-SiO}_2\text{-FeO}$, and natural tektites and X-ray absorption spectroscopic studies of various Fe^{2+} -bearing alkali and alkaline earth silicate glasses (e.g., $\text{Na}_2\text{Fe}^{2+}\text{Si}_3\text{O}_8$, $\text{K}_2\text{Fe}^{2+}\text{Si}_3\text{O}_8$, $\text{LiFe}^{2+}\text{Si}_3\text{O}_8$, $[\text{Ca}_{0.4}\text{Mg}_{0.4}\text{Fe}^{2+}_{0.2}]\text{SiO}_3$, $\text{CaFe}^{2+}\text{Si}_2\text{O}_6$ etc.), $^{4,5}\text{Fe}^{2+}$ in these glasses was concluded to be predominant (Alberto et al., 1996; Calas and Petiau, 1983; Farges et al., 2004; Jackson et al., 2005; Rossano et al., 1999; Rossano et al., 2008; Rossano et al., 2000; Waychunas et al., 1988). A previous Mössbauer study of aluminosilicate glasses on charge-balanced joins (e.g., $\text{NaAlSi}_2\text{O}_6$, $\text{Ca}_{0.5}\text{AlSi}_2\text{O}_6$, and $\text{Mg}_{0.5}\text{AlSi}_2\text{O}_6$) showed that the proportion of $^{4}\text{Fe}^{2+}$ is larger for oxidized glasses than for reduced glasses

(Mysen, 2006). Extensive previous studies have confirmed that viscosity of synthetic and natural magmatic liquids depends on the iron content and its redox state and thus the aforementioned structural role of iron (Bouhifd et al., 2004; Cukierman and Uhlmann, 1974; Dingwell, 1991; Dingwell and Virgo, 1987, 1988; Liebske et al., 2003; Montenero et al., 1986; Toguri et al., 1976; Urbain et al., 1982). For example, the viscosity of iron-bearing sodium silicate melts decreases with increasing iron content at a constant iron redox ratio (Dingwell and Virgo, 1988) and has also been reported to increase with increasing $\text{Fe}^{3+}/\Sigma\text{Fe}$ ratio at a constant total iron content (Dingwell, 1989, 1991; Dingwell and Virgo, 1987). Similar trend has been observed in phosphorus-bearing silicate melts (Toplis et al., 1994). This is in part due to the expected structural role of Fe^{3+} as a network-forming cation (Dingwell and Virgo, 1987; Mysen and Virgo, 1985, 1989). Because a decrease in the degree of melt polymerization can lead to a reduction in the viscosity of silicate melts by several orders of magnitude, the above results imply the effect of iron content and $\text{Fe}^{3+}/\Sigma\text{Fe}$ (and thus the structural role of iron) on the degree of melt polymerization (e.g., Bottinga and Weill, 1972; Giordano and Dingwell, 2003; Lee, 2005; Mazurin, 1983).

Although the degree of melt polymerization can be deduced from the chemical compositions of the melts, experimental estimation of the degree of melt polymerization is not trivial: previous studies of silicate glasses showed that direct probing of non-bridging oxygen (NBO) and bridging oxygen (BO) sites is necessary to determine the degree of melt polymerization (e.g., Lee, 2005). The relevant structural information around oxygen is not currently available for iron-bearing silicate glasses. Together with the coordination environments and the structural role of iron as well as the degree of melt polymerization, atomic and nanoscale configurations around other

framework cations, such as Si and Al have also been suggested to be responsible for the observed changes in the viscosity with varying iron content (e.g., Giordano and Dingwell, 2003). Particularly, Q^n speciation in the silicate glasses (tetrahedral Si groups with n denoting the number of bridging oxygen atoms) is linked to viscosity of diverse silicate melts (e.g., Mysen and Richet, 2018 and references therein). Although the previous spectroscopic and scattering studies have facilitated our understanding of glass and melt structures, the employed techniques could not provide direct information of the Si coordination number, the Q^n speciation, and the degree of polymerization in iron-bearing silicate glasses due to overlap among the peaks and modes corresponding to the atomic configurations.

High-resolution solid-state NMR provides detailed information on the element-specific atomic arrangement around nuclides of interest in the diverse silicate glasses (e.g., Kirkpatrick et al., 1986; Lee, 2011; Malfait et al., 2012; Stebbins, 1995; Stebbins and Xue, 2014 for the recent review; Toplis et al., 2000; Xue and Kanzaki, 2008). Particularly, ^{29}Si MAS NMR allows evaluating the environment around the Si atom and thus the Q^n speciation (Kirkpatrick et al., 1986; Mysen and Richet, 2018; e.g., Schramm et al., 1984; Stebbins, 1995; Stebbins and Xue, 2014). In addition, ^{17}O MAS and 3Q (triple quantum) MAS NMR of oxide glasses have resolved distinct non-bridging oxygen (NBO, e.g., Na-O-Si and Ca-O-Si) and bridging oxygen (BO, e.g., Si-O-Si and Al-O-Si) environments (Allwardt et al., 2003; Angeli et al., 2001; Ashbrook and Smith, 2006; Dirken et al., 1997; Kelsey et al., 2008; Lee, 2011; Lee and Kim, 2015; Lee and Stebbins, 2006; e.g., Schramm and Oldfield, 1984; Stebbins et al., 1999; Stebbins et al., 2001; Thompson and Stebbins, 2013; Xue et al., 1994). The NMR parameters of NBO and BO including isotropic chemical shift (^{17}O δ_{iso}) and quadrupolar coupling product [$P_q = C_q(1 +$

$\eta^2/3)^{1/2}$, where C_q is the quadrupolar coupling constant and η is the quadrupolar asymmetry parameter] are also sensitive to bond angle and bond length distribution in the networks (Clark and Grandinetti, 2005; Clark et al., 2004; Farnan et al., 1992; Lee and Stebbins, 2009; Vermillion et al., 1998). The ^{17}O NMR thus directly allows estimating the degree of polymerization and a variation in topological disorder in diverse oxide glasses and provides atomistic insights into viscosity of the corresponding melts (e.g., Lee, 2011 and references therein).

Despite the utility of solid-state NMR, NMR studies of glasses containing paramagnetic cations (e.g., iron, nickel, and cobalt) remain a challenge. This is because the unpaired electrons in paramagnetic cations induce strong local magnetic fields that mask the original spectroscopic properties, such as chemical shift (and thus, the peak positions), peak shapes and intensities (i.e., paramagnetic effect, see Chapter 2 for more details). The application of this technique has thus been limited to the studies of iron-free silicate glasses. Recent studies, however, have shown that unique structural information, such as iron distribution in the lattice on iron-bearing crystalline silicates can be obtained (Palke and Stebbins, 2011; Palke et al., 2012; Stebbins and Kelsey, 2009). Whereas the utility of the high-resolution 2-dimensional NMR technique to the structure iron-bearing silicates has not been systematically tested, the 2D ^{17}O 3QMAS NMR method can potentially reveal structure of the iron-bearing glasses. Particularly, binary sodium silicate glasses, an archetypal model system for more complex, multi-component silicate glasses, shed light on the opportunity to probe the effect of iron on these structures using high-resolution NMR techniques. This is because the peaks due to Q^n species are resolved in the ^{29}Si MAS NMR spectra of the iron-free sodium disilicate glasses ($\text{Na}_2\text{O}:\text{SiO}_2 = 1:2$) where its average

polymerization corresponds to Q³ (i.e., Q²:Q³:Q⁴ = 1:8:1) (Maekawa et al., 1991). Furthermore, the configurations around BO (Si-O-Si) and NBO (Na-O-Si) are well-resolved in the ¹⁷O 3QMAS NMR spectra where the percentages of these species are ~40% (NBO) and 60% (BO), respectively (Lee and Stebbins, 2009). Therefore, even with the expected spectral broadening due to paramagnetic elements in the glasses, variations of peak intensity, width, and population can be observed for each site.

In this study, we report novel structural insights into Q species, NBO, and BO environments in the iron-bearing silicate glasses with iron content reaching 22.9 wt% Fe₂O₃, using ²⁹Si and ¹⁷O MAS and 2D ¹⁷O 3QMAS NMR. Our results also constitute the direct experimental estimation of the degree of polymerization and iron distribution in iron-bearing sodium silicate glasses. We finally discuss the importance of these structural findings in determining the macroscopic properties of iron-bearing sodium silicate melts.

3.2. Experimental Methods

3.2.1. Sample preparation

Iron-bearing sodium disilicate glasses with varying iron contents [(Na₂O)_{1-x} · (Fe₂O₃)_x · 2(SiO₂) with X_{Fe₂O₃} = Fe₂O₃/(Na₂O + Fe₂O₃) of 0 (NS2), 0.03 (2.6 wt% Fe₂O₃), 0.05 (4.4 wt% Fe₂O₃), 0.1 (8.4 wt% Fe₂O₃), 0.2 (16.1 wt% Fe₂O₃), and 0.3 (22.9 wt% Fe₂O₃)] were synthesized from sodium carbonate (Na₂CO₃) and oxide reagents, including Fe₂O₃ and 20% ¹⁷O-enriched SiO₂ (prepared by hydrolyzing SiCl₄ with 20% ¹⁷O-enriched H₂O). Here, X_{Fe₂O₃} refers to the nominal composition of Fe₂O₃ in the glasses. The observed structural changes are thus dependent on Fe-Na substitution in (Na₂O)_{1-x} · (Fe₂O₃)_x · 2(SiO₂) glasses with varying X_{Fe₂O₃} = Fe₂O₃/(Na₂O + Fe₂O₃): an

Table 3-1. Nominal compositions and ICP analyses of iron-bearing sodium silicate glasses ($\text{Na}_2\text{O}-\text{Fe}_2\text{O}_3-\text{SiO}_2$) with varying $X_{\text{Fe}_2\text{O}_3}$ [= $\text{Fe}_2\text{O}_3/(\text{Na}_2\text{O} + \text{Fe}_2\text{O}_3)$].

Composition		Nominal composition (mol%)			
		Na_2O	$\text{Fe}_2\text{O}_3^{\text{T}}$	SiO_2	
$X_{\text{Fe}_2\text{O}_3}$	0	33.3	0.0	66.7	
	0.03	32.3	1.0	66.7	
	0.05	31.7	1.7	66.7	
	0.1	30.0	3.3	66.7	
	0.2	26.7	6.7	66.7	
	0.3	23.3	10.0	66.7	
Composition		Nominal composition (mol%)		ICP analysis (mol%)	
		Na_2O	$\text{Fe}_2\text{O}_3^{\text{T}}$	Na_2O	$\text{Fe}_2\text{O}_3^{\text{T}}$
$X_{\text{Fe}_2\text{O}_3}$	0	100.0	0.0	99.8 ± 0.1	0.2 ± 0.1
	0.03	97.0	3.0	96.4 ± 0.2	3.6 ± 0.2
	0.05	95.0	5.0	94.5 ± 0.5	5.5 ± 0.5
	0.1	90.0	10.0	88.0 ± 0.3	12.0 ± 0.3
	0.2	80.0	20.0	76.7 ± 0.4	23.3 ± 0.4
	0.3	70.0	30.0	66.0 ± 0.5	34.0 ± 0.5

increase in $X_{\text{Fe}_2\text{O}_3}$ is accompanied by a decrease in Na_2O content [i.e., thus addition of Fe corresponds to removal of Na (network modifier) from the glasses]. Note that in sodium disilicate glasses, ^{44}Si is predominant and experimental NBO fraction of $\sim 60\%$ is consistent with the prediction from composition (Lee and Stebbins, 2009). Approximately 0.2 wt% cobalt oxide was added to the iron-free sodium silicate glass (NS2) for enhancing the spin-lattice relaxation and for reducing the overall collection time. The Pt crucible was saturated with iron during the preliminary glass synthesis to prevent iron loss from the samples. The mixtures were decarbonated at 700–750 °C for 1 h, and subsequently fused at 1000–1100 °C in a through-flow Ar environment for 1 h in a tube furnace. $X_{\text{Fe}_2\text{O}_3} = 0.3$ glass analyzed using ^{29}Si

MAS NMR and Mössbauer spectroscopy was fused in a tube furnace without any atmosphere control. The melt was quenched by removing the Pt crucible from the tube furnace. The crucible was then lowered into water, forming glasses. Table 3-1 shows the nominal compositions and the estimated compositions of iron-bearing sodium silicate glasses studied here using inductively coupled plasma atomic emission spectroscopy (ICP-AES). As reported previously, SiO₂ in the glasses was removed by reacting with the hydrofluoric acid for the ICP analysis (Park and Lee, 2012; Park and Lee, 2014). The estimated ratios of Na₂O to Fe₂O₃ were close to the nominal composition, consistent with the negligible to minor weight loss (up to ~2%) during synthesis and the consistency with ICP analysis.

3.2.2. Ferric-ferrous ratio of iron-bearing silicate glasses

The iron redox ratios ($\text{Fe}^{3+}/\Sigma\text{Fe}$) of samples with high iron contents ($X_{\text{Fe}_2\text{O}_3} = 0.2$ and 0.3) were determined using ⁵⁷Fe resonant absorption Mössbauer spectroscopy at Wonkwang University, Korea. The spectra were collected at 298 K in transmission geometry using a constant acceleration spectrometer, with 30 mCi ⁵⁷Co diffused in rhodium. All spectra were collected with velocity varying from -10 to +10 mm/s. The isomer shifts are reported relative to the reference Fe metal. As shown in Figure 3-A1, the Mössbauer spectra for the glasses with $X_{\text{Fe}_2\text{O}_3} = 0.2$ (fused in an Ar environment) and 0.3 exhibit absorption maxima at -0.2 and 0.7 mm/s for both spectra, regardless of composition and types of atmosphere. These spectra are consistent with the Mössbauer spectra of silicate glasses containing predominantly Fe³⁺ (e.g., Mysen et al., 1980). If the spectra consist only of Fe³⁺ doublets, the isomer shifts of Fe³⁺ are 0.223 and 0.234 mm/s and the quadrupolar splitting of Fe³⁺ is 0.860 and 0.910 mm/s for $X_{\text{Fe}_2\text{O}_3} = 0.2$ and

0.3, respectively. However, as also shown in the previous Mössbauer studies, there could be a minor fraction ($\sim 10\%$) of Fe^{2+} in the spectral patterns similar to those shown in Figure 3-A1 (e.g., Cochain et al., 2012). The similarity between two spectra for the glasses fused in a tube furnace with or without Ar atmosphere control indicates that the atmospheric condition used in the current study does not affect the iron redox ratio, noticeably, in the glass composition studied here. While we have not collected Mössbauer spectra for other glasses, previous Mössbauer studies of silicate glasses have shown that the $\text{Fe}^{3+}/\Sigma\text{Fe}$ ratio for $\text{Na}_2\text{O}-\text{Fe}_2\text{O}_3-\text{SiO}_2$ glasses does not change noticeably with varying iron content. Based on previous studies of iron-bearing silicate glasses whose compositions are similar to those of the currently studied glasses (i.e., 52 \sim 67 wt% SiO_2 and 2 \sim 23 wt% Fe_2O_3) (Dingwell and Virgo, 1987, 1988; Dunaeva et al., 2012; Mysen et al., 1980; Mysen and Virgo, 1985), together with our own Mössbauer measurement, the $\text{Fe}^{3+}/\Sigma\text{Fe}$ ratio for $\text{Na}_2\text{O}-\text{Fe}_2\text{O}_3-\text{SiO}_2$ glasses is 0.89 ± 0.04 (see Appendix 3-A1 and 3-A2 for the detailed discussion regarding the estimation of $\text{Fe}^{3+}/\Sigma\text{Fe}$ ratio from previous Mössbauer studies).

3.2.3. NMR spectroscopy

All NMR spectra were collected using a Varian 400 MHz solid-state NMR spectrometer at 9.4 T (at Seoul National University, Korea) with a 4 mm thick-wall zirconia rotor, in a Doty Scientific double-resonance MAS probe, at the Larmor frequency of 79.48 MHz for ^{29}Si and 54.23 MHz for ^{17}O , using a spinning speed of 14 kHz. ^{29}Si MAS NMR spectra were collected with single pulse acquisition with a pulse length of 1.6 μs (radio frequency tip angle of $\sim 30^\circ$ for solid). The recycle delay was 60 s for the iron-free sample (NS2) and

1 s for the iron-bearing samples. 24,000 to 178,560 scans were averaged in the ^{29}Si MAS NMR spectra to improve the signal-to-noise ratio.

In order to reveal the distribution of iron in glasses we performed ^{29}Si spin-lattice relaxation experiments using a spin-echo pulse sequence [90° - delay time (τ) - 90°] based on the progressive saturation-recovery with varying delay times (ranging from 0.0003 to 1 s) with 0.5 s of recycle delay. The number of scans was varied from 1200 for the longest delay to 50,000 for the shortest delay (see Section 3.3.2 for details on measuring the spin-lattice relaxation behavior). The ^{29}Si NMR spectra were referenced to tetramethylsilane (TMS). ^{17}O MAS NMR spectra were also collected with single pulse acquisition with a pulse length of $0.3\ \mu\text{s}$ (the tip angle of $\sim 30^\circ$ in solids). Recycle delay of 1 s was used for iron-free samples and that of 0.3 s was used for iron-bearing samples to ensure complete relaxation. Approximately 240–48,000 scans were averaged to obtain ^{17}O MAS NMR spectra presented here. In the ^{17}O 3QMAS NMR experiment, a FAM (fast-amplitude modulation) based shifted-echo pulse sequence [$5.5\ \mu\text{s}$ - τ (delay) - $2\ \mu\text{s}$ - echo-delay (approximately 0.17 ms) - $20\ \mu\text{s}$] was used, with recycle delays ranging from 0.5 to 1 s depending on the spin-lattice relaxation time (Lee and Sung, 2008; Park and Lee, 2014 and references therein). A negligible difference between peak shapes of ^{17}O 3QMAS NMR spectra collected with varying echo-delay time was observed. This indicates that the observed NMR peak shape and the relative intensities are not heavily dependent on the paramagnetic effect on spin-spin relaxations and thus echo-delay times used. To achieve the current signal-to-noise ratio in the 3QMAS NMR spectra, about 19,200 (collected for 48 hrs)-192,800 scans (collected for ~ 18 days) were required for the iron-bearing samples. The ^{17}O NMR spectra were referenced

Table 3-2. NMR experimental conditions (at 9.4 T, 14 kHz) used in this study.

Nucleus	Acquisition	Pulse sequence	$X_{\text{Fe}_2\text{O}_3}$	Number of Scans	Delay (s)	Delay time (s)	Time (h)
^{29}Si	MAS	Single-pulse	0	3968	60	-	33
			0.03	59520	1	-	17
			0.05	59520	1	-	17
			0.1	119040	1	-	34
			0.2	119040	1	-	34
			0.3	178560	1	-	50
^{29}Si	T_1 relaxation	Saturation-recovery	0	20000~24	1	0.032~480	24
			0.03	50000~1200	0.5	0.0003~0.1	10
			0.05	50000~2400	0.5	0.0003~0.1	10
			0.1	40000~1500	0.5	0.0003~0.1	10
^{17}O	MAS	Single-pulse	0	240	1	-	0.1
			0.05	21816	0.3	-	2
			0.1	48000	0.3	-	4
			0.2	48000	0.3	-	4
^{17}O	3QMAS	FAM based shifted-echo pulse	0	96 ^a	1	-	3
			0.05	19200 ^a	0.3	-	48
			0.1	57600 ^a	0.3	-	144
			0.2	192000 ^a	0.3	-	420

^a Approximately 80 FIDs (iron-free sample) and 30~35 FIDs (iron-bearing sample) were collected for constructing the 2D spectra.

to tap water. Detailed description of the experimental conditions is given in Table 3-2.

3.3. Results

3.3.1. Effect of iron content on Q species distribution in iron-bearing sodium silicate glasses: ^{29}Si MAS NMR results

Figure 3-1 shows the ^{29}Si MAS NMR spectra of sodium disilicate glass (NS2, $X_{\text{Fe}_2\text{O}_3} = 0$) and iron-bearing sodium silicate glasses with varying $X_{\text{Fe}_2\text{O}_3}$ [$= \text{Fe}_2\text{O}_3 / (\text{Na}_2\text{O} + \text{Fe}_2\text{O}_3)$] at constant SiO_2 content. Three distinct Si environments are partially resolved in the spectrum of iron-free NS2 glass, as previously reported (e.g., Maekawa et al., 1991): the peaks at ~ 75 ppm and ~ 90 ppm correspond to the Q^2 and Q^3 species, and the broad peak at ~ 100 ppm corresponds to the Q^4 species. The spectra of the iron-bearing glasses do not provide a clear resolution of multiple Si environments because the signal intensities of the iron-bearing glasses decrease (Figure 3-1A) and the peak widths increase (Figure 3-1B) with increasing $X_{\text{Fe}_2\text{O}_3}$. Note again that the ^{29}Si NMR spectra for iron-bearing glasses were acquired after full relaxation, which was ensured by a sufficient delay time. The signal loss and peak broadening in the ^{29}Si NMR spectra of the iron-bearing glasses are primarily due to the strong interaction between the unpaired electrons in the d -orbitals of iron and the ^{29}Si nuclear spins, masking the true structural changes that take place with increasing $X_{\text{Fe}_2\text{O}_3}$ [$= \text{Fe}_2\text{O}_3 / (\text{Na}_2\text{O} + \text{Fe}_2\text{O}_3)$]. Due to the signal loss, the signal to noise ratio of the spectra for iron-bearing glasses is significantly lower than that for iron-free glass. We also note that the anomalous peaks due to pseudo-contact shift observed in previous NMR studies of crystalline materials were not observed in the current study of non-

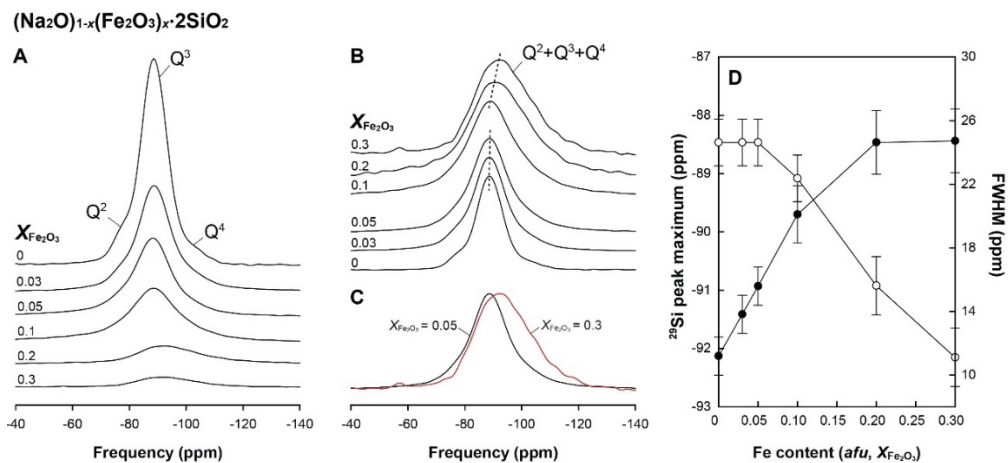


Figure 3-1. ^{29}Si MAS NMR spectra of iron-bearing sodium silicate glasses $[(\text{Na}_2\text{O})_{1-x} \cdot (\text{Fe}_2\text{O}_3)_x \cdot 2\text{SiO}_2]$ at 9.4 T with varying $X_{\text{Fe}_2\text{O}_3}$ [= $\text{Fe}_2\text{O}_3/(\text{Na}_2\text{O} + \text{Fe}_2\text{O}_3)$], as labeled. (A) The spectra are plotted on a vertical scale reflecting signal intensity reduction corresponding to the changes in iron content, and (B) a normalized vertical scale. (C) Comparison of ^{29}Si MAS NMR spectra for glasses with $X_{\text{Fe}_2\text{O}_3}$ of 0.05 (black) and 0.3 (red). (D) Variation of peak maxima (open circles) and FWHM (closed circles) of the peak in ^{29}Si MAS NMR spectra with varying iron content $X_{\text{Fe}_2\text{O}_3}$ [= $\text{Fe}_2\text{O}_3/(\text{Na}_2\text{O} + \text{Fe}_2\text{O}_3)$].

crystalline silicates (Cole et al., 2004; Grey et al., 1989; Nielsen et al., 2005; Palke and Stebbins, 2011; Palke et al., 2012; Stebbins and Kelsey, 2009; Stebbins et al., 2009). Figure 3-1C also shows that the peak shape of the spectra for $X_{\text{Fe}_2\text{O}_3} = 0.3$ glass has an obvious Gaussian component, which is apparently different from that of $X_{\text{Fe}_2\text{O}_3} = 0.05$ (characterized by Lorentzian peak shape due to paramagnetic effect). This result highlights the dependence of peak shape on iron content, with implications regarding the nature of iron distribution in the glasses.

Although a decrease in signal intensity and an increase in peak width of the ^{29}Si NMR spectra of the iron-bearing glasses make it difficult to resolve and quantify the specific environments of silicon, the effect of iron content on peak maxima and broadening patterns is clearly manifested in the ^{29}Si NMR spectra (Figure 3-1D). The peak maximum shifts toward lower frequencies (more negative chemical shift) by replacing Na_2O with Fe_2O_3 [and thus with increasing $X_{\text{Fe}_2\text{O}_3}$ [= $\text{Fe}_2\text{O}_3/(\text{Na}_2\text{O} + \text{Fe}_2\text{O}_3)$]] from -88.5 ppm ($X_{\text{Fe}_2\text{O}_3} = 0$) to -92.2 ppm ($X_{\text{Fe}_2\text{O}_3} = 0.3$). While the peak maximum does not change with iron content up to $X_{\text{Fe}_2\text{O}_3} = 0.05$, a notable shift in the ^{29}Si NMR spectral peak is observed above $X_{\text{Fe}_2\text{O}_3} = 0.1$. The peak widths also increase abruptly with increasing $X_{\text{Fe}_2\text{O}_3}$ up to $X_{\text{Fe}_2\text{O}_3} = 0.05$ and gradually as the iron content increases from $X_{\text{Fe}_2\text{O}_3} = 0.1$ to 0.3. The peak shapes for the glasses with low iron content ($X_{\text{Fe}_2\text{O}_3} = 0.05$) can be roughly described by the Lorentzian (and thus symmetric) function. The peak shows a noticeable asymmetry toward lower frequency: the peak shape can be described by the sum of the multiple Gaussian functions (rather than the Lorentzian function) with increasing $X_{\text{Fe}_2\text{O}_3}$ (Figure 3-1C). The broadening characterized by the Lorentzian function for the glasses with $X_{\text{Fe}_2\text{O}_3} = 0.03$ and 0.05 is likely due to the lifetime broadening (owing to the nuclear spin–electron interaction), whereas the

gradual and inhomogeneous broadening characterized by the Gaussian function for the iron-rich glasses is *partly* affected by the changes in the fractions and topology around Q^n species with changing $X_{Fe_2O_3}$, in addition to lifetime broadening. This observation suggests that the variation of the ^{29}Si NMR spectra with varying $X_{Fe_2O_3}$ may be due to both the paramagnetic cation effect and iron-induced structural changes. However, it is difficult to distinguish the inhomogeneous broadening induced by real structural changes (i.e., the Gaussian component) from the lifetime broadening (i.e., the Lorentzian component): the quantification of the proportion of the Gaussian/Lorentzian components with varying $X_{Fe_2O_3}$ is difficult due to the considerable overlap among the peaks for three Q^n species. The aforementioned interpretation is thus qualitative. Yet, it is clear that the relative fraction of Q^4 species in the normalized spectrum apparently increases by replacing Na_2O with Fe_2O_3 (and thus with increasing $X_{Fe_2O_3}$). While the broadening can primarily stem from the paramagnetic effect, the inhomogeneous broadening observed in the ^{29}Si MAS NMR spectra with increasing $X_{Fe_2O_3}$ is partly due to increased topological disorder around Si. As will be further discussed in Section 3.4.1 below, the experimental observation in ^{29}Si NMR spectra is mostly due to an increase in the degree of polymerization by replacing Na_2O with Fe_2O_3 (and thus with increasing $X_{Fe_2O_3}$).

3.3.2. Iron distribution in the silicate glass networks: Insights from ^{29}Si spin-lattice (T_1) relaxation results and analyses

Detailed information on the distribution of paramagnetic cations in glasses is necessary to understand the observed trend in ^{29}Si MAS NMR spectra (Figure 3-1). The relevant information can be deduced from nuclear

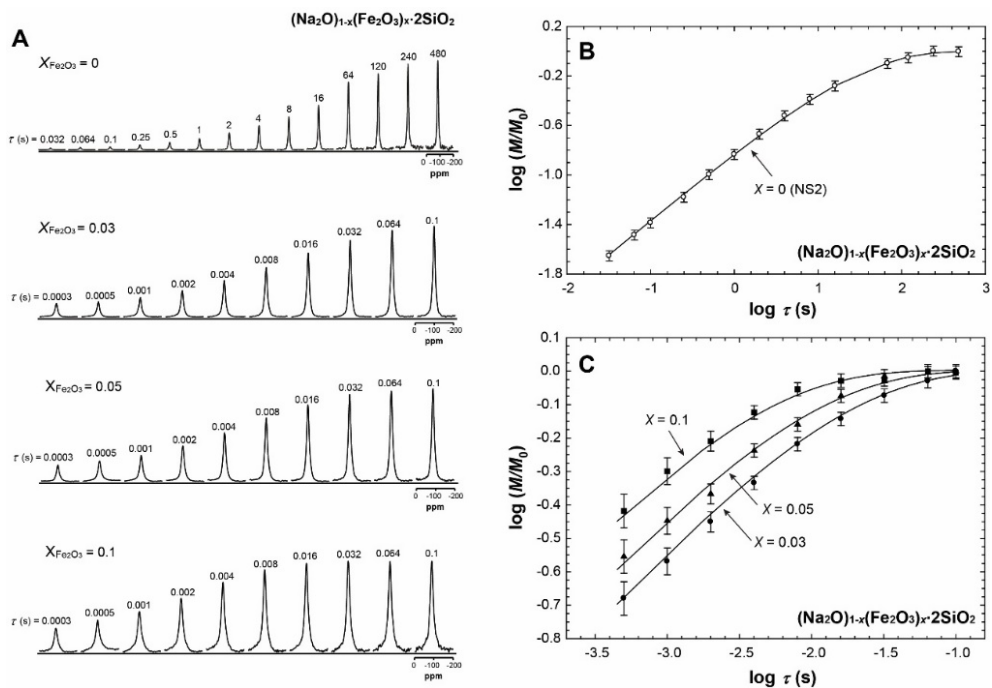


Figure 3-2. (A) Evolution of the ^{29}Si NMR spectra of iron-bearing sodium silicate glasses with $X_{\text{Fe}_2\text{O}_3}$ [$= \text{Fe}_2\text{O}_3/(\text{Na}_2\text{O} + \text{Fe}_2\text{O}_3)$] and increasing delay time (τ), after saturation of magnetization at 9.4 T. (B) Variation of the integrated peak area of the recovered ^{29}Si NMR signal (normalized with respect to the total peak area of a fully relaxed spectrum (M/M_0)) on the delay time (τ), for (A) iron-free sodium disilicate glass (open circle) and (B) iron-bearing sodium silicate glasses (closed symbols), with varying $X_{\text{Fe}_2\text{O}_3}$ [$= \text{Fe}_2\text{O}_3/(\text{Na}_2\text{O} + \text{Fe}_2\text{O}_3)$]. Circles, triangles, and squares correspond to $X_{\text{Fe}_2\text{O}_3}$ of 0.03, 0.05, and 0.1, respectively.

spin-lattice relaxation time measurements. Figure 3-2A shows the ^{29}Si NMR spectra of iron-bearing sodium silicate glasses with iron content reaching $X_{\text{Fe}_2\text{O}_3} = 0.1$ with increasing delay time (τ) after the saturation of nuclear spin magnetization. Increasing the iron content reduces the time required for recovery of total magnetization by four orders of magnitude [e.g., from 240 s (for $X_{\text{Fe}_2\text{O}_3} = 0$, with 0.2 wt% CoO) to 0.03 s (for $X_{\text{Fe}_2\text{O}_3} = 0.1$)].

Figures 3-2B and C show the peak intensity of the ^{29}Si NMR signal (M) normalized with respect to the peak area of a fully relaxed spectrum (M_0) with varying delay time (τ), plotted on double-logarithmic axis. The trend can be described using a stretched exponential equation (Hartman et al., 2007; Stebbins and Kelsey, 2009; Tse and Hartmann, 1968):

$$M/M_0 = 1 - \exp[-(\tau/T')^\beta] \quad (3.1)$$

where β is the stretching exponent and T' is the recovery time constant. When $\beta = 1$ the relaxation curve is exponential and T' is equivalent to the normal T_1 . As shown in Figures 3-2B and C, the ^{29}Si data for iron-free and iron-bearing silicate glasses were well fitted with $\beta = 0.5$. The estimated T' values decreased as the value of $X_{\text{Fe}_2\text{O}_3}$ increased from 0.01 ± 0.002 s ($X_{\text{Fe}_2\text{O}_3} = 0.03$), through 0.0051 ± 0.0007 s ($X_{\text{Fe}_2\text{O}_3} = 0.05$), to 0.0024 ± 0.0003 s ($X_{\text{Fe}_2\text{O}_3} = 0.1$). Decreasing spin-lattice relaxation time (T') with increasing $X_{\text{Fe}_2\text{O}_3}$ could stem from enhancement of the dipolar interaction between ^{29}Si and the paramagnetic centers, indicating increasing spatial proximity between them (Narayanan et al., 1995; Schroeder and Pruett, 1996; Stebbins and Kelsey, 2009; Tse and Hartmann, 1968). The relaxation trend with $\beta = 0.5$ indicates random and homogeneous distribution of the paramagnetic centers, and β between 0.5 and 1 is indicative of heterogeneous distribution (e.g. clustering and phase separation) (Hartman et al., 2007; Hartman et al., 1994; Narayanan et al., 1995; Schroeder and Pruett, 1996; Stebbins and Kelsey, 2009; Tse and Hartmann,

1968). Therefore, the observed relaxation behavior suggests that the distribution of iron in glass networks is homogeneous on the nanometer scale, regardless of its content.

Figure 3-3 shows the normalized ^{29}Si NMR intensity (with respect to that of iron-free silicate glass) with varying $X_{\text{Fe}_2\text{O}_3}$. A decrease in the NMR signal intensity with increasing $X_{\text{Fe}_2\text{O}_3}$ is prevalent. Therefore, we note that not all the Si spins are probed in the MAS NMR spectra. However, the composition-independent stretching exponent β ($=0.5$) strongly indicates the homogeneous iron distribution (see Section 3.4.2 below).

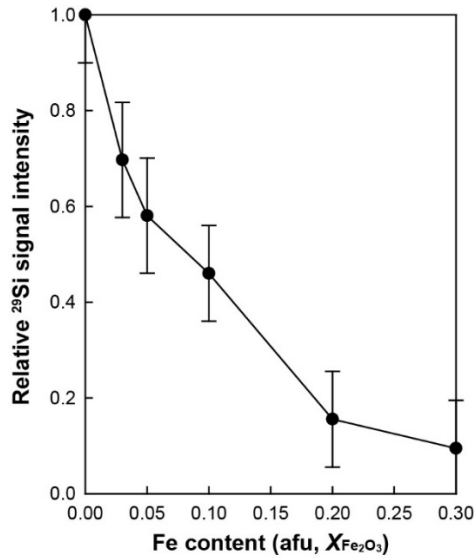


Figure 3-3. ^{29}Si MAS NMR signal intensity of iron-bearing sodium silicate glasses with varying iron contents. The signal is normalized with respect to that of the iron-free sodium disilicate glasses.

3.3.3. Effect of iron content on oxygen configurations in iron-bearing sodium silicate glasses: ^{17}O MAS and 3QMAS NMR results

Figure 3-4 shows the ^{17}O MAS NMR spectra of sodium disilicate glass (NS2) and iron-bearing sodium silicate glasses with varying $X_{\text{Fe}_2\text{O}_3}$. A non-bridging oxygen peak (a narrow component at ~ 35 ppm, Na-O-Si) and a bridging oxygen peak (a broad component, Si-O-Si) are partially resolved in the ^{17}O MAS NMR spectrum of iron-free NS2 ($X_{\text{Fe}_2\text{O}_3} = 0$), consistent with previous results (Lee and Stebbins, 2009; Xue et al., 1994). The corresponding NBO and BO peaks in the spectra, however, overlap due to strong interaction between ^{17}O spins and unpaired electrons in iron, and partially owing to potential changes in the oxygen configuration (chemical and topological disorder). Because of the overlap of the peaks in the ^{17}O MAS spectra, detailed structural information pertaining to the oxygen sites is difficult to obtain from the ^{17}O MAS NMR spectra.

Figure 3-5 presents the ^{17}O 3QMAS NMR spectra of iron-bearing sodium silicate glasses with $X_{\text{Fe}_2\text{O}_3}$ ranging from 0 to 0.2, yielding much improved resolution for Na-O-Si (NBO) and Si-O-Si (BO) species, relative to the resolution obtained from the conventional ^{17}O MAS NMR spectra (Figure 3-4). The Na-O-Si peak (~ -25 ppm along the isotropic dimension) and the Si-O-Si peak (~ -45 ppm along the isotropic dimension) are fully resolved in the case of $X_{\text{Fe}_2\text{O}_3} = 0$ (Lee and Stebbins, 2009). The peaks become broader along both the MAS and isotropic dimensions with increasing $X_{\text{Fe}_2\text{O}_3}$. Despite the pronounced peak broadening, the ^{17}O 3QMAS NMR spectra exhibit relatively well-resolved oxygen cluster peaks, even for relatively high iron content (up to $X_{\text{Fe}_2\text{O}_3} = 0.2$; ~ 16 wt% Fe_2O_3). Because the fraction of Na-O-Si can be used to quantify the degree of melt polymerization (Lee and Stebbins, 2009), the current results provide the unambiguous experimental estimation of the deg-

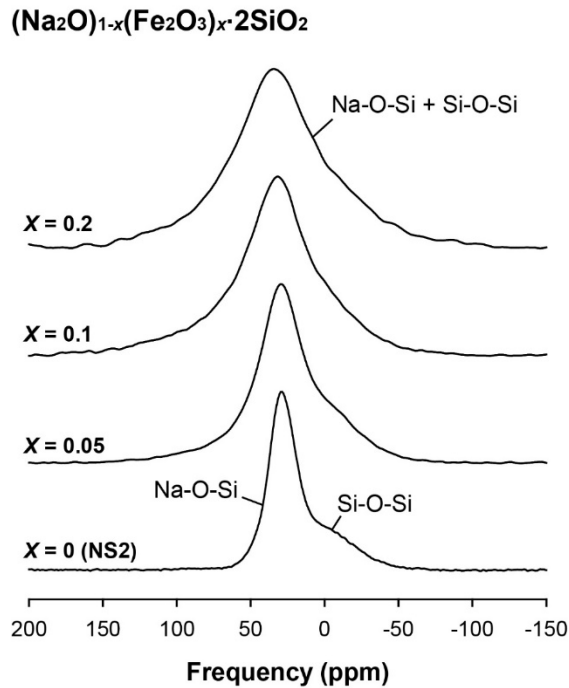


Figure 3-4. ^{17}O MAS NMR spectra of iron-bearing sodium silicate glasses at 9.4 T with varying $X_{\text{Fe}_2\text{O}_3}$ [= $\text{Fe}_2\text{O}_3 / (\text{Na}_2\text{O} + \text{Fe}_2\text{O}_3)$], as labeled.

ree of polymerization. The shape of the 3QMAS NMR peak changes with increasing $X_{\text{Fe}_2\text{O}_3}$: both the Na-O-Si and Si-O-Si peaks for $X_{\text{Fe}_2\text{O}_3} = 0.05$ in the 3QMAS NMR spectrum (in both the MAS and 3QMAS dimensions) are broader than that for iron-free NS2, and the peak shape is symmetric. However, in the 3QMAS NMR spectra for $X_{\text{Fe}_2\text{O}_3} = 0.1$ and 0.2 , the peak profiles are asymmetric, and are stretched along the isotropic dimension. The observed variations of peak shapes with respect to $X_{\text{Fe}_2\text{O}_3}$ along both the MAS and isotropic dimensions stem from the paramagnetic cation effect as well as from the increasing structural disorder (including chemical and topological disorder). Particularly, the broadening pattern in the NMR spectra for iron-

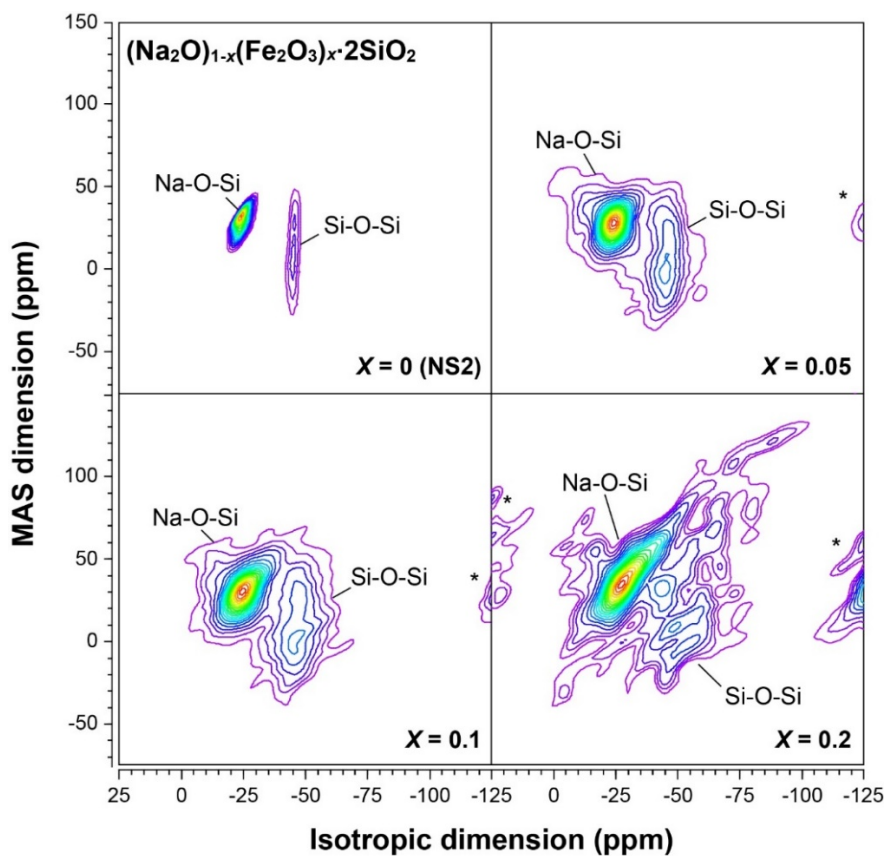


Figure 3-5. 2D ^{17}O 3QMAS NMR spectra of iron-bearing sodium silicate glasses at 9.4 T with varying $X_{\text{Fe}_2\text{O}_3}$ [$= \text{Fe}_2\text{O}_3 / (\text{Na}_2\text{O} + \text{Fe}_2\text{O}_3)$], as labeled. Contour lines are drawn from 13% to 98% relative intensity with a 5% increment and two additional lines at 6% and 9.5% levels, for better presentation of low-intensity peaks.

bearing glasses with high iron content demonstrates the effects of iron concentration on the degree of polymerization and topological disorder, and is consistent with the ^{29}Si MAS NMR results (see Section 3.3.1). Whereas Na-O-Si and Si-O-Si may have distinct paramagnetic relaxation times, the ^{17}O 3QMAS NMR spectra collected with varying echo-delay time do not show preferential changes in peak shapes and intensities for Na-O-Si and Si-O-Si, indicating that the effect of paramagnetic interaction on relative fraction of each oxygen site is negligible.

We note that increasing iron content in sodium silicate glasses can lead to formation of oxygen clusters that are directly bonded to the iron, such as Fe-O-Si and Fe-O-Fe as suggested from the presence of the $(\text{Fe}^{3+},\text{Si})\text{-O}$ stretching mode in the Raman spectra for iron-bearing silicate glasses (e.g., Mysen et al., 1980). To predict the ^{17}O NMR chemical shielding tensor for $^{4}\text{Fe}^{3+}\text{-O-Si}$, we performed quantum chemical calculations using Gaussian03 (Frisch et al., 2004). The detailed conditions for quantum chemical calculations are shown in our previous reports (Lee and Lee, 2009; e.g., Lee, 2004); briefly, the geometry optimization was performed at the HF/6-31G level of theory, and ^{17}O NMR chemical shielding tensor for $^{4}\text{Fe}^{3+}\text{-O-Si}$ cluster was calculated using the gauge-independent atomic orbital (GIAO) methods at the B3LYP/6-311+(d,p) level of theory. The calculated chemical shift for bridging oxygen $^{4}\text{Fe}^{3+}\text{-O-Si}$ cluster is ~ 173 ppm. While we have not calculated these values for $^{5,6}\text{Fe}^{3+}\text{-O-Si}$ clusters, on the basis of previous correlation of NMR chemical shift with varying Al coordination number in $^{4,5,6}\text{Al-O-Si}$, the values for $^{5,6}\text{Fe}^{3+}\text{-O-Si}$ are expected to be larger than the value for $^{4}\text{Fe}^{3+}\text{-O-Si}$ (Lee, 2004). In addition, the potential existence of other Fe-O-Si NBO peaks ($^{4,5,6}\text{Fe}^{2+}\text{-O-Si}$) may contribute to changes in the ^{17}O NMR spectra. These oxygen configurations, however, cannot be observed because

of strong interaction between electrons in Fe and ^{17}O nuclear spins. In Section 3.4.3 below, a detailed discussion of potential hidden species is provided.

Figure 3-6A presents the total isotropic projection of the 2D ^{17}O 3QMAS NMR spectra of sodium disilicate glass (NS2, $X_{\text{Fe}_2\text{O}_3} = 0$) and iron-bearing sodium silicate glasses with varying $X_{\text{Fe}_2\text{O}_3}$. Despite the decreasing signal-to-noise ratio with increasing $X_{\text{Fe}_2\text{O}_3}$, apparent variations of the peak width, position, and intensity for resolved Na-O-Si and Si-O-Si species are observed. Figure 3-6B shows the simulation results for the isotropic projection of the 3QMAS NMR spectra. In order to yield the current results, the variable ranges of peak widths and positions for these BO and NBO were first estimated from the 2D ^{17}O 3QMAS NMR spectra (Figure 3-6). Then, taking into consideration the paramagnetic effect as well as changes in the oxygen configurations with increasing $X_{\text{Fe}_2\text{O}_3}$, each peak is modeled as a combination of the Gaussian and the Lorentzian functions, except for $X_{\text{Fe}_2\text{O}_3} = 0$. For $X_{\text{Fe}_2\text{O}_3} = 0$, the isotropic projection of the 3QMAS NMR spectra can be decomposed into only two Gaussian functions. The Lorentzian shape (due to lifetime broadening) is introduced to imply the paramagnetic effect. Note that it is assumed that the extent of lifetime broadening in NBO and BO peaks is similar, based on the results of ^{29}Si T_1 relaxation time experiments. The ratio of the area under the Lorentzian part to that under the Gaussian part tends to increase as $X_{\text{Fe}_2\text{O}_3}$ increases from 10% ($X_{\text{Fe}_2\text{O}_3} = 0.05$), through 20% ($X_{\text{Fe}_2\text{O}_3} = 0.1$), to 50% ($X_{\text{Fe}_2\text{O}_3} = 0.2$). This is different from the trend observed ^{29}Si NMR spectra where an increase in the Gaussian component (due to disorder) is observed (Section 3.3.1). This difference can be accounted for by the fact that peaks in the total isotropic projection of ^{17}O 3QMAS NMR spectra are relatively well-resolved and thus the individual lifetime broadening characterized by Lorentzian function can be observed. In contrast, severe

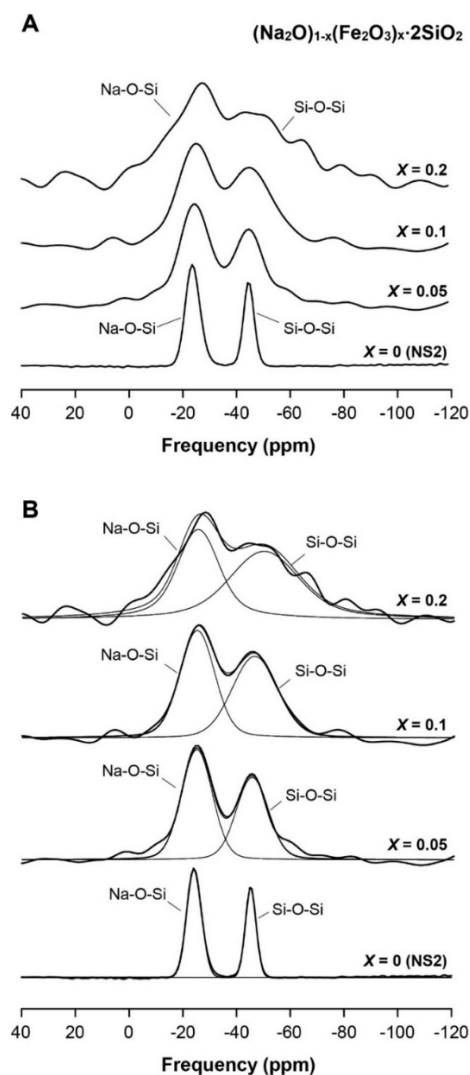


Figure 3-6. (A) Total isotropic projection of ^{17}O 3QMAS NMR spectra of iron-bearing sodium silicate glasses with varying $X_{\text{Fe}_2\text{O}_3}$ [$= \text{Fe}_2\text{O}_3 / (\text{Na}_2\text{O} + \text{Fe}_2\text{O}_3)$], as labeled. (B) Results of fitting the isotropic projection of ^{17}O 3QMAS NMR spectra for iron-bearing sodium silicate glasses with varying $X_{\text{Fe}_2\text{O}_3}$ (fits were performed using 2 Gaussian and 2 Lorentzian functions representing Na-O-Si and Si-O-Si), as labeled. Thick solid lines are the experimental spectra and thin solid lines show the fitted curves and each component.

overlap among Q species in the ^{29}Si NMR spectra does not allow us to observe the Lorentzian component. Rather, the observed Gaussian broadening stems from the distribution of multiple Lorentzian functions with distinct chemical shift (e.g., McHale, 1999).

With these constraints, all spectra (except $X_{\text{Fe}_2\text{O}_3} = 0$) were simultaneously fitted. As the contribution from the paramagnetic effect and that from topological disorder around oxygen cannot be uniquely distinguished for the iron-bearing silicate glasses studied here, the above discussion with varying ratio between components can only provide a qualitative trend on broadening mechanisms. There is a moderate degree of uncertainty associated with the fitting results, especially for $X_{\text{Fe}_2\text{O}_3} = 0.2$, due to the severe overlap. Thus, oxygen populations and peak widths for $X_{\text{Fe}_2\text{O}_3} = 0.2$ should be compared with those for other compositions semi-quantitatively.

Figure 3-7A shows the estimated peak widths of the Na-O-Si and Si-O-Si peaks with $X_{\text{Fe}_2\text{O}_3}$. For Na-O-Si, the peak width increases *nonlinearly* with increasing $X_{\text{Fe}_2\text{O}_3}$, and this broadening is particularly pronounced when moving from 6.6 ppm ($X_{\text{Fe}_2\text{O}_3} = 0$) to 13.4 ppm ($X_{\text{Fe}_2\text{O}_3} = 0.1$). The peak width changes more gradually from 13.4 ppm ($X_{\text{Fe}_2\text{O}_3} = 0.1$) to 18.6 ppm ($X_{\text{Fe}_2\text{O}_3} = 0.2$). The width of the Si-O-Si peak also increases from 4.8 ppm ($X_{\text{Fe}_2\text{O}_3} = 0$) to 31.0 ppm ($X_{\text{Fe}_2\text{O}_3} = 0.2$). While the peak width for Si-O-Si (~ 4.8 ppm) in iron-free sodium disilicate glasses is narrower than that for Na-O-Si (~ 6.6 ppm), the peak width for Si-O-Si (~ 31.0 ppm) is considerably broader than that for Na-O-Si (~ 18.6 ppm) in the glasses for $X_{\text{Fe}_2\text{O}_3} = 0.2$. Figure 3-7B also shows the estimated positions of the Na-O-Si and Si-O-Si peaks. While the Na-O-Si peak position appears to be invariant with respect to $X_{\text{Fe}_2\text{O}_3}$, the Si-O-Si peak position shifts toward lower frequencies from -46.2 ± 0.8 ppm ($X_{\text{Fe}_2\text{O}_3} = 0.1$) to -49.4 ± 1.2 ppm ($X_{\text{Fe}_2\text{O}_3} = 0.2$).

The ^{17}O NMR results demonstrate that changes in atomic configurations of iron-bearing silicate glasses with increasing $X_{\text{Fe}_2\text{O}_3}$ can indeed be observed, despite the pronounced paramagnetic effect on the spectral intensity and broadening. The observed trends of ^{17}O NMR peak width and position in the isotropic projection suggest that adding Fe may yield more significant ‘apparent’ changes in the remaining Si-O-Si than the remaining Na-O-Si species. This is consistent with the ^{29}Si MAS NMR results where the fraction of highly polymerized Q species apparently increases in the normalized spectra with increasing iron content. This apparent change in the Si-O-Si configuration with increasing $X_{\text{Fe}_2\text{O}_3}$ implies an increase in the degree of polymerization. As also manifested from the obvious Gaussian component for each Na-O-Si and Si-O-Si peak, the result suggests that the topological disorder around the remaining oxygen atoms apparently increases with increasing $X_{\text{Fe}_2\text{O}_3}$. Furthermore, the topological disorder for Si-O-Si is larger than the one for Na-O-Si (See Section 3.3.4 for the detailed nature of these interactions). We note that ^{17}O NMR spectra show the oxygens that do not have a close proximity with iron [i.e., Na-O-Si (NBO) and Si-O-Si (BO)]. On the other hand, *Hidden* oxygen species that are directly bonded to the iron are expected to be present in the iron-bearing glasses studied here. Figure 3-8 shows the schematic structures of the potential oxygen species in the iron-bearing silicate glasses. $^{[4]}\text{Fe}^{3+}\text{-O-Si}$, and $^{[4]}\text{Fe}^{3+}\text{-O-}^{[4]}\text{Fe}^{3+}$ are potential hidden BO species. The fractions of these BO species ($\text{Fe}^{3+}\text{-O-Si}$ as well as $\text{Fe}^{3+}\text{-O-Fe}^{3+}$) depend on the degree of chemical disorder between Si^{4+} and Fe^{3+} (e.g., Lee and Stebbins, 2002). The possible hidden NBO species are $\text{Fe}^{2+}\text{-O-Si}$ and mixed (Na, Fe^{2+})-O-Si (see Sections 2.4.3 and 2.4.4 for further details).

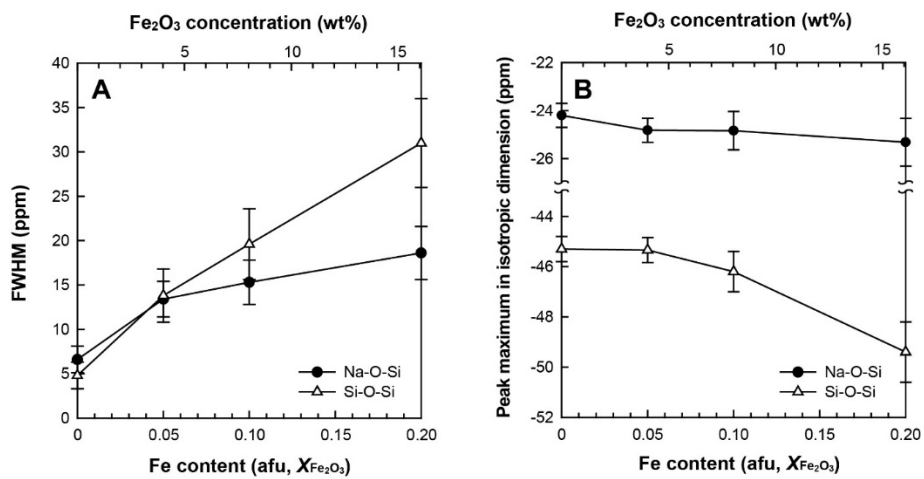
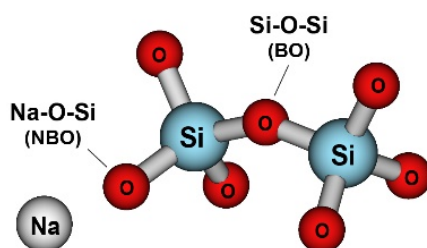


Figure 3-7. Variation of (A) full width at half maximum (FWHM) and (B) peak maximum in isotropic dimension of Na-O-Si (closed circle) and Si-O-Si (open triangle) peaks in the isotropic projection of ^{17}O 3QMAS NMR spectra of iron-bearing sodium silicate glasses with a varying Fe_2O_3 content ($X_{\text{Fe}_2\text{O}_3}$).

Visible oxygen species



Hidden oxygen species

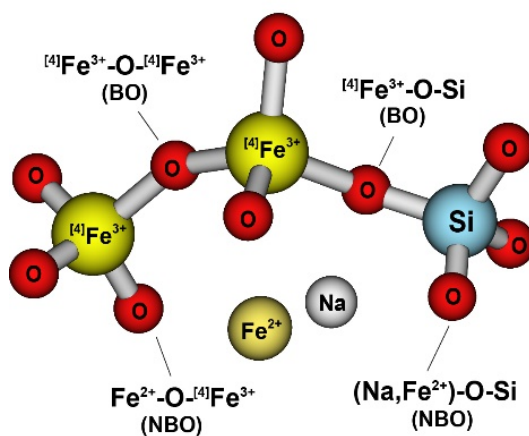


Figure 3-8. Schematic structures describing the potential (visible and hidden in NMR spectra) oxygen clusters in the iron-bearing silicate glasses.

3.3.4. Variation of structurally relevant ^{17}O NMR parameters and oxygen site population in iron-bearing sodium silicate glasses

Table 3-3 and Figure 3-9 show the variation of ^{17}O δ_{iso} (A) and P_{q} (B) for the Si-O-Si and Na-O-Si species, obtained from the centers of gravity of peaks along the MAS dimension and isotropic dimension of the 2D NMR spectra for the glasses with $X_{\text{Fe}_2\text{O}_3}$ (Baltisberger et al., 1996; Lee and Stebbins, 2000). Because of severe overlap between the Na-O-Si and Si-O-Si peaks in the glasses with $X_{\text{Fe}_2\text{O}_3} = 0.2$, it is difficult to decompose peaks into NBO and BO components and obtain the centers of gravity of each peak along the MAS dimension. Therefore, instead of using center of gravity, the NMR parameters of oxygen peaks for $X_{\text{Fe}_2\text{O}_3} = 0.2$ were obtained from the peak positions with maximal intensity along the MAS and isotropic dimensions.

The ^{17}O δ_{iso} of Na-O-Si slightly increases from 38.5 ± 2 ppm to 40.4 ± 2 ppm as $X_{\text{Fe}_2\text{O}_3}$ increases from 0 to 0.2 (Figure 3-9A). The increase in the δ_{iso} of Si-O-Si (~ 7.7 ppm for $X_{\text{Fe}_2\text{O}_3}$ from 0 to 0.2) is larger than the increase in the δ_{iso} of Na-O-Si. On the basis of correlation between ^{17}O δ_{iso} and Si-O bond length (e.g., Ashbrook et al., 2002, and references therein), the Si-O bond lengths in both the remaining Na-O-Si and Si-O-Si species may increase with increasing iron concentration. The stronger change in the ^{17}O δ_{iso} for Si-O-Si may indicate a stronger preferential effect on interaction between iron and Si-O-Si compared with that between iron and Na-O-Si. The ^{17}O P_{q} of Na-O-Si (~ 2.2 MHz) and Si-O-Si (~ 4.8 MHz) do not exhibit noticeable dependence on the iron content (Figure 3-9B). Note again that overlap between the NBO and BO peaks with $X_{\text{Fe}_2\text{O}_3} = 0.2$ makes the current discussion on NMR parameters rather qualitative. While ^{17}O C_{q} is expected to increase with increasing Si-O-Si bond angle (Clark and Grandinetti, 2003; Clark et al., 2001; Grandinetti et al., 1995; Tossell and Lazzarotti, 1988; Xue and Kanzaki, 1998; Xue et al., 1994),

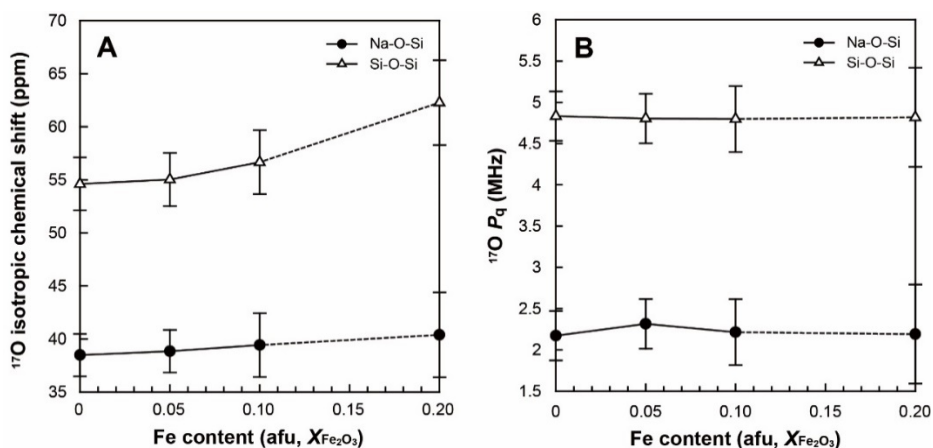


Figure 3-9. Variation of (A) ^{17}O isotropic chemical shifts (δ_{iso}) and (B) quadrupolar coupling products (P_q) of the Na-O-Si (closed circles) and Si-O-Si (open triangles) peaks in ^{17}O 3QMAS NMR spectra of iron-bearing sodium silicate glasses, for different with varying Fe_2O_3 content ($X_{\text{Fe}_2\text{O}_3}$).

the observed trend indicates that the Si-O-Si bond angle may not change for $X_{\text{Fe}_2\text{O}_3}$ below 0.2.

Figure 3-10 shows the variation in the population of Na-O-Si sites ($X_{\text{Na-O-Si}}$) in iron-bearing sodium silicate glasses. Here, $X_{\text{Na-O-Si}}$ was obtained by calculating the ratio of the area under the Na-O-Si component to the total area in the total isotropic projection of ^{17}O 3QMAS NMR spectra. The 3QMAS NMR intensity is affected by the C_q of oxygen sites (Amoureux et al., 1996; Baltisberger et al., 1996; Frydman and Harwood, 1995; Lee and Stebbins, 2000; Massiot et al., 2002; Medek et al., 1995; Wu et al., 1996). Thus, the observed NMR signal intensities were calibrated using a numerically simulated 3QMAS efficiency curve at a given rf field (~ 75 kHz at 9.4 T with an assumed

Table 3-3. NMR parameters (^{17}O δ_{iso} and P_{q}) of oxygen sites in iron-bearing sodium silicate glasses with varying iron content ($X_{\text{Fe}_2\text{O}_3}$)^a.

	$X_{\text{Fe}_2\text{O}_3}$	δ_{iso} (ppm)	P_{q} (MHz)	Populations (%) ^c
Na-O-Si	0	38.5 (± 2)	2.2 (± 0.3)	39.9 (± 2)
	0.05	38.8 (± 2)	2.3 (± 0.3)	33.8 (± 2)
	0.1	39.4 (± 3)	2.2 (± 0.4)	29.5 (± 2)
	0.2 ^b	40.4 (± 4)	2.2 (± 0.6)	24.2 (± 4)
Si-O-Si	0	54.6 (± 2.5)	4.8 (± 0.3)	60.1 (± 2)
	0.05	55.0 (± 2.5)	4.8 (± 0.3)	66.2 (± 2)
	0.1	56.7 (± 3)	4.8 (± 0.4)	70.5 (± 2)
	0.2 ^b	62.3 (± 4)	4.8 (± 0.6)	75.8 (± 4)

^a Numbers in parentheses refer to the uncertainty of the NMR parameters and populations.

^b NMR parameters were calculated from the peak positions.

^c Calibrated population considering 3QMAS efficiency with the magnitude of quadrupolar interactions and experimental conditions (Lee and Stebbins, 2000).

quadrupolar symmetry parameter η set to 0.5). We note that quantifying the NBO fraction in glasses is not trivial because the overlap between Na-O-Si and Si-O-Si in 3QMAS NMR spectra increases with increasing iron content. Nevertheless, the clear resolution of BO and NBO sites allowed us to obtain their corresponding site fractions.

The calibrated $X_{\text{Na-O-Si}}$ (approximately 40%) of the iron-free sodium disilicate glass is consistent with those reported in earlier NMR studies (Lee and Stebbins, 2009; Xue et al., 1994). The Na-O-Si fraction decreases with increasing $X_{\text{Fe}_2\text{O}_3}$, from $\sim 40 \pm 2\%$ for $X_{\text{Fe}_2\text{O}_3} = 0$ to $24.2 \pm 4\%$ for $X_{\text{Fe}_2\text{O}_3} = 0.2$. Although the effect of preferential paramagnetic interaction on oxygen

species remains to be fully confirmed, taking into consideration the homogeneous distribution of iron in the glass network, smaller $X_{\text{Na-O-Si}}$ is indicative of larger degree of polymerization (see Sections 2.3.6 and 2.3.7 below for further discussion).

The NBO fraction can also be estimated from the chemical composition (Lee, 2011; Mysen and Richet, 2018). Taking the iron redox ratio (r , $\text{Fe}^{3+}/\Sigma\text{Fe}$) and the structural roles for Fe^{3+} (tetrahedrally coordinated network-former with charge-balancing Na^+) and Fe^{2+} (network-modifier) into consideration, the relationship between X_{NBO} and the mole fraction of oxides in iron-bearing sodium silicate glasses can be described as:

$$X_{\text{NBO}} = \frac{2 \times [X'_{\text{Na}_2\text{O}} + X'_{\text{Fe}_2\text{O}_3}(1 - 2r)]}{2 - [X'_{\text{Na}_2\text{O}} + X'_{\text{Fe}_2\text{O}_3}(1 - 2r)]} \quad (3.2)$$

where $X'_{\text{Na}_2\text{O}}$ and $X'_{\text{Fe}_2\text{O}_3}$ are the mole fractions of Na_2O and Fe_2O_3 in the glasses [i.e., $X'_{\text{Na}_2\text{O}} = \text{Na}_2\text{O}/(\text{Na}_2\text{O} + \text{Fe}_2\text{O}_3 + \text{SiO}_2)$ and $X'_{\text{Fe}_2\text{O}_3} = \text{Fe}_2\text{O}_3/(\text{Na}_2\text{O} + \text{Fe}_2\text{O}_3 + \text{SiO}_2)$], respectively. Note again that Eq. 3.2 assumes that average ferric iron coordination number is four regardless of its structural role. Furthermore, Na-O-Si, Fe^{2+} -O-Si are counted as NBO (see Section 3.3.4 above). The BO species in Eq. 3.2 include Si-O-Si, ${}^{[4]}\text{Fe}^{3+}$ -O-Si, and ${}^{[4]}\text{Fe}^{3+}$ -O- ${}^{[4]}\text{Fe}^{3+}$. ${}^{[5,6]}\text{Fe}^{3+}$ -O-Si is not taken into consideration. Because the oxygen species such as Fe^{2+} -O-Si (NBO) and ${}^{[4]}\text{Fe}^{3+}$ -O- ${}^{[4]}\text{Fe}^{3+}$ (BO) do not show up in the ${}^{17}\text{O}$ MAS NMR spectra [due to a strong electron (in iron) - nuclear spin (${}^{17}\text{O}$) interaction], the discrepancy between the predicted NBO fraction (from Eq. 3.2) and the those estimated from NMR spectra is expected. Based on Eq. 3.2, the X_{NBO} decreases with iron content at constant iron redox ratio (r , dashed line in Figure 3-10).

The X_{NBO} obtained from the ${}^{17}\text{O}$ NMR spectra of the iron-bearing sodium silicate glasses appears to be roughly consistent with the calculated

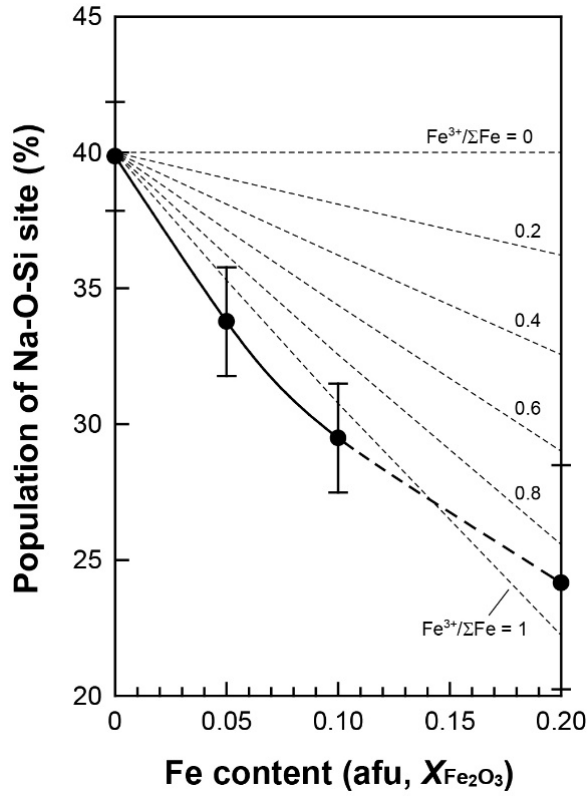


Figure 3-10. Variation of Na-O-Si fraction in iron-bearing sodium silicate glasses with varying Fe_2O_3 content ($X_{\text{Fe}_2\text{O}_3}$). The fractions were obtained from ^{17}O isotropic projections of the spectra at 9.4 T (closed circles). The dotted line represents the hypothetical Na-O-Si fraction values (see text), calculated by considering the Fe^{3+} as a network-forming cation and Fe^{2+} as a network-modifying cation. The assumed iron redox ratio ($\text{Fe}^{3+}/\Sigma\text{Fe}$) values are shown on the dotted lines.

X_{NBO} from Eq. 3.2 with $\text{Fe}^{3+}/\Sigma\text{Fe}$ ratio (~ 0.89) of the current study. The trend confirms that the degree of polymerization in the silicate glasses increases with increasing $X_{\text{Fe}_2\text{O}_3}$, [$= \text{Fe}_2\text{O}_3/(\text{Na}_2\text{O} + \text{Fe}_2\text{O}_3)$], and thus by replacing Na_2O with Fe_2O_3 . In detail, the average $X_{\text{Na-O-Si}}$ values in the iron-bearing silicate glasses are somewhat smaller than the predicted X_{NBO} (in particular at $X_{\text{Fe}_2\text{O}_3}=0.05$ and 0.1). Considering the relatively minor uncertainty associated with the $X_{\text{Na-O-Si}}$ from the ^{17}O NMR, such discrepancy in X_{NBO} at $X_{\text{Fe}_2\text{O}_3}=0.05$ and 0.1 may be real. As the distribution of iron in the glass network is not heterogeneous on the nanoscale, the observed slight discrepancy between the calculated (with Eq. 3.2) and observed $X_{\text{Na-O-Si}}$ may be due to structural changes. Furthermore, while only the presence of $^{4}\text{Fe}^{3+}$ is taken into consideration in Eq. 3.2, $^{5,6}\text{Fe}^{3+}$ in iron-bearing sodium silicate glasses can further reduce the estimated X_{NBO} . Indeed, Fe *K*-edge X-ray absorption spectroscopy and high-temperature measurements of liquid density indicated that the average Fe^{3+} coordination number in iron-bearing alkali-silicate glasses (with $\text{Fe}^{3+}/\Sigma\text{Fe} > 0.8$) varies from 4.5 and 5 (e.g. $\text{K}_2\text{Si}_3\text{O}_7$ and $\text{Na}_2\text{Si}_3\text{O}_7$) (Farges et al., 2004; Liu and Lange, 2006; Wilke et al., 2007). Highly coordinated framework units (e.g. $^{5,6}\text{Al}$ and $^{5,6}\text{Si}$) in the iron-free aluminosilicate glasses at elevated pressure forms at the expense of NBO (Allwardt et al., 2005a; Allwardt et al., 2005b; Lee, 2011; Xue et al., 1991). In addition, framework Al^{3+} (similar to Fe^{3+}) are more likely than Si^{4+} to be highly coordinated, which forms $^{4}\text{Si-O-}^{5,6}\text{Al}$ (Lee, 2011; Poe et al., 1997; Waff, 1975). Therefore, a smaller fraction of NBO for the glasses studied here is likely due to the presence of $^{5,6}\text{Fe}$. While the current results have implications for the structure of iron-bearing melts at high pressure (Lee, 2014 and references therein; e.g., Mysen and Richet, 2018; Sanloup et al., 2013), a

detailed coordination environment of iron in silicate glasses at high pressure needs to be further explored.

3.4. Discussion

3.4.1. Si environments in iron-bearing glasses based on ^{29}Si MAS NMR results

The observed trend in an *apparent* increase in Q^4 species by replacing Na_2O with Fe_2O_3 provides insights into the distribution and structural role of iron. First, if Fe plays any role as a network-former, similar to Al^{3+} , and if the distribution of iron is homogeneous [meaning there is no preferential paramagnetic interaction between Fe and either highly polymerized Si unit (e.g., Q^4) or less polymerized units (e.g., Q^2), as suggested from ^{29}Si T_1 relaxation study, see Section 3.3.2 below], the degree of polymerization and thus the fraction of Q^3 and Q^4 species would increase with increasing $X_{\text{Fe}_2\text{O}_3}$, as Figure 3-1 shows. Second, if the distribution of iron is inhomogeneous and network-forming Fe shows preferential interaction with either highly polymerized Si or less polymerized Si, the fraction of Q^3 and Q^4 would vary with increasing $X_{\text{Fe}_2\text{O}_3}$, depending on the degree of proximity and on the magnitude of interaction. For example, the apparent increase in highly polymerized Q species can result from the distinct inhomogeneous distribution of Fe and its preferential interaction with less polymerized units (e.g., Q^2) and vice versa. The observed trend can thus occur because of a spatial proximity between iron and less polymerized Si units. Third, if Fe can act as a network-modifying cation, similar to Na^+ , and if the distribution of iron is homogeneous, no net differences in the degree of polymerization are expected for glasses with different Fe/Na ratios. The first two schemes can explain the observed trend. Particularly, the former case with network-

forming Fe³⁺ better complies with the suggested role of Fe proposed in the previous studies (e.g., Alberto et al., 1996; Burkhard, 2000; Cochain et al., 2012, and references therein; Mysen et al., 1980). Alternatively, an apparent increase in Q⁴ species can also result from the enhanced disproportionation among Q species (i.e., 2Q³ → Q⁴ + Q²) at the constant degree of polymerization. An increase in the fraction of Q² species, however, was not observed, indicating that an increase in Q⁴ is not due to the enhanced disproportionation among Q species. As will be discussed later, the iron distribution is largely homogeneous (see Section 3.3.2 for spin-lattice relaxation time measurements and assumptions on homogeneous distribution model): thus, the experimental observation in ²⁹Si NMR spectra is mostly likely due to an increase in the degree of polymerization by replacing Na₂O with Fe₂O₃ (and thus with increasing X_{Fe₂O₃})

3.4.2. Homogeneous distribution of Fe in the iron-bearing silicate glasses

As shown in Figure 3-3, ²⁹Si NMR intensity decreases with varying X_{Fe₂O₃}. Based on the observed trend, the effective paramagnetic radius (within which paramagnetic interactions result in NMR signal loss) can be larger than ~1 nm, which is several times the typical Si-Si distance in silicate glasses. The observed trend and the estimated magnitude of interactions (characterized with the effective paramagnetic radius) are consistent with previous NMR results: through-bond Fermi-contact interaction and through-space pseudocontact interaction in Fe-⁷Li interactions (with the effective paramagnetic radius of ~nm) in crystalline oxides are much larger than the magnitude of interactions among nuclear spins (e.g., Grey and Dupre, 2004). Because of the signal loss, not all the Si spins are probed in the MAS NMR. Therefore, the current interpretation of a homogenous Fe distribution is

based on the premise that the observed nuclear spins can represent the structural environments of the whole glass networks, implying inevitable uncertainty in the Fe distribution model. Nevertheless, the stretching exponent β (≈ 0.5) does not depend on $X_{\text{Fe}_2\text{O}_3}$, indicating that the homogeneous spatial correlation between nuclear spins and iron does not change with increasing iron content. While the portion of the nuclear spins indeed decreases with increasing $X_{\text{Fe}_2\text{O}_3}$ and we cannot completely discard potential heterogeneity, it is unlikely that the iron distributions within the effective paramagnetic radii are largely different from those in glass networks that are being observed (i.e., homogeneous distribution).

3.4.3. Hidden oxygen species in ^{17}O NMR spectra

While the presence of *Hidden* oxygen species are expected in the iron-bearing glasses studied here (Figure 3-8), they are not observed in the NMR spectra because the signal is lost due to stronger interaction between oxygen spins and the unpaired electron spins. Therefore, it should be mentioned that the current ^{17}O NMR data do not provide fully details of the network connectivity. Because of the relatively low concentration of Fe^{2+} and higher energy penalty for its formation, metal-bridging oxygen species (MBO) such as $\text{Fe}^{2+}\text{-O-Fe}^{2+}$, Na-O-Fe^{3+} , and $\text{Fe}^{2+}\text{-O-Na}$ are unlikely to form in the disilicate glasses studied here (Lee and Kim, 2015): here, the energy penalty refers to the relative energy difference (DE) among the iron-bearing oxygen clusters in the following quasi-chemical reaction: $[\text{Na-O-Si}] + [\text{Fe}^{2+}\text{-O-Si}]$, $[\text{Na-O-Fe}^{2+}] + [\text{Si-O-Si}]$. Therefore, the fractions of those high energy clusters are likely to be negligible. As the structural role of highly coordinated Fe^{3+} , particularly $^{[5]}\text{Fe}^{3+}$ remains to be determined, it is not clear whether $^{[5,6]}\text{Fe}^{3+}\text{-O-Si}$, and $^{[5,6]}\text{Fe}^{3+}\text{-O-[4]Fe}^{3+}$ should be considered as either BO or NBO species.

3.4.4. Insights into iron distribution, the degree of polymerization, and the extent of chemical disorder in iron-bearing sodium silicate glasses

3.4.4.1. Iron distribution and the degree of polymerization

The high-resolution ^{29}Si and ^{17}O NMR results provide structural details of the effect of iron on Q speciation, spatial distribution of iron, and the extent of polymerization in iron-bearing sodium silicate glasses. Although it is difficult to provide a quantitative description of the extent of topological disorder due to the overlap between the Q species, by taking into consideration the variation of peak width and positions in ^{29}Si MAS NMR spectra and the homogeneity in the ^{29}Si relaxation time study it can be deduced that highly polymerized silicon species increase with increasing $X_{\text{Fe}_2\text{O}_3}$, indicating an increase in the degree of polymerization (Figure 3-1, Section 3.3.2). It should be mentioned that the current results are also consistent with the suggestions from earlier Raman studies of iron-bearing silicate glasses that while there is considerable overlap among the Raman modes due to less polymerized Q species and polymerized $(\text{Fe}^{3+},\text{Si})\text{-O}$ stretching vibrations, the systematic increase in the $(\text{Fe}^{3+},\text{Si})\text{-O}$ stretching vibrational band with increasing $\text{Fe}^{3+}/\text{Fe}^{2+}$ ratio either at constant total iron content and/or variable iron content implies an increase in the degree of polymerization (e.g., Cochain et al., 2012, and references therein; Mysen et al., 1980; Roskosz et al., 2008).

The ^{29}Si spin-lattice relaxation time study for the iron-bearing glasses studied here shows that the distribution of iron in the glass networks is homogeneous on the nanometer scale (Figures 3-2 and 3-3). However, this does not exclude the possibility that there is a moderate degree of preferential distribution of iron between NBO and BO clusters as evidenced from the

preferential broadening of BO peaks (relative to NBO) in the ^{17}O NMR spectra. The broadening of the Gaussian peak with increasing $X_{\text{Fe}_2\text{O}_3}$ also implies that the topological disorder (in addition to the homogeneous lifetime broadening) increases with increasing iron content. ^{17}O 3QMAS NMR spectra indeed confirm that the degree of polymerization increases with increasing iron content in our compositional series.

3.4.4.2. *The extent of chemical disorder in iron-bearing silicate glasses*

Despite the progress and new insights, the following structural aspects of iron-bearing silicate glasses remain to be addressed. First, the degree of chemical disorder (i.e., Si/Fe mixing) cannot be uniquely quantified from the current results because of lack of information on the hidden species (e.g., $^{41}\text{Si}-\text{O}-^{41}\text{Fe}^{3+}$). This is in contrast to sodium aluminosilicate glasses where the extent of framework disorder (Si/Al) was fully quantified from the experimentally derived fraction of bridging oxygen clusters, such as $^{41}\text{Si}-\text{O}-^{41}\text{Al}$ (see, Lee and Stebbins, 2009 and references therein). If the distribution of framework units (Si^{4+} and Fe^{3+}) deviates from complete chemical order, the presence of $\text{Fe}^{3+}-\text{O}-\text{Fe}^{3+}$ in the iron-rich glasses would be expected because the fraction of oxygen atoms linking similar pairs (e.g., $\text{Al}-\text{O}-\text{Al}$ and $\text{Fe}^{3+}-\text{O}-\text{Fe}^{3+}$) increases with increasing deviation from chemical order (e.g., Lee and Stebbins, 2002). Previous studies also showed that an increase in the cation field strength (i.e., charge divided by the square of the cation-oxygen distance) of non-framework cations leads to an increase in the fraction of $\text{Al}-\text{O}-\text{Al}$ (Allwardt et al., 2005b; Bunker et al., 1991; Kelsey et al., 2008; Kelsey et al., 2009; Lee, 2005). The cation field strength of network-modifying Fe^{2+} in iron-bearing sodium silicate glasses (~ 2.9) is larger than that in iron-free sodium

silicate glass (~ 0.4). We thus speculate that the degree of network distortion and disorder increases with increasing Fe^{2+} content.

We note that the current description of the structure and the degree of polymerization in the iron-bearing glasses are certainly similar to those of the partially depolymerized Na-aluminosilicate glasses. For instance, a previous ^{17}O NMR study of glasses in the Na-silicate ($\text{Na}_2\text{Si}_3\text{O}_7$)-fully polymerized Na-aluminosilicate ($\text{NaAlSi}_3\text{O}_8$) join with varying $\text{Na}_2\text{O}/(\text{Na}_2\text{O}+\text{Al}_2\text{O}_3)$ ratio confirmed that the fraction of Na-O-Si decreases with increasing Al contents, forming Al-O-Si (Lee and Stebbins, 2009). While their previous study also showed a preferential proximity between Na and NBO, the results confirms that Na^+ sees both NBO and BO in the first shell, indicating a homogeneous distribution of non-network-formers (Lee and Stebbins, 2009). Similarly, the current study of iron-bearing silicate glasses showed that the degree of polymerization increases with increasing iron content, forming BO, such as $\text{Fe}^{3+}\text{-O-Si}$, as also indicated from an increase in the peak intensity at $\sim 980\text{ cm}^{-1}$ in Raman spectra for the iron-bearing silicate glasses (e.g., Alberto et al., 1996; Burkhard, 2000; Cochain et al., 2012, and references therein; Mysen et al., 1980). While the preferential interactions among iron, NBO, and BO are prevalent (e.g., proximity between Fe^{2+} and NBO, as well as that between $\text{Fe}^{3+}\text{-BO}$), the iron distribution is largely homogeneous in that Fe^{2+} and Fe^{3+} see both BO and NBO in the glass network. For instance, more significant $X_{\text{Fe}_2\text{O}_3}$ dependence of peak width and position in Si-O-Si compared with those in Na-O-Si could also be due to the expected proximity between Fe and Si-O-Si that could result in a larger variation of the observed Si-O-Si peak characteristics (bond angle and length) (Figures 3-7 and 3-9). Therefore, in addition to the fact that the formation of iron-bearing hidden BO ($\text{Fe}^{3+}\text{-O-Si}$) and NBO ($\text{Fe}^{2+}\text{-O-Si}$) cannot be observed (see Section 3.4.3), iron in $\text{Fe}^{3+}\text{-O-Si}$

species (as expected from the composition) can have proximity to Na-O-Si so that the potential interaction between electron in Fe^{3+} and ^{17}O nuclear spin in Na-O-Si (depending on the distance between Fe^{3+} in the BO cluster and Na-O-Si) can reduce the Na-O-Si signal intensity (Figure 3-10). Similarly, though minor, Fe^{2+} -O-Si or (Na, Fe^{2+})-O-Si can affect the signal intensity of Si-O-Si sites. The observed changes in Na-O-Si, and Si-O-Si are thus greatly affected by the local distribution of Fe beyond the first-coordination shell for oxygen and silicon, and thus by the local environments in a medium (and/or intermediate) range length-scale. Note that this interpretation is not contradictory to the ^{29}Si spin-lattice relaxation study where the homogeneous distribution of iron is suggested. Nanoscale homogeneity does not necessary means that there should be no preferential interaction between Fe and local oxygen cluster. The current structural disorder can be described with the perturbed Fe distribution model where there is a preferential interaction between iron and local clusters upon maintaining nanoscale homogeneity in the glasses (Lee and Stebbins, 2003). The unknown effect of Fe^{2+} on the extent of chemical and topological disorder in oxide glasses remains to be explored.

3.4.5. Implications and limitation of the current analysis

The current results show that the experimentally determined X_{NBO} is similar to the X_{NBO} predicted from the composition by assuming that Fe^{3+} acts as a network-forming cation and Fe^{2+} acts as a network-modifying cation. The current results are thus consistent with the hypothesis that Fe^{3+} is framework cation associated with Na^+ in a charge-balancing role: if Fe^{3+} is predominantly a network-former, the degree of polymerization (and thus X_{BO}) is expected to increase with increasing iron content. If Fe^{3+} is predominantly a network-modifier, the degree of polymerization would decrease with iron content. We

believe that the current observations, together with the previous studies, indicate that the former case is most likely. The experimental NMR results shown here, however, cannot uniquely constraint the coordination number of Fe^{3+} . The results have the potential to provide direct insight into the melt viscosity (η) of iron-bearing sodium silicate melts as the latter is known to increase with decreasing X_{NBO} (Bottinga and Weill, 1972; Giordano and Dingwell, 2003; Lee, 2005; Lee et al., 2004; Mazurin, 1983; Richet, 1984; Toplis, 2001). For example, viscosity of melts along the $\text{Na}_2\text{Si}_2\text{O}_5$ - $\text{NaFe}^{3+}\text{Si}_2\text{O}_6$ (acmite) join at ~ 1300 °C increases with increasing iron concentration from $10^{1.47}$ Pa s ($\text{Na}_2\text{O}:\text{Fe}_2\text{O}_3:\text{SiO}_2 = 0.8:0.2:2$ with X_{NBO} approximated from the composition of 0.22) to $10^{1.73}$ Pa s ($\text{Na}_2\text{O}:\text{Fe}_2\text{O}_3:\text{SiO}_2 = 0.5:0.5:2$ with X_{NBO} from the composition of 0) at constant $\text{Fe}^{3+}/\Sigma\text{Fe}$ of ~ 0.98 (Dingwell and Virgo, 1988). Thus, an increase in viscosity of Na_2O - Fe_2O_3 - SiO_2 melts could stem from a decrease in NBO fraction by replacing Na with iron.

The viscosity of silicate melts is affected both by the X_{NBO} and the degree of disorder among framework cations (i.e., Si, Al, and Fe^{3+}), whereas the effect of the latter on melt viscosity decreases at elevated temperature conditions. For aluminosilicate melts, an increase in the degree of chemical disorder between Si and Al leads to a decrease in melt viscosity (Adam and Gibbs, 1965; Lee, 2005; Richet, 1984). The current ^{29}Si and ^{17}O NMR results confirm that Fe^{3+} acts as a network-forming cation, which is similar to Al^{3+} . Viscosity of Na_2O - Fe_2O_3 - SiO_2 melts ($\text{Fe}^{3+}/\Sigma\text{Fe} = \sim 0.95$) at constant X_{NBO} of ~ 0.22 decreases with increasing Fe^{3+}/Si ratio, from $10^{2.31}$ Pa s (for $\text{Fe}^{3+}/\text{Si} = 0.05$) to $10^{0.37}$ Pa s (for $\text{Fe}^{3+}/\text{Si} = 1$) (Dingwell and Virgo, 1988). Based on the current results, the decrease in viscosity with an increase in Fe^{3+}/Si could stem from the increase in the degree of disorder between Si and Fe^{3+} and/or increase in the Fe^{3+} -O-Si fraction with iron content. As the above discussion is based on

the homogeneous distribution of iron in the glass networks and only a part of the nuclear spins in the iron-bearing glasses is being probed, a full, quantitative link between the structure and viscosity cannot be made. Thus, the above discussion only provides qualitative insights into the transport properties of iron-bearing silicate glasses.

3.5. Conclusion

While the iron-bearing and other transition metal-bearing materials are essential components of natural silicate melts, solid-state NMR techniques, one of the most versatile experimental methods to probe the structure of oxide glasses, have not been fully utilized for exploring the structural details of paramagnetic elements-bearing melts and glasses. In this study, we have demonstrated that, despite the inherent paramagnetic effect, high-resolution solid-state NMR techniques can be effectively applied to study the effect of iron concentration on the atomic configurations around silicon and oxygen sites in iron-bearing sodium silicate glasses. The current results show that changes in NMR peaks and relevant parameters reflect iron-induced structural changes, such as degree of polymerization, topological disorder, and iron distribution around silicon and oxygen sites. In particular, ^{29}Si and ^{17}O NMR results indicate that the degree of polymerization apparently increases with increasing iron concentration in our compositional series. This indicates that Fe^{3+} have a proximity to the charge-balancing Na^+ . While alternative interpretations are possible, the results are consistent with the idea that Fe^{3+} mainly acts as a network-former with charge-balancing Na^+ . The ^{17}O NMR spectra also showed that an increase in iron concentration affects Si-O-Si more than Na-O-Si, suggesting an increase in the topological disorder with increasing iron content and much larger changes induced in

Si-O-Si compared with Na-O-Si. As mentioned in Section 3.3.4, the highly coordinated Fe^{3+} may account for the observed variation of oxygen site populations with iron content in the glasses. In addition, the spatial proximity among Fe, Si-O-Si, and Na-O-Si leads to selective changes in their signal intensity. The current results suggest that high-resolution NMR could indirectly allow us to infer the degree of intermixing among framework cations (i.e., Si and Fe^{3+}) and could help improve our understanding of the relationship between the atomic structure and the properties of iron-bearing silicate glasses.

Finally, there are several important limitations of the current study. Because of severe broadening and peak overlaps, there exist uncertainties in the current NMR results, necessitating further experimental studies. The theoretical framework regarding the effect of paramagnetic interaction on NMR spectra in the glasses remains to be established. Furthermore, it is also difficult to distinguish the contribution from structural disorder and that from paramagnetic interaction to the spectral patterns. These lead to an intrinsic uncertainty in the current interpretation. Despite these shortcomings, the current manuscript reports one of the first experimental efforts using NMR. Further experiments and theoretical efforts will provide improved structural insights into the iron-bearing silicate glasses.

APPENDIX

3A-1. Mössbauer spectroscopy of iron-bearing sodium disilicate glasses

The iron redox ratios ($\text{Fe}^{3+}/\Sigma\text{Fe}$) of the studied samples were obtained by using the Mössbauer spectroscopy (see Section 3.2.2 for detailed description of the experimental procedure). Figure 3-A1 shows the Mössbauer spectra for $X_{\text{Fe}_2\text{O}_3} = 0.2$ (fused in an Ar environment) and 0.3 (fused in an air), which exhibit absorption maxima near -0.2 and 0.7 mm/s for both spectra, indicative a doublet due to Fe^{3+} . While the presence of only Fe^{3+} doublet is clear in the Mössbauer spectra, a minor fraction of doublet due to Fe^{2+} could be present in the spectra. To observe the Fe^{2+} doublet with a minor fraction of Fe^{2+} ($< 10\%$), more data points and enhanced signal to noise ratio in the spectra are necessary. We estimated the iron redox ratio of the glasses from previous studies to obtain more accurate values (Dingwell and Virgo, 1987, 1988; Dunaeva et al., 2012; Kukkadapu et al., 2003; Mysen et al., 1980; Mysen and Virgo, 1985). These previous results confirmed that the $\text{Fe}^{3+}/\Sigma\text{Fe}$ ratios vary with oxygen fugacity and composition [e.g., X_{SiO_2} , $X_{\text{Fe}_2\text{O}_3}$, and $\text{Fe}/(\text{Na}+\text{Fe})$]. The $\text{Fe}^{3+}/\Sigma\text{Fe}$ of the alkali silicate glasses synthesized using similar methods is reported to be $\sim 0.89 \pm 0.04$ (Appendix 2A-2 for the detailed results). Note that the glasses in previous studies were synthesized in atmospheric conditions ($f_{\text{O}_2} = 10^{-0.68}$), while the glasses in current studies were synthesized in an Ar environments (as well as in an air). Whereas the current Mössbauer results confirm that the results do not vary with varying atmospheric conditions studied here, the oxygen fugacity of Ar environment in the furnace used in the current study remains to the estimated using the external oxygen fugacity sensor. To further estimate the $\text{Fe}^{3+}/\Sigma\text{Fe}$ ratios of the glasses synthesized in an Ar environment, we assumed that the f_{O_2} of Ar environment is about $10^{-1.98} \sim 10^{-2.68}$ (1/20 to 1/100 of the oxygen fugacity in

atmospheric conditions. Despite the assumption and uncertainty, the iron redox ratio does not change significantly with a decrease in $\log f_{\text{O}_2}$ from -0.68 (in an air) to -2.68 ($1/100 f_{\text{O}_2^{\text{air}}}$) [See Figure 3-A2(A) in Appendix 2A-2. Grey line]. A significant drop in the $\log f_{\text{O}_2}$ is observed with a further decrease in $\log f_{\text{O}_2}$ below -4 (grey dotted line in Figure 3-A2(A) in Appendix 3A-2), confirming that the Fe^{3+} is dominant in the glasses studied here.

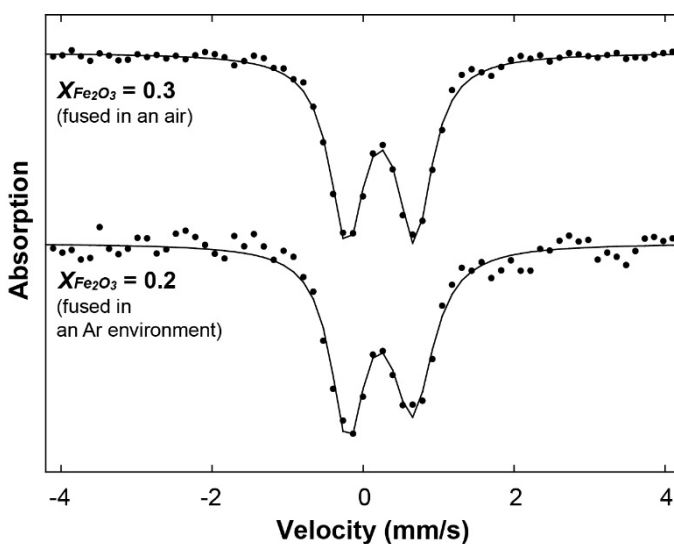


Figure 3-A1. Mössbauer spectra of ^{57}Fe in iron-bearing sodium silicate glasses $[(\text{Na}_2\text{O})_{1-x} \cdot (\text{Fe}_2\text{O}_3)_x \cdot 2\text{SiO}_2]$ at 298 K with varying $X_{\text{Fe}_2\text{O}_3}$ [= $\text{Fe}_2\text{O}_3 / (\text{Na}_2\text{O} + \text{Fe}_2\text{O}_3)$], as labeled.

3A-2. Iron redox ratio of iron-bearing silicate glasses

We summarized the iron redox ratios ($\text{Fe}^{3+}/\Sigma\text{Fe}$) for $\text{Na}_2\text{O}-\text{Fe}_2\text{O}_3-\text{SiO}_2$ glasses reported in previous studies. These previous results confirmed that the $\text{Fe}^{3+}/\Sigma\text{Fe}$ ratios vary with oxygen fugacity and composition [e.g., X_{SiO_2} , $X_{\text{Fe}_2\text{O}_3}$, and $\text{Fe}/(\text{Na}+\text{Fe})$]. Table 3-A1 contains the iron redox ratios ($\text{Fe}^{3+}/\Sigma\text{Fe}$) for $\text{Na}_2\text{O}-\text{Fe}_2\text{O}_3-\text{SiO}_2$ glasses, as reported in previous studies that utilized Mössbauer spectroscopy at 298 K (Dingwell and Virgo, 1987, 1988; Dunaeva et al., 2012; Kukkadapu et al., 2003; Mysen et al., 1980; Mysen and Virgo, 1985). Figure 3-A2 also shows the effect of composition (i.e., its SiO_2 content and Na/Fe ratio) on the redox ratio, for ternary Na-Fe silicate glasses. Particularly, Figure 3-A2(A) shows that the iron redox ratio gradually decreases with a decrease in $\log f_{\text{O}_2}$ up to ~ -4 (grey solid line), while it abruptly decreases with $\log f_{\text{O}_2}$ below -4 (grey dotted line).

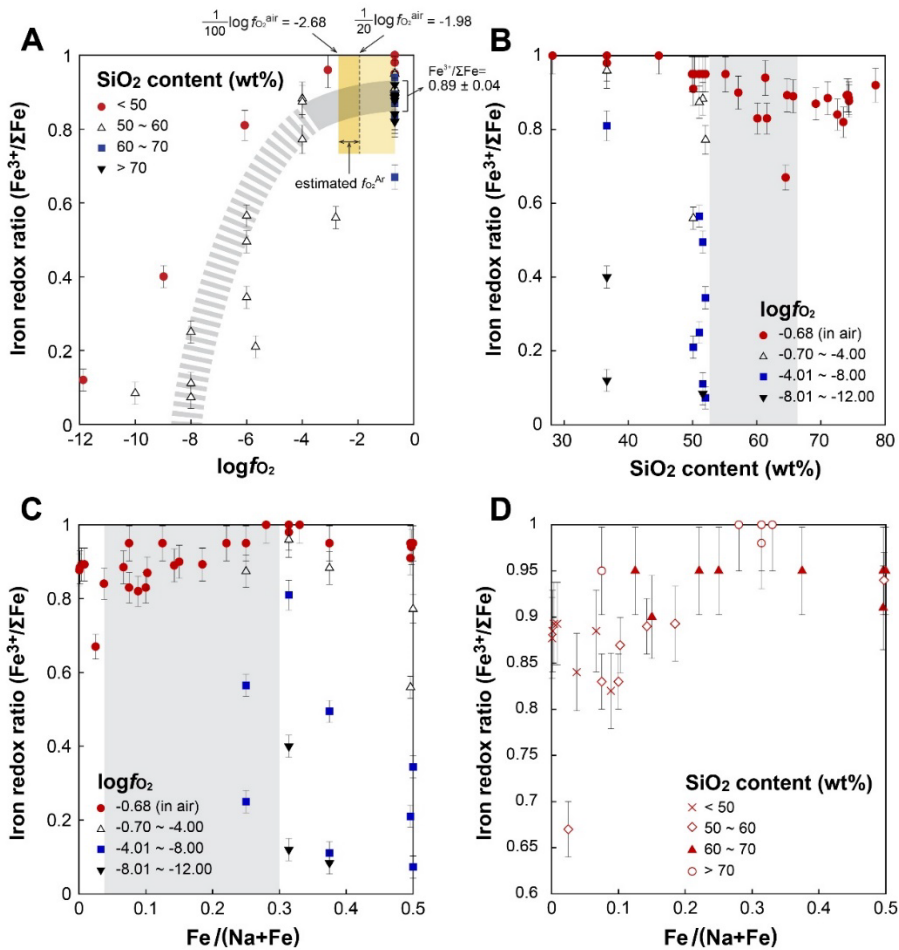


Figure 3-A2. The iron redox ratios ($\text{Fe}^{3+}/\Sigma\text{Fe}$) in the ternary Na-Fe silicate glasses with varying oxygen fugacity (A), SiO₂ content (B), and Fe/(Na+Fe) (C and D). Note that (D) shows the $\text{Fe}^{3+}/\Sigma\text{Fe}$ with varying Fe/(Na+Fe) for the glasses synthesized in air ($\log f_{\text{O}_2} = -0.68$). The shaded area in Figure (A) corresponds to the assumed oxygen fugacity of an Ar environment in the furnace studied here ($1/20 \sim 1/100 f_{\text{O}_2}^{\text{air}}$). Note also that grey solid and dashed lines in (A) are guides to the eye. The shaded areas in (B) and (C) correspond to the composition of the currently studied glasses (see Table 3-A1 for details and references).

Table 3-A1. Iron redox ratios ($\text{Fe}^{3+}/\Sigma\text{Fe}$) for $\text{Na}_2\text{O}-\text{Fe}_2\text{O}_3-\text{SiO}_2$ glasses, as reported in previous studies that used Mössbauer spectroscopy at 298 K.

Reference	Composition (wt%)			$\log f_{\text{O}_2}$	$\text{Fe}^{3+}/\Sigma\text{Fe}$
	SiO_2	Fe_2O_3	Na_2O		
Dingwell and Virgo, 1988	73.48	5.31	21.21	-0.68	0.82
	65.68	10.29	24.03	-0.68	0.89
	55.14	18.93	25.93	-0.68	0.95
	36.68	34.27	29.05	-0.68	0.98
	28.22	40.18	31.61	-0.68	1.00
	78.50	15.54	5.96	-0.68	0.92
	61.34	27.78	10.89	-0.68	0.94
	50.12	35.78	14.10	-0.68	0.95
Dingwell and Virgo, 1987	36.68	34.27	29.05	-0.68	1.00
	36.68	34.27	29.05	-3.08	0.96
	36.68	34.27	29.05	-6.07	0.81
	36.68	34.27	29.05	-8.98	0.4
	36.68	34.27	29.05	-11.87	0.12
	50.12	35.78	14.10	-0.68	0.91
	50.12	35.78	14.10	-2.8	0.560
	50.12	35.78	14.10	-5.68	0.210
Mysen and Virgo, 1985	64.52	2.20	33.28	-0.68	0.670
	61.59	6.64	31.77	-0.68	0.830
	60.11	8.88	31.01	-0.68	0.830
	57.13	13.40	29.47	-0.68	0.900
Dunaeva et al., 2012	64.74	13.00	22.26	-0.68	0.893
	69.20	7.00	23.80	-0.68	0.870
	71.06	4.50	24.44	-0.68	0.885
	72.55	2.50	24.95	-0.68	0.840
	74.34	0.10	25.56	-0.68	0.885
	74.38	0.05	25.57	-0.68	0.877
Mysen et al., 1980	49.92	8.65	41.42	-0.68	0.95
	50.31	13.37	36.32	-0.68	0.95
	51.05	22.61	26.33	-0.68	0.95
	52.02	34.56	13.42	-0.68	0.95
	51.05	22.61	26.33	-4	0.874
	51.05	22.61	26.33	-6	0.565
	51.05	22.61	26.33	-8	0.25
	51.60	29.39	19.01	-4	0.883
	51.60	29.39	19.01	-6	0.495
	51.60	29.39	19.01	-8	0.111
	51.60	29.39	19.01	-10	0.084
	52.02	34.56	13.42	-4	0.772
	52.02	34.56	13.42	-6	0.344
52.02	34.56	13.42	-8	0.073	

REFERENCES

- Adam, G. and Gibbs, J.H. (1965) On temperature dependence of cooperative relaxation properties in glass-forming liquids. *J. Chem. Phys.* 43, 139-146.
- Alberto, H.V., daCunha, J.L.P., Mysen, B.O., Gil, J.M. and deCampos, N.A. (1996) Analysis of Mössbauer spectra of silicate glasses using a two-dimensional Gaussian distribution of hyperfine parameters. *J. Non-Cryst. Solids* 194, 48-57.
- Allwardt, J.R., Lee, S.K. and Stebbins, J.F. (2003) Bonding preferences of non-bridging O atoms: Evidence from ^{17}O MAS and 3QMAS NMR on calcium aluminate and low-silica Ca-aluminosilicate glasses. *Am. Mineral.* 88, 949-954.
- Allwardt, J.R., Poe, B.T. and Stebbins, J.F. (2005a) The effect of fictive temperature on Al coordination in high-pressure (10 GPa) sodium aluminosilicate glasses. *Am. Mineral.* 90, 1453-1457.
- Allwardt, J.R., Stebbins, J.F., Schmidt, B.C., Frost, D.J., Withers, A.C. and Hirschmann, M.M. (2005b) Aluminum coordination and the densification of high-pressure aluminosilicate glasses. *Am. Mineral.* 90, 1218-1222.
- Amoureux, J.P., Fernandez, C. and Frydman, L. (1996) Optimized multiple-quantum magic-angle spinning NMR experiments on half-integer quadrupoles. *Chem. Phys. Lett.* 259, 347-355.
- Angeli, F., Charpentier, T., Gin, S. and Petit, J.C. (2001) ^{17}O 3Q-MAS NMR characterization of a sodium aluminoborosilicate glass and its alteration gel. *Chem. Phys. Lett.* 341, 23-28.
- Ashbrook, S.E., Berry, A.J. and Wimperis, S. (2002) ^{17}O multiple-quantum MAS NMR study of pyroxenes. *J. Phys. Chem. B* 106, 773-778.
- Ashbrook, S.E. and Smith, M.E. (2006) Solid state ^{17}O NMR - an introduction to the background principles and applications to inorganic materials. *Chemical Society Reviews* 35, 718-735.
- Baltisberger, J.H., Xu, Z., Stebbins, J.F., Wang, S.H. and Pines, A. (1996) Triple-quantum two-dimensional ^{27}Al magic-angle spinning nuclear magnetic resonance spectroscopic study of aluminosilicate and aluminate crystals and glasses. *J. Am. Chem. Soc.* 118, 7209-7214.

- Bell, A.S. and Simon, A. (2011) Experimental evidence for the alteration of the $\text{Fe}^{3+}/\Sigma\text{Fe}$ of silicate melt caused by the degassing of chlorine-bearing aqueous volatiles. *Geology* 39, 499-502.
- Bell, P.M., Mao, H.K. and Weeks, R.A. (1976) Optical spectra and electron paramagnetic resonance of lunar and synthetic glasses: A study of the effects of controlled atmosphere, composition, and temperature. *Proc. 7th Lunar Sci. Conf.*, 2543-2559.
- Bezou, A. and Humler, E. (2005) The $\text{Fe}^{3+}/\Sigma\text{Fe}$ ratios of MORB glasses and their implications for mantle melting. *Geochim. Cosmochim. Acta* 69, 711-725.
- Boon, J.A. and Fyfe, W.S. (1972) Coordination number of ferrous ions in silicate glasses. *Chem. Geol.* 10, 287-298.
- Borisov, A. and McCammon, C. (2010) The effect of silica on ferric/ferrous ratio in silicate melts: An experimental study using Mössbauer spectroscopy. *Am. Mineral.* 95, 545-555.
- Bottinga, Y. and Weill, D.F. (1972) Viscosity of magmatic silicate liquids: Model for calculation. *Am. J. Sci.* 272, 438-475.
- Bouhifd, M.A., Richet, P., Besson, P., Roskosz, M. and Ingrin, J. (2004) Redox state, microstructure and viscosity of a partially crystallized basalt melt. *Earth Planet. Sci. Lett.* 218, 31-44.
- Bunker, B.C., Kirkpatrick, R.J., Brow, R.K., Turner, G.L. and Nelson, C. (1991) Local-structure of alkaline-earth boroaluminate crystals and glasses: II, ^{11}B and ^{27}Al MAS NMR-spectroscopy of alkaline-earth boroaluminate glasses. *J. Am. Ceram. Soc.* 74, 1430-1438.
- Burkhard, D.J.M. (2000) Iron-bearing silicate glasses at ambient conditions. *J. Non-Cryst. Solids* 275, 175-188.
- Calas, G. and Petiau, J. (1983) Coordination of iron in oxide glasses through high-resolution K-edge spectra: Information from the pre-edge. *Solid State Commun.* 48, 625-629.
- Chevrel, M.O., Giordano, D., Potuzak, M., Courtial, P. and Dingwell, D.B. (2013) Physical properties of $\text{CaAl}_2\text{Si}_2\text{O}_8$ - $\text{CaMgSi}_2\text{O}_6$ - FeO - Fe_2O_3 melts: Analogues for extra-terrestrial basalt. *Chem. Geol.* 346, 93-105.

- Clark, T.M. and Grandinetti, P.J. (2003) Dependence of bridging oxygen ^{17}O quadrupolar coupling parameters on Si-O distance and Si-O-Si angle. *J. Phys.-Condens. Ma.* 15, S2387-S2395.
- Clark, T.M. and Grandinetti, P.J. (2005) Calculation of bridging oxygen ^{17}O quadrupolar coupling parameters in alkali silicates: A combined *ab initio* investigation. *Solid State Nucl. Magn. Reson.* 27, 233-241.
- Clark, T.M., Grandinetti, P.J., Florian, P. and Stebbins, J.F. (2001) An ^{17}O NMR investigation of crystalline sodium metasilicate: Implications for the determination of local structure in alkali silicates. *J. Phys. Chem. B* 105, 12257-12265.
- Clark, T.M., Grandinetti, P.J., Florian, P. and Stebbins, J.F. (2004) Correlated structural distributions in silica glass. *Phys. Rev. B* 70, 064202.
- Cochain, B., Neuville, D.R., Henderson, G.S., McCammon, C.A., Pinet, O. and Richet, P. (2012) Effects of the iron content and redox state on the structure of sodium borosilicate glasses: A raman, Mössbauer and boron k-edge XANES spectroscopy study. *J. Am. Ceram. Soc.* 95, 962-971.
- Cole, K.E., Paik, Y., Reeder, R.J., Schoonen, M. and Grey, C.P. (2004) ^2H MAS NMR studies of deuterated goethite ($\alpha\text{-FeOOD}$). *J. Phys. Chem. B* 108, 6938-6940.
- Cottrell, E. and Kelley, K.A. (2011) The oxidation state of Fe in MORB glasses and the oxygen fugacity of the upper mantle. *Earth Planet. Sci. Lett.* 305, 270-282.
- Cukierman, M. and Uhlmann, D.R. (1974) Effects of iron oxidation-state on viscosity, lunar composition 15555. *J. Geophys. Res.* 79, 1594-1598.
- Dingwell, D.B. (1989) Shear viscosities of ferrosilicate liquids. *Am. Mineral.* 74, 1038-1044.
- Dingwell, D.B. (1991) Redox viscometry of some Fe-bearing silicate melts. *Am. Mineral.* 76, 1560-1562.
- Dingwell, D.B., Brearley, M. and Dickinson, J.E. (1988) Melt densities in the Na_2O - FeO - Fe_2O_3 - SiO_2 system and the partial molar volume of tetrahedrally-coordinated ferric iron in silicate melts. *Geochim. Cosmochim. Acta* 52, 2467-2475.

- Dingwell, D.B. and Virgo, D. (1987) The effect of oxidation-state on the viscosity of melts in the system $\text{Na}_2\text{O-FeO-Fe}_2\text{O}_3\text{-SiO}_2$. *Geochim. Cosmochim. Acta* 51, 195-205.
- Dingwell, D.B. and Virgo, D. (1988) Viscosities of melts in the $\text{Na}_2\text{O-FeO-Fe}_2\text{O}_3\text{-SiO}_2$ system and factors controlling relative viscosities of fully polymerized silicate melts. *Geochim. Cosmochim. Acta* 52, 395-403.
- Dirken, P.J., Kohn, S.C., Smith, M.E. and vanEck, E.R.H. (1997) Complete resolution of Si-O-Si and Si-O-Al fragments in an aluminosilicate glass by ^{17}O multiple quantum magic angle spinning NMR spectroscopy. *Chem. Phys. Lett.* 266, 568-574.
- Dunaeva, E.S., Uspenskaya, I.A., Pokholok, K.V., Minin, V.V., Efimov, N.N., Ugolkova, E.A. and Brunet, E. (2012) Coordination and RedOx ratio of iron in sodium-silicate glasses. *J. Non-Cryst. Solids* 358, 3089-3095.
- Farges, F., Lefrere, Y., Rossano, S., Berthereau, A., Calas, G. and Brown, G.E. (2004) The effect of redox state on the local structural environment of iron in silicate glasses: a molecular dynamics, combined XAFS spectroscopy, and bond valence study. *J. Non-Cryst. Solids* 344, 176-188.
- Farnan, I., Grandinetti, P.J., Baltisberger, J.H., Stebbins, J.F., Werner, U., Eastman, M.A. and Pines, A. (1992) Quantification of the disorder in network-modified silicate glasses. *Nature* 358, 31-35.
- Fox, K.E., Furukawa, T. and White, W.B. (1982) Transition-metal ions in silicate melts. Part II. Iron in sodium-silicate glasses. *Phys. Chem. Glasses* 23, 169-178.
- Frisch, M.J., Trucks, G.W. and others, a. (2004) Gaussian 03, Gaussian, Inc., Wallingford, Connecticut.
- Frydman, L. and Harwood, J.S. (1995) Isotropic spectra of half-integer quadrupolar spins from bidimensional magic-angle spinning NMR. *J. Am. Chem. Soc.* 117, 5367-5368.
- Fudali, R.F. (1965) Oxygen fugacities of basaltic and andesitic magmas. *Geochim. Cosmochim. Acta* 29, 1063-1075.
- Giordano, D. and Dingwell, D.B. (2003) Non-Arrhenian multicomponent melt viscosity: A model. *Earth Planet. Sci. Lett.* 208, 337-349.

- Goldman, D.S. and Berg, J.I. (1980) Spectral study of ferrous iron in Ca-Al-borosilicate glass at room and melt temperatures. *J. Non-Cryst. Solids* 38-9, 183-188.
- Grandinetti, P.J., Baltisberger, J.H., Farnan, I., Stebbins, J.F., Werner, U. and Pines, A. (1995) Solid-state ^{17}O magic-angle and dynamic-angle spinning NMR-study of the SiO_2 polymorph coesite. *J. Phys. Chem.* 99, 12341-12348.
- Grey, C.P., Dobson, C.M., Cheetham, A.K. and Jakeman, R.J.B. (1989) Studies of rare-earth stannates by ^{119}Sn MAS NMR: The use of paramagnetic shift probes in the solid-state. *J. Am. Chem. Soc.* 111, 505-511.
- Grey, C.P. and Dupre, N. (2004) NMR studies of cathode materials for lithium-ion rechargeable batteries. *Chem. Rev.* 104, 4493-4512.
- Hannoyer, B., Lenglet, M., Durr, J. and Cortes, R. (1992) Spectroscopic evidence of octahedral iron(III) in soda-lime silicate glasses. *J. Non-Cryst. Solids* 151, 209-216.
- Hara, S., Irie, K., Gaskell, D.R. and Ogino, K. (1988) Densities of melts in the $\text{FeO-Fe}_2\text{O}_3\text{-CaO}$ and $\text{FeO-Fe}_2\text{O}_3\text{-2CaO-SiO}_2$ systems. *Transactions of the Japan Institute of Metals* 29, 977-989.
- Hartman, J.S., Narayanan, A., Rigby, S.S., Sliwinski, D.R., Halden, N.M. and Bain, A.D. (2007) Heterogeneities in sol-gel-derived paramagnetics-doped forsterites and willemites: Electron microprobe analysis and stretched-exponential ^{29}Si MAS NMR spin-lattice relaxation studies. *Can. J. Chem.* 85, 56-65.
- Hartman, J.S., Narayanan, A. and Wang, Y.X. (1994) Spin-lattice relaxation in the 6H polytype of silicon-carbide. *J. Am. Chem. Soc.* 116, 4019-4027.
- Holland, D., Mekki, A., Gee, I.A., McConville, C.F., Johnson, J.A., Johnson, C.E., Appleyard, P. and Thomas, M. (1999) The structure of sodium iron silicate glass: A multi-technique approach. *J. Non-Cryst. Solids* 253, 192-202.
- Jackson, W.E., Farges, F., Yeager, M., Mabrouk, P.A., Rossano, S., Waychunas, G.A., Solomon, E.I. and Brown, G.E. (2005) Multi-spectroscopic study of Fe(II) in silicate glasses: Implications for the coordination environment of Fe(II) in silicate melts. *Geochim. Cosmochim. Acta* 69, 4315-4332.
- Jayasuriya, K.D., O'Neill, H.S., Berry, A.J. and Campbell, S.J. (2004) A Mössbauer study of the oxidation state of Fe in silicate melts. *Am. Mineral.* 89, 1597-1609.

- Kelsey, K.E., Allwardt, J.R. and Stebbins, J.F. (2008) Ca-Mg mixing in aluminosilicate glasses: An investigation using ^{17}O MAS and 3QMAS and ^{37}Al MAS NMR. *J. Non-Cryst. Solids* 354, 4644-4653.
- Kelsey, K.E., Stebbins, J.F., Singer, D.M., Brown, G.E., Mosenfelder, J.L. and Asimow, P.D. (2009) Cation field strength effects on high pressure aluminosilicate glass structure: Multinuclear NMR and La XAFS results. *Geochim. Cosmochim. Acta* 73, 3914-3933.
- Kilinc, A., Carmichael, I.S.E., Rivers, M.L. and Sack, R.O. (1983) The ferric-ferrous ratio of natural silicate liquids equilibrated in air. *Contrib. Mineral. Petrol.* 83, 136-140.
- Kirkpatrick, R.J., Dunn, T., Schramm, S., Smith, K.A., Oestrike, R. and Turner, G. (1986) Magic-angle sample-spinning nuclear magnetic resonance spectroscopy of silicate glasses: A review, in: Walrafen, G.E., Revesz, A.G. (Eds.), *Structure and Bonding in Noncrystalline Solids*. Plenum Press, New York, pp. 302-327.
- Kukkadapu, R.K., Li, H., Smith, G.L., Crum, J.D., Jeoung, J.S., Poisl, W.H. and Weinberg, M.C. (2003) Mössbauer and optical spectroscopic study of temperature and redox effects on iron local environments in a Fe-doped (0.5 mol% Fe_2O_3) $18\text{Na}_2\text{O}-72\text{SiO}_2$ glass. *J. Non-Cryst. Solids* 317, 301-318.
- Lange, R.A. and Carmichael, I.S.E. (1989) Ferric-ferrous equilibria in $\text{Na}_2\text{O}-\text{FeO}-\text{Fe}_2\text{O}_3-\text{SiO}_2$ melts: Effects of analytical techniques on derived partial molar volumes. *Geochim. Cosmochim. Acta* 53, 2195-2204.
- Lee, B.H. and Lee, S.K. (2009) Effect of lattice topology on the adsorption of benzyl alcohol on kaolinite surfaces: Quantum chemical calculations of geometry optimization, binding energy, and NMR chemical shielding. *Am. Mineral.* 94, 1392-1404.
- Lee, S.K. (2004) Structure of silicate glasses and melts at high pressure: Quantum chemical calculations and solid-state NMR. *J. Phys. Chem. B* 108, 5889-5900.
- Lee, S.K. (2005) Microscopic origins of macroscopic properties of silicate melts and glasses at ambient and high pressure: Implications for melt generation and dynamics. *Geochim. Cosmochim. Acta* 69, 3695-3710.

- Lee, S.K. (2011) Simplicity in melt densification in multicomponent magmatic reservoirs in Earth's interior revealed by multinuclear magnetic resonance. *P. Natl. Acad. Sci. USA* 108, 6847-6852.
- Lee, S.K. (2014) Absence of pressure-induced electron spin-state transition of iron in silicate glasses upon compression. *Am. Mineral.* 99, 877-878.
- Lee, S.K., Cody, G.D., Fei, Y. and Mysen, B.O. (2004) Nature of polymerization and properties of silicate melts and glasses at high pressure. *Geochim. Cosmochim. Acta* 68, 4189-4200.
- Lee, S.K. and Kim, E.J. (2015) Probing metal-bridging oxygen and configurational disorder in amorphous lead silicates: Insights from ^{17}O solid-state nuclear magnetic resonance. *J. Phys. Chem. C* 119, 748-756.
- Lee, S.K. and Stebbins, J.F. (2000) The structure of aluminosilicate glasses: High-resolution ^{17}O and ^{27}Al MAS and 3QMAS. *J. Phys. Chem. B* 104, 4091-4100.
- Lee, S.K. and Stebbins, J.F. (2002) Extent of intermixing among framework units in silicate glasses and melts. *Geochim. Cosmochim. Acta* 66, 303-309.
- Lee, S.K. and Stebbins, J.F. (2003) The distribution of sodium ions in aluminosilicate glasses: A high-field Na-23 MAS and 3Q MAS NMR study. *Geochim. Cosmochim. Acta* 67, 1699-1709.
- Lee, S.K. and Stebbins, J.F. (2006) Disorder and the extent of polymerization in calcium silicate and aluminosilicate glasses: O-17 NMR results and quantum chemical molecular orbital calculations. *Geochim. Cosmochim. Acta* 70, 4275-4286.
- Lee, S.K. and Stebbins, J.F. (2009) Effects of the degree of polymerization on the structure of sodium silicate and aluminosilicate glasses and melts: An ^{17}O NMR study. *Geochim. Cosmochim. Acta* 73, 1109-1119.
- Lee, S.K. and Sung, S. (2008) The effect of network-modifying cations on the structure and disorder in peralkaline Ca-Na aluminosilicate glasses: O-17 3QMAS NMR study. *Chem. Geol.* 256, 326-333.
- Liebske, C., Behrens, H., Holtz, F. and Lange, R.A. (2003) The influence of pressure and composition on the viscosity of andesitic melts. *Geochim. Cosmochim. Acta* 67, 473-485.

- Liu, Q. and Lange, R.A. (2006) The partial molar volume of Fe₂O₃ in alkali silicate melts: Evidence for an average Fe³⁺ coordination number near five. *Am. Mineral.* 91, 385-393.
- Maekawa, H., Maekawa, T., Kawamura, K. and Yokokawa, T. (1991) The structural groups of alkali silicate-glasses determined from ²⁹Si MAS NMR. *J. Non-Cryst. Solids* 127, 53-64.
- Malfait, W.J., Verel, R., Ardia, P. and Sanchez-Valle, C. (2012) Aluminum coordination in rhyolite and andesite glasses and melts: Effect of temperature, pressure, composition and water content. *Geochim. Cosmochim. Acta* 77, 11-26.
- Mao, H.K., Virgo, D. and Bell, P.M. (1973) Analytical study of the orange lunar soil returned by the Apollo 17 astronauts, Year Book Carnegie Institution of Washington, pp. 631-638.
- Massiot, D., Fayon, F., Capron, M., King, I., Le Calve, S., Alonso, B., Durand, J.O., Bujoli, B., Gan, Z.H. and Hoatson, G. (2002) Modelling one- and two-dimensional solid-state NMR spectra. *Magn. Reson. Chem.* 40, 70-76.
- Mazurin, O.V. (1983) Handbook of glass data: Silica glass and binary silicate glasses. Elsevier Science, Amsterdam.
- McHale, J.L. (1999) Molecular spectroscopy. Prentice Hall, Upper Saddle River, N. J.
- Medek, A., Harwood, J.S. and Frydman, L. (1995) Multiple-quantum magic-angle spinning NMR: A new method for the study of quadrupolar nuclei in solids. *J. Am. Chem. Soc.* 117, 12779-12787.
- Montenero, A., Friggeri, M., Giori, D.C., Belkhiria, N. and Pye, L.D. (1986) Iron soda silica glasses: Preparation, properties, structure. *J. Non-Cryst. Solids* 84, 45-60.
- Mysen, B.O. (2006) The structural behavior of ferric and ferrous iron in aluminosilicate glass near meta-aluminosilicate joins. *Geochim. Cosmochim. Acta* 70, 2337-2353.
- Mysen, B.O. and Richet, P. (2018) Silicate glasses and melts: Properties and structure, 2nd ed. Elsevier, Amsterdam.
- Mysen, B.O., Seifert, F. and Virgo, D. (1980) Structure and redox equilibria of iron-bearing silicate melts. *Am. Mineral.* 65, 867-884.

- Mysen, B.O. and Virgo, D. (1978) Influence of pressure, temperature, and bulk composition on melt structures in system $\text{NaAlSi}_2\text{O}_6$ - $\text{NaFe}^{3+}\text{Si}_2\text{O}_6$. *Am. J. Sci.* 278, 1307-1322.
- Mysen, B.O. and Virgo, D. (1985) Iron-bearing silicate melts: Relations between pressure and redox equilibria. *Phys. Chem. Miner.* 12, 191-200.
- Mysen, B.O. and Virgo, D. (1989) Redox equilibria, structure, and properties of Fe-bearing aluminosilicate melts: Relationships among temperature, composition, and oxygen fugacity in the system Na_2O - Al_2O_3 - SiO_2 - Fe - O . *Am. Mineral.* 74, 58-76.
- Mysen, B.O., Virgo, D., Neumann, E.R. and Seifert, F.A. (1985a) Redox equilibria and the structural states of ferric and ferrous iron in melts in the system CaO - MgO - Al_2O_3 - SiO_2 - Fe - O : Relationships between redox equilibria, melt structure and liquidus phase-equilibria. *Am. Mineral.* 70, 317-331.
- Mysen, B.O., Virgo, D., Scarfe, C.M. and Cronin, D.J. (1985b) Viscosity and structure of iron-bearing and aluminum-bearing calcium silicate melts at 1 atm. *Am. Mineral.* 70, 487-498.
- Mysen, B.O., Virgo, D. and Seifert, F.A. (1984) Redox equilibria of iron in alkaline-earth silicate melts: Relationships between melt structure, oxygen fugacity, temperature and properties of iron-bearing silicate liquids. *Am. Mineral.* 69, 834-847.
- Narayanan, A., Hartman, J.S. and Bain, A.D. (1995) Characterizing nonexponential spin-lattice relaxation in solid-state NMR by fitting to the stretched exponential. *J. Magn. Reson., Ser A* 112, 58-65.
- Nielsen, U.G., Paik, Y., Julmis, K., Schoonen, M.A.A., Reeder, R.J. and Grey, C.P. (2005) Investigating sorption on iron-oxyhydroxide soil minerals by solid-state NMR spectroscopy: A ^6Li MAS NMR study of adsorption and absorption on goethite. *J. Phys. Chem. B* 109, 18310-18315.
- Nolet, D.A. (1980) Optical-absorption and Mössbauer-spectra of Fe, Ti silicate-glasses. *J. Non-Cryst. Solids* 37, 99-110.
- Palke, A.C. and Stebbins, J.F. (2011) Variable-temperature ^{27}Al and ^{29}Si NMR studies of synthetic forsterite and Fe-bearing Dora Maira pyrope garnet: Temperature

- dependence and mechanisms of paramagnetically shifted peaks. *Am. Mineral.* 96, 1090-1099.
- Palke, A.C., Stebbins, J.F., Frost, D.J. and McCammon, C.A. (2012) Incorporation of Fe and Al in MgSiO₃ perovskite: An investigation by ²⁷Al and ²⁹Si NMR spectroscopy. *Am. Mineral.* 97, 1955-1964.
- Park, S.Y. and Lee, S.K. (2012) Structure and disorder in basaltic glasses and melts: Insights from high-resolution solid-state NMR study of glasses in diopside–Ca-tschermakite join and diopside–anorthite eutectic composition. *Geochim. Cosmochim. Acta* 80, 125-142.
- Park, S.Y. and Lee, S.K. (2014) High-resolution solid-state NMR study of the effect of composition on network connectivity and structural disorder in multi-component glasses in the diopside and jadeite join: Implications for structure of andesitic melts. *Geochim. Cosmochim. Acta* 147, 26-42.
- Philpotts, A.R. (1982) Compositions of immiscible liquids in volcanic rocks. *Contrib. Mineral. Petrol.* 80, 201-218.
- Poe, B.T., McMillan, P.F., Rubie, D.C., Chakraborty, S., Yarger, J. and Diefenbacher, J. (1997) Silicon and oxygen self-diffusivities in silicate liquids measured to 15 gigapascals and 2800 kelvin. *Science* 276, 1245-1248.
- Richet, P. (1984) Viscosity and configurational entropy of silicate melts. *Geochim. Cosmochim. Acta* 48, 471-483.
- Roskosz, M., Toplis, M.J., Neuville, D.R. and Mysen, B.O. (2008) Quantification of the kinetics of iron oxidation in silicate melts using Raman spectroscopy and assessment of the role of oxygen diffusion. *Am. Mineral.* 93, 1749-1759.
- Rossano, S., Balan, E., Morin, G., Bauer, J.P., Calas, G. and Brouder, C. (1999) ⁵⁷Fe Mössbauer spectroscopy of tektites. *Phys. Chem. Miner.* 26, 530-538.
- Rossano, S., Behrens, H. and Wilke, M. (2008) Advanced analyses of ⁵⁷Fe Mössbauer data of alumino-silicate glasses. *Phys. Chem. Miner.* 35, 77-93.
- Rossano, S., Ramos, A., Delaye, J.M., Creux, S., Filipponi, A., Brouder, C. and Calas, G. (2000) EXAFS and Molecular Dynamics combined study of CaO-FeO-2SiO₂ glass: New insight into site significance in silicate glasses. *Europhys. Lett.* 49, 597-602.

- Sanloup, C., Drewitt, J.W.E., Creppisson, C., Kono, Y., Park, C., McCammon, C., Hennet, L., Brassamin, S. and Bytchkov, A. (2013) Structure and density of molten fayalite at high pressure. *Geochim. Cosmochim. Acta* 118, 118-128.
- Schramm, C.M., Dejong, B. and Parziale, V.E. (1984) ^{29}Si magic angle spinning NMR-study on local silicon environments in amorphous and crystalline lithium silicates. *J. Am. Chem. Soc.* 106, 4396-4402.
- Schramm, S. and Oldfield, E. (1984) High-resolution oxygen-17 NMR of solids. *J. Am. Chem. Soc.* 106, 2502-2506.
- Schroeder, P.A. and Pruett, R.J. (1996) Fe ordering in kaolinite: Insights from ^{29}Si and ^{27}Al MAS NMR spectroscopy. *Am. Mineral.* 81, 26-38.
- Seifert, F. and Olesch, M. (1977) Mössbauer-spectroscopy of grandidierite, $(\text{Mg,Fe})\text{Al}_3\text{BSiO}_9$. *Am. Mineral.* 62, 547-553.
- Stebbins, J.F. (1995) Dynamics and structure of silicate and oxide melts: Nuclear magnetic resonance studies, in: Stebbins, J.F., McMillan, P.F., Dingwell, D.B. (Eds.), *Reviews in Mineralogy*. Mineralogical Society of America, Washington, D.C., pp. 191-246.
- Stebbins, J.F. and Kelsey, K.E. (2009) Anomalous resonances in ^{29}Si and ^{27}Al NMR spectra of pyrope ($[\text{Mg,Fe}]_3\text{Al}_2\text{Si}_3\text{O}_{12}$) garnets: Effects of paramagnetic cations. *Phys. Chem. Chem. Phys.* 11, 6906-6917.
- Stebbins, J.F., Lee, S.K. and Oglesby, J.V. (1999) Al-O-Al oxygen sites in crystalline aluminates and aluminosilicate glasses: High-resolution oxygen-17 NMR results. *Am. Mineral.* 84, 983-986.
- Stebbins, J.F., Panero, W.R., Smyth, J.R. and Frost, D.J. (2009) Forsterite, wadsleyite, and ringwoodite (Mg_2SiO_4): ^{29}Si NMR constraints on structural disorder and effects of paramagnetic impurity ions. *Am. Mineral.* 94, 626-629.
- Stebbins, J.F. and Xue, X. (2014) NMR spectroscopy of inorganic Earth materials, in: Henderson, G.S., Neuville, D.R., Downs, R.T. (Eds.), *Reviews in Mineralogy and Geochemistry*. Mineralogical Society of America, Chantilly, Virginia, pp. 605-653.
- Stebbins, J.F., Zhao, P.D., Lee, S.K. and Oglesby, J.V. (2001) Direct observation of multiple oxygen sites in oxide glasses: Recent advances from triple-quantum magic-angle spinning nuclear magnetic resonance. *J. Non-Cryst. Solids* 293, 67-73.

- Thompson, L.M. and Stebbins, J.F. (2013) Interaction between composition and temperature effects on non-bridging oxygen and high-coordinated aluminum in calcium aluminosilicate glasses. *Am. Mineral.* 98, 1980-1987.
- Toguri, J.M., Kaiura, G.H. and Marchant, G. (1976) The viscosity of the molten FeO-Fe₂O₃-SiO₂ system, In *Extractive metallurgy of Cooper I* Vol. 1. Physical Chemistry of Copper Smelting. Met. Soc. AIME, New York, pp. 259-273.
- Toplis, M.J. (2001) Quantitative links between microscopic properties and viscosity of liquids in the system SiO₂-Na₂O. *Chem. Geol.* 174, 321-331.
- Toplis, M.J., Dingwell, D.B. and Libourel, G. (1994) The effect of phosphorus on the iron redox ratio, viscosity, and density of an evolved ferro-basalt. *Contrib. Mineral. Petrol.* 117, 293-304.
- Toplis, M.J., Kohn, S.C., Smith, M.E. and Poplett, I.J.F. (2000) Fivefold-coordinated aluminum in tectosilicate glasses observed by triple quantum MAS NMR. *Am. Mineral.* 85, 1556-1560.
- Tossell, J.A. and Lazzarotti, P. (1988) Calculation of NMR parameters for bridging oxygens in H₃T-O-T'H₃, linkages (T, T' = Al, Si, P) for oxygen in SiH₃O, SiH₃OH and SiH₃OMg⁺ and for bridging fluorine in H₃SiF₂SiH₃⁺. *Phys. Chem. Miner.* 15, 564-569.
- Tse, D. and Hartmann, S.R. (1968) Nuclear spin-lattice relaxation via paramagnetic centers without spin diffusion. *Phys. Rev. Lett.* 21, 511-514.
- Urbain, G., Bottinga, Y. and Richet, P. (1982) Viscosity of liquid silica, silicates and aluminosilicates. *Geochim. Cosmochim. Acta* 46, 1061-1072.
- Vermillion, K.E., Florian, P. and Grandinetti, P.J. (1998) Relationships between bridging oxygen ¹⁷O quadrupolar coupling parameters and structure in alkali silicates. *J. Chem. Phys.* 108, 7274-7285.
- Virgo, D. and Mysen, B.O. (1985) The structural state of iron in oxidized vs reduced glasses at 1 atm: A ⁵⁷Fe Mössbauer study. *Phys. Chem. Miner.* 12, 65-76.
- Waff, H.S. (1975) Pressure-induced coordination changes in magmatic liquids. *Geophysical Research Letters* 2, 193-196.
- Waychunas, G.A., Brown, G.E., Ponader, C.W. and Jackson, W.E. (1988) Evidence from X-ray absorption for network-forming Fe²⁺ in molten alkali silicates. *Nature* 332, 251-253.

- Wilke, M., Farges, F., Partzsch, G.M., Schmidt, C. and Behrens, H. (2007) Speciation of Fe in silicate glasses and melts by in-situ XANES spectroscopy. *Am. Mineral.* 92, 44-56.
- Wright, T.L. and Fiske, R.S. (1971) Origin of differentiated and hybrid lavas of Kilauea volcano, Hawaii. *J. Petrol.* 12, 1-65.
- Wu, G., Rovnyank, D., Sun, B.Q. and Griffin, R.G. (1996) High-resolution multiple quantum MAS NMR spectroscopy of half-integer quadrupolar nuclei. *Chem. Phys. Lett.* 249, 210-217.
- Xue, X. and Kanzaki, M. (1998) Correlations between ^{29}Si , ^{17}O , and ^1H NMR properties and local structures in silicates: an ab initio calculation. *Phys. Chem. Miner.* 26, 14-30.
- Xue, X. and Kanzaki, M. (2008) Structure of hydrous aluminosilicate glasses along the diopside-anorthite join: A comprehensive one- and two-dimensional ^1H and ^{27}Al NMR study. *Geochim. Cosmochim. Acta* 72, 2331-2348.
- Xue, X.Y., Stebbins, J.F. and Kanzaki, M. (1994) Correlations between ^{17}O NMR parameters and local-structure around oxygen in high-pressure silicates: Implications for the structure of silicate melts at high pressure. *Am. Mineral.* 79, 31-42.
- Xue, X.Y., Stebbins, J.F., Kanzaki, M., McMillan, P.F. and Poe, B. (1991) Pressure-induced silicon coordination and tetrahedral structural-changes in alkali oxide-silica melts up to 12 GPa: NMR, Raman, and infrared-spectroscopy. *Am. Mineral.* 76, 8-26.

Chapter 4. The degree of polymerization and structural disorder in (Mg,Fe)SiO₃ glasses and melts: Insights from high-resolution ²⁹Si and ¹⁷O solid-state NMR

Hyo-Im Kim and Sung Keun Lee

Published in *Geochimica et Cosmochimica Acta* (2019) **250** 268-291

ABSTRACT

Probing the degree of polymerization and structural disorder of (Mg,Fe)SiO₃ glasses and melts remains a challenging problem, despite their strong implications for the properties of natural volcanic glasses and dense melts in Earth's surface and interior. Here, we explore the iron-induced changes in silicon and the oxygen configurations of (Mg_{1-x}Fe_x)SiO₃ glasses ($\text{Fe}^{3+}/\Sigma\text{Fe} = 0.22 \pm 0.07$) with varying X_{Fe} [$=\text{Fe}/(\text{Mg}+\text{Fe})$, containing up to 13.5 wt% FeO] using high-resolution ²⁹Si and ¹⁷O MAS, and 2D ¹⁷O 3QMAS NMR, unveiling the effect of Fe²⁺ on the extent of disorder in these glasses. The ²⁹Si MAS NMR spectra show the apparent peak broadening in less polymerized species (i.e., Q¹) and an increase in the fraction of highly polymerized (i.e., Q³) species with increasing X_{Fe} . These changes imply the selective decrease in NMR signal intensity of Q¹ and Q² due to their spatial proximity to Fe²⁺ (i.e., paramagnetic effect), and slight increase in the degree of polymerization due to the presence of minor fraction of Fe³⁺. The 2D ¹⁷O NMR spectra revealed that the fraction of Si-O-Si apparently increases with X_{Fe} and more significant

changes in peak width for Mg-O-Si are observed with varying X_{Fe} . The results indicate that Mg-O-Si is more strongly affected by Fe^{2+} than Si-O-Si, suggesting a moderate degree of preferential proximity between iron and non-bridging oxygen. The results allow us to conceptualize the scheme to account for paramagnetic interaction between the nuclear spins and Fe^{2+} . The scheme provides a systematic protocol to interpret the NMR spectra of diverse iron-bearing silicate glasses. The current NMR results, in conjunction with the results in the previous study for Fe^{3+} -dominant sodium silicate glasses, suggest that paramagnetic effect depends on the valence state of Fe, indicating the presence of a moderate degree of preferential interaction between Fe^{2+} and NBO and less polymerized Si units as well as that between Fe^{3+} and highly polymerized Si units and BO. Though qualitative, the current NMR results for $(\text{Mg,Fe})\text{SiO}_3$ glasses shed light on an opportunity to explore the detailed structures of iron-bearing natural volcanic glasses and can improve understanding of the transport properties of the basaltic melts.

4.1. Introduction

Iron-bearing MgSiO_3 is one of the important compositions in the present and early Earth's interior. MgSiO_3 bridgmanite, the most abundant mineral in lower mantle, incorporates 5–10 mol% of FeSiO_3 (Irifune, 1994; Katsura and Ito, 1996; Wood and Rubie, 1996). The iron concentration in the MgSiO_3 crystals and melts of early Earth before the chemical differentiation would have been higher than that of present Earth as suggested from undifferentiated chondrite (McDonough and Sun, 1995; e.g., Sun, 1982). Particularly, iron-bearing magnesium silicate *liquids* are among the essential constituents of the Hadean magma ocean (e.g., Ohtani, 1985; Tonks and

Melosh, 1993). The iron-rich melts above the core-mantle boundary have also been regarded as remnants of magma ocean (e.g., Davies, 1985; Murakami and Bass, 2011; Petitgirard et al., 2015; Taylor and Norman, 1990). Iron-bearing silicate *glasses* are ubiquitous on Earth's surface and consist of major components of basaltic glasses (~ 9 wt% FeO), submarine pillow rim glasses (~ 11 wt% FeO), obsidian (~ 2 wt% FeO), and tektites (~ 5 wt% FeO) (e.g., Fridleifsson et al., 1982; Kelley and Cottrell, 2009; White and Minser, 1984). The style of volcanic eruption depends on magma composition and iron content: a relatively small change in melt composition can lead to a drastic transition of eruption style (Di Genova et al., 2017a; Di Genova et al., 2017b). Recent studies have revealed the formation of amorphous SiO₂-rich phases in a Hawaiian basaltic glasses in contact with aqueous fluids (Chemtob et al., 2010; Chemtob et al., 2012; Zhu et al., 2006). The phase is somewhat similar to those observed on the surface of the Mars (covered by basaltic glasses) (Squyres et al., 2008). The similarity implies the potential interaction between basaltic glasses and aqueous solutions. Although the dissolution may play an important role in the formation of the deposits, the origin of SiO₂-rich deposits remains to be explored. Atomic structures of Mg-rich iron-bearing glasses may allow us to reveal the structural insights into the formation of SiO₂-rich phases from basaltic glasses.

The changes in the properties and rheological transition of iron-bearing Mg-silicate glasses and melts are affected by iron concentration and iron redox ratio ($\text{Fe}^{3+}/\Sigma\text{Fe}$): the density of iron-bearing glasses and melt increases with an increase in iron concentration (e.g., Dingwell et al., 1988; Lange and Carmichael, 1989; Sumita et al., 1983; Toropov and Bryantsev, 1965). The viscosity of iron-bearing melts decreases with an increase in iron concentration and a decrease in iron redox ratio (e.g., Chevrel et al., 2014;

Cukierman and Uhlmann, 1974; Dingwell, 1991; Dingwell et al., 2004; Mysen and Richet, 2018; Mysen et al., 1985b; Mysen et al., 1982; Toplis et al., 1994). Whereas these changes in the properties must depend on their structures, detailed atomistic origins of the changes in properties of iron-bearing Mg-silicate glasses and melts remain to be fully understood. Therefore, the current study aims to present the structural information of iron-bearing magnesium silicate glasses in (Mg,Fe)SiO₃ join by exploring changes in the local configurations around *silicon* and *oxygen* using solid-state NMR.

The atomic structure of *iron-free* MgSiO₃ glass and melt at ambient and high pressure has been studied extensively using diverse scattering and spectroscopic experimental tools and theoretical methods. Earlier Raman and infrared spectroscopy provided the vibrational density of state of MgSiO₃ glasses at ambient and high pressure (up to 80 GPa) (Kalampounias et al., 2009; Kubicki et al., 1992; e.g., McMillan, 1984; Shim and Catalli, 2009). Brillouin scattering studies have reported the elastic properties of MgSiO₃ melts at ambient pressure (e.g., VoThanh et al., 1996) and pressure-induced changes in the acoustic wave velocity of glassy analogs upon compression up to 203 GPa (e.g., Murakami and Bass, 2011; Sanchez-Valle and Bass, 2010). Synchrotron X-ray Raman scattering has shown that the formation of oxygen tricluster at high pressure above 20 GPa (Lee et al., 2008). A recent *in-situ* X-ray absorption study has revealed the *in-situ* density of MgSiO₃ glass under high pressure (up to 127 GPa) (Petitgirard et al., 2015).

Synchrotron or conventional scattering and diffraction studies have provided information regarding the average Si and Mg coordination numbers, distribution of Mg, and structural disorder in the MgSiO₃ glasses and melts at ambient and high pressure (e.g., Cormier and Cuello, 2011, 2013; Funamori et al., 2004; Wilding et al., 2004; Wilding et al., 2010). Theoretical

approaches such as classical and *ab-initio* (first-principle) molecular dynamics simulations have also provided information on the structure and properties, which are experimentally unachievable (Ghosh et al., 2014; e.g., Kubicki and Lasaga, 1991; Shimoda and Okuno, 2006; Stixrude and Karki, 2005; Wan et al., 2007; Zhao et al., 2014).

Relatively small number of spectroscopic and scattering studies have been carried out for *iron-bearing* MgSiO₃ glass with important geochemical implications in Earth's interior. The valence state and local structure of iron (i.e., coordination number and cation-oxygen distances) in the iron-bearing silicate glasses have been explored using various experimental techniques such as Mössbauer, scattering, and X-ray spectroscopy (see Tables 4A-1 and 4A-2). For example, pioneering studies using Mössbauer spectroscopy provided the information on iron coordination number and redox state (Mysen et al., 1980; Mysen et al., 1984). The ferrous iron (Fe²⁺) in silicate glasses is suggested to be a network-modifier and is four to six coordinated (Alderman et al., 2017a; Calas and Petiau, 1983; Drewitt et al., 2013; Farges et al., 2004; Jackson et al., 2005; Mysen, 2006; Rossano et al., 2000; Sanloup et al., 2013; Waychunas et al., 1988). The ferric iron (Fe³⁺) is considered to be a network-former with multiple coordination numbers of 4 to 6 (depending on chemical composition) (Cochain et al., 2012; Holland et al., 1999; Iwamoto et al., 1987; Mysen, 2006; Mysen et al., 1980; Mysen and Virgo, 1989; Weigel et al., 2008; Wilke et al., 2007). Previous studies have shown that 4- and 6-coordinated Fe are dominant, and that the fraction of 5-coordinated Fe is minor (e.g., Drewitt et al., 2013; Farges et al., 2004). More detailed descriptions of previous progress in determining the Fe coordination number and bond length have been provided in our previous paper (Kim et al., 2016) and Section 4A-1. The degree of polymerization is expected to increase with

increasing Fe^{3+} content and decrease with increasing Fe^{2+} content in iron-bearing silicate glasses and melts (Mysen and Richet, 2018; Mysen and Virgo, 1989; Mysen et al., 1985a). Furthermore, the local structure of iron (e.g., iron coordination number) in $(\text{Mg}_{0.75}\text{Fe}_{0.25})\text{SiO}_3$ and $(\text{Mg}_{0.5}\text{Fe}_{0.5})\text{SiO}_3$ melts was investigated using in-situ Fe K-edge X-ray absorption spectroscopy (Alderman et al., 2017b). Progress of synchrotron X-ray emission spectroscopy has allowed the exploration of the electron spin state of $(\text{Mg}_{0.8}\text{Fe}_{0.2})\text{SiO}_3$ glasses at ambient and high pressure (Gu et al., 2012). In addition, the acoustic velocities of $(\text{Mg}_{0.9}\text{Fe}_{0.1})\text{SiO}_3$ glasses at high-pressure have been measured using Brillouin spectroscopy (Liu and Lin, 2014).

Despite such progress, the direct spectroscopic measure of the degree of polymerization in iron-bearing MgSiO_3 glasses has not been reported. It has been known that an increase in the degree of melt-polymerization tends to increase the overall viscosity. The degree of polymerization for iron-bearing silicate glasses has often been estimated from their chemical compositions and assumed structural role (and thus the coordination number) of iron. Alternatively, the suggested structural proxies for the melt-polymerization are the non-bridging oxygen per tetrahedral cation (NBO/T), which are the NBO fraction and Q^n species (Si species with n bridging oxygens) (e.g., Giordano and Dingwell, 2003; Lee, 2005; Mysen and Richet, 2018; Neuvville, 2006 and references therein).

High-resolution solid-state NMR is an effective experimental tool for elucidating detailed information on atomic structures, including Q^n speciation and oxygen configurations in diverse oxides and silicate materials (e.g., Farnan et al., 1992; Farnan and Stebbins, 1990; Kirkpatrick et al., 1986; Lee et al., 2016; Maekawa et al., 1991; Schramm et al., 1984; Schramm et al., 1983; Stebbins and Xue, 2014). The local configurations in MgSiO_3 glasses

have also been extensively investigated using high-resolution solid-state NMR techniques. ^{29}Si and ^{25}Mg MAS NMR studies have shown that the types of Q species and Mg local environments (i.e., MgO_x species), respectively (e.g., Davis et al., 2011; Gaudio et al., 2008; Libourel et al., 1992; Sen et al., 2009; Shimoda et al., 2007; Stebbins and McMillan, 1993). In addition, ^{17}O MAS and 3QMAS NMR studies revealed the specific oxygen configurations of MgSiO_3 glass, providing the details of connectivity in the glass network (e.g., Allwardt and Stebbins, 2004; Lee et al., 2016; Lee et al., 2003a). The same level of effectiveness has not been demonstrated in revealing structures of materials containing paramagnetic elements (e.g., Fe) because of the NMR signal loss and peak broadening caused by the interaction between unpaired electrons in *d*-orbitals and nuclear spins of interest (i.e., paramagnetic effect) (Geiger et al., 1992; Grimmer et al., 1983; Murdoch et al., 1985; Oldfield et al., 1983; Sherriff and Hartman, 1985). Despite the inherent difficulties, solid-state NMR has been recently used to study the Fe distribution in diverse crystalline oxide, such as forsterite (Mg_2SiO_4), diopside ($\text{CaMgSi}_2\text{O}_6$), and pyrope ($[\text{Mg,Fe}]_3\text{Al}_2\text{Si}_3\text{O}_{12}$) with paramagnetic cations (e.g., Fe^{2+} , Ni^{2+} , and Co^{2+}) (Begaudeau et al., 2012; McCarty et al., 2015; Palke and Stebbins, 2011; Palke et al., 2015; Stebbins, 2017; Stebbins and Kelsey, 2009) and transition metal-bearing hydroxide/oxyhydroxide minerals (e.g., goethite, lepidocrocite, and jarosite) (Kim et al., 2015; Kim et al., 2008; Nielsen et al., 2008; Nielsen et al., 2005) (see Chapter 2 for the summary of previous studies). These studies on crystalline materials have shown the paramagnetic effect on each NMR peak representing the distinct local structural sites, providing useful information on the spatial configuration of Fe atoms around target nuclides. For example, the coupling of nuclear spins (e.g., ^{29}Si and ^{27}Al) with the unpaired electron spins of paramagnetic cations leads to a shift in peak position in the spectra.

These shifts, such as Fermi contact shifts (through-bond hyperfine interaction) and pseudocontact shifts (through-space dipole interaction), were analyzed to infer the local symmetry of paramagnetic site and the configurations between the paramagnetic cation and resonating nuclei (e.g., Al and Si) (e.g., Palke and Stebbins, 2011), revealing the distribution of Al and Fe in bridgmanite (Palke et al., 2012). The spatial proximity between the paramagnetic center (e.g., Fe and Mn) and both constituent cations (e.g., B and Al) in tourmaline was estimated from the quantification of NMR signal loss with increasing paramagnetic cations (Lussier et al., 2009). The NMR signals from ^{29}Si and ^{27}Al nuclides in the first nearest shell of Fe cannot be observed for pyrope (Stebbins and Kelsey, 2009).

The information regarding spatial distribution of paramagnetic cations in the crystalline lattice and glass network (e.g., random distribution and clustering) can also be suggested from ^{29}Si spin-lattice relaxation studies for crystalline silicates (e.g., forsterite, pyrope, and Portland cements with alite [Ca_3SiO_5] and belite [Ca_2SiO_4]) and silicate glasses with iron, neodymium, and gadolinium (Hartman et al., 2007; Hartman and Sherriff, 1991; Poulsen et al., 2009; Sen and Stebbins, 1994, 1995; Stebbins and Kelsey, 2009). Recent NMR studies revealed short-range structure of organic compounds with paramagnetic elements (e.g., metalloproteins) (e.g., Bertini et al., 2005; Koehler and Meiler, 2011) and cathode materials for lithium-ion batteries (e.g., Grey and Dupre, 2004; Lee and Grey, 2002). In particular, ^6Li and ^7Li MAS NMR studies of lithium manganite in cathode materials showed that local symmetry at the site of the paramagnetic cation is reflected in the hyperfine shifts and spinning sideband manifold patterns (Grey and Lee, 2003; Lee and Grey, 2002). These advances allow us to interpret the NMR spectra of silicate glasses with varying Fe content.

Although relatively few studies have been performed hitherto, the recent studies have demonstrated that solid-state NMR can be a potentially useful structural probe of iron-bearing silicate *glasses* with varying iron concentration up to ~ 5 wt% FeO (Kelsey et al., 2009). Furthermore, we have used high-resolution ^{29}Si and ^{17}O solid-state NMR to show the effect of iron content on Q speciation, spatial distribution of iron, and the extent of polymerization in Na-silicate glasses containing up to 23 wt% Fe_2O_3 (Kim et al., 2016). In the previous study, iron is predominantly Fe^{3+} and the degree of polymerization increases when Na_2O is replaced with Fe_2O_3 .

Whereas the aforementioned advances provide the structural details about iron-bearing silicate glasses, several questions regarding the structure and disorder of iron-bearing silicate glasses have remained unanswered. First, the detailed structure of geologically important iron-bearing Mg-silicate glasses has not been explored using solid-state NMR. In our previous study, the effect of iron on the structure of Na-silicate glasses was investigated (Kim et al., 2016). This is because the iron-bearing sodium disilicate glasses have spectroscopic advantages, exhibiting well-resolved peaks in NMR spectra (e.g., Lee and Stebbins, 2009; Maekawa et al., 1991). Although the substantial broadening in peaks and structure factors caused by the presence of Mg^{2+} , in addition to the paramagnetic broadening, makes it difficult to explore the atomic structure of the Mg-rich silicate glasses, the iron-bearing Mg-silicates better reflect the composition of natural volcanic glasses (e.g., basaltic glasses) and natural silicate melts in Earth's crust and mantle. Second, another intriguing question is the effect of iron valence state (i.e., Fe^{2+} vs. Fe^{3+}) on Q speciation and oxygen configurations of silicate glasses. While the previous study on iron-bearing Na-silicate glasses showed that an increase in the degree of polymerization stems from network-forming Fe^{3+} (Kim et al., 2016),

the changes in structure and disorder with increasing Fe^{2+} in silicate glasses are not clearly understood. Third, the distribution of paramagnetic cations and the preferential paramagnetic interaction between iron and local configurations remain to be explored, although the previous study of Fe^{3+} -bearing Na-silicate glasses yields the first glimpse of effect of composition (e.g., iron content) on the distribution of iron in silicate melts. Thus, further theoretical and experimental efforts based on the detailed comparison of signal loss and spin-lattice relaxation time (T_1) between iron-bearing magnesium and sodium silicate glasses should be directed towards understanding the interaction between nuclear spins and paramagnetic centers in a varying length scale (from $\sim \text{\AA}$ to nm). In the previous study, it was often assumed that the NMR signal intensities of the peak representing each structural site were equally affected by the paramagnetic cation (Kim et al., 2016). This assumption was based on ^{29}Si T_1 relaxation behavior of iron-bearing sodium silicate glasses, which suggests that the paramagnetic centers (i.e., Fe) are homogeneously distributed in glass network on a nanoscale (e.g., Narayanan et al., 1995; Tse and Hartmann, 1968). However, the possibility of heterogeneous iron distribution and preferential interaction with particular NBO/BO sites and/or Q^n species may not be disregarded. If so, the selective decrease in NMR intensity and preferential peak broadening should be expected. Thus, the assumption based on homogeneous distribution of iron needs further clarification and confirmation.

In this study, we explore the extent of polymerization (i.e., Q^n speciation and oxygen configurations) of $(\text{Mg,Fe})\text{SiO}_3$ glasses with varying iron concentrations up to 13.5 wt% FeO using high-resolution ^{29}Si and ^{17}O magic angle spinning (MAS), and 2D ^{17}O triple-quantum MAS (3QMAS) NMR, unveiling the effect of Fe^{2+} on the atomic structure and extent of

disorder in (Mg,Fe)SiO₃ glasses. We report the changes in NMR signal intensity and ²⁹Si *T*₁ relaxation behavior caused by the paramagnetic effect, constraining the nature of iron distribution in the glasses. In conjunction with the previous study of Fe³⁺-dominant Na-silicate glasses, we also explore the effect of valence state of iron on the structure and disorder in silicate glasses. Based on these results, we propose schemes to account for the paramagnetic effect depending on the distance between paramagnetic center and nuclear spins. Finally, we discuss the qualitative link between these observed structural findings and the diverse properties of iron-bearing magnesium silicate glasses and melts, providing atomic-level insights into the compositional dependence (i.e., iron contents) of evolution of melts.

4.2. Experimental methods

4.2.1. Sample synthesis

Iron-bearing magnesium silicate glasses with varying iron contents [(Mg_{1-x}Fe_x)SiO₃ with $X_{\text{Fe}} = \text{Fe}/(\text{Mg} + \text{Fe})$ of 0, 0.05 (3.5 wt% FeO), 0.1 (7 wt% FeO) and 0.2 (13.5 wt% FeO)] were synthesized from oxides (MgO and FeO) and ¹⁷O-enriched SiO₂ prepared by hydrolyzing SiCl₄ with 20% ¹⁷O-enriched H₂O. This compositional series involves Mg-Fe substitution at constant SiO₂ contents of 50 mol% in the glasses. The mixture was prepared as a stoichiometric mix of starting oxide powders, which were dried at 300 °C (~48 h) for FeO and 1300 °C (2 h) for MgO. About 0.2 wt% of cobalt oxide was added to the iron-free MgSiO₃ sample ($X_{\text{Fe}} = 0$) to enhance the spin-lattice relaxation and thus reduce the total collection time. The mixed powders were then fused in a Pt crucible for 1 h at 1650 °C in a through-flow Ar environment. Note that the Pt crucible was saturated with iron during the preliminary glass

Table 4-1. Nominal compositions and ICP analyses for MgO-FeO-SiO₂ glasses with varying X_{Fe} [=Fe/(Mg + Fe)].

Composition		Nominal composition (mol%)		
		MgO	FeO ^T	SiO ₂
X_{Fe}	0	50.0	0.0	50.0
	0.05	47.5	2.5	50.0
	0.1	45.0	5.0	50.0
	0.2	40.0	10.0	50.0

Composition		Nominal composition (mol%)		ICP analysis (mol%)	
		MgO	FeO ^T	MgO	FeO ^T
X_{Fe}	0	100.0	0.0	99.9 ± 0.1	0.1 ± 0.1
	0.05	95.0	5.0	94.8 ± 0.1	5.2 ± 0.1
	0.1	90.0	10.0	90.3 ± 0.1	9.7 ± 0.1
	0.2	80.0	20.0	80.8 ± 0.2	19.2 ± 0.2

synthesis to prevent iron loss from the samples. The oxygen fugacity (f_{O_2}) of an Ar environment in the furnace studied here was measured directly using a Y₂O₃-doped ZrO₂ oxygen sensor (Sato, 1971), and the $\log f_{\text{O}_2}$ of an Ar environment is -2.15 ± 0.04 where the $\text{Fe}^{3+}/\Sigma\text{Fe}$ values of the current glasses (melted in an Ar environment) are expected to be roughly 0.22 ± 0.07 , based also on the previous Mössbauer studies of iron-bearing magnesium silicate glasses (see Section 4A-2). The melt was quenched by manually lowering the Pt crucible into the water. Previous studies with similar synthesis condition presented that quench rate is ~ 100 °C/s (e.g., Dubinsky and Stebbins, 2006). The chemical compositions of the iron-bearing magnesium silicate glasses were analyzed using inductively coupled plasma atomic emission spectroscopy (ICP-AES); the results are summarized in Table 4-1. The

analysis was performed for MgO and FeO because SiO₂ is removed by reacting with the hydrofluoric acid for the ICP analysis, as reported previously (Park and Lee, 2012). The negligible weight loss (up to ~ 1 wt%) and the consistency with ICP analysis for MgO and FeO components indicate that the compositions of the glasses are close to the nominal composition.

The structure of the glasses represents the structure of supercooled melts at the glass transition temperature (T_g) where the mobility of fluids drastically decreases and thus the structures are frozen. Therefore, there is an intrinsic difference between the structure of the silicate glasses and that of the liquids, as the melting temperature is much higher than the T_g . For example of iron-bearing silicate glasses and melts, the fraction of 4-coordinated Fe²⁺ and Fe³⁺ in the silicate melts is slightly higher than that in the silicate glasses by up to 10% (e.g., Wilke et al., 2007) due to the effect of temperature and quenching rate. Thus, the effect of temperature on the melt structure remains to be explored. On the other hand, the experimental studies performed by varying the quench rate (and thus varying in T_g) show that the effect of temperature on the glass structure [e.g., coordination number of framework cations (such as Si) and degree of polymerization] is rather minor (see McMillan and Wolf, 1995; Mysen and Richet, 2018; Stebbins, 1995; Stebbins et al., 2008 for the review).

4.2.2. Iron redox ratio of (Mg_{1-x}Fe_x)SiO₃ glasses

The iron redox ratio ($\text{Fe}^{3+}/\Sigma\text{Fe}$) of the samples with high iron contents ($X = 0.1$ and 0.2) were determined using ⁵⁷Fe absorption Mössbauer spectroscopy using a MS-96 Mössbauer spectrometer (Regional Centre of Advanced Technologies and Materials). The Mössbauer experiments were

conducted with a ~ 30 mCi ^{57}Co flat source operating in the constant acceleration symmetric mode between -4 and 4 mm/s. The drives were calibrated with an α -Fe foil with thickness of 28 μm . The isomer shifts of Fe^{3+} and Fe^{2+} are reported relative to α -Fe foil. As shown in Figure 4-A1, the Mössbauer spectra for both samples can be deconvoluted with one absorption doublet of Fe^{2+} (which exhibited maxima near 0 and 2 mm/s), and that of Fe^{3+} (which exhibit maxima near -0.1 and 0.1 mm/s), confirming that the glasses contain both Fe^{2+} and Fe^{3+} . The measured $\text{Fe}^{3+}/\Sigma\text{Fe}$ values for $X = 0.1$ and $X = 0.2$ are approximately 0.23 and 0.26 , respectively. Finally, based on $\text{Fe}^{3+}/\Sigma\text{Fe}$ values from the previous Mössbauer and XANES studies of $(\text{Mg,Fe})\text{SiO}_3$ glasses, whose compositions are similar to those of the glasses studied in the current study, the $\text{Fe}^{3+}/\Sigma\text{Fe}$ values of the $(\text{Mg,Fe})\text{SiO}_3$ glasses in the current study is expected to be $\sim 0.22 \pm 0.07$. This is consistent with the measured $\text{Fe}^{3+}/\Sigma\text{Fe}$ values using Mössbauer spectroscopy (see Section 4A-2 for details).

4.2.3. NMR spectroscopy

^{29}Si MAS NMR spectra were collected on a Varian 400 MHz solid-state NMR spectrometer (9.4 T) at a Larmor frequency of 79.47 MHz with a 4 mm thick-wall zirconia rotor, in a Doty Scientific double-resonance MAS probe. A single-pulse sequence with an approximately 30° pulse (1.6 μs) and spinning speed of 14 kHz were used. The recycle delay was 10 s for the iron-free sample ($X_{\text{FeO}} = 0$) and $0.5 \sim 1$ s for the iron-bearing samples. 10,000-80,000 scans were averaged in the ^{29}Si MAS NMR spectra to achieve the current signal-to-noise ratio. The ^{29}Si spin-lattice relaxation time (T_1) for each sample was measured with the saturation-recovery method using a spin-echo pulse sequence [90° - delay time (τ) - 90°] with varying delay time (ranging from

Table 4-2. NMR experimental conditions used in this study (at 9.4 T).

Spin rate (kHz)	Nucleus	Acquisition	Pulse sequence	X_{Fe}	Number of Scans ^a	Relaxation delay (s)	Time (h)
14	²⁹ Si	MAS	Single-pulse	0	10000	10	27
				0.05	40000	1	11
				0.1	40000	1	11
				0.2	80000	0.5	11
15	¹⁷ O	MAS	Single-pulse	0	4000	1	1
				0.05	1200	0.5	0.2
				0.1	4000	0.5	0.6
				0.2	20000	0.5	3
	¹⁷ O	3QMAS	FAM based shifted-echo pulse	0	6720	1	112
				0.05	2880	0.5	10
				0.1	15360	0.5	53
				0.2	115200	0.5	480

^aApproximately 60 FIDs (iron-free sample) and 25~30 FIDs (iron-bearing sample) were collected for constructing 2D spectra

0.0003 to 960 s) with 1 s of recycle delay. The ²⁹Si NMR spectra were measured using tetramethylsilane (TMS) as the external reference.

¹⁷O NMR experiments were performed on a Varian 400 MHz solid-state NMR spectrometer (9.4 T) at a Larmor frequency of 54.23 MHz with a Doty Scientific MAS double-resonance MAS probe (4 mm Si₃N₄ rotor) with spinning speed of 15 kHz. For the ¹⁷O MAS NMR study, single-pulse sequence with a pulse length of 0.4 μs, which corresponds to the tip angle of about 30° for solids, was used with a recycle delay of 1 s for the iron-free sample ($X_{\text{FeO}} = 0$) and 0.5 s for the iron-bearing samples. ¹⁷O 3QMAS NMR spectra were collected using fast amplitude modulation (FAM)-based shifted-echo pulse sequences [4.5 μs - τ (delay) - 1.1 μs - echo delay (approximately

0.18 ms) – 19.5 μ s] with recycle delays ranging from 0.5 to 1 s depending on the spin-lattice relaxation time. Approximately 2,860-92,160 scans were required for the iron-bearing samples to achieve the current signal-to-noise ratio in the 3QMAS NMR spectra. For example, ~20 days of signal averaging was necessary to collect the ^{17}O 3QMAS NMR spectrum for iron-bearing magnesium silicate glasses $[(\text{Mg}_{1-x}\text{Fe}_x)\text{SiO}_3]$ at $X_{\text{Fe}} [= \text{FeO}/(\text{MgO} + \text{FeO})]$ of 0.2. The ^{17}O NMR spectra were referenced to the tap water. Detailed description of the experimental conditions is given in Table 4-2.

4.3. Results

4.3.1. Effect of iron content on Si coordination environments in $(\text{Mg,Fe})\text{SiO}_3$ glasses: ^{29}Si MAS NMR results

Structural evolution of glasses upon addition of iron is presented in the ^{29}Si MAS NMR spectra of MgSiO_3 glass ($X_{\text{Fe}} = 0$) and iron-bearing magnesium silicate glasses $[(\text{Mg}_{1-x}\text{Fe}_x)\text{SiO}_3]$ with varying $X_{\text{Fe}} [= \text{FeO}/(\text{MgO} + \text{FeO})]$ (Figure 4-1). The spectrum for iron-free MgSiO_3 glass shows a single broad peak corresponding to four-coordinated Si (^4Si) centered at ~ -83 ppm with a slightly asymmetric shape, consistent with the earlier results (Gaudio et al., 2008; Murdoch et al., 1985; Stebbins and McMillan, 1993). While the peak overlap between the Q species in the ^{29}Si NMR spectrum does not provide explicit information on the distribution of Q species in the glass, the Q^1 , Q^2 , and Q^3 species are reported to be dominant in the MgSiO_3 glass (Davis et al., 2011; Sen et al., 2009).

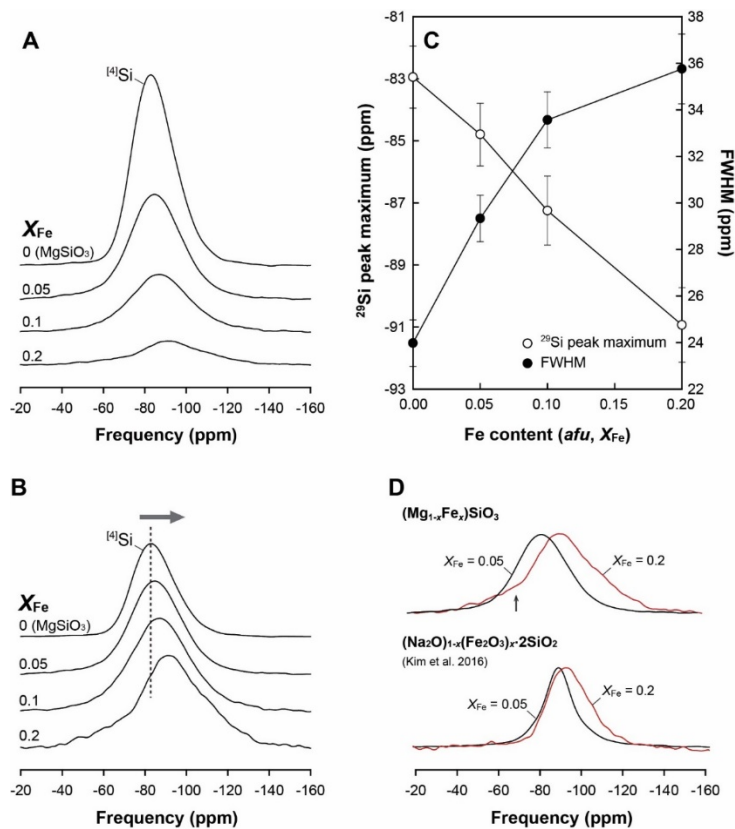


Figure 4-1. ^{29}Si MAS NMR spectra of iron-bearing magnesium silicate glasses $[(\text{Mg}_{1-x}\text{Fe}_x)\text{SiO}_3]$ with varying $X_{\text{Fe}} [= \text{Fe}/(\text{Mg} + \text{Fe})]$ at 9.4 T, as labeled. (A) The spectra are plotted on a vertical scale reflecting signal intensity reduction corresponding to the changes in iron content, and (B) a normalized vertical scale. Comparison of ^{29}Si MAS NMR spectra for glasses with X_{Fe} of 0.05 (black) and 0.2 (red) is also shown. (C) Variation of peak maxima (open circles) and FWHM (closed circles) of the peak in ^{29}Si MAS NMR spectra with varying iron content X_{Fe} . (D) The previously reported ^{29}Si MAS NMR spectra of iron-bearing sodium silicate glasses $[(\text{Na}_2\text{O})_{1-x} \cdot (\text{Fe}_2\text{O}_3)_x \cdot 2\text{SiO}_2]$ with X_{Fe} of 0.05 (black) and 0.2 (red) is also shown (Kim et al., 2016).

4.3.1.1. Iron-induced changes in peak intensity

As shown in Figure 4-1A, the signal intensity decreases with increasing iron content because of an increase in the degree of interaction between the unpaired electrons in iron and the ^{29}Si nuclear spins. Figure 4-2 shows the normalized ^{29}Si MAS NMR peak intensity (with respect to that of iron-free MgSiO_3 glass) of iron-bearing magnesium silicate glasses $[(\text{Mg}_{1-x}\text{Fe}_x)\text{SiO}_3]$ with increasing X_{Fe} . The ^{29}Si NMR signal intensities were further calibrated with the weight of each glass. The normalized ^{29}Si NMR peak intensity decreases from 1 for the iron-free MgSiO_3 glass to 0.21 for $X_{\text{Fe}} = 0.2$ glass, indicating that a moderate fraction of Si nuclear spins near Fe is not detected. This trend is similar to that for iron-bearing sodium silicate glasses (Kim et al., 2016). The observed trend of a decreasing ^{29}Si NMR signal intensity with X_{Fe} allows us to infer the length scale where the NMR signal is lost due to paramagnetic effect (i.e., cutoff radius). See discussion Section 4.4.1 and Section 4A-3 for further details.

4.3.1.2. Iron-induced changes in peak width and peak position

The ^{29}Si MAS NMR peak widths also increase as X_{Fe} increases (Figure 4-1B). The broadening pattern in the peak by paramagnetic interaction can be characterized by the Lorentzian function, $a[\sigma/((x - x_0)^2 + \sigma^2)]$, where $a \cdot \pi$ is amplitude, x_0 is peak center, and $\sigma/2$ is the peak width (FWHM, full-width at half-maximum). In addition to the paramagnetic effect, the iron-induced changes in the extent of polymerization and structural disorder in the silicon environment could increase the peak width. As for the latter, the peak shape can be described with the Gaussian function, $A \cdot \exp[-(x - x_0)^2/2c^2]$ with a FWHM of $2.35c$. This may account for the peak shift (not from paramagnetic shift) and/or asymmetrical peak broadening. Figure 4-1C exhibits the vari-

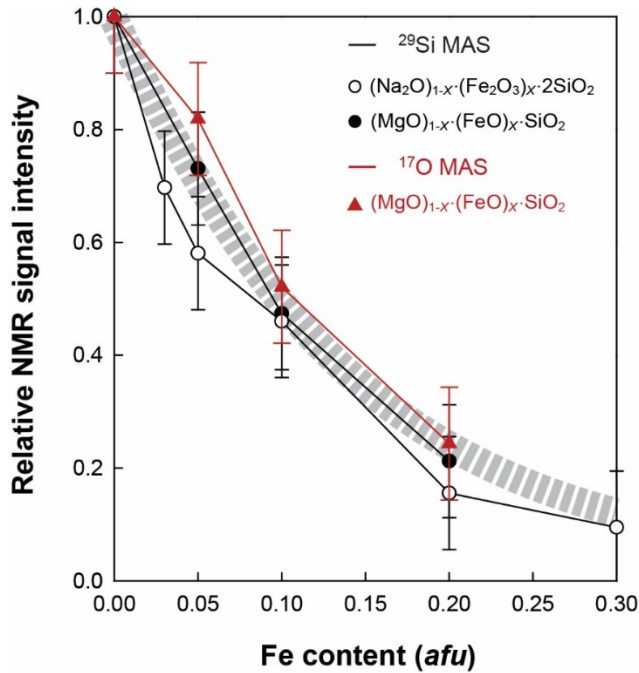


Figure 4-2. ^{29}Si (black closed circles) and ^{17}O (red closed triangles) NMR signal intensities of iron-bearing silicate glasses with varying iron content in atoms per formula unit (*afu*) of $(\text{Mg}_{1-x}\text{Fe}_x)\text{SiO}_3$ glasses. Black open circles represent the ^{29}Si NMR signal intensities for $(\text{Na}_2\text{O})_{1-x} \cdot (\text{Fe}_2\text{O}_3)_x \cdot 2\text{SiO}_2$ glasses (Kim et al., 2016). Note that the line width of the gray dotted line corresponds to the 95% confidence interval centered on the average values of the 20 iterations of simulations for each composition (see Section 4.4.1).

ations of peak widths (FWHM) and peak maximum with varying X_{Fe} for $(\text{Mg}_{1-x}\text{Fe}_x)\text{SiO}_3$ glasses. The peak width abruptly increases from 24 ppm ($X_{\text{Fe}} = 0$) to 34 ppm ($X_{\text{Fe}} = 0.1$). A further increase in X_{Fe} results in an increase in the peak width from 34 ppm ($X_{\text{Fe}} = 0.1$) to 36 ppm ($X_{\text{Fe}} = 0.2$) where a significant Lorentzian broadening of the spectrum is manifested. Finally, the systematic shift in peak maximum toward lower frequencies (more negative chemical shift) is also observed with increasing X_{Fe} : the peak maximum changes gradually with X_{Fe} from -83 ppm ($X_{\text{Fe}} = 0$) to -91 ppm ($X_{\text{Fe}} = 0.2$). In addition to the apparent increase in Q^3 fraction with increasing X_{Fe} from 0 to 0.2, the peak broadening in the higher frequency shoulder at ~ -40 to -90 ppm (corresponding to Q^1) is manifested in the spectrum for $X_{\text{Fe}} = 0.2$. Note that such a shoulder is not evident for the glasses with $X_{\text{Fe}} = 0.05$ and 0.1. While the peak broadening in the Q^1 region in $X_{\text{Fe}} = 0.2$ may indicate the increase in the topological disorder of less polymerized Q species, the peak shape (with a significant contribution from the Lorentzian broadening factor) implies stronger paramagnetic interaction between Fe^{2+} and Q^1 (see Section 4A-3 for further details).

4.3.1.3. Interpretation

It should be noted that observed NMR spectra in current study show only the information of 'survived' nuclear spins. Observed changes in the ^{29}Si MAS NMR spectra with increasing X_{Fe} stem from three distinct processes, including, 1) a peak shift potentially due to the paramagnetic effect, 2) a peak broadening due to preferential iron enrichment into a specific domain, and finally, 3) an increase in the degree of polymerization and chemical/topological disorder. While it is difficult to quantify whether the observed change is mainly due to structural changes in the glass network (e.g., scheme 3) or results from the paramagnetic interaction (e.g., schemes 1 & 2 above), it

is evident that all mechanisms prevail to some degree and the contribution from the paramagnetic effect increases with increasing iron content. As it is difficult to consider these three mechanisms simultaneously, the simulations of the ^{29}Si MAS NMR spectra were performed considering each 'extreme' case where only a single factor contributes to the changes in the NMR spectra with X_{Fe} . Section 4A-3 reports the detailed spectral analyses for the extreme schemes.

First, if we *assume* that there would be no preferential paramagnetic signal loss and thus the spectra for the survived spins would fully represent that of the whole glass structure, the observed changes in the ^{29}Si NMR spectra could stem from the iron-induced structural changes. In particular, the asymmetrical broadening of the peaks for highly polymerized Q species (e.g., Q^3) and peak shifts toward the lower frequency with increasing X_{Fe} from 0 to 0.2 may be attributed to an increase in the fraction of highly polymerized Q species, suggesting that the degree of melt polymerization increases by replacing Mg with Fe (and thus increasing X_{Fe}). This is due to the presence of the minor fraction of Fe^{3+} as a network-forming cation in the glasses studied here. Alternatively, the observed broadening patterns indicate the moderate degree of preferential distribution of iron among Q species. An apparent increase in the fraction of Q^3 species at X_{Fe} of 0.2 stem from the selective decrease in the NMR signal intensity from less polymerized Q species (e.g., Q^1 and Q^2) due to the preferential interaction between iron and Q^1 and/or Q^2 . This can also explain the pronounced broadening of the Q^1 region observed at $X_{\text{Fe}} = 0.2$. Taking this into consideration, there could be two distinct domains in the glass network for the iron-bearing glasses. The domain with a larger fraction of iron leads to an enhanced structural broadening and vice

versa. Therefore, the broader spectral feature for Q¹ suggests the higher iron concentration around Q¹ in (Mg,Fe)SiO₃ glasses.

Based on detailed spectral analyses (with both contributions from the Lorentzian and the Gaussian components) (see Section 4A-3), the apparent increase in the Q³ fraction and asymmetrical broadening at higher Fe content stem from both the slight increase in the degree of polymerization due to the presence of minor fraction of Fe³⁺ and the selective decrease in the NMR signal intensity of Q¹ and Q² due to paramagnetic effect. Nevertheless, the explicit peak broadening of the Q¹ region in the NMR spectra can be attributed to the increase in the topological disorder of Q¹ and mainly to the preferential paramagnetic interaction between Fe and Q¹. Note that the significant changes in the less polymerized Q species have not been observed in the Fe³⁺-dominant iron-bearing sodium silicate glasses, as shown in Figure 4-1D (Kim et al., 2016). Thus, this demonstrates the stronger interaction between Fe²⁺ and less polymerized Q species and the effect of valence state of iron on the nature of paramagnetic interactions (see Section 4.4.3). Note that we collected the Raman spectra of Fe²⁺-dominant (Mg,Fe)SiO₃ silicate glasses with varying iron content (not shown here), but the changes in the Qⁿ species with increasing Fe contents (by replacing Mg with Fe) in the Raman spectra is not fully demonstrated. This is due to the considerable overlap among the Raman modes due to the less polymerized Q species and small amount of the polymerized (Fe³⁺-Si)-O stretching vibrational bands. Earlier and recent Raman studies have also reported the severely overlapped Raman modes in the spectra for various iron-bearing silicate glasses (Baert et al., 2011; Cochain et al., 2013; Cochain et al., 2012; Di Genova et al., 2016; Di Genova et al., 2017b; Magnien et al., 2006; Mercier et al., 2009; Mysen et al., 1980; Mysen et al., 1984; Neuville et al., 2014; Roskosz et al., 2008; Wang et al., 1995).

4.3.2. Distribution of iron in iron-bearing Mg-silicate glasses: A view from ^{29}Si T_1 relaxation time measurement

To obtain detailed knowledge of the interaction between the ^{29}Si nuclear spins and paramagnetic cations, and its distribution in the glass network, the spin-lattice relaxation behavior of iron-bearing silicate glasses was investigated with the saturation-recovery measurement. Figure 4-3 shows the ^{29}Si NMR spectra of $(\text{Mg}_{1-x}\text{Fe}_x)\text{SiO}_3$ glasses with increasing delay time (τ) after the saturation of nuclear spin magnetization. The recovery time of magnetization decreases with increasing X_{Fe} from ~ 120 s (for $X_{\text{Fe}} = 0$, with 0.2 wt% CoO) to ~ 1 s (for $X_{\text{Fe}} = 0.1$), as interaction between nuclear ^{29}Si spins and unpaired electrons in Fe increases with X_{Fe} . Figure 4-4 shows the peak intensity in a ^{29}Si NMR spectrum (M) normalized with respect to that of the fully relaxed spectrum (M_0) with varying τ . The peak area of the recovered NMR signal for iron-bearing sodium silicate glasses with varying τ is also shown for comparison (open circles in Figure 4-4) (Kim et al., 2016). The ^{29}Si spin-lattice relaxation behaviors of the iron-bearing Mg-silicate glasses are described with the stretched-exponential equation (Bakhmutov, 2008; Hartman et al., 2007; Hartman and Sherriff, 1991; Kim et al., 2016; Stebbins and Kelsey, 2009; Tse and Hartmann, 1968):

$$M/M_0 = 1 - \exp[-(\tau/T')^\beta] \quad (4.1)$$

where β is the stretching exponent and T' is the time constant for the recovery of magnetization. Estimated β and T' values are given in Table 4-3, confirming that β is approximately 0.5, regardless of the iron content (X_{Fe}). The observed trend of iron-bearing magnesium silicate glasses is also consistent with that of iron-bearing sodium silicate glasses (Kim et al., 2016). The β of 0.5 for both Na- and Mg-silicate glasses indicates a homogeneous iron distribution in the

Table 4-3. Summary of fitting parameters [stretched exponent (β) and time constant for the recovery of magnetization (T')] for spin-lattice relaxation curves for MgO-FeO-SiO₂ glasses with varying X_{Fe} [=Fe/(Mg + Fe)], based on the stretched-exponential equation.

Nucleus	X_{Fe}	Stretched-exponent (β)	T' (s)
²⁹ Si	0 ^a	0.51 ± 0.02	8.8 ± 0.8
	0.05	0.50 ± 0.04	0.086 ± 0.010
	0.1	0.50 ± 0.04	0.046 ± 0.005

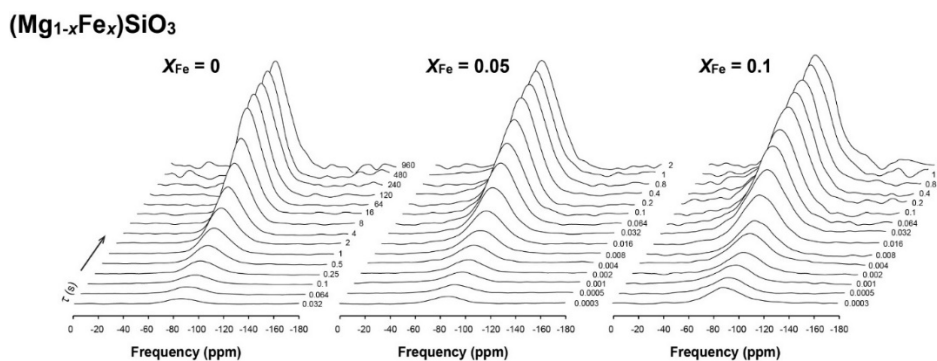


Figure 4-3. Evolution of the ²⁹Si NMR spectra of (Mg_{1-x}Fe_x)SiO₃ glasses with X_{Fe} [= Fe/(Mg + Fe)] and increasing delay time (τ , in s), after saturation of magnetization at 9.4 T.

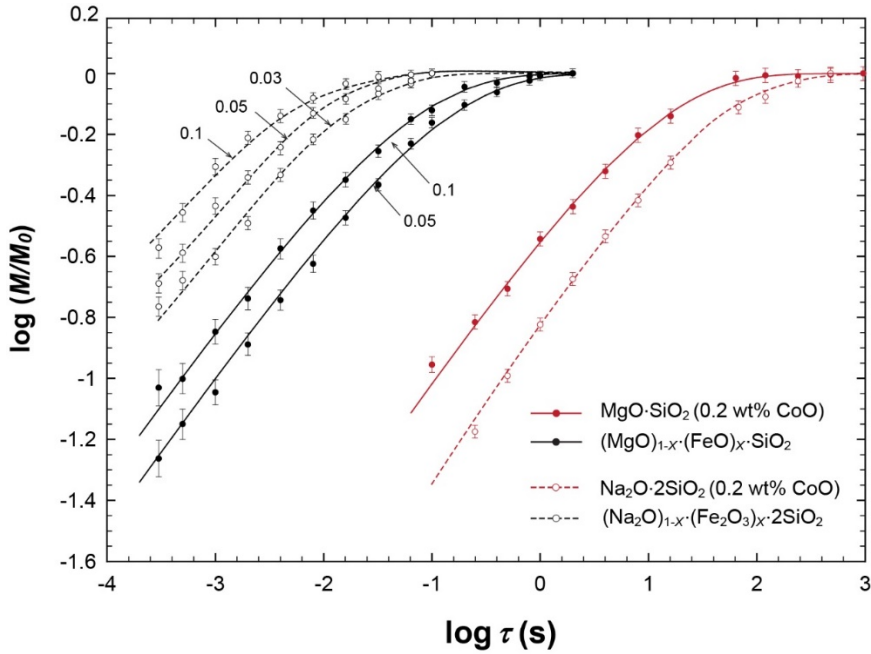


Figure 4-4. Variation in the integrated peak area of the recovered ^{29}Si NMR signal [normalized with respect to the total peak area of a fully relaxed spectrum (M/M_0)] on the delay time (τ) for iron-free MgSiO_3 glass (closed red circles) and iron-bearing magnesium silicate glasses (closed black circles) with varying X_{Fe} [= $\text{Fe}/(\text{Mg} + \text{Fe})$]. The M/M_0 values for iron-free sodium disilicate glass (open red circles) and iron-bearing sodium silicate glasses (open black circles) with iron concentration are also shown for comparison. The solid and dash lines refer to the relaxation trend described using the stretched exponential equation for the iron-bearing magnesium and sodium silicate glasses, respectively.

intermediate range length scale (~ 1 nm). Furthermore, β ($= 0.5$) does not change with iron content in the glasses studied here.

Figure 4-5 shows the normalized time constant for recovery of magnetization (T'/T_0 , T' for iron-bearing glasses divided by the T_0 for iron-free glass) of $(\text{Mg,Fe})\text{SiO}_3$ glasses with iron contents (i.e., the number of iron atoms in a formula unit, *afu*). The previously reported T'/T_0 values for iron-bearing sodium silicate glasses (Kim et al., 2016) are also shown. The time constant for recovery of magnetization (T') decreases as X_{Fe} increases from 8.8 ± 0.8 s ($X_{\text{Fe}} = 0$), through 0.086 ± 0.010 s ($X_{\text{Fe}} = 0.05$), to 0.046 ± 0.005 s ($X_{\text{Fe}} = 0.1$) for $(\text{Mg}_{1-X}\text{Fe}_X)\text{SiO}_3$. A decrease in spin-lattice relaxation time (T') with increasing X_{Fe} stems from an increase in the through-space dipolar interaction between ^{29}Si nuclear spins and Fe, suggesting an increase in the spatial proximity between ^{29}Si atoms and iron.

Figure 4-5 also reveals the effect of iron concentration on the T'/T_0 in iron-bearing magnesium and sodium silicate glasses. For iron-bearing Mg-silicate glasses, the T'/T_0 for $X_{\text{Fe}} = 0.2$ is about 2 orders of magnitude smaller than that for $X_{\text{Fe}} = 0$. In contrast, the T'/T_0 for iron-bearing Na-silicate glass with $X = 0.2$ is about 4 orders of magnitude smaller than that for iron-free Na-silicate glass. The difference in the trend of decreasing T'/T_0 between iron-bearing magnesium and sodium silicate glasses indicates the control of iron redox ratio ($\text{Fe}^{3+}/\Sigma\text{Fe}$) on spin-lattice relaxation behavior and thus the overall difference in the nature of iron distribution in the glass networks: although a homogeneous distribution of Fe^{2+} and Fe^{3+} in the iron-bearing oxide glasses in the intermediate range length scale (~ 1 nm) are manifested, the distribution of iron in the shorter length scale relevant to the size of Q species and NBO/BO clusters in iron-bearing Na and Mg-silicate glasses may be largely different (see Section 4.4.1 and 4.4.3 for further details).

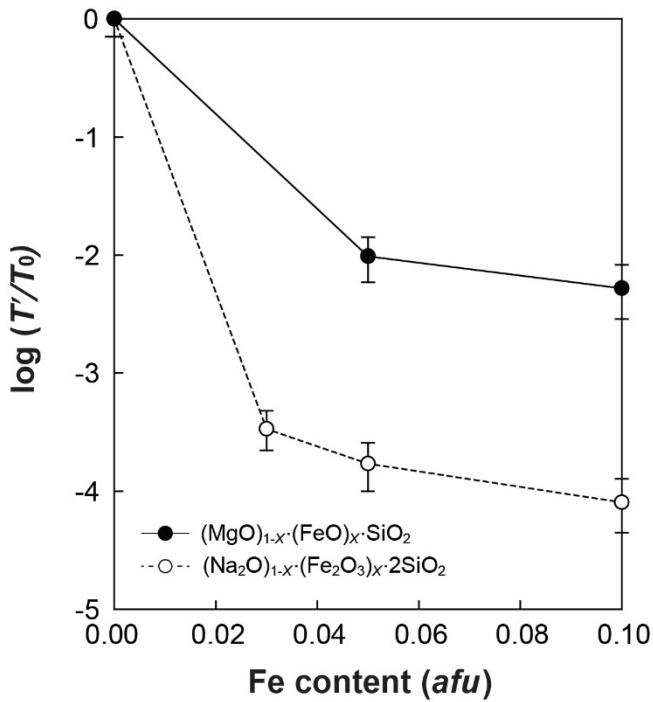


Figure 4-5. Variation in the normalized time constant for the recovery of magnetization (T'/T_0 , refers to T' for iron-bearing glasses divided by the T_0 for iron-free glass) in the stretched exponential equation for the iron-bearing magnesium (closed circles) and sodium (open circles) silicate glasses with varying iron concentration (atoms in a formula unit). The solid and dashed lines are guides for the eye.

4.3.3. Changes in the oxygen configurations with increasing X_{Fe} : ^{17}O MAS and 3QMAS NMR results

Figure 4-6 shows the ^{17}O MAS NMR spectra of MgSiO_3 glass ($X_{\text{Fe}} = 0$) and $(\text{Mg}_{1-x}\text{Fe}_x)\text{SiO}_3$ glasses with varying X_{Fe} . The ^{17}O MAS NMR spectrum for iron-free MgSiO_3 glass exhibits a single broad peak (-30 to 75 ppm) that results from overlapping Mg-O-Si (non-bridging oxygen, NBO) and Si-O-Si (bridging oxygen, BO), consistent with previous results (Allwardt and Stebbins, 2004; Kirkpatrick et al., 1983; Lee et al., 2003a). With increasing X_{Fe} , the signal intensity decreases (as shown in Figure 4-2) and the peak width of the glasses increases, manifesting the paramagnetic effect and possibly iron-induced changes in the network structure, consistent with the results of the ^{29}Si MAS NMR spectra. The position of the peak maximum for the combined peak (i.e., Mg-O-Si + Si-O-Si) is ~ 32 ppm and does not change significantly from $X_{\text{Fe}} = 0$ to 0.1. They slightly shift to a lower frequency (more negative chemical shift) to 28 ppm with a further increase in X_{Fe} up to 0.2.

Figure 4-7 presents the 2-dimensional ^{17}O 3QMAS NMR spectra of MgSiO_3 glass ($X_{\text{Fe}} = 0$) and $(\text{Mg}_{1-x}\text{Fe}_x)\text{SiO}_3$ glasses with X_{Fe} ranging from 0.05 to 0.2. The Mg-O-Si (~ -32 ppm in the isotropic dimension) and Si-O-Si (~ -48 ppm in the isotropic dimension) peaks in MgSiO_3 glass were well-resolved (See, Allwardt and Stebbins, 2004; Lee et al., 2016 and references therein for the NBO and BO peak assignments in the ^{17}O NMR spectra; Lee et al., 2003a; Stebbins and Xue, 2014; Timken et al., 1987; Xue et al., 1994). Despite the peak broadening, the Mg-O-Si and Si-O-Si peaks for $(\text{Mg}_{1-x}\text{Fe}_x)\text{SiO}_3$ glasses are relatively well-resolved, even at X_{Fe} of 0.2 (~ 13.5 wt% FeO). An increase in iron concentration promotes the formation of oxygen species that are directly bonded to iron (e.g., $\text{Fe}^{2+}\text{-O-Si}$, $\text{Fe}^{3+}\text{-O-Si}$, and $\text{Fe}^{3+}\text{-O-Fe}^{3+}$, etc.) (e.g., Mysen et al., 1980). However, the presence of the iron-bearing oxygen species is not

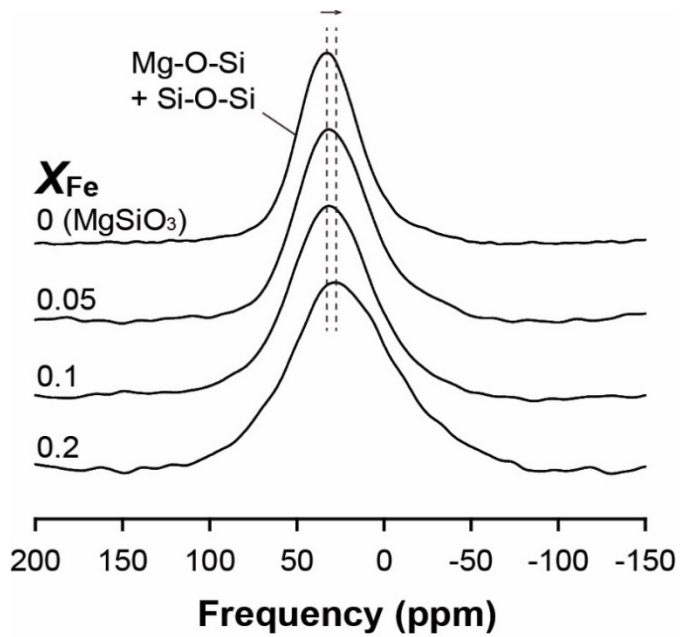


Figure 4-6. ^{17}O MAS NMR spectra of iron-bearing magnesium silicate glasses $[(\text{Mg}_{1-x}\text{Fe}_x)\text{SiO}_3]$ at 9.4 T with varying X_{Fe} [= $\text{Fe}/(\text{Mg} + \text{Fe})$], as labeled.

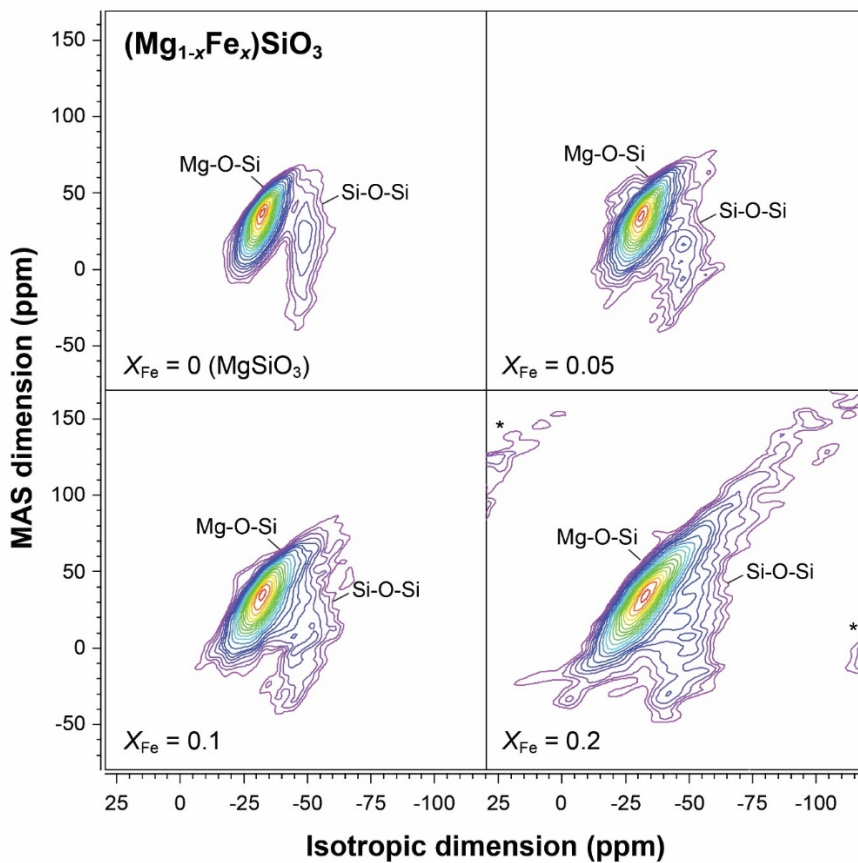


Figure 4-7. 2D ^{17}O 3QMAS NMR spectra of iron-bearing magnesium silicate glasses at 9.4 T with varying X_{Fe} [= Fe/(Mg + Fe)], as labeled. Contour lines are drawn from 8% to 98% relative intensity with a 6% increment and four additional lines at 4, 6, 11, and 17% levels, for better presentation of the low-intensity peaks.

evident in the ^{17}O 3QMAS NMR spectra. To check whether the potential existence of a signal from oxygen sites directly bonded to iron contributes to the changes in the 2D ^{17}O NMR spectra, the ^{17}O NMR chemical shielding tensor for the $\text{Fe}^{2+}\text{-O-Si}$ was estimated from quantum chemical calculations (see Section 4A-5). The presence of any feature near the expected position of $\text{Fe}^{2+}\text{-O-Si}$ for iron-bearing glasses is not observed, indicating that the signals from the oxygen sites bonded directly to iron are lost.

The broadening pattern for each peak is somewhat different: the peak broadening for Si-O-Si in the isotropic dimension (x-axis in Figure 4-7) is apparently more dominant than in the MAS dimension (y-axis in Figure 4-7). In contrast, the Mg-O-Si peak becomes broader along both the MAS and isotropic dimension with increasing X_{Fe} . While the peak widths for both Mg-O-Si and Si-O-Si in the isotropic dimension apparently increase, it is evident that the relative increase in the peak width is more significant for Mg-O-Si than for Si-O-Si. There is also a 'tail' on the Mg-O-Si peak at lower frequencies in the isotropic dimension for the glasses with $X_{\text{Fe}} = 0.2$ (Figure 4-7). Considering preferential broadening of Mg-O-Si with X_{Fe} , the observed trend suggests that the addition of Fe yields more significant changes in the Mg-O-Si than in the Si-O-Si species.

The observed trend in peak broadening in iron-bearing Mg-silicate glasses with X_{Fe} is also distinct from that in iron-bearing Na-silicate glasses. For the latter, a drastic peak broadening is observed for an addition with 0.9 at.% of Fe. However, the severe broadening in Mg-O-Si and Si-O-Si peaks for the iron-bearing Mg-silicate glasses with low iron content (1.3 at.% of Fe, $X_{\text{Fe}} = 0.05$) is not clearly shown in the ^{17}O NMR spectra (Figures 4-7 and 4-8). This difference can be attributed to the fact that the ^{17}O NMR spectrum for iron-free MgSiO_3 glass is intrinsically broadened due to the enhanced structural

disorder caused by Mg^{2+} and, thus, the initial life-time broadening by the paramagnetic effect may not significantly alter the peak with an addition of small amounts of Fe. Figure 4-8 presents the isotropic projection of the 2D ^{17}O 3QMAS NMR spectra of MgSiO_3 glass and $(\text{Mg}_{1-x}\text{Fe}_x)\text{SiO}_3$ glasses. The positions of the peak maximum of each oxygen site do not change significantly with increasing X_{Fe} . Both the Mg-O-Si and Si-O-Si peaks for iron-bearing glasses are broader than those for iron-free MgSiO_3 .

In order to provide a *semi-quantitative* trend of the effect of Fe on the peak intensity for each oxygen site, the 2D ^{17}O 3QMAS NMR spectra were decomposed into two corresponding NBO and BO, respectively. Here, we found that shearing of the 2D spectra (rotation of the peaks in the 2D spectra) provides more robust information of peak intensity than that based on fitting of 1D projection alone (See Section 4A-4 for the detailed spectral analyses). The sheared spectra revealed that NBO and BO fractions in the $(\text{Mg}_{1-x}\text{Fe}_x)\text{SiO}_3$ glasses vary with varying iron content. We note that the oxygen site fractions were calibrated as the peak intensity in the 2D 3QMAS NMR spectra depends on quadrupolar coupling constant (C_q). Here, C_q 's for Mg-O-Si and Si-O-Si for iron-free MgSiO_3 glasses are ~ 2.8 MHz, and ~ 4.4 MHz, respectively. Calibrated Mg-O-Si fraction of iron-free MgSiO_3 glass is about $65 \pm 2.0\%$, consistent with the previous NMR results and the prediction from chemical composition of the glasses (e.g., Allwardt and Stebbins, 2004; Lee et al., 2016; Lee et al., 2003a). The fraction of Mg-O-Si in iron-bearing $(\text{Mg}_{1-x}\text{Fe}_x)\text{SiO}_3$ glasses decreases with X_{Fe} .

Note that the fraction of Mg-O-Si is expected to decrease with increasing X_{Fe} due to the formation of $[\text{Fe},\text{Mg}]\text{-O-Si}$ (see Section 4A-4). Furthermore, inability to detect Fe-O-Si (and nearby Mg-O-Si) may decrease the observed fraction of Mg-O-Si. Previous NMR studies showed that net-

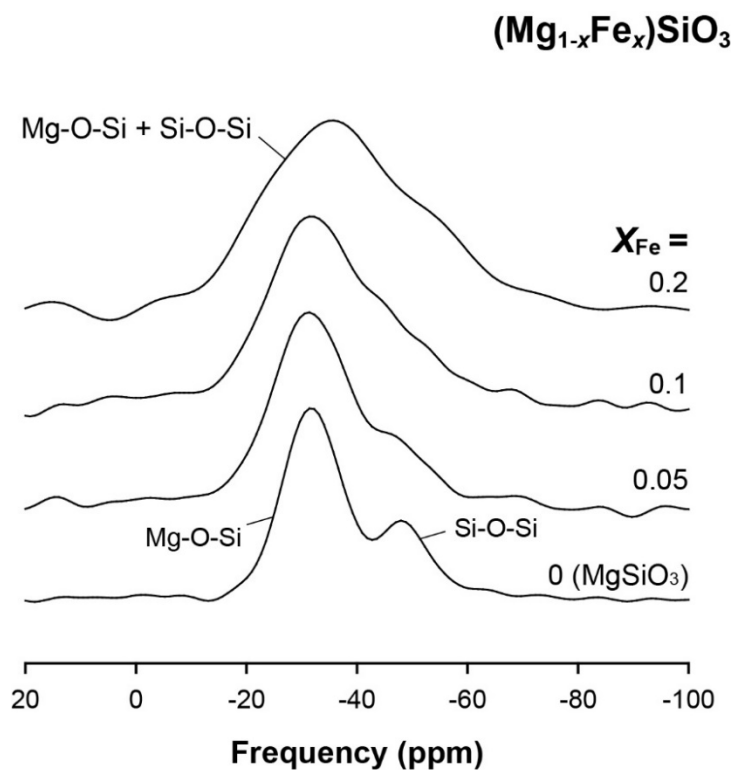


Figure 4-8. Total isotropic projection of ^{17}O 3QMAS NMR spectra of iron-bearing magnesium silicate glasses at 9.4 T with varying X_{Fe} [= Fe/(Mg + Fe)], as labeled.

work-modifying cation with high-field strength (e.g., Mg^{2+}) in ternary Mg-aluminosilicate glasses interacts strongly with both NBO and BO (Lee et al., 2016). Therefore, it is expected that both Mg^{2+} and Fe^{2+} have proximity to NBOs and BOs, leading to a decrease in NBO and BO signals (see Section 4.4.2 for further discussion). The current result with a decrease in NBO fraction is also consistent with ^{29}Si MAS NMR results where the fraction of highly polymerized Q species (i.e., Q^3) apparently increases with increasing X_{Fe} .

Furthermore, the noticeable changes in Mg-O-Si configurations may stem from the relative spatial proximity between the network-modifying Fe^{2+} and NBO. The results comply with the observed preferential broadening of the less polymerized species in the ^{29}Si MAS NMR spectra for the $X_{\text{Fe}}=0.2$ glasses (Figure 4-1, see Section 4.4.2 for further discussion).

4.4. Discussion

4.4.1. Nature of paramagnetic interactions between Fe and melt networks with varying length scale

The paramagnetic effect results in the rapid spin-lattice relaxation behavior of nuclear spins around paramagnetic cations due to the dipolar interaction between the paramagnetic center and nuclear spins. The dipolar coupling is inversely proportional to the sixth power of the distance between the paramagnetic center and nuclear spins (Bakhmutov et al., 2009; Bertini et al., 2002; Bertini et al., 2005). Figure 4-9 shows a schematic figure illustrating the paramagnetic interaction between the nuclear spins and paramagnetic center. The model is designed to conceptualize the paramagnetic effect on the nuclear spins. A similar analysis was proposed in the previous NMR study on metalloproteins (Bertini et al., 2005). The nuclear spins in Region I (a dark gray area in Figure 4-9) cannot be observed in the NMR spectra because of the overall signal loss in the NMR spectra with increasing concentration of the paramagnetic cation (as shown in Section 4.3.1.1). Here, the size of Region I is determined by the “*cutoff radius* (r_c)”, which is the distance within which paramagnetic interaction results in complete NMR signal loss. Region I is thus a “blind zone”, where the nuclear spins within a certain distance from the paramagnetic cation would not be observed (Bertini et al., 2005). As the

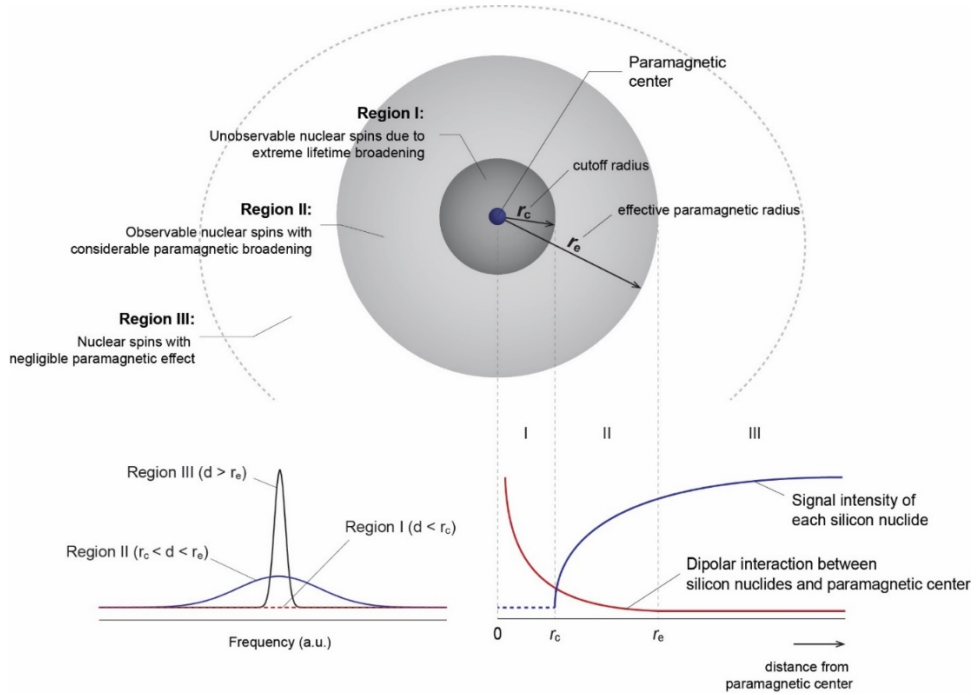


Figure 4-9. Schematic diagram of the variation in the paramagnetic effect depending on the distance between paramagnetic center and nuclear spins.

distance between the paramagnetic cation and nuclear spins ($d_{\text{para-nuclear}}$) increases, the dipolar paramagnetic interaction decreases drastically. The nuclear spins in Region II (a light gray area in Figure 4-9), thus, are observed in the NMR spectra, while the NMR signals for nuclear spins in Region II are broadened. The paramagnetic effect becomes negligible with further increase in $d_{\text{para-nuclear}}$. The nuclear spins in Region III are not affected by the paramagnetic effect. The hypothetical distance in which the paramagnetic effect becomes negligible (i.e., the boundary of Region II) is called “*effective paramagnetic radius* (r_e)”.

The nuclear spins in the $r_c < d_{\text{para-nuclear}}$ (Regions II and III) are detectable in the NMR spectra, allowing us to understand the atomic structure of iron-bearing silicate glasses. Among them, the nuclear spins in the $r_c < d_{\text{para-nuclear}} < r_e$ (Region II) are mostly under the influence of paramagnetic effect without losing the NMR signal, and also can be shown in the NMR spectrum. While the spectrum is significantly broadened, the spins in the region provide the opportunity to explore the nature of the interaction between paramagnetic cations and nuclides. It is worth noting again that the current distinction is somewhat arbitrary, and the changes in the paramagnetic interactions with increasing $d_{\text{para-nuclear}}$ are gradual. Because the signal loss and peak broadening occur simultaneously in the nuclear spins, the current hypothetical division of the distance from the center is thus for the conceptual interpretation of the nature of the paramagnetic interaction and peak intensity loss with an increase in iron concentration. The semi-quantitative parameterization of the r_c and r_e allows us to distinguish whether the change in the NMR spectra is due to a structural change ($d_{\text{para-nuclear}} > r_e$) and/or a preferential paramagnetic interaction ($r_c < d_{\text{para-nuclear}} < r_e$). The size of the r_c can be estimated by observing the trend of decreasing NMR signal intensity with increasing iron

content, as mentioned Section 4.3.1.1. To estimate the size of the r_c , the ^{29}Si NMR signal intensities for $(\text{Mg}_{1-x}\text{Fe}_x)\text{SiO}_3$ with varying X_{Fe} were estimated by calculating the fractions of the unobservable nuclear spins in the 3-dimensional space that contains the N atoms of silicon and randomly distributed iron, when the NMR signal from the next-nearest Si from Fe is removed. Based on the stoichiometry of $(\text{Mg}_{1-x}\text{Fe}_x)\text{SiO}_3$ composition for the current glasses, the number of iron atoms in 3-dimensional space with N atoms of silicon can be calculated from $N \cdot X_{\text{Fe}}$. The T_1 relaxation behavior indicates the homogeneous distribution of iron in $(\text{Mg,Fe})\text{SiO}_3$ glasses (see Section 4.3.2). If we assume that the NMR spins within the sphere with the radius of the next nearest neighbors distance between paramagnetic centers and Si are removed, the predicted ^{29}Si NMR signal intensities are similar with the measured signal intensities from ^{29}Si MAS NMR spectra (Figure 4-2). This suggests that r_c is similar to the distance between the paramagnetic cation and the next nearest silicon nucleus. The previous NMR study on an iron-bearing pyrope also suggested that the NMR signals of ^{29}Si and ^{27}Al nuclear spins in the first coordination shell of Fe^{2+} are not observed (Stebbins and Kelsey, 2009). The r_c for the iron-bearing pyrope is thus similar to $d(\text{Fe}^{2+}\text{-Si})$ (the mean distance between Fe^{2+} and next nearest Si) of $\sim 3.3 \text{ \AA}$ (e.g., Armbruster et al., 1992; Hazen and Finger, 1989). The exact r_c value is difficult to quantify for the silicate glasses, because of a statistical distribution of the distance between the paramagnetic centers and silicon nuclei. While different nuclides may have distinct r_c values, the decrease in signal intensity in ^{29}Si MAS NMR and ^{17}O NMR spectra are rather identical (Figure 4.2), indicating that the r_c for these nuclides are not largely different: although the first coordination shell of iron consists mainly of oxygens, both Si and O within the estimated r_c ($\sim 3.3 \text{ \AA}$) are lost.

A portion of the nuclear spins located in $r_c < d_{\text{para-nuclear}} < r_e$ (Region II) could be observed in NMR spectra (with the characteristic Lorentzian peak shape), while the quantitative estimation of r_e is not trivial. Qualitatively, the previous NMR studies on crystalline oxides also suggested that the through-bond Fermi-contact interaction and through-space pseudo-contact interaction in Fe- ^7Li interactions occurred within ~ 1 nm (e.g., Grey and Dupre, 2004; Grey and Lee, 2003). Taking this estimation into consideration, the observed ^{29}Si spin-lattice relaxation behavior with $\beta = 0.5$ indicates the homogeneous distribution of the paramagnetic cation in an intermediate (and/or medium) length scale (~ 1 nm). Therefore, homogeneous distribution of paramagnetic cations in intermediate length scale does not fully discard for the moderate degree of preferential distribution of iron on the short-range scale (less than ~ 1 nm). The preferential changes in the peak shape and intensity for ^{29}Si and ^{17}O NMR spectra, thus, stem from both the moderate degree of preferential distribution of iron between local configurations and iron-induced structural changes. While more precise and robust modeling efforts are necessary, this allowed us to describe the distribution of paramagnetic cations in iron-bearing silicate glasses.

4.4.2. Variation in structure and extent of disorder of (Mg,Fe)SiO₃ glasses with iron concentration

The current NMR results for the (Mg,Fe)SiO₃ glasses show the apparent changes in the peak shape for less polymerized (i.e., Q¹) and the increases in peak intensity for Q³ with increasing X_{Fe} , together with the peak shift toward the lower frequency. While the paramagnetic interaction is homogeneous over the range of the intermediate length scale (see ^{29}Si spin-lattice relaxation time measurement in Section 4.3.2), the preferential

distribution of iron between local configurations on the *short-range* length scale (below 1 nm) can result in the observed changes in the ^{29}Si NMR spectra. Based on the spectral analyses (Section 4A-3), it is clear that both structural (configurational) and paramagnetic effects control the overall spectral changes. On the basis of the simulation of the sheared ^{17}O 3QMAS NMR spectra for $(\text{Mg}_{1-x}\text{Fe}_x)\text{SiO}_3$ glasses (Section 4A-4), the fraction of Mg-O-Si in iron-bearing $(\text{Mg}_{1-x}\text{Fe}_x)\text{SiO}_3$ glasses may decrease with increasing X_{Fe} , consistent with ^{29}Si MAS NMR results (i.e., an apparent increase in the Q^3 fraction with X_{Fe}). The ^{17}O NMR results for iron-rich Mg-silicate glasses also reveal the differential paramagnetic effect on each oxygen site: within r_c , while the Mg-O-Si and Si-O-Si are both affected by iron, slight preferential interaction between iron and NBO are observed, leading to a larger decay in NBO signal. Within r_e , NBO has stronger interaction with Fe^{2+} as evidenced by the preferential broadening in Mg-O-Si peak with X_{Fe} . Therefore, Mg-O-Si is more strongly affected by iron than Si-O-Si. We note that the degree of melt polymerization based on the current ^{17}O and ^{29}Si NMR results is overall consistent with those suggested from the previous studies where the coordination environments of iron were specifically explored (e.g., Mysen et al., 1980; Farges et al., 2004; Mysen 2006; Wilke et al., 2007).

By adding Fe into binary Mg-silicate glasses, mixed NBO environments (such as $[\text{Mg},\text{Fe}^{2+}]\text{-NBO}$) form. The formation of $[\text{Mg},\text{Fe}^{2+}]\text{-NBO}$ would cause a decrease in the fraction of Mg-O-Si. Depending on the degree of intermixing between Mg^{2+} and Fe^{2+} (i.e., random, chemical order or clustering), the observed Mg-O-Si fraction would be different. If the mixing between Mg^{2+} and Fe^{2+} is favored, the fraction of Mg-O-Si would be underestimated. On the other hand, if the Mg^{2+} and Fe^{2+} are phase separated, the observed Mg-O-Si fraction would be overestimated. While it is difficult

to quantify the degree of intermixing between Mg^{2+} and Fe^{2+} from the current study, the distribution among Mg^{2+} and Fe^{2+} is expected to be random because the cation field strengths (i.e., charge/ionic radius) of Mg^{2+} (~ 2.78) and Fe^{2+} (~ 2.56) are similar, according to previous NMR studies (Lee et al., 2003a; Park and Lee, 2016). Together with the decrease in the Mg-O-Si fraction, the formation of $[\text{Mg},\text{Fe}^{2+}]$ -NBO could lead to the variations in chemical disorder of NBO sites as shown in other ternary mixed-cation silicate glasses (Allwardt and Stebbins, 2004; e.g., Florian et al., 1996; Lee et al., 2003a; Lee and Stebbins, 2003a; Lee and Sung, 2008; see Park and Lee, 2016, Table 1 for the review of the previous NMR studies). This results in more significant changes in the peak width for Mg-O-Si than that for Si-O-Si. While the presence of non-framework cations also affects the Si-O-Si configurations, the BO sites are less affected by the type of network-modifying cation (e.g., Lee et al., 2003a; Lee and Stebbins, 2009; Mysen and Richet, 2018; Shelby, 2005). The current 2D ^{17}O NMR results confirm the stronger interaction of Fe^{2+} with Mg-O-Si than with Si-O-Si. Thus, the increase in the extent of chemical disorder (i.e., formation of mixed-NBO sites) for iron-bearing Mg-silicate glasses would result in an increase in the configurational disorder. This is consistent with the previous studies of the iron-bearing silicate melts (e.g., calcium silicate and aluminosilicate melts) (Mysen et al., 1985b; Neuville et al., 1993; Richet, 1984; Sipowska et al., 2009) where the configurational entropy increases with increasing iron concentration (see Section 4.5 for a detailed discussion).

We note that the current NMR results with a preferential signal decay in the less polymerized species may indicate that the structural information obtained from the NMR spectra for the survived spins may not be fully representative of the entire glass structure. This may not fully comply with

the premise in our previous study for iron-bearing Na-silicate glasses (i.e., the homogeneous distribution of Fe^{3+}) where the structural information presented in NMR spectra for the 'survived spins' can represent the entire glass structure (Kim et al., 2016). While the earlier postulate is still valid, the difference address the intrinsic difference between Mg- and Na-silicate glasses where the distribution of Fe^{3+} in Na-silicate glasses can be relatively more homogeneous and uniform and that of Fe^{2+} in Mg-silicate can be more heterogeneous and disordered.

4.4.3. Effect of the valence state of iron on the paramagnetic effect and the structure of iron-bearing silicate glasses: Insights from the comparison with iron-bearing sodium silicate glasses

4.4.3.1. Variation in the size of the cutoff radius and effective paramagnetic radius with the valence state of iron

To systematically investigate the effect of the valence state of iron on the paramagnetic effect (i.e., signal loss and rapid spin-lattice relaxation), a comparison between the results for Fe^{2+} -bearing glasses and Fe^{3+} -bearing glasses is needed. A comparison of the NMR data for iron-bearing Mg-silicate glasses with $\text{Fe}^{3+}/\Sigma\text{Fe} = \sim 0.2$ in the current study and iron-bearing Na-silicate glasses with $\text{Fe}^{3+}/\Sigma\text{Fe} = 0.89$ in our previous study allows us to explore the effect of the valence state of iron in the structures of silicate glasses. As mentioned in Section 4.3.1, the trends of the decrease in the signal intensity with increasing iron concentration for both iron-bearing magnesium and sodium silicate glasses are similar, indicating that the size of r_c does not seem to be significantly affected by the valence state of iron in the silicate glasses. Whereas there is no significant difference in the trend of decreasing signal

intensity, the spin-lattice relaxation time (T') for iron-bearing silicate glasses with varying iron concentration is affected by the valence state of iron in the silicate glasses. As shown in Figure 4-5, the T'/T_0 values for iron-bearing magnesium silicate glasses (i.e., Fe^{2+} -dominant) in the current study decrease by about two orders of magnitude with increasing X_{Fe} , while those for iron-bearing sodium silicate glasses (i.e., Fe^{3+} -dominant) in our previous study decreased by four orders of magnitude with the addition of iron. For the iron-free silicate glasses, the measured T' value for magnesium metasilicate glass is ~ 8.8 s, consistent with the findings of the previous study (Davis et al., 2011). This value is considerably lower than that for sodium disilicate glass (~ 29.8 s). Although a direct comparison is somewhat difficult owing to the difference in glass composition (i.e., SiO_2 content and type of network-modifying cation), the observed difference in the trend of decreasing T' with iron concentration may partly result from the difference in the electronic configurations of iron. The Fe^{2+} has the electronic configuration $3d^6$ with four unpaired electrons, while the Fe^{3+} has the electronic configuration $3d^5$ with five unpaired electrons. The rapid decrease in T' for iron-bearing sodium silicate glasses may stem from the stronger interaction between Fe^{3+} (5 unpaired electrons) and ^{29}Si spins in iron-bearing Na-silicate glasses than that between Fe^{2+} (4 unpaired electrons) and ^{29}Si spins in iron-bearing Mg-silicate glasses. Therefore, the iron redox ratio affects the size of r_e , and thus the nature of the interaction between nuclear spin and the paramagnetic cation.

4.3.2. Preferential interaction between iron and local structure: Fe^{2+} with less polymerized Q species and NBO vs. Fe^{3+} with highly polymerized Q species and BO

The observed variations in Q^n speciation (as shown in the ^{29}Si NMR results) and atomic environments around oxygen (as shown in the ^{17}O NMR results) with increasing Fe^{2+} in the current study and Fe^{3+} in the previous study suggest the effect of the valence state of iron on the spatial proximity of the local configurations in silicate glasses. An apparent increase in highly polymerized Q species in Fe^{3+} -dominant sodium silicate glasses with increasing iron concentration suggests an increase in the degree of polymerization. On the other hand, changes in the peak shape at higher frequencies (corresponding to less polymerized Si units) are observed in Fe^{2+} -dominant $(\text{Mg,Fe})\text{SiO}_3$ glasses with increasing X_{Fe} , accompanied by an increase in the fraction of Q^3 species (see Section 4.3.1). The increase in Fe^{3+} leads to an increase in the degree of polymerization and the topological disorder of highly polymerized silicon environments. The increase in Fe^{2+} content results in an increase in the topological disorder of less polymerized silicon environments. Overall, the current ^{29}Si NMR results confirm that the Fe^{2+} in the MgSiO_3 glasses has a moderate degree of preferential interaction with the less polymerized Si units and the minor fraction of Fe^{3+} (owing to $\text{Fe}^{3+}/\Sigma\text{Fe} = 0.2$) has relatively stronger effects in the highly polymerized Si units owing to the structural role of Fe^{3+} as a network-forming cation.

The changes in the oxygen configurations with increasing iron concentration are also affected by the valence state of iron in the iron-bearing silicate glasses. While adding Fe^{3+} may yield more significant apparent changes in the Si-O-Si than in the Na-O-Si in the Fe^{3+} -dominant sodium silicate glasses, the addition of Fe^{2+} in the MgSiO_3 glass leads to more significant changes in the Mg-O-Si peak than Si-O-Si peak, indicating the presence of a moderate degree of preferential interaction between Fe^{2+} with NBO and Fe^{3+} with BO. The difference in preferential interactions between

iron, Q species, and oxygen configurations (e.g., proximity between Fe²⁺ and less polymerized Si units and NBO, as well as that between Fe³⁺ and highly polymerized Si units and BO) would stem from the difference in the structural role of Fe²⁺ as a network-modifying cation and Fe³⁺ as a network-forming cation.

4.4.4. Nature of hidden NBO sites in iron-bearing Mg-silicate glasses: Insights from quantum chemical calculations of ¹⁷O NMR chemical shift

The theoretical calculations of the NMR chemical shielding tensor for oxygen sites directly bonded to iron allow for the prediction of the NMR peak position of hidden oxygen sites. Figure 4-10A shows the model cluster containing Fe²⁺-NBO [i.e., Fe²⁺Si₃O₂^{BO}O₂^{Fe-NBO}(OH)₆]. The peak position of the NBO site directly bonded to iron in the ¹⁷O NMR spectra compares to the peak positions with other NBO sites in the glasses, such as Mg²⁺-NBO and Ca²⁺-NBO. The ¹⁷O isotropic chemical shift (δ_{iso}) of Ca-NBO (~104.7 ppm) in calcium silicate glass (CaO:SiO₂ = 4:6) is larger than that of Mg-NBO (~49.2 ppm) in magnesium silicate glass (MgO:SiO₂ = 1:1), based on previous experimental studies (Allwardt and Stebbins, 2004; Lee et al., 2003a; Lee and Stebbins, 2003a). The current results also show that the calculated ¹⁷O δ_{iso} of Ca-NBO (~150 ppm) in the model cluster (Figure 4-10B) is larger than that of Mg-NBO (~43 ppm) in the model cluster (Figure 4-10C), which is qualitatively consistent with the trend revealed in the experimental studies (see Section 4A-5). The calculated ¹⁷O δ_{iso} for Fe²⁺-NBO (~ -730 ppm) in an optimized model cluster is significantly more shielded (negative chemical shift) than that of the ¹⁷O δ_{iso} for Mg²⁺-NBO (~43 ppm), indicating that the

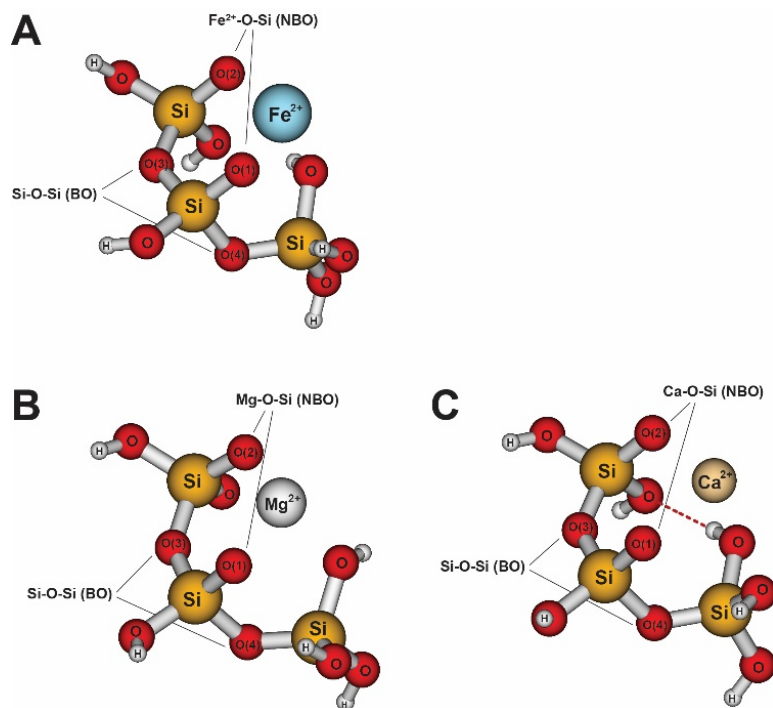


Figure 4-10. The optimized geometry of the non-bridging oxygen cluster in alkaline-earth silicate glasses with (A) Fe²⁺-NBO (Fe²⁺Si₃O₂BO₂Fe-NBO(OH)₆), (B) Mg²⁺-NBO (Mg²⁺Si₃O₂BO₂Fe-NBO(OH)₆), and (C) Ca²⁺-NBO (Ca²⁺Si₃O₂BO₂Fe-NBO(OH)₆).

observed changes in the 1D ^{17}O NMR signal from Mg-O-Si and Si-O-Si (Figure 4-6) with increasing iron concentration is not due to the potential existence of a signal from Fe^{2+} -NBO. The estimated ^{17}O δ_{iso} of Fe^{3+} -BO (i.e., Fe^{3+} -O-Si) is ~ -287 ppm, which is also significantly more shielded than those of Mg-O-Si and Si-O-Si. The calculated ^{17}O δ_{iso} for both hidden species are significantly different than those of the oxygen species in the NMR spectra (i.e., Mg-O-Si and Si-O-Si). We note that there are large uncertainties in the preliminary results for ^{17}O δ_{iso} of iron-bearing species. Nonetheless, the observed ^{17}O NMR spectra with signals from Mg-O-Si and Si-O-Si are not likely to be affected by the potential existence of signals from oxygen sites directly bonded to iron (i.e., Fe^{2+} -NBO and Fe^{3+} -BO).

4.4.5. Limitations of the current study

It is necessary to address the limitations of the current study. First, the current study on iron-bearing magnesium silicate glasses could not provide *quantitative* estimation of the degree of chemical disorder between frameworks (i.e., Si and Fe^{3+}) and configurational disorder between the nonframework cations (in this case, Mg^{2+} and Fe^{2+}) because of a lack of information on the hidden oxygen species directly bonded to iron, such as Fe^{3+} -O-Si. Second, while the iron coordination number could be uniquely constrained by X-ray absorption and Mössbauer spectroscopy (e.g., Farges et al., 2004; Jackson et al., 2005; Mysen and Virgo, 1989; Wilke et al., 2007), it is difficult to directly obtain the local structural environment of iron from the solid-state NMR techniques. Third, while the theoretical framework for the paramagnetic effect on the NMR spectra has been presented in this study, it is still difficult to quantify the contribution from the changes in the NMR

spectra due to iron-induced structural changes and those from the paramagnetic effect. Finally, the quantification of the distribution of Mg^{2+} and degree of intermixing among the constituent non-framework cations (i.e., Mg^{2+} and Fe^{2+}) in $(\text{Mg,Fe})\text{SiO}_3$ is still challenging due to the invisibility of the oxygen which directly bonded to iron in the NMR spectra.

We have studied the structure of the quenched glasses (i.e., supercooled liquid frozen below the T_g , which is much lower than the liquidus temperature). As indicated in section 4.2.1, there are differences between the structure of the melts and that of the glasses. However, we note that the effect of fictive temperature on the Q species (i.e., Si environment) and NBO/BO configurations (which are the focus of this study) has been reported to be rather minor (e.g., Stebbins, 1995; 2008 for the review). Therefore, the structural information of silicate glasses presented in the current study can partly provide insight into the structure and properties of the corresponding melts (Lee, 2005; Mysen and Richet, 2018; Richet et al., 2009; e.g., Stebbins, 1995).

Note that we have investigated the samples that are previously thought to be impossible to characterize using solid-state NMR spectroscopy. Therefore, the current discussion about the structures and degree of network polymerizations is not fully quantitative and thus, somewhat speculative. Because the paramagnetic centers lead to significant signal loss, the current discussion on the Q^n distribution should be considered with great care. These lead to an intrinsic uncertainty in the current interpretation. Ongoing NMR studies will further elaborate on such issues. Despite the aforementioned limitations, the purpose of the current study is to determine the iron-induced structural transitions in iron-bearing Mg-silicate glasses, where the NMR spectra are perturbed by the paramagnetic effect. Therefore, the focus of the

current study is careful measurement, interpretation, and collection of NMR spectra of unprecedented quality “despite severe paramagnetic broadening and signal loss”, allowing us to provide insights into the structure of iron-bearing glasses.

4.5. Implications

The current NMR results for (Mg,Fe)SiO₃ glasses, together with those from our earlier (Na,Fe)-silicate glasses revealed the structural details of diverse iron-bearing natural silicate glasses. The observed structural changes in the iron-bearing glasses can provide insights into the evolution of silicate melts undergoing volcanic eruption. For example, recent studies established the relationship among compositions of natural volcanic glasses, eruption style, and the viscosity of silicate melts. The study showed that approximately 0.5 wt% changes in constituent oxides composition can lead to a drastic rheological transition (Di Genova et al., 2017a; Di Genova et al., 2017b). This drastic transition (from effusive to eruptive) of silicate melts is attributed to changes in the degree of polymerization resulting from variation of the ratio between network-forming cations (e.g., Si, Al, and Fe³⁺) and network-modifying cations (e.g., Na, Mg, and Fe²⁺). Although detailed structures around oxygens in natural volcanic glasses with varying iron content using solid-state NMR has not been well understood, the current study qualitatively traces the effect of iron content on the evolution of its oxygen environment in molten silicate during eruption. The high-resolution NMR technique presented here will be potentially useful in exploring diverse volcanic glasses with varying iron content.

Basaltic volcanic glasses are also ubiquitous on Earth's surface environments, particularly on the oceanic crust. Reaching of basaltic glasses in an aqueous solutions leads to the formation of silica-rich amorphous phases (Chemtob et al., 2010; Chemtob and Rossman, 2014; Chemtob et al., 2012; e.g., Zhu et al., 2006). Similar amorphous SiO₂ deposits have been found on the surface of Mars (Squyres et al., 2008). Although the formation mechanism of amorphous silica from the basaltic glasses remains to be fully understood, the current study of Mg-rich iron-bearing silicate glasses – as a model system for basaltic glasses – showed well-resolved BO and NBO. The reactivity of these oxygen clusters is likely to be largely different (Lee and Stebbins, 2003b; Lee et al., 2003b; Lee and Weiss, 2008): NBO is expected to be more prone to hydrolysis (forming Si-O-H) and, thus, more susceptible to overall dissolution. Therefore, the formation of silica-rich amorphous phases is due largely to the selective reaching of NBO from the basaltic glasses. This preferential dissolution leads to the formations of a network composed mainly of Si-O-Si, accounting for the observed formation of silica layers.

Furthermore, the structures of glasses yield *indirect* insights into the melt viscosity by revealing the information of configurational disorder of the frozen super-cooled liquids (Lee, 2005; Mysen and Richet, 2018; Neuville, 2006; Richet et al., 2009 and references therein; i.e., glasses, see Stebbins and Xu, 1997). Here, we discuss the atomistic origins of the *melt* viscosity on the basis of observed structural changes in the iron-bearing silicate *glasses*. Because of the known differences in structures of glasses and melts (though minor, and aforementioned in Section 4.5), the following discussion is qualitative.

Experimental measurements of the viscosity of iron-bearing magnesium silicate melts are challenging because of the high melting

temperature and low viscosities (Liebske et al., 2005; Mysen and Richet, 2018; Spice et al., 2015). Nevertheless, earlier studies have shown that the viscosity of iron-bearing magnesium silicate melts and slags decreases with increasing iron concentration (e.g., Dai et al., 2003; Ji et al., 1998; Toropov and Bryantsev, 1965). For example, the viscosity of synthetic MgO-FeO-SiO₂ melts at a constant SiO₂ concentration of 55 wt% (at 1350 °C) slightly decreases with increasing Fe²⁺/Mg ratio, from 10^{0.66} Pa·s (for Fe²⁺/Mg = 0.45) to 10^{0.32} Pa·s (for Fe²⁺/Mg = 4.5) at constant Fe³⁺/ΣFe < 0.02 (Toropov and Bryantsev, 1965). A previous viscosity measurements of the synthetic silicate melts with a composition similar to the magma of Mars (i.e., tholeiitic and alkaline Fe-rich silicate melts with about 43~50 wt% SiO₂, 8~14 wt% Al₂O₃, 8~12 wt% MgO, 2~5 wt% Na₂O+K₂O, and 14~21 wt% FeO_{tot}) showed that the viscosity of the Martian basaltic melts with 20 wt% FeO_{tot} is about 10^{0.5} Pa·s lower than that with 14 wt% FeO_{tot}, regardless of the iron redox ratio (Chevrel et al., 2014).

The current ¹⁷O NMR results show the increase in the configurational (mixing of cations) and topological (bond angle-and length distribution) disorder of NBO sites with increasing iron content: the chemical disorder stems partly from the formation of mixed NBO environments (such as [Mg,Fe²⁺]-NBO). An increase in the topological disorder of the Qⁿ species and oxygen configurations with increasing X_{Fe} was also observed in the current ²⁹Si and ¹⁷O NMR results (i.e., ²⁹Si NMR results in Section 4.3.1 and Figure 4-1, and ¹⁷O NMR results in Section 4.3.3, Figures 4-7 and 4-8). These overall increases in the degree of disorder affect melt viscosity with iron content. An increase in configurational entropy due to mixing of Mg and Fe around NBO decreases melt viscosity (e.g., Adam and Gibbs, 1965; Le Losq et al., 2014; Neuville, 2006; Neuville et al., 1993; Neuville and Richet, 1991; Richet, 1984). With a further increase in topological disorder (and thus topological entropy),

the melt viscosity tends to decrease further. Thus, the current results suggest a decrease in the viscosity of (Mg,Fe)SiO₃ melts with increasing Fe²⁺. Although a direct comparison is certainly premature, the current atomistic insights is consistent with the decrease in the viscosity of Martian basaltic melts with increasing iron content (Chevrel et al., 2014) and the estimated decrease in viscosity of iron-bearing magnesium silicate melts and slags (i.e., MgO-FeO-SiO₂) (Toropov and Bryantsev, 1965).

The current results may provide atomistic insights into the changes in the viscosity with varying oxygen fugacity. The viscosity of silicate melts tends to decrease with decreasing Fe³⁺/ΣFe. For instance, the viscosity of silicate melts with iron-bearing calcium silicate melts (i.e., CaFeSi₂O_x, *x* varies with the iron redox ratio) slightly decreases by about 10^{0.2} Pa·s as Fe³⁺/ΣFe decreases from 0.9 to 0.2 (Dingwell and Virgo, 1988), while the atomistic origins of the changes in the viscosity remain to be understood. The current results for Fe²⁺-bearing silicate glasses and the previous study on Fe³⁺-bearing silicate glasses showed that the variations in Q^{*n*} speciation and oxygen configurations with increasing iron concentration are influenced by the valence state of iron. In particular, the ¹⁷O NMR results for Fe²⁺-dominant MgSiO₃ glasses show more significant changes in the peak for Mg-O-Si than in that for Si-O-Si, while those for Fe³⁺-dominant sodium silicate glasses in the previous study present larger changes in the Si-O-Si than in the Na-O-Si (see Section 4.4.3). These results *indirectly* confirm that Fe²⁺ acts as a network-modifying cation and Fe³⁺ acts as a network-forming cation (e.g., Calas and Petiau, 1983; Farges et al., 2004; Mysen and Virgo, 1985, 1989; Waychunas et al., 1988).

The high-resolution solid-state NMR study for (Mg,Fe)SiO₃ glasses aids to account for the effect of the atomic structure on the nature of the

viscous flow of the mafic silicate melts. As the crystallization of melts in a magma ocean occurs, the residual partial melts are greatly enriched with iron because the iron tends to be preferentially partitioned into liquid at ambient and high pressure (e.g., Andrault et al., 2012; Mysen, 1975). While experimental and theoretical confirmation are necessary, the viscosity of Fe²⁺-rich silicate melts of the Hadean magma ocean is expected to be low. Thus, the iron-enriched melts would be considerably denser and less viscous, facilitating the rapid descent of the mafic silicate melts.

The Fe²⁺-rich partial melts have been considered one of the constituents of the ultra-low velocity zone at the core-mantle boundary (Rost et al., 2005; Williams, 1998), while other possibilities have also been proposed [e.g., iron-enriched (Mg,Fe)O (Wicks et al., 2010), iron-enriched post-perovskite (Mao et al., 2006), and subducted banded iron formation (Dobson and Brodholt, 2005), etc.]. As we studied the structure of quenched glasses at ambient pressure, it is difficult to apply our findings directly to the mafic silicate liquids at the core-mantle boundary (high temperature and high pressure). That being said, it is expected that the Fe²⁺-rich MgSiO₃ melts in the Earth's interior are also expected to have a lower viscosity than the of Fe²⁺-poor silicate melts. The previous mantle dynamics simulations have suggested that the shape and thickness of the ultra-low velocity zone depends on the viscosity of the silicate melts (Hernlund and Jellinek, 2010; McNamara et al., 2010). Thus, the decrease in the viscosity of Fe²⁺-rich silicate melts with increasing Fe²⁺ content could promote the dynamics of the ultra-low velocity zone. On-going high pressure studies may provide better constraints. While we studied the structure of glasses at ambient pressure, the ongoing study of silicate melts at high pressure may allow us to better constrain the atomistic

origins of the properties of complex iron-bearing melts in Earth's interior (Kelsey et al., 2009; Lee, 2011).

4.6. Conclusion

While it has been challenging to probe the atomic structure and disorder of the geologically relevant iron-bearing magnesium silicate glasses using solid-state NMR, the current NMR results provided the structural details of (Mg,Fe)SiO₃ glasses with varying iron concentration. The ²⁹Si MAS NMR spectra present the peak shift toward lower frequency and the apparent increase in the Q³ species with increasing X_{Fe} with preferential broadening of less polymerized Si units. The results suggest an increase in the degree of polymerization owing to the presence of Fe³⁺ and the spatial proximity between Fe²⁺ and less polymerized Q species. The ¹⁷O NMR spectra show the variations in the peak widths and relative fractions for Mg-O-Si and Si-O-Si with increasing X_{Fe} , indicating that the relative increase in the peak width is more significant for Mg-O-Si than for Si-O-Si. These results suggest both the preferential interaction between NBO and Fe²⁺ and iron-induced increase in topological and chemical disorder in NBO. The apparent changes in the NMR spectra at high Fe content indicate the preferential interaction between iron with local configurations (i.e., Qⁿ species, NBO/BO site) characterized with the moderate degree of preferential interaction between the Fe²⁺ and Q¹ species (over Q³ species), and NBO (over BO). While it is difficult to quantify the contribution from the changes in the NMR spectra due to the iron-induced structural changes and those from the paramagnetic effect, the current NMR results confirm the changes in the Qⁿ speciation and oxygen configurations due to adding Fe²⁺ and the preferential interaction between Fe

and local configurations. These structural findings with X_{Fe} help explain the decrease in the viscosity of iron-bearing magnesium silicate melts with increasing iron concentration and improve our understanding of the relationship between atomic structure and the transport properties of $(\text{Mg,Fe})\text{SiO}_3$ melts. While further efforts are certainly necessary, the present NMR results hold strong promise for studying the structure and disorder of natural silicate glasses and melts with paramagnetic cations using solid-state NMR.

APPENDIX

4A-1. Summary of previous studies on the atomic structure of iron-free MgSiO₃, iron-bearing magnesium silicate, and iron-bearing silicate glasses and melts using various experimental and theoretical methods

In this section, we provide the summary of the valuable previous studies on the structure of iron-free and iron-bearing silicate glasses and melts at ambient and high pressure.

Structure of iron-free MgSiO₃ glasses and melts at ambient and high pressure. The atomic structures of *iron-free* MgSiO₃ glasses and melts at ambient and high pressure have been studied extensively using diverse experimental and theoretical methods. Here, we summarize these previous studies. Earlier Raman and infrared spectroscopy provided the vibrational density of state of MgSiO₃ glasses at ambient and high pressure (up to 80 GPa) (Kalampounias et al., 2009; Kubicki et al., 1992; e.g., McMillan, 1984; Shim and Catalli, 2009). Brillouin scattering studies have reported the elastic properties of MgSiO₃ melts at ambient pressure (e.g., VoThanh et al., 1996) and pressure-induced changes in the acoustic wave velocity of glassy analogs upon compression up to 203 GPa (e.g., Murakami and Bass, 2011; Sanchez-Valle and Bass, 2010). The local configurations in MgSiO₃ glasses have also been extensively investigated using high-resolution solid-state NMR techniques. ²⁹Si and ²⁵Mg MAS NMR studies have shown that the types of Q species and Mg local environments (i.e., MgO_x species), respectively (e.g., Davis et al., 2011; Gaudio et al., 2008; Libourel et al., 1992; Sen et al., 2009; Shimoda et al., 2007; Stebbins and McMillan, 1993). In addition, ¹⁷O MAS and 3QMAS NMR

studies revealed the specific oxygen configurations of MgSiO₃ glass, providing the details of connectivity in the glass network (e.g., Allwardt and Stebbins, 2004; Lee et al., 2016; Lee et al., 2003a). Synchrotron X-ray Raman scattering has shown that the formation of oxygen tricluster at high pressure above 20 GPa (Lee et al., 2008). A recent *in-situ* X-ray absorption study has revealed the in-situ density of MgSiO₃ glass under high pressure (up to 127 GPa) (Petitgirard et al., 2015).

Synchrotron or conventional X-ray and neutron scattering or diffraction have provided information regarding the average Si and Mg coordination numbers, distribution of Mg, and structural disorder in the MgSiO₃ glasses and melts at ambient and high pressure (e.g., Cormier and Cuello, 2011, 2013; Funamori et al., 2004; Wilding et al., 2004; Wilding et al., 2010). Reverse Monte Carlo modeling has been often used to fit the results of the scattering and diffraction studies for the glasses and melts (e.g., Cormier and Cuello, 2011; Kohara et al., 2011). Theoretical approaches such as classical and *ab-initio* (first-principle) molecular dynamics simulations have also provided information on the structure and properties, which are experimentally unachievable (Ghosh et al., 2014; e.g., Kubicki and Lasaga, 1991; Shimoda and Okuno, 2006; Stixrude and Karki, 2005; Wan et al., 2007; Zhao et al., 2014).

Previous studies on iron-bearing magnesium silicate glasses and melts. A relatively small number of spectroscopic and scattering studies have been carried out for iron-bearing MgSiO₃ glasses with important geochemical implications in the Earth's interior. The results of previous studies on iron-

bearing Mg-silicate glasses and melts at ambient and high pressures are shown in Table 4A-1.

Previous X-ray and neutron scattering studies of iron-bearing silicate glasses and melts. The structures of iron-bearing silicate glasses and melts (e.g., coordination number and bond length) have also been explored by X-ray and neutron scattering methods (e.g., Brown et al. 1995). Table 4A-2 summarizes the results of previous X-ray and neutron scattering studies on the coordination number and T-O distance in various iron-bearing silicate glasses and melts (Alderman et al., 2017a; Drewitt et al., 2013; Fleet et al., 1984; Henderson et al., 1984; Holland et al., 1999; Iwamoto et al., 1987; Johnson et al., 1999; Magini et al., 1984; Johnson, 1999 #1737; Waseda and Toguri, 1978).

Table 4-A1. The previous studies for iron-bearing Mg-silicate glasses and melts at ambient and high pressures

Composition	Methods	Sample	Pressure	References
(Mg _{0.95} Fe _{0.05})SiO ₃	Mössbauer	Glass	ambient P	Mysen et al., 1980
MgO-FeO-SiO ₂	Mössbauer	Glass	ambient P	Mysen et al., 1984
CaO-MgO-SiO ₂ with 1wt% Fe ₂ O ₃	XANES and EXAFS	Glass	ambient P	Farge et al., 2004
(Mg _{0.95} Fe _{0.05})SiO ₃	XES	Glass	~ 85 GPa	Nomura et al., 2011
(Mg _{0.8} Fe _{0.2})SiO ₃	XES	Glass	~ 135 GPa	Gu et al., 2012
(Mg _{0.9} Fe _{0.1})SiO ₃	Brillouin	Glass	~ 25 GPa	Liu and Lin, 2014
(Mg _{0.75} Fe _{0.25})SiO ₃ and (Mg _{0.5} Fe _{0.5})SiO ₃	XANES	Melt	ambient P	Alderman et al., 2017

Table 4-A2. Cation-oxygen distances [d(T-O)] and coordination number in iron-bearing silicate glasses and melts from X-ray and neutron scattering studies.

Composition	T (K)	Bond	Coordination number	d(T-O) (Å)	Reference
<i>X-ray scattering</i>					
NaFeSi ₃ O ₈	298	T-O	4	1.7	Henderson et al. (1984)
KFeSi ₃ O ₈	298	T-O	4	1.7	Fleet et al. (1984)
Fe ₂ SiO ₄	1573	Si-O	4	1.62	Waseda and Toguri (1978)
Fe ₂ SiO ₄	1623	Si-O	4	1.64	Drewitt et al. (2013)
		Fe-O	4.8	2.04	
FeSiO ₃	1683	Si-O	4	1.66	
		Fe-O	5.1	2.08	
CaFeSi ₂ O ₆	1623	Si-O	4	1.64	
	300	Si-O	4	1.64	
0.2Fe ₂ O ₃ ·0.8(Na ₂ O·2SiO ₂)	298	Fe-O	5.88	1.96	Iwamoto et al. (1987)
Na ₂ O-Fe ₂ O ₃ -B ₂ O ₃ -SiO ₂	298	Fe-O	3.7~4.0	1.87~1.95	Magini et al. (1984)
Fe ₂ SiO _{4+x}	2200	Fe-O	4.4~4.7	2.05	Alderman et al. (2017)
<i>Neutron scattering</i>					
Na ₂ O-Fe ₂ O ₃ -SiO ₂	298	Si-O	3.6	1.63	Holland et al. (1999)
		Fe-O	4~5	1.9~2.0	
NaFeSi ₂ O ₆	298	Si-O	4	1.61	Weigel et al. (2008)
		Fe-O	4.4	1.89	
		Na-O	7	2.3	
0.3Na ₂ O-0.2Fe ₂ O ₃ -0.5SiO ₂	298	Fe-O	4	1.885	Johnson et al. (1999)

4A-2. Ferric-ferrous ratio of iron-bearing magnesium silicate glasses

4A-2.1. Mössbauer spectroscopy

The iron redox ratios ($\text{Fe}^{3+}/\Sigma\text{Fe}$) of the studied samples were obtained using Mössbauer spectroscopy (see Section 4.2.2 for the detailed experimental procedure). Figure 4A-1 shows the Mössbauer spectra at 298 K for $(\text{Mg}_{1-X}\text{Fe}_X)\text{SiO}_3$ glasses with $X = 0.1$ and 0.2 , which were synthesized in an Ar environment ($\log f\text{O}_2 = -2.3 \pm 0.2$). Note that the spectra for $X = 0.05$ could not be obtained due to the small amount of Fe. The spectra were fitted using two doublets representing Fe^{2+} (which exhibit maxima near 0 and 2 mm/s) and Fe^{3+} (which exhibit maxima near -0.1 and 0.1 mm/s). The isomer shifts of Fe^{2+} are 0.75 for $X = 0.1$ and 1.05 for $X = 0.2$, and those of Fe^{3+} are 0.49 for $X = 0.1$ and 1.05 for $X = 0.2$. The quadrupolar splittings of Fe^{2+} are 1.97 for $X = 0.1$ and 1.94 for $X = 0.2$, and those of Fe^{3+} are 1.00 for $X = 0.1$ and 1.26 for $X = 0.2$. The $\text{Fe}^{3+}/\Sigma\text{Fe}$ ratios were calculated from the areas of the Fe^{3+} absorption doublets relative to the total area, indicating that the $\text{Fe}^{3+}/\Sigma\text{Fe}$ values were calculated to be about 0.23 for $X = 0.1$ and about 0.26 for $X = 0.2$.

4A-2.2. Prediction from previous Mössbauer and XANES studies

The iron redox ratios of iron-bearing silicate glasses depend on the oxygen fugacity ($\log f\text{O}_2$), temperature, pressure, and the composition of the glasses (e.g., Jayasuriya et al., 2004; Kilinc et al., 1983; Mysen and Virgo, 1985; Virgo and Mysen, 1985). Previous Mössbauer and XANES studies report that the $\text{Fe}^{3+}/\Sigma\text{Fe}$ values of iron-bearing magnesium silicate glasses equilibrated under atmospheric conditions ($\log f\text{O}_2 = -0.68$) vary with the composition (i.e., SiO_2 contents) (Mysen et al., 1980; Mysen et al., 1984). In particular, the iron-bearing magnesium metasilicate glass (i.e., MgSiO_3) with 2.4 mol% FeO

(similar composition to the currently studied glasses) has the $\text{Fe}^{3+}/\Sigma\text{Fe}$ value of 0.22 for the sample melted in air at 1585°C (Mysen et al., 1980). The $\text{Fe}^{3+}/\Sigma\text{Fe}$ values of iron-bearing magnesium silicate glasses, whose composition is slightly off the MgSiO_3 stoichiometry (i.e., $\text{MgO}:\text{SiO}_2 = 1:1.2$ and $1:1.4$), are about 0.5 when the glasses are equilibrated in air at 1550°C (Mysen et al., 1984). As shown in Figure 4A-2(A), The change in $\text{Fe}^{3+}/\Sigma\text{Fe}$ with varying oxygen fugacity for the 5 wt% Fe_2O_3 -bearing magnesium silicate glasses with $\text{MgO}:\text{SiO}_2 = 1:1.2$ and $1:1.4$ has been reported: the $\text{Fe}^{3+}/\Sigma\text{Fe}$ decreases dramatically from 0.5 to 0.2 as $\log f\text{O}_2$ decreases from -0.68 (in air) to -2.5 (similar to the Ar environment). A recent XANES study has also reported that the $\text{Fe}^{3+}/\Sigma\text{Fe}$ values of $\text{Fe}_{0.5}\text{Mg}_{0.5}\text{SiO}_3$ glasses with varying oxygen fugacities decreases from 0.46 ($\log f\text{O}_2 = -0.3$) to 0.1 ($\log f\text{O}_2 = -7.5$) (Alderman et al., 2017b). Note that the ferric iron (Fe^{3+}) is dominant (i.e., $\text{Fe}^{3+}/\Sigma\text{Fe} > 0.8$) in the iron-bearing sodium silicate glasses melted under atmospheric conditions and the iron redox ratio does not change significantly with a decrease in $\log f\text{O}_2$ from 0 to -4 (e.g., Dingwell and Virgo, 1987; Dunaeva et al., 2012; Mysen and Virgo, 1985), as shown in Figure 4A-2(B). As the $(\text{Mg}_{1-x}\text{Fe}_x)\text{SiO}_3$ glasses in the current study were melted in an Ar environment ($\log f\text{O}_2 = -2.3 \pm 0.2$, measured using a Y_2O_3 -doped ZrO_2 oxygen sensor), it is expected that the $\text{Fe}^{3+}/\Sigma\text{Fe}$ values of the $(\text{Mg}_{1-x}\text{Fe}_x)\text{SiO}_3$ glasses in the current study are about 0.22 ± 0.07 , which is consistent with the measured $\text{Fe}^{3+}/\Sigma\text{Fe}$ in current study. Our previous study has shown that the estimated $\text{Fe}^{3+}/\Sigma\text{Fe}$ values (about 0.89 ± 0.04) of iron-bearing sodium silicate glasses from previous studies are consistent with the $\text{Fe}^{3+}/\Sigma\text{Fe}$ value measured using Mössbauer spectroscopy.

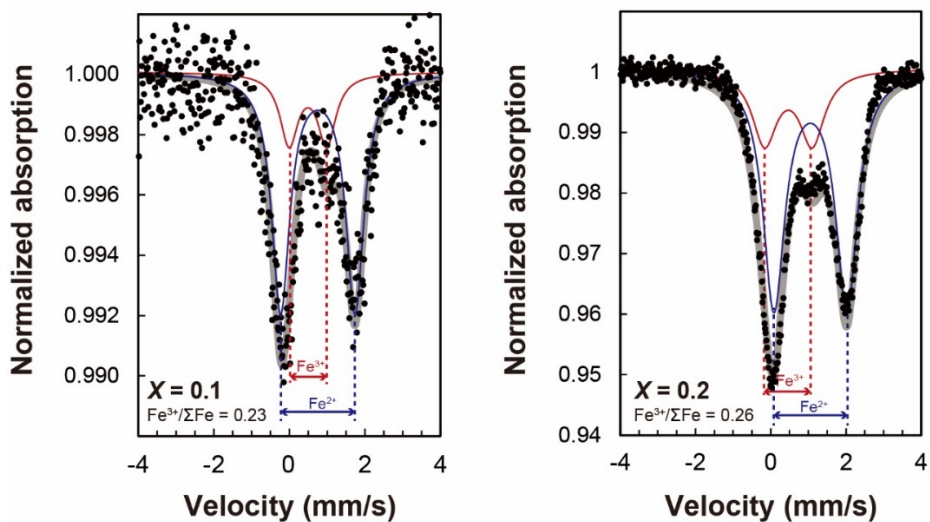


Figure 4A-1. Mössbauer spectra (dots) and fitting results (gray thick line) of ^{57}Fe in $(Mg_{1-x}Fe_x)SiO_3$ glasses with $X = 0.1$ (left) and 0.2 (right) at 298 K. The spectra were fitted with two doublets, corresponding to Fe^{3+} (red line) and Fe^{2+} (blue line).

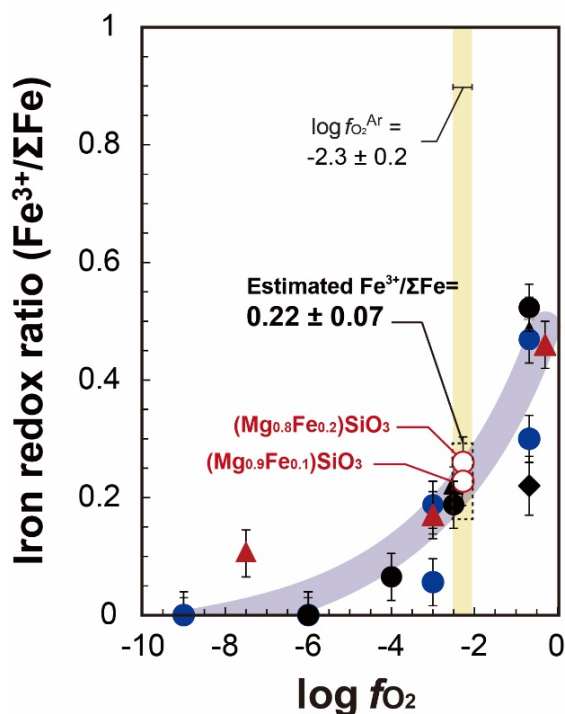


Figure 4A-2. Iron redox ratios ($\text{Fe}^{3+}/\Sigma\text{Fe}$) in iron-bearing magnesium silicate and aluminosilicate glasses with varying oxygen fugacities [closed symbols; black circles and triangles represent MgO-FeO-SiO₂ glasses (Mysen et al., 1984), black diamonds represent the (Mg_{0.95}Fe_{0.05})SiO₃ glasses, and blue circles represent MgO-Al₂O₃-Fe₂O₃-SiO₂ glasses (Mysen et al., 1985), as reported in previous Mössbauer studies. The $\text{Fe}^{3+}/\Sigma\text{Fe}$ values of (Mg_{0.5}Fe_{0.5})SiO₃ glasses from X-ray absorption spectroscopy are also shown (red closed triangles)(Alderman et al., 2017). Open circles represent the directly measured $\text{Fe}^{3+}/\Sigma\text{Fe}$ values using Mössbauer spectroscopy for the glasses studied here ($X = 0.1$ and 0.2). The yellow shaded area corresponds to the measured oxygen fugacity of an Ar environment in the furnace studied here. The blue line is a guide to the eye.

4A-3. Simulation of ^{29}Si MAS NMR spectra for $(\text{Mg,Fe})\text{SiO}_3$ glasses

To better understand the changes in the local configurations around silicon for $(\text{Mg,Fe})\text{SiO}_3$ glasses with increasing X_{Fe} , the spectral analysis through detailed fitting and/or simulations of the ^{29}Si MAS NMR spectra is necessary. Explicit information on the distribution of Q species, however, is difficult to obtain because of severe overlap among the Q species, even for iron-free MgSiO_3 glass. Despite the uncertainty, the simulation results are shown here in order to provide a *qualitative* trend and relevant discussion on iron distribution in silicate glass networks.

Iron-free MgSiO_3 glass. The ^{29}Si MAS NMR spectrum for iron-free MgSiO_3 glass was simulated with three Gaussian functions representing Q^1 , Q^2 , and Q^3 . The peak positions and their relative fractions of the Q species are based on the results of a previous study (Sen et al., 2009): the peak positions for Q^1 , Q^2 , and Q^3 are at approximately -75, -84, and -95.5 ppm, respectively, and the relative fractions for those species are about 25%, 49%, and 26%, respectively. Note that the presence of a small fraction of Q^4 species in MgSiO_3 glass, which was considered for fitting in the previous study, was not included in the simulation in the current study.

Iron-bearing Mg silicate glasses. Observed changes in the ^{29}Si MAS NMR spectra with increasing X_{Fe} could stem from three distinct processes, including, a peak shift potentially due to the paramagnetic effect, a peak broadening due to preferential iron enrichment into a specific domain, and finally, an increase in the degree of polymerization. It is difficult to consider these three factors simultaneously. Thus, we performed the simulation of the

^{29}Si MAS NMR spectra considering each 'extreme' scheme where only a single factor contributes to the changes in the NMR spectra with X_{Fe} . We note that the fits and simulation results are largely non-unique. The simulations of ^{29}Si MAS NMR spectra for $(\text{Mg,Fe})\text{SiO}_3$ glasses in the current study, hence, were performed to obtain *qualitative* trend.

Scheme 1) Simulation of ^{29}Si MAS NMR spectra for $(\text{Mg,Fe})\text{SiO}_3$ glasses with the changes in peak position with increasing X_{Fe} due to the paramagnetic effect.

In this scheme, we assumed that the peak positions for Q^1 , Q^2 , and Q^3 species may shift as the X_{Fe} increases. For $(\text{Mg,Fe})\text{SiO}_3$ glasses, each peak is modeled as a combination of the Gaussian and the Lorentzian functions, taking into consideration the paramagnetic effect. The ratio of the area under the Lorentzian part to that under the Gaussian part tends to increase with increasing X_{Fe} from $\sim 20\%$ ($X_{\text{Fe}} = 0.1$) to 35% ($X_{\text{Fe}} = 0.2$). As X_{Fe} increases, upon simulation, the peak positions of the Q species were allowed to change. The results show that the Q^2 position shifts from -84 ppm ($X_{\text{Fe}} = 0$) to -90.5 ppm ($X_{\text{Fe}} = 0.2$), and Q^3 position also significantly changes from -95.5 ppm ($X_{\text{Fe}} = 0$) to -108 ppm ($X_{\text{Fe}} = 0.2$), respectively, while the position of the Q^1 species (~ 74 ppm) does not change significantly. In addition, the peak widths of all Q species dramatically increase with increasing X_{Fe} : among them, the degree of peak broadening for the Q^1 peak with X_{Fe} is significantly larger than those for other two species (i.e., Q^2 and Q^3). This shows that the relative fractions of Q species are similar to those at iron-free MgSiO_3 glasses and do not change noticeably. While such a scheme (with a pronounced iron-induced peak shift) may in part contribute to the observed spectral changes, the estimated magnitude of peak shift up to ~ 13 ppm for Q^3 species with increasing X_{Fe} up

to 0.2 is not likely. Furthermore, whereas the current simulation shows a larger peak shift for the highly polymerized species, a larger peak shift is expected for the less polymerized species (i.e., Q¹) in the iron-bearing Mg silicate glasses.

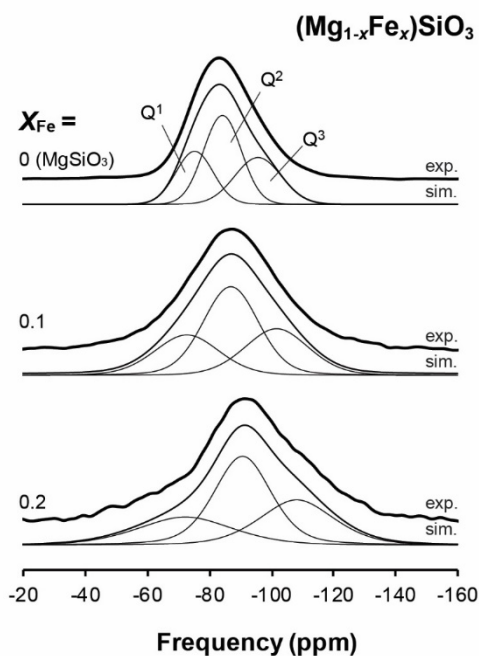


Figure 4A-3. ²⁹Si MAS NMR spectra and simulation results for (Mg,Fe)SiO₃ glasses with varying X_{Fe}. Upon simulation peak positions of each Q species are allowed to vary with increasing X_{Fe}. The thick lines represent the observed spectra and thin lines refer to simulation results using the combination of the Gaussian and Lorentzian functions.

Scheme 2) Simulation of ^{29}Si MAS NMR spectra for $(\text{Mg,Fe})\text{SiO}_3$ glasses with two components representing the domain with a larger fraction of iron and that with a smaller fraction of iron.

The changes in ^{29}Si MAS NMR spectra can be explained by the preferential interaction between iron and the local configuration of Si units, as discussed Section 4.3.1. If the iron is heterogeneously distributed (less than 1 nm length-scale) in glass network, there are two distinct domains: the domain with a larger fraction of iron and that with a smaller fraction of iron. Therefore, the ^{29}Si MAS NMR spectrum for $X_{\text{Fe}} = 0.2$ was simulated with two components representing the domain with a larger fraction of iron and that with a smaller fraction of iron, as shown in Figure 4A-4. The current mechanism can partly account for the preferential broadening in the spectra.

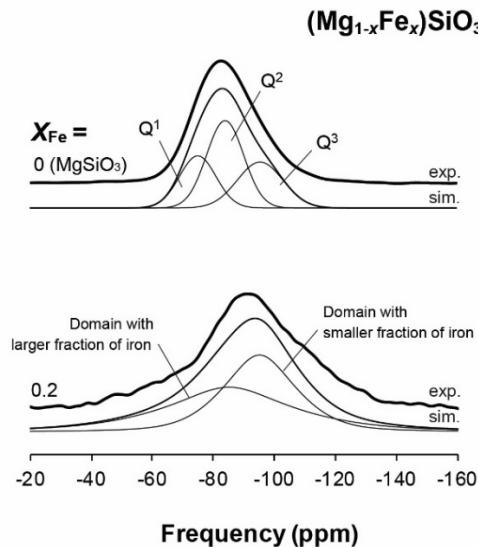


Figure 4A-4. ^{29}Si MAS NMR spectra and simulation results for $(\text{Mg,Fe})\text{SiO}_3$ glasses with $X_{\text{Fe}} = 0$ and 0.2. The simulation was based on the scheme 2.

Scheme 3) Simulation of ^{29}Si MAS NMR spectra for $(\text{Mg,Fe})\text{SiO}_3$ glasses at the constant peak position of each Q species with increasing X_{Fe} .

Here, the simulation was performed with the assumption of the constant peak position of each Q species. Furthermore, the formation of Q^4 is also taken into consideration (Figure 4A-5): the peak positions of Q species are fixed at -75 ppm for Q^1 , -84 ppm for Q^2 , and -95.5 ppm for Q^3 , respectively. For iron-bearing glasses, the presence of Q^4 (at -109 ppm) is considered. Taking into consideration of the preferential paramagnetic broadening in less polymerized Q species, we also assumed that the degree of an increase in the peak width of Q^1 and Q^2 species was larger than that of Q^3 and Q^4 species. The simulation results show that the fractions of Q^3 and Q^4 increase significantly with increasing X_{Fe} : Q^3 fraction is $\sim 26\%$ for $X_{\text{Fe}} = 0$, $\text{Q}^3 + \text{Q}^4$ fraction is $\sim 37\%$ for $X_{\text{Fe}} = 0.1$ and $\sim 54\%$ for $X_{\text{Fe}} = 0.2$, respectively. These results suggest that the degree of polymerization noticeably increases with increasing X_{Fe} . For the current scheme, the changes in the ^{29}Si MAS NMR spectra stem from the increase in the fraction of highly polymerized Q species and thus the degree of polymerization. Although the current mechanism accounts partly for the observed spectral changes, the significant increase in the Q^3 and Q^4 fractions obtained by the current simulation is much larger than those expected from the compositional change (i.e., Mg^{2+} substitution of Fe^{2+}). Therefore, if the current scheme would be valid, the observed NMR spectra for the iron-bearing silicate glasses (for the survived spins beyond r_c) may not be representative of the entire glass structure.

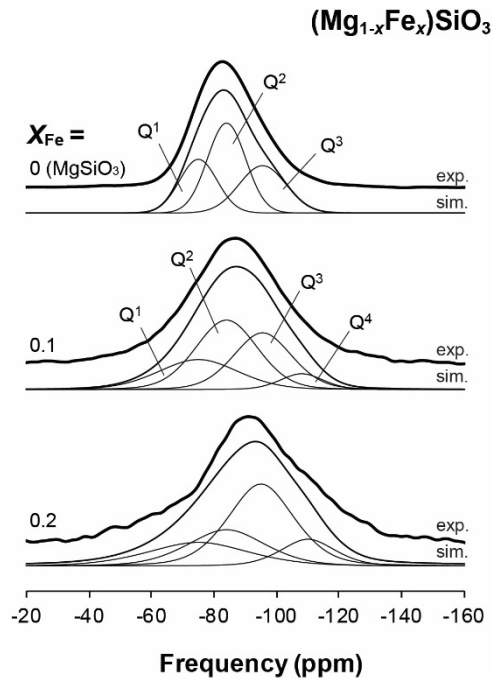


Figure 4A-5. ²⁹Si MAS NMR spectra and simulation results for (Mg,Fe)SiO₃ glasses with varying X_{Fe} . The simulation was performed with the constant peak position for Q species. The thick lines represent the observed spectra and thin lines refer to results fitted using the combination of the Gaussian and Lorentzian functions.

Based on the three simulation results, it is expected that the changes in the ²⁹Si MAS NMR spectra can be explained by an increase in the fractions of highly polymerized Q species (with an addition of Fe²⁺), and may reflect a decrease in the fraction of less polymerized Q species, mostly due to a preferential interaction between Fe²⁺ and NBO. The current interpretation is consistent with results from the ¹⁷O NMR spectra where the NBO fraction decreases with increasing X_{Fe} .

4A-4. Qualitative estimation of changes in the oxygen configurations for iron-bearing magnesium silicate glasses with varying X_{Fe}

The simulation of ^{17}O 3QMAS NMR spectra was performed from the total isotropic projection of the ‘sheared’ ^{17}O 3QMAS NMR spectra where the oxygen sites are better resolved (see Figures 4A-6 and 4A-7). Here, we sheared the 2D spectra using the shearing factor of $\sim 15 \mu\text{s}$. Thus, the Mg-O-Si and Si-O-Si could be effectively resolved in the isotropic projection. As shown in Figure 4A-6, the calibrated Si-O-Si fraction increases with increasing X_{Fe} from $\sim 35\%$ at $X_{\text{Fe}} = 0$ to $\sim 47\%$ for $X_{\text{Fe}} = 0.2$, respectively. The results revealed that the apparent degree of polymerization increases with increasing X_{Fe} for the observed nuclear spins (i.e., nuclear spins far away from iron).

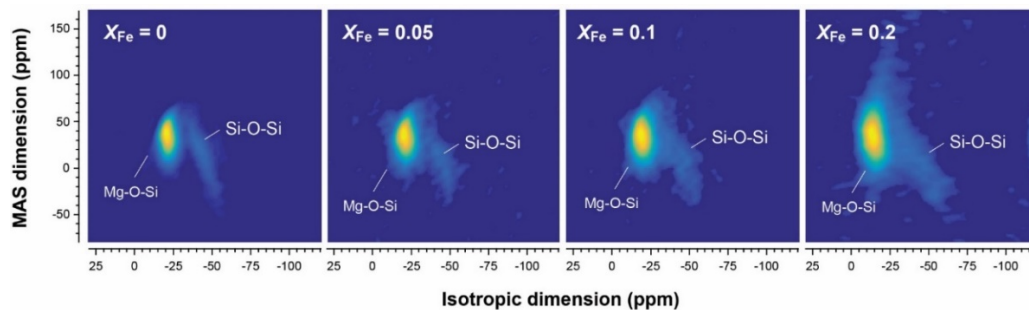


Figure 4A-6. “Sheared” 2D ^{17}O 3QMAS NMR spectra of iron-bearing magnesium silicate glasses with varying X_{Fe} [= $\text{Fe}/(\text{Mg} + \text{Fe})$], as labeled. To obtain better resolution of oxygen sites in the spectra, the 2D spectra were sheared with shearing factor of $\sim 15 \mu\text{s}$.

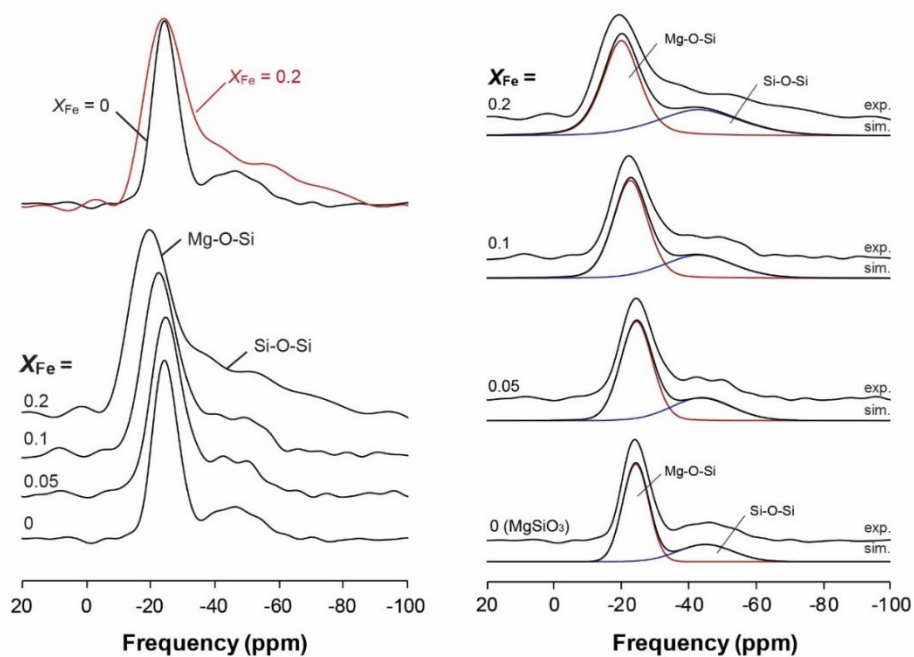


Figure 4A-7. Total isotropic projection of ‘sheared’ ^{17}O 3QMAS NMR spectra with varying X_{Fe} . Comparison of total isotropic projection for ‘sheared’ ^{17}O 3QMAS NMR spectra for $X_{\text{Fe}} = 0$ (black) and $X_{\text{Fe}} = 0.2$ (red) is also shown. Note that the spectrum at $X_{\text{Fe}} = 0.2$ was moved to align the spectra horizontally. The simulation was performed using the 2 Gaussian and 2 Lorentzian functions representing Mg-O-Si (red thin lines) and Si-O-Si (blue thin lines) (Right).

4A-5. Quantum chemical calculations of ^{29}Si and ^{17}O NMR chemical shifts for ^{44}Si cluster and Fe^{2+} -NBO

The ^{29}Si and ^{17}O chemical shielding tensors for silicon sites (^{44}Si) and NBO sites (i.e., Fe^{2+} -O-Si) of model cluster containing Fe^{2+} -NBO [i.e., $\text{Fe}^{2+}\text{Si}_3\text{O}_2\text{BO}_2\text{Fe-NBO}(\text{OH})_6$] (as shown in Figure 4-10A) are calculated using quantum chemical calculations with Gaussian03 (Frisch et al., 2004) to predict the peak positions of the silicon and oxygen sites in iron-bearing magnesium silicate glasses. For comparison, we also obtained the ^{29}Si chemical shielding tensors of ^{44}Si and ^{17}O chemical shielding tensors of Mg^{2+} - and Ca^{2+} -NBO for optimized model clusters [i.e., $\text{Mg}^{2+}\text{Si}_3\text{O}_2\text{BO}_2\text{Fe-NBO}(\text{OH})_6$ in Figure 4-10B and $\text{Ca}^{2+}\text{Si}_3\text{O}_2\text{BO}_2\text{Fe-NBO}(\text{OH})_6$ in Figure 4-10C, respectively]. Note that the hydrogen in the model cluster has been added to the dangling bond of the model cluster in Figure 4-10 to balance the charge of the clusters. This routine has been used to calculate the structure of small- and finite-size model clusters in typical quantum chemical calculations (e.g., Lee, 2004; Lee et al., 2001; Li et al., 2009). The geometries of the model clusters were optimized at the Hartree-Fock (HF) level of theory with a 6-31G(d) basis, and the ^{29}Si and ^{17}O NMR chemical shielding tensors were calculated using the gauge-independent atomic orbital (GIAO) methods at the B3LYP level of theory with 6-311+G(2d, p) basis. Tables 4A-3 and 4A-4 present the calculated ^{29}Si chemical shielding tensors of ^{44}Si clusters and ^{17}O isotropic chemical shielding tensors of M^{2+} -NBO (where M is network modifying cation), showing that the ^{29}Si and ^{17}O chemical shielding tensors depend on the types of network-modifying cations. Note that the NMR chemical shielding tensor can be used to calculate the isotropic chemical shift (δ_{iso}) from the difference between the chemical shielding tensor (C. S.) of the reference [tetramethylsilane (TMS) for ^{29}Si and $\text{H}_2\text{O}(l)$ for ^{17}O , respectively] and that of

the cluster: the C. S. values of TMS and H₂O(*l*) as a reference are 327.4 ppm and 287.5 ppm, respectively (Wasylishen and Bryce, 2002). Note that the calculated ²⁹Si and ¹⁷O chemical shielding tensors could not accurately represent the actual NMR chemical shielding tensor because our quantum chemical calculations are performed for the model cluster.

The trend of the calculated ¹⁷O chemical shielding tensor for the model clusters with various network-modifying cations is similar to the trend of the experimental results. The estimated ¹⁷O δ_{iso} for Fe²⁺-NBO (~ -730 ppm) from calculations of the ¹⁷O chemical shielding tensor for Fe²⁺-NBO (~1017 ppm) in a model cluster is significantly more shielded than that of the ¹⁷O δ_{iso} for Mg²⁺-NBO (~43 ppm). On the basis of the preliminary quantum chemical calculations for ¹⁷O δ_{iso} with varying types of network-modifying cation, the observed changes in the 1D ¹⁷O NMR signal from Mg-O-Si and Si-O-Si (Figure 4-6) with increasing iron concentration are not due to the Fe²⁺-NBO.

Table 4A-3. NMR parameters of silicon sites (^{29}Si chemical shielding) in model clusters calculated from quantum chemical calculations.

^{41}Si cluster	Chemical shielding (ppm)
$\text{Fe}^{2+}\text{Si}_3\text{O}_2\text{BO}_2\text{Fe-NBO}(\text{OH})_6$	
Si(1)	413.95
Si(2)	407.78
Si(3)	417.59
$\text{Mg}^{2+}\text{Si}_3\text{O}_2\text{BO}_2\text{Fe-NBO}(\text{OH})_6$	
Si(1)	401.76
Si(2)	396.69
Si(3)	403.19
$\text{Ca}^{2+}\text{Si}_3\text{O}_2\text{BO}_2\text{Fe-NBO}(\text{OH})_6$	
Si(1)	418.19
Si(2)	408.55
Si(3)	414.93

Table 4A-4. Equilibrium geometries and NMR parameters of non-bridging oxygen sites (NBO, up) and bridging oxygen sites (BO, bottom) in model clusters calculated from quantum chemical calculations.

NBO cluster		M-O (Å)	¹⁷ O chemical shielding tensor (ppm)	
$\text{Fe}^{2+}\text{Si}_3\text{O}_2^{\text{BO}}\text{O}_2^{\text{Fe-NBO}}(\text{OH})_6$				
O(1)	Fe-NBO	1.881	1009.92	
O(2)	Fe-NBO	1.860	1024.59	
$\text{Mg}^{2+}\text{Si}_3\text{O}_2^{\text{BO}}\text{O}_2^{\text{Fe-NBO}}(\text{OH})_6$				
O(1)	Mg-NBO	1.883	259.66	
O(2)	Mg-NBO	1.837	227.81	
$\text{Ca}^{2+}\text{Si}_3\text{O}_2^{\text{BO}}\text{O}_2^{\text{Fe-NBO}}(\text{OH})_6$				
O(1)	Ca-NBO	2.235	128.19	
O(2)	Ca-NBO	2.194	139.75	
BO cluster		average Si-O (Å)	Si-O-Si (deg)	¹⁷ O chemical shielding tensor (ppm)
$\text{Fe}^{2+}\text{Si}_3\text{O}_2^{\text{BO}}\text{O}_2^{\text{Fe-NBO}}(\text{OH})_6$				
O(3)	Si-O-Si	1.646	130.11	220.82
O(4)	Si-O-Si	1.643	121.23	212.99
$\text{Mg}^{2+}\text{Si}_3\text{O}_2^{\text{BO}}\text{O}_2^{\text{Fe-NBO}}(\text{OH})_6$				
O(3)	Si-O-Si	1.641	139.99	220.51
O(4)	Si-O-Si	1.643	121.44	212.42
$\text{Ca}^{2+}\text{Si}_3\text{O}_2^{\text{BO}}\text{O}_2^{\text{Fe-NBO}}(\text{OH})_6$				
O(3)	Si-O-Si	1.645	135.39	217.03
O(4)	Si-O-Si	1.650	124.24	216.41

4A-6. Chemical compositions of $(\text{Mg}_{1-x}\text{Fe}_x)\text{SiO}_3$ glasses determined by energy-dispersive X-ray spectrometer (EDS)

Table 4A-5 shows the nominal compositions and estimated compositions of $(\text{Mg}_{1-x}\text{Fe}_x)\text{SiO}_3$ glasses with varying X_{Fe} [$=\text{Fe}/(\text{Mg}+\text{Fe})$] using energy-dispersive X-ray spectrometer (EDS) and ICP-AES. A polished thick section of the glasses (coated with carbon) is used. A field emission scanning electron microprobe (FE-SEM; JEOL JSM-7100F in Seoul National University) equipped with EDS (Oxford INCA) system was utilized to obtain back-scattered electron (BSE) images and quantitative information about chemical composition of glasses. Each glass composition was obtained at five different points on the glass surface. The chemical compositions of glasses estimated by EDS technique are within the errors of $\sim 1\%$, indicating that the composition of resulting glasses is expected to be close to nominal values. Note that the measured FeO^{T} of $X_{\text{Fe}} = 0.2$ glass is slightly lower than nominal value due to the iron loss from the sample to Pt crucible.

Table 4A-5. Nominal compositions and estimated composition for MgO-FeO-SiO₂ glasses with varying X_{Fe} [=Fe/(Mg + Fe)] using EDS and ICP-AES

Composition	Nominal composition (mol%)			EDS analysis (mol%)*			
	MgO	FeO _{total}	SiO ₂	MgO	FeO ^T	SiO ₂	
X_{Fe}	0.05	47.5	2.5	50.0	47 (1)	2 (1)	51 (1)
	0.1	45.0	5.0	50.0	45 (1)	5 (1)	50 (1)
	0.2	40.0	10.0	50.0	40 (1)	9 (1)	51 (1)

Composition	Nominal composition (mol%)		ICP analysis (mol%)		EDS analysis (mol%)		
	MgO	FeO ^T	MgO	FeO ^T	MgO	FeO ^T	
X_{Fe}	0.05	95.0	5.0	95 (1)	5 (1)	95 (1)	5 (1)
	0.1	90.0	10.0	90 (1)	10 (1)	90 (1)	10 (1)
	0.2	80.0	20.0	81 (1)	19 (1)	81 (1)	19 (1)

*Number in parentheses denotes the 2 standard error [e.g., 47 (1) = 47 ± 1].

REFERENCES

- Adam, G. and Gibbs, J.H. (1965) On temperature dependence of cooperative relaxation properties in glass-forming liquids. *J. Chem. Phys.* 43, 139-146.
- Alderman, O.L.G., Lazareva, L., Wilding, M.C., Benmore, C.J., Heald, M., Johnson, C.E., Johnson, J.A., Hah, H.Y., Sendelbach, S., Tamalonis, A., Skinner, L.B., Parise, J.B. and Weber, J.K.R. (2017a) Local structural variation with oxygen fugacity in $\text{Fe}_2\text{SiO}_{4+x}$ fayalitic iron silicate melts. *Geochim. Cosmochim. Acta* 203, 15-36.
- Alderman, O.L.G., Wilding, M.C., Tamalonis, A., Sendelbach, S., Heald, S.M., Benmore, C.J., Johnson, C.E., Johnson, J.A., Hah, H.Y. and Weber, J.K.R. (2017b) Iron K-edge X-ray absorption near-edge structure spectroscopy of aerodynamically levitated silicate melts and glasses. *Chem. Geol.* 453, 169-185.
- Allwardt, J.R. and Stebbins, J.F. (2004) Ca-Mg and K-Mg mixing around non-bridging O atoms in silicate glasses: An investigation using ^{17}O MAS and 3QMAS NMR. *Am. Mineral.* 89, 777-784.
- Andrault, D., Petitgirard, S., Lo Nigro, G., Devidal, J.L., Veronesi, G., Garbarino, G. and Mezouar, M. (2012) Solid-liquid iron partitioning in Earth's deep mantle. *Nature* 487, 354-357.
- Armbruster, T., Geiger, C.A. and Lager, G.A. (1992) Single-crystal X-ray structure study of synthetic pyrope almandine garnets at 100 K and 293 K. *Am. Mineral.* 77, 512-521.
- Baert, K., Meulebroeck, W., Wouters, H., Cosyns, P., Nys, K., Thienpont, H. and Terryn, H. (2011) Using Raman spectroscopy as a tool for the detection of iron in glass. *Journal of Raman Spectroscopy* 42, 1789-1795.
- Bakmutov, V.I. (2008) The ^{29}Si T_1 and T_2 NMR relaxation in porous paramagnetic material $\text{SiO}_2\text{-MnO-Al}_2\text{O}_3$. *Solid State Nucl. Magn. Reson.* 34, 197-201.
- Bakmutov, V.I., Shpeizer, B.G., Prosvirin, A.V., Dunbar, K.R. and Clearfield, A. (2009) On ^{29}Si NMR relaxation as a structural criterion for studying paramagnetic supermicroporous silica-based materials: silica-based materials incorporating Mn^{2+} ions into the silica matrix of $\text{SiO}_2\text{-Al}_2\text{O}_3\text{-MnO}$. *Solid State Nucl. Magn. Reson.* 36, 129-136.

- Begaudeau, K., Morizet, Y., Florian, P., Paris, M. and Mercier, J.C. (2012) Solid-state NMR analysis of Fe-bearing minerals: Implications and applications for Earth sciences. *Eur. J. Mineral.* 24, 535-550.
- Bertini, I., Luchinat, C. and Parigi, G. (2002) Magnetic susceptibility in paramagnetic NMR. *Prog. Nucl. Magn. Reson. Spectrosc.* 40, 249-273.
- Bertini, I., Luchinat, C., Parigi, G. and Pierattelli, R. (2005) NMR spectroscopy of paramagnetic metalloproteins. *Chembiochem* 6, 1536-1549.
- Calas, G. and Petiau, J. (1983) Coordination of iron in oxide glasses through high-resolution K-edge spectra: Information from the pre-edge. *Solid State Commun.* 48, 625-629.
- Chemtob, S.M., Jolliff, B.L., Rossman, G.R., Eiler, J.M. and Arvidson, R.E. (2010) Silica coatings in the Ka'u Desert, Hawaii, a Mars analog terrain: A micromorphological, spectral, chemical, and isotopic study. *Journal of Geophysical Research-Planets* 115.
- Chemtob, S.M. and Rossman, G.R. (2014) Timescales and mechanisms of formation of amorphous silica coatings on fresh basalts at Kilauea Volcano, Hawai'i. *Journal of Volcanology and Geothermal Research* 286, 41-54.
- Chemtob, S.M., Rossman, G.R. and Stebbins, J.F. (2012) Natural hydrous amorphous silica: Quantitation of network speciation and hydroxyl content by ^{29}Si MAS NMR and vibrational spectroscopy. *Am. Mineral.* 97, 203-211.
- Chevrel, M.O., Baratoux, D., Hess, K.U. and Dingwell, D.B. (2014) Viscous flow behavior of tholeiitic and alkaline Fe-rich martian basalts. *Geochim. Cosmochim. Acta* 124, 348-365.
- Cochain, B., Neuville, D.R., de Ligny, D., Malki, M., Testemale, D., Pinet, O. and Richet, P. (2013) Dynamics of iron-bearing borosilicate melts: Effects of melt structure and composition on viscosity, electrical conductivity and kinetics of redox reactions. *J. Non-Cryst. Solids* 373, 18-27.
- Cochain, B., Neuville, D.R., Henderson, G.S., McCammon, C.A., Pinet, O. and Richet, P. (2012) Effects of the iron content and redox state on the structure of sodium borosilicate glasses: A raman, Mössbauer and boron k-edge XANES spectroscopy study. *J. Am. Ceram. Soc.* 95, 962-971.

- Cormier, L. and Cuello, G.J. (2011) Mg coordination in a MgSiO₃ glass using neutron diffraction coupled with isotopic substitution. *Phys. Rev. B* 83.
- Cormier, L. and Cuello, G.J. (2013) Structural investigation of glasses along the MgSiO₃-CaSiO₃ join: Diffraction studies. *Geochim. Cosmochim. Acta* 122, 498-510.
- Cukierman, M. and Uhlmann, D.R. (1974) Effects of iron oxidation-state on viscosity, lunar composition 15555. *J. Geophys. Res.* 79, 1594-1598.
- Dai, X., Gan, X.P. and Zhang, C.F. (2003) Viscosities of Fe_nO-MgO-SiO₂ and Fe_nO-MgO-CaO-SiO₂ slags. *Transactions of Nonferrous Metals Society of China* 13, 1451-1453.
- Davies, G.F. (1985) Heat deposition and retention in a solid planet growing by impacts. *Icarus* 63, 45-68.
- Davis, M.C., Sanders, K.J., Grandinetti, P.J., Gaudio, S.J. and Sen, S. (2011) Structural investigations of magnesium silicate glasses by ²⁹Si 2D Magic-Angle Flipping NMR. *J. Non-Cryst. Solids* 357, 2787-2795.
- Di Genova, D., Hess, K.U., Crevrel, M.O. and Dingwell, D.B. (2016) Models for the estimation of Fe³⁺/Fe_{tot} ratio in terrestrial and extraterrestrial alkali- and iron-rich silicate glasses using Raman spectroscopy. *Am. Mineral.* 101, 943-952.
- Di Genova, D., Kolzenburg, S., Wiesmaier, S., Dallanave, E., Neuville, D.R., Hess, K.U. and Dingwell, D.B. (2017a) A compositional tipping point governing the mobilization and eruption style of rhyolitic magma. *Nature* 552, 235-238.
- Di Genova, D., Vasseur, J., Hess, K.U., Neuville, D.R. and Dingwell, D.B. (2017b) Effect of oxygen fugacity on the glass transition, viscosity and structure of silica- and iron-rich magmatic melts. *J. Non-Cryst. Solids* 470, 78-85.
- Dingwell, D. and Virgo, D. (1988) Viscosity-oxidation state relationship for hedenbergitic melt, *Carnegie Institution of Washington Year Book*, pp. 48-53.
- Dingwell, D.B. (1991) Redox viscometry of some Fe-bearing silicate melts. *Am. Mineral.* 76, 1560-1562.
- Dingwell, D.B., Brearley, M. and Dickinson, J.E. (1988) Melt densities in the Na₂O-FeO-Fe₂O₃-SiO₂ system and the partial molar volume of tetrahedrally-coordinated ferric iron in silicate melts. *Geochim. Cosmochim. Acta* 52, 2467-2475.

- Dingwell, D.B., Courtial, P., Giordano, D. and Nichols, A.R.L. (2004) Viscosity of peridotite liquid. *Earth Planet. Sci. Lett.* 226, 127-138.
- Dingwell, D.B. and Virgo, D. (1987) The effect of oxidation-state on the viscosity of melts in the system $\text{Na}_2\text{O}-\text{FeO}-\text{Fe}_2\text{O}_3-\text{SiO}_2$. *Geochim. Cosmochim. Acta* 51, 195-205.
- Dobson, D.P. and Brodholt, J.P. (2005) Subducted banded iron formations as a source of ultralow-velocity zones at the core-mantle boundary. *Nature* 434, 371-374.
- Drewitt, J.W.E., Sanloup, C., Bytchkov, A., Brassamin, S. and Hennet, L. (2013) Structure of $(\text{Fe}_x\text{Ca}_{1-x}\text{O})_y(\text{SiO}_2)_{1-y}$ liquids and glasses from high-energy x-ray diffraction: Implications for the structure of natural basaltic magmas. *Phys. Rev. B* 87, 224201.
- Dubinsky, E.V. and Stebbins, J.F. (2006) Quench rate and temperature effects on framework ordering in aluminosilicate melts. *Am. Mineral.* 91, 753-761.
- Dunaeva, E.S., Uspenskaya, I.A., Pokholok, K.V., Minin, V.V., Efimov, N.N., Ugolkova, E.A. and Brunet, E. (2012) Coordination and RedOx ratio of iron in sodium-silicate glasses. *J. Non-Cryst. Solids* 358, 3089-3095.
- Farges, F., Lefrere, Y., Rossano, S., Berthereau, A., Calas, G. and Brown, G.E. (2004) The effect of redox state on the local structural environment of iron in silicate glasses: a molecular dynamics, combined XAFS spectroscopy, and bond valence study. *J. Non-Cryst. Solids* 344, 176-188.
- Farnan, I., Grandinetti, P.J., Baltisberger, J.H., Stebbins, J.F., Werner, U., Eastman, M.A. and Pines, A. (1992) Quantification of the disorder in network-modified silicate glasses. *Nature* 358, 31-35.
- Farnan, I. and Stebbins, J.F. (1990) High-temperature Si-29 NMR investigation of solid and molten silicates. *J. Am. Chem. Soc.* 112, 32-39.
- Fleet, M.E., Herzberg, C.T., Henderson, G.S., Crozier, E.D., Osborne, M.D. and Scarfe, C.M. (1984) Coordination of Fe, Ga and Ge in high-pressure glasses by Mössbauer, Raman and x-ray absorption-spectroscopy, and geological implications. *Geochim. Cosmochim. Acta* 48, 1455-1466.
- Florian, P., Vermillion, K.E., Grandinetti, P.J., Farnan, I. and Stebbins, J.F. (1996) Cation distribution in mixed alkali disilicate glasses. *J. Am. Chem. Soc.* 118, 3493-3497.

- Fridleifsson, I.B., Furnes, H. and Atkins, F.B. (1982) Subglacial volcanics - on the control of magma chemistry on pillow dimensions. *Journal of Volcanology and Geothermal Research* 13, 103-117.
- Frisch, M.J., Trucks, G.W. and others, a. (2004) Gaussian 03, Gaussian, Inc., Wallingford, Connecticut.
- Funamori, N., Yamamoto, S., Yagi, T. and Kikegawa, T. (2004) Exploratory studies of silicate melt structure at high pressures and temperatures by in situ X-ray diffraction. *Journal of Geophysical Research-Solid Earth* 109.
- Gaudio, S.J., Sen, S. and Lesher, C.E. (2008) Pressure-induced structural changes and densification of vitreous MgSiO₃. *Geochim. Cosmochim. Acta* 72, 1222-1230.
- Geiger, C.A., Merwin, L. and Sebald, A. (1992) Structural investigation of pyrope garnet using temperature-dependent FTIR and ²⁹Si and ²⁷Al MAS NMR spectroscopy. *Am. Mineral.* 77, 713-717.
- Ghosh, D.B., Karki, B.B. and Stixrude, L. (2014) First-principles molecular dynamics simulations of MgSiO₃ glass: Structure, density, and elasticity at high pressure. *Am. Mineral.* 99, 1304-1314.
- Giordano, D. and Dingwell, D.B. (2003) Non-Arrhenian multicomponent melt viscosity: A model. *Earth Planet. Sci. Lett.* 208, 337-349.
- Grey, C.P. and Dupre, N. (2004) NMR studies of cathode materials for lithium-ion rechargeable batteries. *Chem. Rev.* 104, 4493-4512.
- Grey, C.P. and Lee, Y.J. (2003) Lithium MAS NMR studies of cathode materials for lithium-ion batteries. *Solid State Sciences* 5, 883-894.
- Grimmer, A.R., Vonlanpe, F., Magi, M. and Lippmaa, E. (1983) Solid-state high-resolution ²⁹Si NMR of silicates: Influence of Fe²⁺ in olivines. *Z. Chem.* 23, 343-344.
- Gu, C., Catalli, K., Grocholski, B., Gao, L.L., Alp, E., Chow, P., Xiao, Y.M., Cynn, H., Evans, W.J. and Shim, S.H. (2012) Electronic structure of iron in magnesium silicate glasses at high pressure. *Geophysical Research Letters* 39.
- Hartman, J.S., Narayanan, A., Rigby, S.S., Sliwinski, D.R., Halden, N.M. and Bain, A.D. (2007) Heterogeneities in sol-gel-derived paramagnetics-doped forsterites and willemites: Electron microprobe analysis and stretched-exponential ²⁹Si MAS NMR spin-lattice relaxation studies. *Can. J. Chem.* 85, 56-65.

- Hartman, J.S. and Sherriff, B.L. (1991) ^{29}Si MAS NMR of the aluminosilicate mineral kyanite: Residual dipolar coupling to ^{27}Al and nonexponential spin-lattice relaxation. *J. Phys. Chem.* 95, 7575-7579.
- Hazen, R.M. and Finger, L.W. (1989) High-pressure crystal-chemistry of andradite and pyrope: Revised procedures for high-pressure diffraction experiments. *Am. Mineral.* 74, 352-359.
- Henderson, G.S., Fleet, M.E. and Bancroft, G.M. (1984) An x-ray-scattering study of vitreous KFeSi_3O_8 and $\text{NaFeSi}_3\text{O}_8$ and reinvestigation of vitreous SiO_2 using quasi-crystalline modeling. *J. Non-Cryst. Solids* 68, 333-349.
- Hernlund, J.W. and Jellinek, A.M. (2010) Dynamics and structure of a stirred partially molten ultralow-velocity zone. *Earth Planet. Sci. Lett.* 296, 1-8.
- Holland, D., Mekki, A., Gee, I.A., McConville, C.F., Johnson, J.A., Johnson, C.E., Appleyard, P. and Thomas, M. (1999) The structure of sodium iron silicate glass: A multi-technique approach. *J. Non-Cryst. Solids* 253, 192-202.
- Irfune, T. (1994) Absence of an aluminous phase in the upper part of the Earth's lower mantle. *Nature* 370, 131-133.
- Iwamoto, N., Umesaki, N. and Atsumi, T. (1987) EXAFS and x-ray-diffraction studies of iron ions in a $0.2(\text{Fe}_2\text{O}_3) \cdot 0.8(\text{Na}_2\text{O} \cdot 2\text{SiO}_2)$ glass. *J. Mater. Sci. Lett.* 6, 271-273.
- Jackson, W.E., Farges, F., Yeager, M., Mabrouk, P.A., Rossano, S., Waychunas, G.A., Solomon, E.I. and Brown, G.E. (2005) Multi-spectroscopic study of Fe(II) in silicate glasses: Implications for the coordination environment of Fe(II) in silicate melts. *Geochim. Cosmochim. Acta* 69, 4315-4332.
- Jayasuriya, K.D., O'Neill, H.S., Berry, A.J. and Campbell, S.J. (2004) A Mössbauer study of the oxidation state of Fe in silicate melts. *Am. Mineral.* 89, 1597-1609.
- Ji, F.Z., Sichen, D. and Seetharaman, S. (1998) Experimental studies of viscosities in $\text{Fe}_n\text{O-MgO-SiO}_2$ and $\text{Fe}_n\text{O-MnO-SiO}_2$ slags. *Ironmaking & Steelmaking* 25, 309-316.
- Johnson, J.A., Johnson, C.E., Holland, D., Mekki, A., Appleyard, P. and Thomas, M.F. (1999) Transition metal ions in ternary sodium silicate glasses: a Mössbauer and neutron study. *J. Non-Cryst. Solids* 246, 104-114.

- Kalampounias, A.G., Nasikas, N.K. and Papatheodorou, G.N. (2009) Glass formation and structure in the MgSiO_3 - Mg_2SiO_4 pseudobinary system: From degraded networks to ioniclike glasses. *J. Chem. Phys.* 131.
- Katsura, T. and Ito, E. (1996) Determination of Fe-Mg partitioning between perovskite and magnesiowustite. *Geophysical Research Letters* 23, 2005-2008.
- Kelley, K.A. and Cottrell, E. (2009) Water and the oxidation state of subduction zone magmas. *Science* 325, 605-607.
- Kelsey, K.E., Stebbins, J.F., Singer, D.M., Brown, G.E., Mosenfelder, J.L. and Asimow, P.D. (2009) Cation field strength effects on high pressure aluminosilicate glass structure: Multinuclear NMR and La XAFS results. *Geochim. Cosmochim. Acta* 73, 3914-3933.
- Kilinc, A., Carmichael, I.S.E., Rivers, M.L. and Sack, R.O. (1983) The ferric-ferrous ratio of natural silicate liquids equilibrated in air. *Contrib. Mineral. Petrol.* 83, 136-140.
- Kim, H.-I., Sur, J.C. and Lee, S.K. (2016) Effect of iron content on the structure and disorder of iron-bearing sodium silicate glasses: A high-resolution ^{29}Si and ^{17}O solid-state NMR study. *Geochim. Cosmochim. Acta* 173, 160-180.
- Kim, J., Ilott, A.J., Middlemiss, D.S., Chernova, N.A., Pinney, N., Morgan, D. and Grey, C.P. (2015) ^2H and ^{27}Al solid-state nmr study of the local environments in al-doped 2-line ferrihydrite, goethite, and lepidocrocite. *Chem. Mater.* 27, 3966-3978.
- Kim, J., Nielsen, U.G. and Grey, C.P. (2008) Local environments and lithium adsorption on the iron oxyhydroxides lepidocrocite ($\gamma\text{-FeOOH}$) and goethite ($\alpha\text{-FeOOH}$): A H-2 and Li-7 solid-state MAS NMR study. *J. Am. Chem. Soc.* 130, 1285-1295.
- Kirkpatrick, R.J., Dunn, T., Schramm, C.M., Smith, K.A., Oestrike, R. and Turner, G. (1983) Magic-angle spinning nuclear magnetic resonance spectroscopy of silicate glasses: A review, in: Walgreen, G.E., Reeves, A.G. (Eds.), *Structure and bonding in non-crystalline solids*. Plenum Press, New York, pp. 303-328.
- Kirkpatrick, R.J., Oestrike, R., Weiss, C.A., Smith, K.A. and Oldfield, E. (1986) High-resolution ^{27}Al and ^{29}Si NMR-spectroscopy of glasses and crystals along the join $\text{CaMgSi}_2\text{O}_6$ - $\text{CaAl}_2\text{SiO}_6$. *Am. Mineral.* 71, 705-711.

- Koehler, J. and Meiler, J. (2011) Expanding the utility of NMR restraints with paramagnetic compounds: Background and practical aspects. *Prog. Nucl. Magn. Reson. Spectrosc.* 59, 360-389.
- Kohara, S., Akola, J., Morita, H., Suzuya, K., Weber, J.K.R., Wilding, M.C. and Benmore, C.J. (2011) Relationship between topological order and glass forming ability in densely packed enstatite and forsterite composition glasses. *P. Natl. Acad. Sci. USA* 108, 14780-14785.
- Kubicki, J.D., Hemley, R.J. and Hofmeister, A.M. (1992) Raman and infrared study of pressure-induced structural-changes in MgSiO_3 , $\text{CaMgSi}_2\text{O}_6$, and CaSiO_3 glasses. *Am. Mineral.* 77, 258-269.
- Kubicki, J.D. and Lasaga, A.C. (1991) Molecular-dynamics simulations of pressure and temperature effects on MgSiO_3 and Mg_2SiO_4 melts and glasses. *Phys. Chem. Miner.* 17, 661-673.
- Lange, R.A. and Carmichael, I.S.E. (1989) Ferric-ferrous equilibria in $\text{Na}_2\text{O-FeO-Fe}_2\text{O}_3\text{-SiO}_2$ melts: Effects of analytical techniques on derived partial molar volumes. *Geochim. Cosmochim. Acta* 53, 2195-2204.
- Le Losq, C., Neuville, D.R., Florian, P., Henderson, G.S. and Massiot, D. (2014) The role of Al^{3+} on rheology and structural changes in sodium silicate and aluminosilicate glasses and melts. *Geochim. Cosmochim. Acta* 126, 495-517.
- Lee, S.K. (2004) Structure of silicate glasses and melts at high pressure: Quantum chemical calculations and solid-state NMR. *J. Phys. Chem. B* 108, 5889-5900.
- Lee, S.K. (2005) Microscopic origins of macroscopic properties of silicate melts and glasses at ambient and high pressure: Implications for melt generation and dynamics. *Geochim. Cosmochim. Acta* 69, 3695-3710.
- Lee, S.K. (2011) Simplicity in melt densification in multicomponent magmatic reservoirs in Earth's interior revealed by multinuclear magnetic resonance. *P. Natl. Acad. Sci. USA* 108, 6847-6852.
- Lee, S.K., Kim, H.-I., Kim, E.J., Mun, K.Y. and Ryu, S. (2016) Extent of disorder in magnesium aluminosilicate glasses: Insights from ^{27}Al and ^{17}O NMR. *J. Phys. Chem. C* 120, 737-749.
- Lee, S.K., Lin, J.F., Cai, Y.Q., Hiraoka, N., Eng, P.J., Okuchi, T., Mao, H.K., Meng, Y., Hu, M.Y., Chow, P., Shu, J., Li, B., Fukui, H., Lee, B.H., Kim, H.N. and Yoo, C.S.

- (2008) X-ray Raman scattering study of MgSiO₃ glass at high pressure: implication for triclustered MgSiO₃ melt in Earth's mantle. P. Natl. Acad. Sci. USA 105, 7925-7929.
- Lee, S.K., Musgrave, C.B., Zhao, P.D. and Stebbins, J.F. (2001) Topological disorder and reactivity of borosilicate glasses: Quantum chemical calculations and ¹⁷O and ¹¹B NMR study. J. Phys. Chem. B 105, 12583-12595.
- Lee, S.K., Mysen, B.O. and Cody, G.D. (2003a) Chemical order in mixed-cation silicate glasses and melts. Phys. Rev. B 68.
- Lee, S.K. and Stebbins, J.F. (2003a) Nature of cation mixing and ordering in Na-Ca silicate glasses and melts. J. Phys. Chem. B 107, 3141-3148.
- Lee, S.K. and Stebbins, J.F. (2003b) O atom sites in natural kaolinite and muscovite: O-17 MAS and 3QMAS NMR study. Am. Mineral. 88, 493-500.
- Lee, S.K. and Stebbins, J.F. (2009) Effects of the degree of polymerization on the structure of sodium silicate and aluminosilicate glasses and melts: An ¹⁷O NMR study. Geochim. Cosmochim. Acta 73, 1109-1119.
- Lee, S.K., Stebbins, J.F., Weiss, C.A. and Kirkpatrick, R.J. (2003b) O-17 and Al-27 MAS and 3QMAS NMR study of synthetic and natural layer silicates. Chem. Mater. 15, 2605-2613.
- Lee, S.K. and Sung, S. (2008) The effect of network-modifying cations on the structure and disorder in peralkaline Ca-Na aluminosilicate glasses: O-17 3QMAS NMR study. Chem. Geol. 256, 326-333.
- Lee, S.K. and Weiss, C.A. (2008) Multiple oxygen sites in synthetic phyllosilicates with expandable layers: ¹⁷O solid-state NMR study. Am. Mineral. 93, 1066-1071.
- Lee, Y.J. and Grey, C.P. (2002) Determining the lithium local environments in the lithium manganates LiZn_{0.5}Mn_{1.5}O₄ and Li₂MnO₃ by analysis of the Li-6 MAS NMR spinning sideband manifolds. J. Phys. Chem. B 106, 3576-3582.
- Li, X., Zhao, H., Tang, M. and Liu, Y. (2009) Theoretical prediction for several important equilibrium Ge isotope fractionation factors and geological implications. Earth Planet. Sci. Lett. 287, 1-11.
- Libourel, G., Geiger, C.A., Merwin, L. and Sebald, A. (1992) ²⁹Si and ²⁷Al MAS-NMR spectroscopy of glasses in the system CaSiO₃-MgSiO₃-Al₂O₃. Chem. Geol. 96, 387-397.

- Liebske, C., Schmickler, B., Terasaki, H., Poe, B.T., Suzuki, A., Funakoshi, K., Ando, R. and Rubie, D.C. (2005) Viscosity of peridotite liquid up to 13 GPa: Implications for magma ocean viscosities. *Earth Planet. Sci. Lett.* 240, 589-604.
- Liu, J. and Lin, J.-F. (2014) Abnormal acoustic wave velocities in basaltic and (Fe, Al)-bearing silicate glasses at high pressures. *Geophysical Research Letters* 41, 8832-8839.
- Lussier, A.J., Aguiar, P.M., Michaelis, V.K., Kroeker, S. and Hawthorne, F.C. (2009) The occurrence of tetrahedrally coordinated Al and B in tourmaline: An ^{11}B and ^{27}Al MAS NMR study. *Am. Mineral.* 94, 785-792.
- Maekawa, H., Maekawa, T., Kawamura, K. and Yokokawa, T. (1991) The structural groups of alkali silicate-glasses determined from ^{29}Si MAS NMR. *J. Non-Cryst. Solids* 127, 53-64.
- Magini, M., Sedda, A.F., Licheri, G., Paschina, G., Piccaluga, G., Pinna, G. and Cocco, G. (1984) On the coordination of iron ions in sodium borosilicate glasses .1. A wide angle x-ray-diffraction investigation. *J. Non-Cryst. Solids* 65, 145-159.
- Magnien, V., Neuville, D.R., Cormier, L., Roux, J., Hazemann, J.L., Pinet, O. and Richet, P. (2006) Kinetics of iron redox reactions in silicate liquids: A high-temperature X-ray absorption and Raman spectroscopy study. *J. Nucl. Mater.* 352, 190-195.
- Mao, W.L., Mao, H.K., Sturhahn, W., Zhao, J., Prakapenka, V.B., Meng, Y., Shu, J., Fei, Y. and Hemley, R.J. (2006) Iron-rich post-perovskite and the origin of ultralow-velocity zones. *Science* 312, 564-565.
- McCarty, R.J., Palke, A.C., Stebbins, J.F. and Hartman, J.S. (2015) Transition metal cation site preferences in forsterite (Mg_2SiO_4) determined from paramagnetically shifted NMR resonances. *Am. Mineral.* 100, 1265-1276.
- McDonough, W.F. and Sun, S.S. (1995) The composition of the Earth. *Chem. Geol.* 120, 223-253.
- McMillan, P. (1984) A raman-spectroscopic study of glasses in the system CaO-MgO-SiO_2 . *Am. Mineral.* 69, 645-659.
- McMillan, P.F. and Wolf, G.H. (1995) Vibrational spectroscopy of silicate liquids. *Structure, Dynamics and Properties of Silicate Melts* 32, 247-315.

- McNamara, A.K., Garnero, E.J. and Rost, S. (2010) Tracking deep mantle reservoirs with ultra-low velocity zones. *Earth Planet. Sci. Lett.* 299, 1-9.
- Mercier, M., Di Muro, A., Giordano, D., Metrich, N., Lesne, P., Pichavant, M., Scaillet, B., Clocchiatti, R. and Montagnac, G. (2009) Influence of glass polymerisation and oxidation on micro-Raman water analysis in aluminosilicate glasses. *Geochim. Cosmochim. Acta* 73, 197-217.
- Murakami, M. and Bass, J.D. (2011) Evidence of denser MgSiO₃ glass above 133 gigapascal (GPa) and implications for remnants of ultradense silicate melt from a deep magma ocean. *P. Natl. Acad. Sci. USA* 108, 17286-17289.
- Murdoch, J.B., Stebbins, J.F. and Carmichael, I.S.E. (1985) High-resolution ²⁹Si NMR study of silicate and aluminosilicate glasses: The effect of network-modifying cations. *Am. Mineral.* 70, 332-343.
- Mysen, B. (1975) Partitioning of iron and magnesium between crystals and partial melts in peridotite upper mantle. *Contrib. Mineral. Petrol.* 52, 69-76.
- Mysen, B.O. (2006) The structural behavior of ferric and ferrous iron in aluminosilicate glass near meta-aluminosilicate joins. *Geochim. Cosmochim. Acta* 70, 2337-2353.
- Mysen, B.O. and Richet, P. (2018) *Silicate glasses and melts: Properties and structure*, 2nd ed. Elsevier, Amsterdam.
- Mysen, B.O., Seifert, F. and Virgo, D. (1980) Structure and redox equilibria of iron-bearing silicate melts. *Am. Mineral.* 65, 867-884.
- Mysen, B.O. and Virgo, D. (1985) Iron-bearing silicate melts: Relations between pressure and redox equilibria. *Phys. Chem. Miner.* 12, 191-200.
- Mysen, B.O. and Virgo, D. (1989) Redox equilibria, structure, and properties of Fe-bearing aluminosilicate melts: Relationships among temperature, composition, and oxygen fugacity in the system Na₂O-Al₂O₃-SiO₂-Fe-O. *Am. Mineral.* 74, 58-76.
- Mysen, B.O., Virgo, D., Neumann, E.R. and Seifert, F.A. (1985a) Redox equilibria and the structural states of ferric and ferrous iron in melts in the system CaO-MgO-Al₂O₃-SiO₂-Fe-O: Relationships between redox equilibria, melt structure and liquidus phase-equilibria. *Am. Mineral.* 70, 317-331.

- Mysen, B.O., Virgo, D., Scarfe, C.M. and Cronin, D.J. (1985b) Viscosity and structure of iron-bearing and aluminum-bearing calcium silicate melts at 1 atm. *Am. Mineral.* 70, 487-498.
- Mysen, B.O., Virgo, D. and Seifert, F.A. (1982) The structure of silicate melts: Implications for chemical and physical-properties of natural magma. *Rev. Geophys.* 20, 353-383.
- Mysen, B.O., Virgo, D. and Seifert, F.A. (1984) Redox equilibria of iron in alkaline-earth silicate melts: Relationships between melt structure, oxygen fugacity, temperature and properties of iron-bearing silicate liquids. *Am. Mineral.* 69, 834-847.
- Narayanan, A., Hartman, J.S. and Bain, A.D. (1995) Characterizing nonexponential spin-lattice relaxation in solid-state NMR by fitting to the stretched exponential. *J. Magn. Reson., Ser A* 112, 58-65.
- Neuvill, D.R. (2006) Viscosity, structure and mixing in (Ca, Na) silicate melts. *Chem. Geol.* 229, 28-41.
- Neuvill, D.R., Courtial, P., Dingwell, D.B. and Richet, P. (1993) Thermodynamic and rheological properties of rhyolite and andesite melts. *Contrib. Mineral. Petrol.* 113, 572-581.
- Neuvill, D.R., de Ligny, D. and Henderson, G.S. (2014) Advances in Raman Spectroscopy Applied to Earth and Material Sciences, in: Henderson, G.S., Neuvill, D.R., Downs, R.T. (Eds.), *Spectroscopic Methods in Mineralogy and Materials Sciences*, pp. 509-541.
- Neuvill, D.R. and Richet, P. (1991) Viscosity and mixing in molten (Ca, Mg) pyroxenes and garnets. *Geochim. Cosmochim. Acta* 55, 1011-1019.
- Nielsen, U.G., Majzlan, J. and Grey, C.P. (2008) Determination and quantification of the local environments in stoichiometric and defect jarosite by solid-state H-2 NMR spectroscopy. *Chem. Mater.* 20, 2234-2241.
- Nielsen, U.G., Paik, Y., Julmis, K., Schoonen, M.A.A., Reeder, R.J. and Grey, C.P. (2005) Investigating sorption on iron-oxyhydroxide soil minerals by solid-state NMR spectroscopy: A ⁶Li MAS NMR study of adsorption and absorption on goethite. *J. Phys. Chem. B* 109, 18310-18315.

- Ohtani, E. (1985) The primordial terrestrial magma ocean and its implication for stratification of the mantle. *Phys. Earth Planet. In.* 38, 70-80.
- Oldfield, E., Kinsey, R.A., Smith, K.A., Nichols, J.A. and Kirkpatrick, R.J. (1983) High-resolution NMR of inorganic solids - influence of magnetic centers on magic-angle sample-spinning lineshapes in some natural aluminosilicates. *J. Magn. Reson.* 51, 325-329.
- Palke, A.C. and Stebbins, J.F. (2011) Variable-temperature ^{27}Al and ^{29}Si NMR studies of synthetic forsterite and Fe-bearing Dora Maira pyrope garnet: Temperature dependence and mechanisms of paramagnetically shifted peaks. *Am. Mineral.* 96, 1090-1099.
- Palke, A.C., Stebbins, J.F., Frost, D.J. and McCammon, C.A. (2012) Incorporation of Fe and Al in MgSiO_3 perovskite: An investigation by ^{27}Al and ^{29}Si NMR spectroscopy. *Am. Mineral.* 97, 1955-1964.
- Palke, A.C., Stebbins, J.F., Geiger, C.A. and Tippelt, G. (2015) Cation order-disorder in Fe-bearing pyrope and grossular garnets: A ^{27}Al and ^{29}Si MAS NMR and ^{57}Fe Mössbauer spectroscopy study. *Am. Mineral.* 100, 536-547.
- Park, S.Y. and Lee, S.K. (2012) Structure and disorder in basaltic glasses and melts: Insights from high-resolution solid-state NMR study of glasses in diopside-Ca-tschermakite join and diopside-anorthite eutectic composition. *Geochim. Cosmochim. Acta* 80, 125-142.
- Park, S.Y. and Lee, S.K. (2016) Effects of difference in ionic radii on chemical ordering in mixed-cation silicate glasses: Insights from solid-state ^{17}O and ^6Li NMR of Li-Ba silicate glasses. *J. Am. Ceram. Soc.* 99, 3948-3956.
- Petitgirard, S., Malfait, W.J., Sinmyo, R., Kuppenko, I., Hennet, L., Harries, D., Dane, T., Burghammer, M. and Rubie, D.C. (2015) Fate of MgSiO_3 melts at core-mantle boundary conditions. *P. Natl. Acad. Sci. USA* 112, 14186-14190.
- Poulsen, S.L., Kocaba, V., Le Saout, G., Jakobsen, H.J., Scrivener, K.L. and Skibsted, J. (2009) Improved quantification of alite and belite in anhydrous Portland cements by ^{29}Si MAS NMR: Effects of paramagnetic ions. *Solid State Nucl. Magn. Reson.* 36, 32-44.
- Richtet, P. (1984) Viscosity and configurational entropy of silicate melts. *Geochim. Cosmochim. Acta* 48, 471-483.

- Richet, P., Nidaira, A., Neuville, D.R. and Atake, T. (2009) Aluminum speciation, vibrational entropy and short-range order in calcium aluminosilicate glasses. *Geochim. Cosmochim. Acta* 73, 3894-3904.
- Roskosz, M., Toplis, M.J., Neuville, D.R. and Mysen, B.O. (2008) Quantification of the kinetics of iron oxidation in silicate melts using Raman spectroscopy and assessment of the role of oxygen diffusion. *Am. Mineral.* 93, 1749-1759.
- Rossano, S., Ramos, A., Delaye, J.M., Creux, S., Filipponi, A., Brouder, C. and Calas, G. (2000) EXAFS and Molecular Dynamics combined study of CaO-FeO-2SiO₂ glass: New insight into site significance in silicate glasses. *Europhys. Lett.* 49, 597-602.
- Rost, S., Garnero, E.J., Williams, Q. and Manga, M. (2005) Seismological constraints on a possible plume root at the core-mantle boundary. *Nature* 435, 666-669.
- Sanchez-Valle, C. and Bass, J.D. (2010) Elasticity and pressure-induced structural changes in vitreous MgSiO₃-enstatite to lower mantle pressures. *Earth Planet. Sci. Lett.* 295, 523-530.
- Sanloup, C., Drewitt, J.W.E., Creppisson, C., Kono, Y., Park, C., McCammon, C., Hennet, L., Brassamin, S. and Bytchkov, A. (2013) Structure and density of molten fayalite at high pressure. *Geochim. Cosmochim. Acta* 118, 118-128.
- Sato, M. (1971) Electrochemical measurements and control of oxygen fugacity and other gaseous fugacities with solid electrolyte sensors, *Research techniques for high pressure and high temperature*. Springer, pp. 43-99.
- Schramm, C.M., Dejong, B. and Parziale, V.E. (1984) ²⁹Si magic angle spinning NMR-study on local silicon environments in amorphous and crystalline lithium silicates. *J. Am. Chem. Soc.* 106, 4396-4402.
- Schramm, S., Kirkpatrick, R.J. and Oldfield, E. (1983) Observation of high-resolution O-17 NMR spectra of inorganic solids. *J. Am. Chem. Soc.* 105, 2483-2485.
- Sen, S., Maekawa, H. and Papatheodorou, G.N. (2009) Short-range structure of invert glasses along the pseudo-binary join MgSiO₃-Mg₂SiO₄: Results from ²⁹Si and ²⁵Mg MAS NMR spectroscopy. *J. Phys. Chem. B* 113, 15243-15248.
- Sen, S. and Stebbins, J.F. (1994) Phase-separation, clustering, and fractal characteristics in glass: A magic-angle-spinning NMR spin-lattice relaxation study. *Phys. Rev. B* 50, 822-830.

- Sen, S. and Stebbins, J.F. (1995) Structural role of Nd³⁺ and Al³⁺ cations in SiO₂ glass: a ²⁹Si MAS NMR spin-lattice relaxation, ²⁷Al NMR and EPR study. *J. Non-Cryst. Solids* 188, 54-62.
- Shelby, J.E. (2005) Introduction to glass science and technology. Royal Society of Chemistry.
- Sherriff, B.L. and Hartman, J.S. (1985) Solid-state high-resolution ²⁹Si NMR of feldspars: Al-Si disorder and the effects of paramagnetic centers. *Can. Mineral.* 23, 205-212.
- Shim, S.-H. and Catalli, K. (2009) Compositional dependence of structural transition pressures in amorphous phases with mantle-related compositions. *Earth Planet. Sci. Lett.* 283, 174-180.
- Shimoda, K. and Okuno, M. (2006) Molecular dynamics study of CaSiO₃-MgSiO₃ glasses under high pressure. *J. Phys.-Condens. Ma.* 18, 6531-6544.
- Shimoda, K., Tobu, Y., Hatakeyama, M., Nemoto, T. and Saito, K. (2007) Structural investigation of Mg local environments in silicate glasses by ultra-high field Mg-25 3QMAS NMR spectroscopy. *Am. Mineral.* 92, 695-698.
- Sipowska, J.T., Atake, T., Mysen, B.O. and Richet, P. (2009) Entropy and structure of oxidized and reduced iron-bearing silicate glasses. *Geochim. Cosmochim. Acta* 73, 3905-3913.
- Spice, H., Sanloup, C., Cochain, B., de Grouchy, C. and Kono, Y. (2015) Viscosity of liquid fayalite up to 9 GPa. *Geochim. Cosmochim. Acta* 148, 219-227.
- Squyres, S.W., Arvidson, R.E., Ruff, S., Gellert, R., Morris, R.V., Ming, D.W., Crumpler, L., Farmer, J.D., Des Marais, D.J., Yen, A., McLennan, S.M., Calvin, W., Bell, J.F., Clark, B.C., Wang, A., McCoy, T.J., Schmidt, M.E. and de Souza, P.A. (2008) Detection of silica-rich deposits on Mars. *Science* 320, 1063-1067.
- Stebbins, J.F. (1995) Dynamics and structure of silicate and oxide melts: Nuclear magnetic resonance studies, in: Stebbins, J.F., McMillan, P.F., Dingwell, D.B. (Eds.), *Reviews in Mineralogy*. Mineralogical Society of America, Washington, D.C., pp. 191-246.
- Stebbins, J.F. (2008) Temperature effects on the network structure of oxide melts and their consequences for configurational heat capacity. *Chem. Geol.* 256, 80-91.

- Stebbins, J.F. (2017) Toward the wider application of Si-29 NMR spectroscopy to paramagnetic transition metal silicate minerals: Copper(II) silicates. *Am. Mineral.* 102, 2406-2414.
- Stebbins, J.F., Dubinsky, E.V., Kanehashi, K. and Kelsey, K.E. (2008) Temperature effects on non-bridging oxygen and aluminum coordination number in calcium aluminosilicate glasses and melts. *Geochim. Cosmochim. Acta* 72, 910-925.
- Stebbins, J.F. and Kelsey, K.E. (2009) Anomalous resonances in ^{29}Si and ^{27}Al NMR spectra of pyrope ($[\text{Mg,Fe}]_3\text{Al}_2\text{Si}_3\text{O}_{12}$) garnets: Effects of paramagnetic cations. *Phys. Chem. Chem. Phys.* 11, 6906-6917.
- Stebbins, J.F. and McMillan, P. (1993) Compositional and temperature effects on 5-coordinated silicon in ambient-pressure silicate-glasses. *J. Non-Cryst. Solids* 160, 116-125.
- Stebbins, J.F. and Xu, Z. (1997) NMR evidence for excess non-bridging oxygen in an aluminosilicate glass. *Nature* 390, 60-62.
- Stebbins, J.F. and Xue, X. (2014) NMR spectroscopy of inorganic Earth materials, in: Henderson, G.S., Neuville, D.R., Downs, R.T. (Eds.), *Reviews in Mineralogy and Geochemistry*. Mineralogical Society of America, Chantilly, Virginia, pp. 605-653.
- Stixrude, L. and Karki, B. (2005) Structure and freezing of MgSiO_3 liquid in Earth's lower mantle. *Science* 310, 297-299.
- Sumita, S., Morinaga, K. and Yanagase, T. (1983) Physical-properties and structure of binary ferrite melts. *Transactions of the Japan Institute of Metals* 24, 35-41.
- Sun, S.S. (1982) Chemical composition and origin of the earths primitive mantle. *Geochim. Cosmochim. Acta* 46, 179-192.
- Taylor, S.R. and Norman, M.D. (1990) Accretion of Differentiated Planetesimals to the Earth, in: Newsom, H.E., Jones, J.R. (Eds.), *Origin of the Earth*. Oxford University Press, New York, pp. 23-43.
- Timken, H.K.C., Schramm, S.E., Kirkpatrick, R.J. and Oldfield, E. (1987) Solid-state O-17 nuclear-magnetic-resonance spectroscopic studies of alkaline-earth metasilicates. *J. Phys. Chem.* 91, 1054-1058.
- Tonks, W.B. and Melosh, H.J. (1993) Magma ocean formation due to giant impacts. *Journal of Geophysical Research-Planets* 98, 5319-5333.

- Toplis, M.J., Dingwell, D.B. and Libourel, G. (1994) The effect of phosphorus on the iron redox ratio, viscosity, and density of an evolved ferro-basalt. *Contrib. Mineral. Petrol.* 117, 293-304.
- Toropov, N.A. and Bryantsev, B.A. (1965) *Structural Transformations in Glasses at High Temperatures*. Consultant Bureau, Moscow.
- Tse, D. and Hartmann, S.R. (1968) Nuclear spin-lattice relaxation via paramagnetic centers without spin diffusion. *Phys. Rev. Lett.* 21, 511-514.
- Virgo, D. and Mysen, B.O. (1985) The structural state of iron in oxidized vs reduced glasses at 1 atm: A ^{57}Fe Mössbauer study. *Phys. Chem. Miner.* 12, 65-76.
- VoThanh, D., Polian, A. and Richet, P. (1996) Elastic properties of silicate melts up to 2350 K from Brillouin scattering. *Geophysical Research Letters* 23, 423-426.
- Wan, J.T.K., Duffy, T.S., Scandolo, S. and Car, R. (2007) First-principles study of density, viscosity, and diffusion coefficients of liquid MgSiO_3 at conditions of the Earth's deep mantle. *Journal of Geophysical Research-Solid Earth* 112, B03208.
- Wang, Z.F., Cooney, T.F. and Sharma, S.K. (1995) In-situ structural investigation of iron-containing silicate liquids and glasses. *Geochim. Cosmochim. Acta* 59, 1571-1577.
- Waseda, Y. and Toguri, J.M. (1978) Structure of the molten FeO-SiO_2 system. *Metallurgical Transactions B-Process Metallurgy* 9, 595-601.
- Wasylishen, R.E. and Bryce, D.L. (2002) A revised experimental absolute magnetic shielding scale for oxygen. *J. Chem. Phys.* 117, 10061-10066.
- Waychunas, G.A., Brown, G.E., Ponader, C.W. and Jackson, W.E. (1988) Evidence from X-ray absorption for network-forming Fe^{2+} in molten alkali silicates. *Nature* 332, 251-253.
- Weigel, C., Cormier, L., Calas, G., Galois, L. and Bowron, D.T. (2008) Nature and distribution of iron sites in a sodium silicate glass investigated by neutron diffraction and EPSR simulation. *J. Non-Cryst. Solids* 354, 5378-5385.
- White, W.B. and Minser, D.G. (1984) Raman-spectra and structure of natural glasses. *J. Non-Cryst. Solids* 67, 45-59.
- Wicks, J.K., Jackson, J.M. and Sturhahn, W. (2010) Very low sound velocities in iron-rich $(\text{Mg,Fe})\text{O}$: Implications for the core-mantle boundary region. *Geophysical Research Letters* 37.

- Wilding, M.C., Benmore, C.J., Tangeman, J.A. and Sampath, S. (2004) Evidence of different structures in magnesium silicate liquids: coordination changes in forsterite- to enstatite-composition glasses. *Chem. Geol.* 213, 281-291.
- Wilding, M.C., Benmore, C.J. and Weber, J.K.R. (2010) Changes in the local environment surrounding magnesium ions in fragile MgO-SiO₂ liquids. *Epl* 89.
- Wilke, M., Farges, F., Partzsch, G.M., Schmidt, C. and Behrens, H. (2007) Speciation of Fe in silicate glasses and melts by in-situ XANES spectroscopy. *Am. Mineral.* 92, 44-56.
- Williams, Q. (1998) A correlation between ultra-low basal velocities in the mantle and hot spots. *Science* 281, 546-549.
- Wood, B.J. and Rubie, D.C. (1996) The effect of alumina on phase transformations at the 660-kilometer discontinuity from Fe-Mg partitioning experiments. *Science* 273, 1522-1524.
- Xue, X.Y., Stebbins, J.F. and Kanzaki, M. (1994) Correlations between ¹⁷O NMR parameters and local-structure around oxygen in high-pressure silicates: Implications for the structure of silicate melts at high pressure. *Am. Mineral.* 79, 31-42.
- Zhao, G., Mu, H.F., Tan, X.M., Wang, D.H. and Yang, C.L. (2014) Structural and dynamical properties of MgSiO₃ melt over the pressure range 200-500 GPa: Ab initio molecular dynamics. *J. Non-Cryst. Solids* 385, 169-174.
- Zhu, C., Veblen, D.R., Blum, A.E. and Chipera, S.J. (2006) Naturally weathered feldspar surfaces in the Navajo Sandstone aquifer, Black Mesa, Arizona: Electron microscopic characterization. *Geochim. Cosmochim. Acta* 70, 4600-4616.

Chapter 5. Extent of disorder in iron-bearing albite and anorthite melts: Insights from multi-nuclear (^{29}Si , ^{27}Al , and ^{17}O) solid-state NMR study of iron-bearing $\text{NaAlSi}_3\text{O}_8$ and $\text{CaAl}_2\text{Si}_2\text{O}_8$ glasses

Hyo-Im Kim and Sung Keun Lee

Submitted to Chemical Geology

ABSTRACT

Knowledge of the detailed structure of iron-bearing aluminosilicate glasses is essential to unraveling the effects of iron on the macroscopic properties of natural silicate glasses and melts. However, the local structures around the framework cations (such as Al and Si) and the extent of network polymerization in iron-bearing aluminosilicate glasses are not well understood. This is mainly because the high-resolution solid-state NMR - one of the effective probes of the structures of aluminosilicate glasses - has limited utility in delving into the local configurations of oxide glasses with paramagnetic elements (i.e., iron). Here, we use multi-nuclear (^{29}Si , ^{27}Al , and ^{17}O) high-resolution solid-state NMR to investigate the effect of iron content on the local structure around framework cations and oxygen species in $\text{Na}(\text{Al}_{1-x}\text{Fe}_x)\text{Si}_3\text{O}_8$ glasses with varying X [$= \text{Fe}/(\text{Al}+\text{Fe})$] ($\text{Fe}^{3+}/\Sigma\text{Fe} = \sim 0.8$), $\text{NaAlSi}_3\text{O}_8$ glasses with varying Fe_2O_3 ($\text{NaAlSi}_3\text{O}_8 + \text{Fe}_2\text{O}_3$, $\text{Fe}^{3+}/\Sigma\text{Fe} = \sim 0.5$),

and $\text{CaAl}_2\text{Si}_2\text{O}_8$ glasses with varying Fe_2O_3 ($\text{CaAl}_2\text{Si}_2\text{O}_8 + \text{Fe}_2\text{O}_3$, $\text{Fe}^{3+}/\Sigma\text{Fe} = \sim 0.3$).

The NMR results for $\text{Na}(\text{Al}_{1-x}\text{Fe}_x)\text{Si}_3\text{O}_8$ glasses reveal preferential interaction between Fe^{3+} and Si-rich framework and thus an extensive mixing between ^{29}Si and $^{57}\text{Fe}^{3+}$. The presence of a small amount of ^{27}Al in $\text{Na}(\text{Al}_{0.5}\text{Fe}_{0.5})\text{Si}_3\text{O}_8$ glass suggests that the extent of disorder around Al increases by Al- Fe^{3+} substitution. The NMR results for $\text{NaAlSi}_3\text{O}_8 + \text{Fe}_2\text{O}_3$ glasses suggest that Fe^{2+} interacts more strongly with Al-rich framework and reveal the presence of a non-negligible fraction of Na-NBO, confirming Fe^{2+} -induced structural disorder. The absence of ^{27}Al in $\text{NaAlSi}_3\text{O}_8 + \text{Fe}_2\text{O}_3$ glasses indicates that Fe^{3+} is more likely to form a highly-coordinated framework (i.e., $^{57}\text{Fe}^{3+}$) when excess Fe^{3+} is added to charge-balanced glasses. The NMR spectra for $\text{CaAlSi}_2\text{O}_8 + \text{Fe}_2\text{O}_3$ glasses showed an iron-induced increase in the ^{27}Al fraction and confirmed that the overall degree of disorder increases with increasing Fe_2O_3 content. The noble NMR results for iron-bearing aluminosilicate glasses revealed the nature of diverse aspect of iron-induced structural disorder, mainly characterized by the intermixing between Si and Fe^{3+} , preferential interaction between Al and Fe^{2+} , and formation of highly coordinated $^{57}\text{Fe}^{3+}$. The detailed iron-induced structural evolution is largely dependent on the composition of melts as well as the valence state of iron. The observed increase in the extent of structural disorder in charge-balanced Na- and Ca-aluminosilicate glasses with increasing Fe^{2+} and Fe^{3+} can account for the iron-induced decrease in viscosity of the corresponding iron-bearing aluminosilicate melts.

5.1. Introduction

Knowledge of the detailed structure of iron-bearing silicate and aluminosilicate glasses is essential to unraveling the effects of iron on the macroscopic properties of natural silicate melts and glasses in the Earth's surface and interior. For example, the structural role of iron and various aspects of structural disorder are known to control the melt viscosity (e.g., Bouhifd et al., 2004; Cukierman and Uhlmann, 1974; Dingwell et al., 1988; Dingwell and Virgo, 1987, 1988; Sehlke and Whittington, 2016; Spice et al., 2015): the viscosity tends to increase with an increase in network-forming Fe^{3+} when the iron content is constant (Di Genova et al., 2017; Dingwell, 1991; Osugi et al., 2013; Toplis et al., 1994). The viscosity decreases with increasing iron content when the estimated non-bridging oxygen per tetrahedral cation (NBO/T) from stoichiometry is constant (Chevrel et al., 2013; Dingwell et al., 1988; Mysen et al., 1985). The decrease in the viscosity at constant NBO/T has been attributed to an increase in the extent of topological and chemical disorder with increasing iron content (Kim and Lee, 2019; Kim et al., 2016b; e.g., Lee, 2005).

The local atomic configurations around iron (e.g., bond length of Si-O and Fe-O, coordination number, and the distortion of Fe-O polyhedra) in iron-bearing *silicate* glasses and melts have been obtained using Mössbauer spectroscopy, X-ray absorption spectroscopy (e.g., XANES and EXAFS), neutron and X-ray scattering, and Raman spectroscopy (e.g., Alderman et al., 2017a; Alderman et al., 2017b; Drewitt et al., 2013; Fleet et al., 1984; Henderson et al., 1984; Holland et al., 1999; Iwamoto et al., 1987; Johnson et al., 1999; Mysen et al., 1980; Mysen et al., 1984; Waseda and Toguri, 1978; Weigel et al., 2008). The cation-oxygen distances (e.g., Si-O and Fe^{3+} -O) in Na_2O - Fe_2O_3 - SiO_2 glasses have been obtained using X-ray and neutron diffraction methods,

showing that the Fe^{3+} -O distance decreases with increasing Fe^{3+} content in the $(\text{Na}_2\text{O})_{0.3}\cdot(\text{SiO}_2)_{0.7} - (\text{Na}_2\text{O})_{0.3}\cdot(\text{Fe}_2\text{O}_3)_{0.7}$ join (Holland et al., 1999; Johnson et al., 1999). Earlier studies for Na_2O - Fe_2O_3 - SiO_2 and CaO - FeO - SiO_2 glasses have shown that the average coordination number of Fe is higher than 4, suggesting the presence of highly-coordinated Fe (i.e., $^{5,6}\text{Fe}$) (Drewitt et al., 2013; Farges et al., 2004; Farges et al., 2005; Henderson et al., 1995; Iwamoto et al., 1987; Rossano et al., 2000). The decrease in the isomer shifts of the $\text{Na}_2\text{Si}_2\text{O}_5$ - Fe_2O_3 join with increasing Fe^{3+} content obtained from Mössbauer spectroscopy also indicates that the Fe^{3+} -O distance decreases with increasing Fe^{3+} (Dingwell and Virgo, 1988; Virgo et al., 1983). While there are considerable overlaps among Raman modes, the previous Raman studies for Na_2SiO_3 - $\text{NaFe}^{3+}\text{Si}_2\text{O}_6$ glasses have suggested that the structural role of Fe^{3+} changes with varying Na/Fe ratio (Mysen et al., 1980). Earlier studies of iron-bearing *silicate* glasses suggest that the degree of network polymerization increases with increasing Fe^{3+} , which is primarily considered as a network-former (similar with Al^{3+}) (Cochain et al., 2012; Farges et al., 2004; Hannoyer et al., 1992; Holland et al., 1999; Mysen et al., 1980; Mysen and Virgo, 1985). In contrast, the addition of network-modifying Fe^{2+} (similar with Mg^{2+}) would depolymerize the silicate network (Mao et al., 1973; Mysen and Virgo, 1978; Nolet, 1980; Rossano et al., 2000). It has been suggested that the coordination number of Fe^{3+} and Fe^{2+} varies from 4 to 6 depending on the composition of silicate glasses and melts (Alberto et al., 1996; Calas and Petiau, 1983; Farges et al., 2004; Farges et al., 2005; Jackson et al., 2005; Rossano et al., 2000; Waychunas et al., 1988).

Despite its being considered impossible to explore the structural details of iron-bearing glasses using solid-state NMR, recent NMR studies for iron-bearing *silicate* glasses (e.g., Na_2O - Fe_2O_3 - SiO_2 and MgO - FeO - SiO_2) have

revealed structural information (i.e., the topological disorder, extent of polymerization, and spatial distribution of Fe) (Kim and Lee, 2019; Kim et al., 2016b). These results show that an increase in Fe³⁺ in silicate glasses leads to an increase in the extent of polymerization. The type of oxygen site that preferentially interacts with iron depends on the valence state of the iron: specifically, the ¹⁷O NMR results indicate the presence of a moderate degree of preferential interaction between Fe²⁺ and non-bridging oxygen (NBO), as well as that between Fe³⁺ and bridging oxygen (BO) in the iron-bearing silicate glasses (Kim and Lee, 2019; Kim et al., 2016b).

The structure and disorder of iron-bearing *aluminosilicate* glasses are the key to understanding the properties of natural volcanic melts and glasses. In general, Al₂O₃ is the second most abundant oxide of natural silicate melts after SiO₂ (e.g., Philpotts, 1982; Winter, 2009). The concentration of Al₂O₃ in natural silicate magma can be as high as about 15 wt%, and, in particular, phonolitic melts contain ~20 wt% Al₂O₃ (Kelly et al., 2008; Mysen and Richet, 2018; Philpotts and Ague, 2009). Thus, understanding the local configurations around Al³⁺ in the aluminosilicate glasses and melts provides insight into the atomic structure of natural silicate glasses and melts. Because of their importance, the structural role and coordination environments of Al³⁺ in *iron-free* aluminosilicate melts and glasses have been extensively studied using diverse experimental techniques such as X-ray diffraction, Raman spectroscopy, and solid-state NMR (Allwardt et al., 2005a; Angeli et al., 2000; Cormier et al., 2003; Engelhardt et al., 1985; Lee et al., 2005; Lee et al., 2016; Lee and Stebbins, 2006; Lee and Sung, 2008; Mysen and Richet, 2018; Mysen and Toplis, 2007; Mysen et al., 1981; Neuville et al., 2004a; Neuville et al., 2008; Neuville et al., 2007; Park and Lee, 2014; Stebbins et al., 1999; Toplis et al., 1997). In particular, solid-state NMR provides element-specific and

quantitative information about the local environments around Al, revealing that the coordination number and structural role of Al³⁺ in iron-free aluminosilicate glasses strongly depend on the glass composition (e.g., Eckert, 1992; Kirkpatrick et al., 1986; Le Losq et al., 2014; Lee et al., 2016; Libourel et al., 1992; Murdoch et al., 1985; Oestrike et al., 1987; Park and Lee, 2018; Schramm et al., 1984; Stebbins and Xu, 1997). Recent progress in solid-state NMR techniques, including two-dimensional (2D) triple-quantum magic angle spinning (3QMAS) NMR, also allows us to unveil detailed structural information about the effect of composition on the atomic configurations in diverse oxide and silicate glasses (e.g., Allwardt and Stebbins, 2004; Florian et al., 2007; Le Losq et al., 2014; Lee and Ryu, 2018; Neuville et al., 2007; Sen et al., 2009; Stebbins, 2017a), including the complex multi-component silicate glasses corresponding to natural magma (Kelsey et al., 2008a; Lee et al., 2016; Lee et al., 2012a; Malfait et al., 2012; Neuville et al., 2008; Park and Lee, 2012; Park and Lee, 2014, 2018), high-pressure oxide/silicate glasses (Allwardt et al., 2005b; Allwardt et al., 2007; Kelsey et al., 2009; Lee, 2010; Lee et al., 2012b), and glasses with volatile components (Kim et al., 2018; Kim et al., 2016a; Morizet et al., 2010; Mysen, 2013; Xue, 2009).

Figure 5-1 illustrates a ternary composition diagram with SiO₂, Mⁿ⁺O_{n/2} (M refers to non-framework cations, such as Na⁺, Ca²⁺, and Fe²⁺), and Z₂O₃ [Z refers to framework cations (except SiO₂), such as Al³⁺ and Fe³⁺] as the respective vertices. Here, the ratio between Mⁿ⁺O_{n/2} and Z₂O₃ is one of the important factors determining the structural behavior of Al. For *iron-free* peralkaline glasses (Mⁿ⁺O_{n/2}/Al₂O₃ > 1), Al³⁺ is commonly 4-coordinated with a small amount of ^[5,6]Al for glasses with cations of high field strength (Z/r², where Z refers to the charge and r refers to the ionic radius), and the non-framework cations mainly act as a network-modifier. In this case, an increase

in Al content leads to a decrease in the fraction of NBO, indicating an increase in the extent of polymerization. On the other hand, a significant fraction of $^{[5,6]}\text{Al}$ exists in peraluminous glasses ($M^{n+}O_{n/2}/\text{Al}_2\text{O}_3 < 1$). The non-framework cations in peraluminous glasses preferentially act as charge-balancing cations, which do not tend to form NBO. In this case, an increase in Al content results in an increase in the fraction of $^{[5,6]}\text{Al}$. Along the charge-balanced join ($M^{n+}O_{n/2}/\text{Al}_2\text{O}_3 = 1$), the Al coordination number and structural role of non-framework cations are heavily dependent on the Z/r^2 of non-framework cations. In charge-balanced Na-aluminosilicate glasses, $^{[4]}\text{Al}$ is predominant and NBO is not observed. The glasses with high value of Z/r^2 (such as Ca^{2+} and Mg^{2+}), however, can contain a few percent of NBO fractions and $^{[5,6]}\text{Al}$ fractions, even though the nominal NBO/T (based on stoichiometry) is 0 in the charge-balanced join. Here, the non-framework cations in the charge-balanced aluminosilicate glasses with high Z/r^2 play a dual role as charge-balancing and network-modifying.

While detailed knowledge about the local configurations around Al and non-framework cations in *iron-free* aluminosilicate glasses has been systematically studied using various experimental techniques including solid-state NMR, the structure and disorder of *iron-bearing* aluminosilicate glasses are not well understood. In particular, the structural role and coordination number of Al and Fe in iron-bearing aluminosilicate glasses (in which Al and Fe coexist) still need to be explored. Considering the different ionic radii of Al^{3+} ($\sim 0.39 \text{ \AA}$ for $^{[4]}\text{Al}$) and Fe^{3+} ($\sim 0.49 \text{ \AA}$ for $^{[4]}\text{Fe}^{3+}$) with the same charge, an increase in Fe^{3+} content in aluminosilicate glasses would lead to structural perturbation of the local configuration around Al environments. This is because Al in the silicate glasses may compete with Fe^{3+} as a network-former. Further, if the overall glass composition becomes more peraluminous

$[M^{n+}O_{n/2} / (Al_2O_3 + Fe_2O_3) < 1]$ due to the addition of network-forming Fe^{3+} , the formation of highly coordinated Al and Fe^{3+} would be inevitable. In addition, the increase in network-modifying Fe^{2+} in aluminosilicate glasses may cause changes in the structure and disorder of aluminosilicate glasses including the Al coordination number. As the peralkalinity ($M^{n+}O_{n/2} / Z_2O_3$) increases with increasing Fe^{2+} in aluminosilicate glasses, the fraction of highly coordinated Al would decrease and the fraction of NBO would increase with increasing Fe^{2+} .

So far, there have been no direct experimental observations of changes in the local environments around cations and anions constituting aluminosilicate glasses (i.e., Al, O, and Si) with increasing iron content. This is because it is challenging to unambiguously resolve characteristic features in diffraction patterns and spectra of multi-component silicate glasses (i.e., ternary and quaternary glasses) obtained by conventional experimental techniques. Solid-state NMR for iron-bearing glasses have also been limited to rather simple composition because the interpretation of NMR spectra for iron-bearing multi-component silicate glasses such as aluminosilicate glasses is further complicated by severe overlaps and broadening among the peaks due to multiple configurations. Few NMR studies for silicate glasses comprising paramagnetic cations have been carried out (Kelsey et al., 2009; Kim and Lee, 2019; Kim et al., 2016b; Murdoch et al., 1985; Stebbins, 2017c), while information about the specific structural configurations around Fe (i.e., site occupancy and local symmetry) in various crystalline materials including transition metal minerals and compounds has been effectively obtained using NMR (Grey et al., 1989; Lee and Grey, 2002; Li et al., 2018; Lussier et al., 2009; McCarty et al., 2015; Nielsen et al., 2005; Palke and Stebbins, 2011; Palke et al., 2012; Palke et al., 2015; Stebbins, 2017b, c; Stebbins and Kelsey, 2009).

Previous detailed studies on crystals and glasses containing paramagnetic cations using solid-state NMR are summarized in Chapter 2 and Table 2-1.

$\text{Na}_2\text{O}-\text{Al}_2\text{O}_3-\text{SiO}_2$ and $\text{CaO}-\text{Al}_2\text{O}_3-\text{SiO}_2$ glasses are important and simple model systems for slab-driven melts at convergent plate margins and essential components of island-arc volcanos (Coltorti et al., 2000; Robinson et al., 1998). In particular, charge-balanced Na- and Ca-aluminosilicate glasses (i.e., $\text{NaAlSi}_3\text{O}_8$ and $\text{CaAl}_2\text{Si}_2\text{O}_8$ glasses which correspond to tectosilicate glasses) in the current study can serve as the model system for rhyolitic melts and glasses. Charge-balanced aluminosilicate glasses, one of the simplest aluminosilicate glasses, are expected to be fully polymerized (i.e., $\text{NBO}/\text{T} = 0$), and thus can be an effective system to systematically observe changes in the local configurations around Al with varying iron content. In addition, slight compositional variations (i.e., Fe content) near charge-balanced joins would result in noticeable structural changes in local configurations around Al and O (Neuville et al., 2004a; Neuville et al., 2004b; Toplis et al., 2000).

In this study, we explore the effect of iron content on the atomic configurations around silicon, aluminum, and oxygen of $\text{Na}(\text{Al}_{1-x}\text{Fe}_x)\text{Si}_3\text{O}_8$ glasses with varying $X [= \text{Fe}/(\text{Fe}+\text{Al})]$ ($\text{Fe}^{3+}/\Sigma\text{Fe} \sim 0.8$), $\text{NaAlSi}_3\text{O}_8$ glasses with additional Fe_2O_3 ($\text{NaAlSi}_3\text{O}_8 + \text{Fe}_2\text{O}_3$, $\text{Fe}^{3+}/\Sigma\text{Fe} \sim 0.5$), and $\text{CaAl}_2\text{Si}_2\text{O}_8$ glasses with additional Fe_2O_3 ($\text{CaAl}_2\text{Si}_2\text{O}_8 + \text{Fe}_2\text{O}_3$, $\text{Fe}^{3+}/\Sigma\text{Fe} \sim 0.3$) using Mössbauer and solid-state NMR. We used multi-nuclear (^{29}Si , ^{27}Al , and ^{17}O) high-resolution solid-state NMR to delve into the effect of iron content on the local configurations around framework cations (in particular, Si and Al) and oxygen species. Although the complexity of the composition of aluminosilicate glasses and the paramagnetic effect make it difficult to resolve the atomic configurations of iron-bearing aluminosilicate glasses in the NMR spectra, ^{27}Al 1D and 2D NMR methods give rise to a new

opportunity to explore the local configurations around Al of iron-bearing aluminosilicate glasses. Thus, multi-nuclear (^{29}Si , ^{17}O , and ^{27}Al) solid-state NMR can be utilized to explain the diverse structural information of the distribution of iron among framework cations and the spatial proximity to specific configurations. We also explore the effect of iron content on the Al coordination environments in Na- and Ca-aluminosilicate glasses. The current ^{27}Al NMR results provide information about the local atomic configurations around Fe^{3+} and Fe^{2+} in aluminosilicate glasses. Based on the NMR results, we discuss the variations in the degree of structural disorder depending on the composition of aluminosilicate glasses.

5.2. Experimental Methods

5.2.1. Sample synthesis

Na-aluminosilicate glasses along $\text{NaAlSi}_3\text{O}_8$ - $\text{NaFe}^{3+}\text{Si}_3\text{O}_8$ join [i.e., $\text{Na}(\text{Al}_{1-x}\text{Fe}_x)\text{Si}_3\text{O}_8$ composition] containing 0 ($X = 0$, albite), 5 ($X = 0.05$), 10 ($X = 0.1$), and 20 ($X = 0.2$) mol% $\text{NaFeSi}_3\text{O}_8$ component was synthesized from the oxides (Al_2O_3 , Fe_2O_3 , and SiO_2) and carbonates (Na_2CO_3 and CaCO_3). The ^{17}O -enriched Na- and Ca-aluminosilicate glasses of albite ($\text{NaAlSi}_3\text{O}_8$) and anorthite ($\text{CaAl}_2\text{Si}_2\text{O}_8$) composition (NBO/T = 0) with varying additional iron concentration of 0, 5, and 10 wt% Fe_2O_3 ($\text{NaAlSi}_3\text{O}_8 + \text{Fe}_2\text{O}_3$ and $\text{CaAl}_2\text{Si}_2\text{O}_8 + \text{Fe}_2\text{O}_3$) were also synthesized from mixtures of carbonates and oxides, including 40% ^{17}O -enriched SiO_2 prepared by hydrolyzing SiCl_4 in 40% ^{17}O -enriched H_2O . For iron-free glasses, ~0.2 wt% of Co oxide was added to reduce spin-lattice relaxation time. The starting reagents (except ^{17}O -enriched SiO_2) were dried at 300 °C for 2 days. The mixtures in iron-saturated Pt crucible were heated at 1500-1600 °C for 30 min in an Ar environment (after

Table 5-1. Nominal compositions for iron-bearing Na- and Ca-aluminosilicate glasses with varying iron content.

Glass composition	Nominal composition (mol%)					Calibrated composition (mol%) ²⁾				$X_{\text{NBO}}^{5)}$
	Na ₂ O	CaO	Al ₂ O ₃	Fe ₂ O ₃ ^T	SiO ₂	Fe ³⁺ /ΣFe ¹⁾	M ⁿ⁺ O _{n/2} ³⁾	Z ₂ O ₃ ⁴⁾	SiO ₂	
<i>Na(Al_{1-x}Fe_x)Si₃O₈ glasses</i>										
X = 0 (Ab)	12.5		12.5	0.0	75.0	-	12.5	12.5	75.0	0
X = 0.1	12.5		11.3	1.3	75.0	0.77*	13.0	12.3	74.7	0.01
X = 0.3	12.5		8.8	3.8	75.0	0.77*	14.1	11.6	74.3	0.03
X = 0.5	12.5		6.3	6.3	75.0	0.77	15.2	11.0	73.9	0.04
<i>NaAlSi₃O₈ (Ab) + Fe₂O₃ glasses</i>										
Ab + 5 wt% Fe ₂ O ₃	12.2		12.3	2.1	73.4	0.48	14.2	13.2	72.0	0.01
Ab + 10 wt% Fe ₂ O ₃	11.9		12.0	4.4	71.8	0.48	16.1	13.8	70.1	0.02
<i>CaAl₂Si₂O₈ (An) + Fe₂O₃ glasses</i>										
CaAl ₂ Si ₂ O ₈ (An)		25.0	25.0	0.0	50.0	-	25.0	25.0	50.0	0
An + 5 wt% Fe ₂ O ₃		24.3	24.3	2.2	49.2	0.33	26.9	24.7	48.5	0.02
An + 10 wt% Fe ₂ O ₃		23.6	23.7	4.6	58.1	0.35	28.8	24.6	46.7	0.05

¹⁾ Iron redox ratio obtained from Mössbauer experiment

²⁾ The composition is calibrated on the assumption that Fe³⁺ is a framework cation and Fe²⁺ is non-framework cation based on Fe³⁺/ΣFe.

³⁾ M refers to non-framework cation (Na⁺, Ca²⁺, and Fe²⁺).

⁴⁾ Z refers to framework cation (Al³⁺ and Fe³⁺)

⁵⁾ X_{NBO} is estimated from their compositions and assumed structural role.

*Fe³⁺/ΣFe for Na(Al_{1-x}Fe_x)Si₃O₈ glasses with X = 0.1 and 0.3 was not measured, but assumed to be similar to X = 0.5. Note that previous Mössbauer studies have been reported that the Fe³⁺/ΣFe for Na-aluminosilicate glasses (~75 wt% SiO₂) is not heavily dependent on the iron content (e.g., Mysen, 2006)

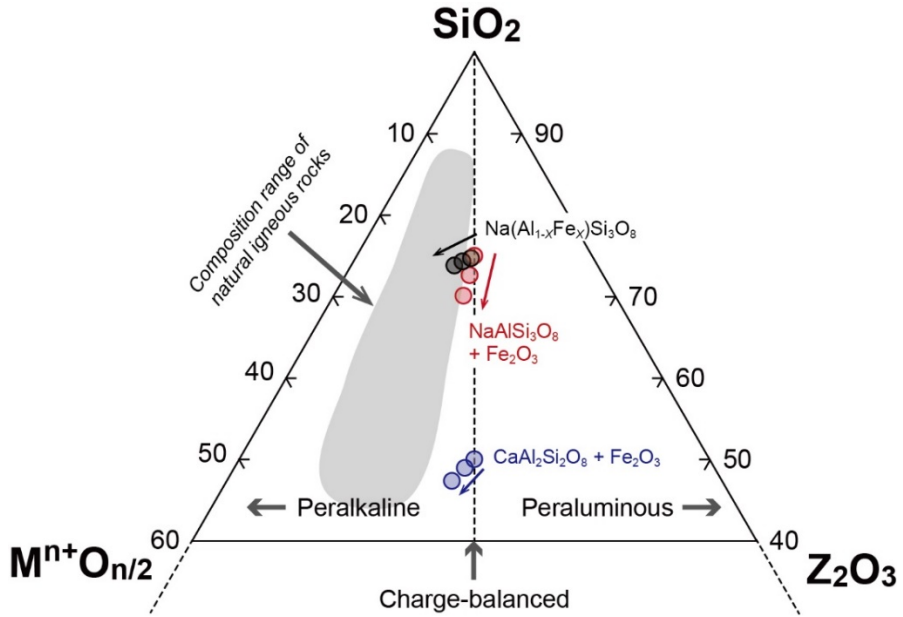


Figure 5-1. A ternary phase diagram showing the glass compositions in this study [Black symbols: $\text{Na}(\text{Al}_{1-x}\text{Fe}_x)\text{Si}_3\text{O}_8$, Red symbols: $\text{NaAlSi}_3\text{O}_8 + \text{Fe}_2\text{O}_3$, and Blue symbols: $\text{CaAl}_2\text{Si}_2\text{O}_8 + \text{Fe}_2\text{O}_3$]. M refers to non-framework cation (Na^+ , Ca^{2+} , and Fe^{2+}) and Z refers to framework cation (Al^{3+} and Fe^{3+}). The directions of the arrow for each glass composition refer to the increase in the iron contents.

decarbonation at 750-800 °C for 1 h), and then quenched. The oxygen fugacity in furnace (Ar environment) is about -2.15 ± 0.04 , which was measured using Y_2O_3 -doped ZrO_2 oxygen sensor. Taking into consideration a small amount of weight loss (about 0.5 – 1 wt%) during sample synthesis, it is expected that the compositions of glasses used in this study are close to nominal values. Nominal compositions for each glasses are shown in Table 5-1 and Figure 5-1.

5.2.2. Iron redox ratio of iron-bearing Na- and Ca-aluminosilicate glasses: Mössbauer experiment

^{57}Fe absorption Mössbauer spectra of 5 samples [i.e., $Na(Al_{0.5}Fe_{0.5})Si_3O_8$, $NaAlSi_3O_8 + 5$ wt% and 10 wt% Fe_2O_3 , and $CaAl_2Si_2O_8 + 5$ wt% and 10 wt% Fe_2O_3] were collected using constant acceleration Mössbauer spectrometer (MS-96). Approximately 30 mCi ^{57}Co flat source was used in the Mössbauer experiments which operated between -4 and 4 mm/s. The Mössbauer spectra were simultaneously fitted with two doublets corresponding to Fe^{2+} (which exhibits maxima ~ 0 and 2 mm/s) and Fe^{3+} (which exhibits maxima ~ 0 and 1 mm/s) to obtain $Fe^{3+}/\Sigma Fe$ and hyperfine parameters (isomer shift and quadrupole splitting). 28 μm -thick α -Fe foil was used for calibration. The $Fe^{3+}/\Sigma Fe$ is obtained from the relative area of the Fe^{3+} and Fe^{2+} doublets.

5.2.3. NMR spectroscopy

^{29}Si and ^{17}O NMR spectra were collected using a Varian 400 MHz system with a 4 mm Doty magic angle spinning probe (ZrO_2 rotor for ^{29}Si and Si_3N_4 rotor for ^{17}O , respectively). For ^{29}Si NMR experiment (at a 79.49 MHz), the pulse length of 1.6 μs ($\sim 30^\circ$ angle for solids) was used for single pulse

acquisition. The relaxation delay of 60 s for iron-free glass and that of 1 s for iron-bearing glasses were used with spinning speed of 14 kHz. The ^{29}Si NMR spectra were referenced to TMS (tetramethylsilane). ^{17}O NMR spectra for ^{17}O -enriched $\text{NaAlSi}_3\text{O}_8 + \text{Fe}_2\text{O}_3$ and $\text{CaAl}_2\text{Si}_2\text{O}_8 + \text{Fe}_2\text{O}_3$ glasses were collected with a relaxation delay of 0.5-1 s and *rf* pulse length of 0.2 μs ($\sim 30^\circ$ angle for solids). A fast-amplitude modulation (FAM)-based shifted-echo pulse sequence [4.5 μs for 3Q excitation - delay -1.1 μs (FAM pulse train) - ~ 0.4 ms for iron-free samples and ~ 0.18 ms for iron-bearing samples (echo-delay) - 19.5 μs] with relaxation delay of 1 s was used for ^{17}O 3QMAS NMR experiment. Tap water was used as a reference of ^{17}O NMR spectra.

^{27}Al MAS and 3QMAS NMR spectra were collected using two magnetic fields on a Varian 400 MHz system (9.4 T, at 104.23 MHz) using 3.2 mm probe, and on a Bruker Avance 600 MHz system (14.1 T, at 156.47 MHz) using 1.9 mm Bruker triple-resonance probe. Relaxation delays for ^{27}Al MAS NMR experiment were 1 s for iron-free glasses and 0.3-0.5 s for iron-bearing samples, with single *rf* pulse corresponding to $\sim 30^\circ$ angle (0.3 μs at 9.4 T, and 0.4 μs at 14.1 T). The FAM-based shifted-echo pulse sequence was used to obtain 3QMAS NMR spectra at 9.4 T, comprising two hard pulses with 3 μs and 0.7 μs , a soft pulse with 15 μs , and an echo-delay of ~ 0.5 ms for iron-free glasses and ~ 0.15 ms for iron-bearing glasses. ^{27}Al 3QMAS NMR spectra at 14.1 T were obtained using a similar pulse sequence [4.6 μs - delay - 1.0 μs - ~ 0.23 ms for iron-free samples and ~ 0.11 ms for iron-bearing samples (echo-delay) - 15 μs]. The ^{27}Al NMR spectra were referenced to 1 M AlCl_3 solution. The spinning speed was 17 kHz (9.4 T) and 35 kHz (14.1 T), respectively. Detailed information on the NMR experimental conditions including collection time in this study is summarized in Section 5A-1.

5.3. Results

5.3.1. Iron redox ratio and hyperfine parameters of $\text{Na}(\text{Al}_{1-x}\text{Fe}_x)\text{Si}_3\text{O}_8$, $\text{NaAlSi}_3\text{O}_8 + \text{Fe}_2\text{O}_3$, and $\text{CaAl}_2\text{Si}_2\text{O}_8 + \text{Fe}_2\text{O}_3$ glasses with varying iron contents: Mössbauer results

Figure 5-2 shows the Mössbauer spectra at 298 K for iron-bearing Na- and Ca-aluminosilicate glasses [i.e., $\text{Na}(\text{Al}_{0.5}\text{Fe}_{0.5})\text{Si}_3\text{O}_8$, $\text{NaAlSi}_3\text{O}_8 + 5$ wt% and 10 wt% Fe_2O_3 , and $\text{CaAl}_2\text{Si}_2\text{O}_8 + 5$ wt% and 10 wt% Fe_2O_3]. All Mössbauer spectra show the typical features of silicate glasses containing both Fe^{3+} and Fe^{2+} , exhibiting absorption maxima near 0, 1, and 2 mm/s. The fitting parameters, which are $\text{Fe}^{3+}/\Sigma\text{Fe}$, isomer shifts (δ), and quadrupole splitting (Δ), are given in Table 5-2, showing that the $\text{Fe}^{3+}/\Sigma\text{Fe}$ depends on the composition of the glasses. Previous Mössbauer studies have shown that $\text{Fe}^{3+}/\Sigma\text{Fe}$ tends to decrease with increasing Z/r^2 and increase with increasing $\text{Fe}/(\text{Fe}+\text{Al})$ (Mysen, 2006; e.g., Mysen and Virgo, 1985). The $\text{Fe}^{3+}/\Sigma\text{Fe}$ of the $\text{NaAlSi}_3\text{O}_8 + \text{Fe}_2\text{O}_3$ glasses (~ 0.5) is larger than that of the $\text{CaAl}_2\text{Si}_2\text{O}_8 + \text{Fe}_2\text{O}_3$ glasses (~ 0.3), consistent with the previous results. For the glasses, the $\text{Fe}^{3+}/\Sigma\text{Fe}$ value does not change much with additional Fe_2O_3 content from 5 wt% to 10 wt%. As mentioned above, $\text{Fe}^{3+}/\Sigma\text{Fe}$ is also dependent on the $\text{Fe}/(\text{Fe}+\text{Al})$ ratio when the type of non-framework cation is the same. The $\text{Fe}^{3+}/\Sigma\text{Fe}$ of $\text{Na}(\text{Al}_{0.5}\text{Fe}_{0.5})\text{Si}_3\text{O}_8$ glass (~ 0.8) is larger than that of the $\text{NaAlSi}_3\text{O}_8 + \text{Fe}_2\text{O}_3$ glasses (~ 0.5) due to a larger $\text{Fe}/(\text{Fe}+\text{Al})$ value (Mysen, 2006). The current trend is consistent with the earlier Mössbauer results (Kress and Carmichael, 1991; Lange and Carmichael, 1989; Mysen, 2006; Mysen and Virgo, 1989).

As shown in Table 5-2, the isomer shift of Fe^{3+} ($\delta^{\text{Fe}^{3+}}$) is approximately 0.3, indicating that 4-coordinated Fe^{3+} is dominant in the glasses (Dyar et al., 2006; Mysen, 2006; e.g., Mysen and Richet, 2018). The $\delta^{\text{Fe}^{3+}}$ value of $\text{CaAl}_2\text{Si}_2\text{O}_8$

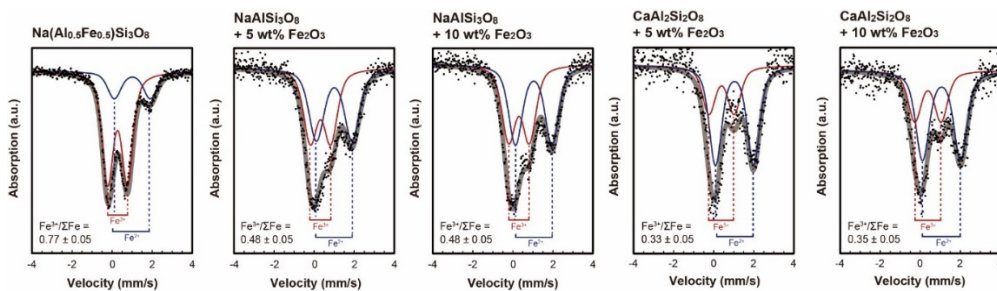


Figure 5-2. Mössbauer spectra obtained at 298 K (dots) and fitting results (gray thick line) of $\text{Na}(\text{Al}_{0.5}\text{Fe}_{0.5})\text{Si}_3\text{O}_8$ glass, $\text{NaAlSi}_3\text{O}_8$ + 5 and 10 wt% Fe_2O_3 glasses, and $\text{CaAl}_2\text{Si}_2\text{O}_8$ + 5 and 10 wt% Fe_2O_3 glasses, respectively (as labeled). The spectra were fitted with two doublets corresponding to Fe^{3+} (red line) and Fe^{2+} (blue line).

Table 5-2. Fitting parameters [isomer shift (δ , mm/s) and quadrupole splitting (Δ , mm/s)] and iron redox ratio ($\text{Fe}^{3+}/\Sigma\text{Fe}$) of room-temperature ^{57}Fe Mössbauer spectra for iron-bearing Na- and Ca-aluminosilicate glasses.

Composition	$\text{Fe}^{3+}/\Sigma\text{Fe}^{1)}$	Fe^{3+}		Fe^{2+}	
		$\delta^{2)}$	$\Delta^{3)}$	$\delta^{2)}$	$\Delta^{3)}$
$\text{Na}(\text{Al}_{0.5}\text{Fe}_{0.5})\text{Si}_3\text{O}_8$	0.77(5)*	0.27(3)	1.00(2)	1.01(3)	1.79(3)
Ab + 5 wt% Fe_2O_3	0.48(5)	0.32(7)	1.02(7)	1.00(7)	1.79(7)
Ab + 10 wt% Fe_2O_3	0.48(5)	0.31(5)	1.03(5)	1.04(5)	1.83(5)
An + 5 wt% Fe_2O_3	0.33(5)	0.39(7)	1.26(7)	1.04(7)	1.90(7)
An + 10 wt% Fe_2O_3	0.35(5)	0.38(5)	1.32(5)	1.06(5)	1.91(5)

¹⁾ $\text{Fe}^{3+}/\Sigma\text{Fe}$: Ratio of Fe^{3+} over total iron ($\text{Fe}^{3+} + \text{Fe}^{2+}$)

²⁾ δ : Isomer shift

³⁾ Δ : Quadrupole splitting

*Number in parentheses denotes uncertainty from spectra deconvolution [e.g., 0.77(5) = 0.77 ± 0.05]

glasses is slightly larger than that of NaAlSi₃O₈ glasses, suggesting that the average coordination number of Fe³⁺ for CaAl₂Si₂O₈ glasses may be larger than that of NaAlSi₃O₈ glasses. The $\delta^{\text{Fe}^{2+}}$ of all glasses is ~ 1.0 (corresponding to the 6-coordinated Fe²⁺) and does not change with the type of non-framework cation. The quadrupole splitting of Fe³⁺ and Fe²⁺ ($\Delta^{\text{Fe}^{3+}}$ and $\Delta^{\text{Fe}^{2+}}$) for CaAl₂Si₂O₈ + Fe₂O₃ glasses is also larger than that of NaAlSi₃O₈ + Fe₂O₃ glasses: $\Delta^{\text{Fe}^{3+}}$ and $\Delta^{\text{Fe}^{2+}}$ for CaAl₂Si₂O₈ + Fe₂O₃ glasses are approximately 1.3 and 1.9, respectively, and those for NaAlSi₃O₈ + Fe₂O₃ glasses are ~ 1.0 and ~ 1.8 , respectively. The obtained hyperfine parameters are similar to those from previous Mössbauer studies (Hannoyer et al., 1992; Mysen, 2006; Mysen and Virgo, 1989). The former indicates that the extent of distortion of Fe³⁺-O and Fe²⁺-O polyhedra in CaAl₂Si₂O₈ glasses is larger than that in NaAlSi₃O₈ glasses.

We note that there can be an uncertainty in Fe³⁺/ΣFe and the hyperfine parameters obtained from the fitting results of the Mössbauer spectra (see Table 5-2). This is because the ⁵⁷Fe abundance in the glasses is only $\sim 2.12\%$ (natural abundance), resulting in a low signal-to-noise ratio. It is clear, however, that Fe³⁺ is dominant for Na(Al_{1-x}Fe_x)Si₃O₈ glasses, Fe²⁺ is dominant for CaAl₂Si₂O₈ + Fe₂O₃ glasses, and Fe²⁺ and Fe³⁺ are present in similar proportions for NaAlSi₃O₈ + Fe₂O₃ glasses.

5.3.2. The Si and Al environments and extent of intermixing among framework cations in $\text{Na}(\text{Al}_{1-x}\text{Fe}_x)\text{Si}_3\text{O}_8$ glasses with varying X [$=\text{Fe}/(\text{Al}+\text{Fe})$]: ^{29}Si and ^{27}Al NMR results

5.3.2.1. ^{29}Si NMR results

Figure 5-3 presents the normalized ^{29}Si MAS NMR spectra for the $\text{Na}(\text{Al}_{1-x}\text{Fe}_x)\text{Si}_3\text{O}_8$ glasses with varying X [i.e., $\text{Fe}/(\text{Fe}+\text{Al})$, $\text{Fe}^{3+}/\Sigma\text{Fe} \sim 0.8$]. The peak at ~ 98 ppm for iron-free and iron-bearing $\text{Na}(\text{Al}_{1-x}\text{Fe}_x)\text{Si}_3\text{O}_8$ glasses corresponds to 4-coordinated Si with Q^4 species, consistent with earlier ^{29}Si MAS NMR studies (Kohn et al., 1989; Lee and Stebbins, 1999; Merzbacher et al., 1990; Murdoch et al., 1985; Oestrike et al., 1987). Note that the peak position of Q^4 varies with the number of Al in the next-nearest neighbor from 4-coordinated Si [i.e., $\text{Q}^4_{\text{Si}}(m\text{Al})$, where m refers to the number of next-nearest Al from Si], depending on the glass composition. Previous studies have shown that the peak position of $\text{Q}^4_{\text{Si}}(m\text{Al})$ moves to lower frequency (more negative chemical shift) with increasing Si/Al ratio (Engelhardt et al., 1985; Lee and Stebbins, 1999; Murdoch et al., 1985). The peak at ~ 98 ppm indicates that $\text{Q}^4_{\text{Si}}(2\text{Al})$ and $\text{Q}^4_{\text{Si}}(1\text{Al})$ species are dominant for $\text{NaAlSi}_3\text{O}_8$ glasses.

Iron-induced changes in peak intensity. As Al is substituted with Fe (increasing X), the ^{29}Si NMR signal intensity for $\text{Na}(\text{Al}_{1-x}\text{Fe}_x)\text{Si}_3\text{O}_8$ glasses significantly decreases (see Section 5A-4). This is because the silicon atoms, near iron, are effectively removed by the paramagnetic effect. We note that the distance within which paramagnetic interaction results in complete NMR signal loss (defined as the cutoff radius) was estimated to be ~ 3.3 Å (the distance of the first coordination shell of iron) (Kim and Lee, 2019). The

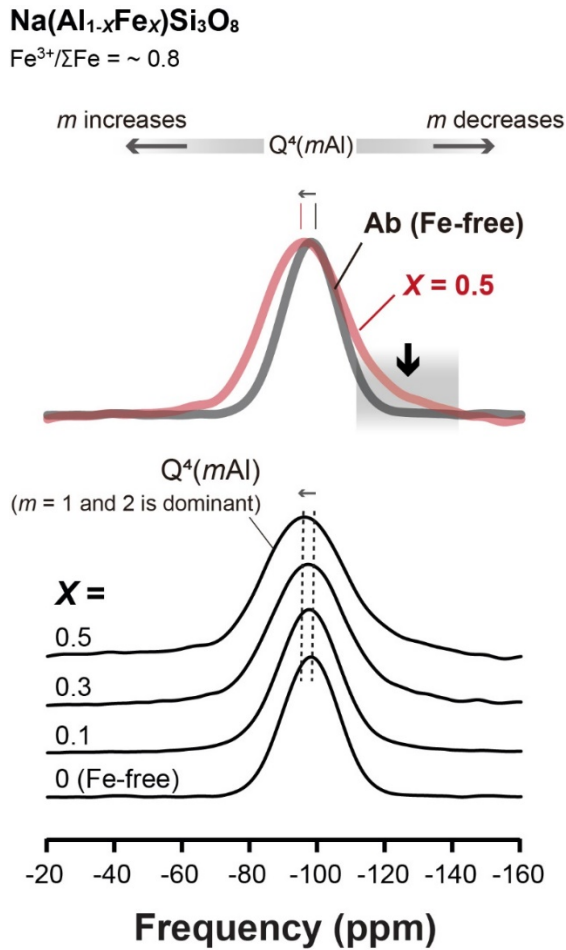


Figure 5-3. ^{29}Si MAS NMR spectra for $\text{Na}(\text{Al}_{1-x}\text{Fe}_x)\text{Si}_3\text{O}_8$ glasses with varying X [i.e., $\text{Fe}/(\text{Fe}+\text{Al})$], as labeled. The spectra are plotted on a normalized vertical scale. A comparison of the ^{29}Si MAS NMR spectra for the iron-free (thick grey line) and iron-bearing (thick red line) is also shown. The shaded area with black arrow shows the preferential broadening of $Q^4_{\text{Si}}(m\text{Al})$ species with smaller m number by replacing Al with Fe.

detailed discussion on the variations in the ^{29}Si peak intensities with varying iron content is provided in Section 5.4.5.

Iron-induced changes in peak width and position by replacing Al with Fe.

Due to the signal loss of the nuclear spins located close to iron, the observed changes in peak position and width of ^{29}Si NMR spectra for the iron-bearing glasses represent the survived spins located beyond the cutoff radius. As the Al is replaced with Fe, the obvious peak broadening (due to the paramagnetic effect) accompanied by the changes in peak position is clearly observed (Figure 5-3), the $Q^4_{\text{Si}}(m\text{Al})$ peak position for the $\text{Na}(\text{Al}_{1-x}\text{Fe}_x)\text{Si}_3\text{O}_8$ glasses ($\text{Fe}^{3+}/\Sigma\text{Fe} \sim 0.8$) slightly changes from ~ -98 ppm to ~ -96 ppm with increasing iron content [i.e., increasing $\text{Fe}/(\text{Fe}+\text{Al})$]. In addition to the shift of peak maxima toward higher frequency, the shoulder in the lower frequency is preferentially broadened (black arrow in Figure 5-3).

Interpretation. The changes in peak position and width with increasing Fe content could originate both from structural changes, paramagnetic broadening, and preferential loss in peak intensity for particular species. First, if we assume that there is *no preferential* lifetime broadening and *no selective* decrease in the particular $Q^4_{\text{Si}}(m\text{Al})$ species in the glass structure, the current observation can be interpreted by iron-induced structural changes (i.e., the changes in the relative fraction of each $Q^4_{\text{Si}}(m\text{Al})$ species and/or topological disorder). As described in our previous study, the changes in peak shape due to iron-induced structural changes could involve peak shift and asymmetric peak broadening (characterized by Gaussian function) (Kim and Lee, 2019; Kim et al., 2016b). For the Fe^{3+} -dominant $\text{Na}(\text{Al}_{1-x}\text{Fe}_x)\text{Si}_3\text{O}_8$ glasses ($\text{Fe}^{3+}/\Sigma\text{Fe} \sim 0.8$), the peak position moves slightly toward a higher frequency. In addition,

the shoulder at the lower frequency is preferentially broadened. These observations suggest that the average number of next-nearest Al from Si [i.e., m of $Q^4_{Si}(mAl)$] increases and/or there is a relatively large increase in the degree of topological disorder of the $Q^4_{Si}(mAl)$ species with a smaller m (i.e., 0 and 1) compared to that with a larger m (i.e., 2 and 3).

Alternatively, if the preferential broadening and selective decrease in $Q^4_{Si}(mAl)$ species originate from paramagnetic interaction, the observed changes in NMR spectra with increasing iron content reflect relative spatial proximity between Fe and each $Q^4_{Si}(mAl)$ species. With the assumption that NMR spectra reflect preferential paramagnetic interaction among $Q^4_{Si}(mAl)$ species, the apparent increase in NMR signal of the particular species suggests a selective decrease in the NMR signal intensity of the other species. The apparent increase in the fraction of the features at the higher frequency [corresponding to the $Q^4_{Si}(mAl)$ with a larger m] of the spectra for the Fe^{3+} -dominant $Na(Al_{1-x}Fe_x)Si_3O_8$ glasses may be counter-evidence for the spatial proximity between Fe^{3+} and $Q^4_{Si}(mAl)$ with a smaller m . In addition, the observed NMR signal from the *survived* nuclear spins affected by the paramagnetic cation involves significant lifetime broadening characterized by the Lorentzian function. The pronounced broadened features at lower frequency for the Fe^{3+} -dominant $Na(Al_{1-x}Fe_x)Si_3O_8$ glasses suggest that there is preferential spatial proximity between Fe^{3+} and $Q^4_{Si}(mAl)$ with a smaller m (i.e., Si-rich framework).

While it is difficult to distinguish whether the changes in NMR spectra with increasing iron content are due to structural changes and/or paramagnetic effects, the fraction of $Q^4_{Si}(mAl)$ with larger m apparently increases by replacing Al with Fe. However, the increase in the fraction of Q^4 species with a larger number of Al as the second nearest neighbors is

inconsistent with the fact that the Al content decreases (by replacing Al with Fe). Thus, the observed peak shift toward higher frequency [corresponding to $Q^4_{\text{Si}}(m\text{Al})$ species with larger m] and the explicit peak broadening of the $Q^4_{\text{Si}}(m\text{Al})$ region with a smaller m can primarily stem from the selective loss and preferential broadening of the Q^4 species with a smaller number of Al as the second nearest neighbors (i.e., Si-rich framework).

4.3.2.2. ^{27}Al NMR results

^{27}Al MAS NMR results. Figure 5-4 shows the normalized ^{27}Al MAS NMR spectra for the $\text{Na}(\text{Al}_{1-x}\text{Fe}_x)\text{Si}_3\text{O}_8$ glasses with varying X [$=\text{Fe}/(\text{Fe}+\text{Al})$] at 9.4 T. The dominant peak at ~ 50.4 ppm corresponds to 4-coordinated Al ($^{[4]}\text{Al}$). Note that overlap among the central transition peak and spinning sideband in the ^{27}Al MAS NMR spectra for the iron-free and iron-bearing glasses is not observed (see Section 5A-6). We also note that the Al background signal (mostly $^{[6]}\text{Al}$) from the empty rotor is subtracted from the spectra (see Section 5A-5). The shape of the Al peak is characterized by long tails extending to lower frequencies, resulting from distributions of the quadrupolar constant (C_q) and the isotropic chemical shift (δ_{iso}) of Al environments (Baltisberger et al., 1996; Lee and Stebbins, 2000b; e.g., Lippmaa et al., 1986).

By replacing Al with Fe [i.e., increasing $X = \text{Fe}/(\text{Fe}+\text{Al})$], the ^{27}Al MAS NMR signal intensities for $\text{Na}(\text{Al}_{1-x}\text{Fe}_x)\text{Si}_3\text{O}_8$ glasses exponentially decrease, consistent with the results of ^{29}Si MAS NMR. The detailed discussion on the variations in the ^{27}Al peak intensities with varying iron content is provided in the Section 5.4.5. The $^{[4]}\text{Al}$ peaks with a maximum at ~ 50 ppm for the $\text{Na}(\text{Al}_{1-x}\text{Fe}_x)\text{Si}_3\text{O}_8$ glasses do not change significantly, whereas the peak



$$\text{Fe}^{3+}/\Sigma\text{Fe} = \sim 0.8$$

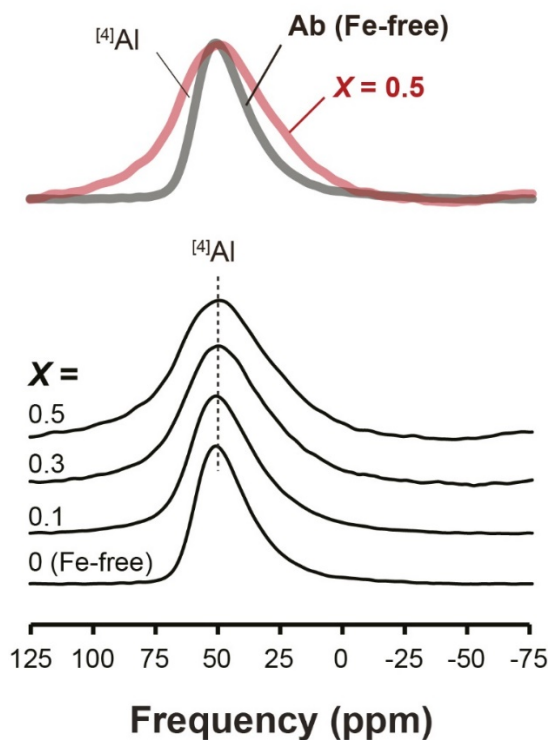


Figure 5-4. ^{27}Al MAS NMR spectra for $\text{Na}(\text{Al}_{1-x}\text{Fe}_x)\text{Si}_3\text{O}_8$ glasses with varying X [i.e., $\text{Fe}/(\text{Fe}+\text{Al})$], as labeled. The spectra are plotted on a normalized vertical scale. The rotor backgrounds were subtracted from the spectra (see Section 5A-5). A comparison of the ^{27}Al MAS NMR spectra for the iron-free (thick grey line) and iron-bearing (thick red line) is also shown.

widths of the ^{27}Al MAS NMR spectra increase significantly with increasing iron content. The significant peak broadening results in changes in peak shape of ^{41}Al from the shape characterized by quadrupolar broadening (with the long tail toward the lower frequency) to a more symmetrical shape. The observed symmetrical broadening stems from the paramagnetic effect.

^{27}Al 3QMAS NMR results. Figure 5-5A presents the ^{27}Al 3QMAS NMR spectra for the $\text{Na}(\text{Al}_{1-x}\text{Fe}_x)\text{Si}_3\text{O}_8$ glasses with varying X [and thus, $\text{Fe}/(\text{Fe}+\text{Al})$] at 9.4 T, showing the predominant ^{41}Al (~ -37 ppm in the isotropic dimension). Note that the rotor backgrounds (mostly ^{61}Al at ~ 0 ppm in the isotropic dimension) were subtracted (see Section 5A-5). As X increases (by replacing Al with Fe), the ^{41}Al peak broadens along both the MAS and isotropic dimensions. While peak widths along both dimensions significantly increases with increasing iron content, the estimated C_q for ^{41}Al of the $\text{Na}(\text{Al}_{1-x}\text{Fe}_x)\text{Si}_3\text{O}_8$ glasses is $\sim 4.4 \pm 0.5$ MHz, which does not change significantly by replacing Al with Fe. Note that we estimated the quadrupolar coupling product (P_q) from the center of gravity of the ^{41}Al peak in the ^{27}Al 3QMAS NMR spectra, and the asymmetry parameter (η) was assumed to be 0.5 to calculate C_q [$=P_q / (1 + \eta^2/3)^{1/2}$] (see Section 5A-7). Whereas ^{41}Al environments in $\text{Na}(\text{Al}_{1-x}\text{Fe}_x)\text{Si}_3\text{O}_8$ glasses with varying $\text{Fe}/(\text{Fe}+\text{Al})$ are not significantly different, a small feature of ^{51}Al around -20 ppm in the isotropic dimension is observed for the $\text{Fe}/(\text{Fe}+\text{Al}) = 0.5$ glass.

Figure 5-5B shows the total isotropic projections of the ^{27}Al 3QMAS NMR spectra for the $\text{Na}(\text{Al}_{1-x}\text{Fe}_x)\text{Si}_3\text{O}_8$ glasses with varying $\text{Fe}/(\text{Fe}+\text{Al})$ at 9.4 T. Here, the isotropic projections shown here are background subtracted (Section 5A-5). The peak broadening is characterized by the Lorentzian function with increasing Fe from $\text{Fe}/(\text{Fe}+\text{Al}) = 0$ (Fe-free) to 0.1. The ^{41}Al peak

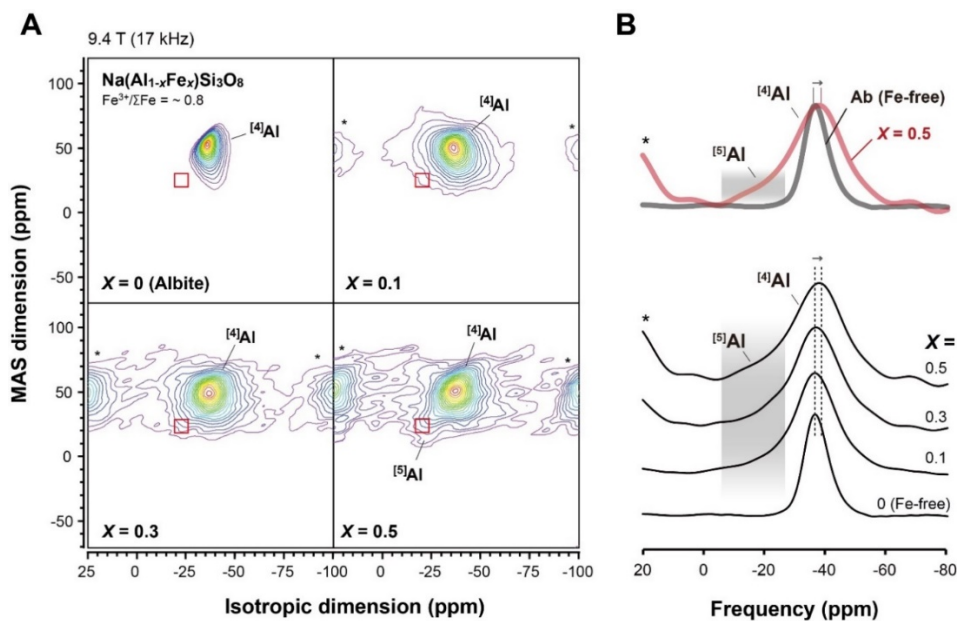


Figure 5-5. (A) 2D ^{27}Al 3QMAS NMR spectra (at 9.4 T) for $\text{Na}(\text{Al}_{1-x}\text{Fe}_x)\text{Si}_3\text{O}_8$ glasses with varying X [i.e., $\text{Fe}/(\text{Fe}+\text{Al})$], as labeled. Contour lines are drawn from 8% to 98% relative intensity with a 5% increment and an additional line at 6% levels. The red square in the spectra refers to the expected position of $^{[5]}\text{Al}$. (B) Total isotropic projection of ^{27}Al 3QMAS NMR spectra. A comparison of spectrum for the iron-free (thick grey line) and iron-bearing (thick red line) is also shown. The shaded area correspond to the $^{[5]}\text{Al}$.

width does not increase significantly from $\text{Fe}/(\text{Fe}+\text{Al}) = 0.1$ to 0.5. As described below, the trends in peak broadening along the isotropic dimension are similar for $\text{NaAlSi}_3\text{O}_8 + \text{Fe}_2\text{O}_3$ and $\text{CaAl}_2\text{Si}_2\text{O}_8 + \text{Fe}_2\text{O}_3$ glasses. The peak broadening along the isotropic dimension stems from both an increase in the extent of structural disorder (topological and configurational) and enhanced spin-spin relaxation (T_2) by paramagnetic interaction. The abrupt increase in peak width along the isotropic dimension with increasing X [$=\text{Fe}/(\text{Fe}+\text{Al})$] from 0 to 0.1 implies that peak broadening due to enhanced spin-spin relaxation predominates when a small amount of Fe is added. The peak maximum of ^{41}Al in the glass shifted slightly from -36.5 ± 1.5 ppm ($X = 0$) to -38.1 ± 1.5 ppm ($X = 0.5$) in the isotropic dimension, indicating a change in the $\text{Q}^4_{\text{Al}}(n\text{Si})$ species by replacing Al with Fe. On the basis of the previously established trend between peak positions of the $\text{Q}^4_{\text{Al}}(n\text{Si})$ species and n , the observed changes in peak maxima indicate that the fraction of $\text{Q}^4_{\text{Al}}(n\text{Si})$ species with a smaller n (e.g., 1 or 2) increases (Lee and Stebbins, 2000b and references therein). The apparent increase in $\text{Q}^4_{\text{Al}}(1,2\text{Si})$ by replacing Al with Fe^{3+} may stem from a reduction of the signal from $\text{Q}^4_{\text{Al}}(3,4\text{Si})$ due to the proximity to Fe^{3+} , suggesting that Fe^{3+} interacts more strongly with the Si-rich framework than the Al-rich framework, consistent with the current ^{29}Si MAS NMR results. The small shoulder at ~ -20 ppm in the isotropic projection in the spectrum for X [$=\text{Fe}/(\text{Fe}+\text{Al})$] = 0.5 corresponds to ^{51}Al (see Section 5.4.1 for further discussion). There is, however, an uncertainty in peak assignment due to the low signal-to-noise ratio and significant peak broadening.

5.3.3. The changes in the local configurations around framework cations and oxygen sites with increasing excess Fe₂O₃ in the NaAlSi₃O₈ glasses (NaAlSi₃O₈ + Fe₂O₃): ²⁹Si, ²⁷Al, and ¹⁷O NMR results

5.3.3.1. ²⁹Si NMR results.

Figure 5-6 shows normalized ²⁹Si MAS NMR spectra for NaAlSi₃O₈ glasses with varying amount of Fe₂O₃ (NaAlSi₃O₈ + Fe₂O₃, Fe³⁺/ΣFe ~0.5), exhibiting a single broad peak at ~-98 ppm which corresponds to the Q⁴_{Si}(*m*Al) species. As mentioned Section 5.3.2.1, Q⁴_{Si}(2Al) and Q⁴_{Si}(1Al) are dominant in the NaAlSi₃O₈ glasses. With increasing Fe₂O₃ content, the ²⁹Si signal intensity decreases and the peak width increases. The trend of decreasing ²⁹Si signal intensity for NaAlSi₃O₈ + Fe₂O₃ glasses is similar to that for Na(Al_{1-x}Fe_x)SiO₃ glasses. However, the trends in peak broadening and peak shift for NaAlSi₃O₈ + Fe₂O₃ glasses are different from those for Na(Al_{1-x}Fe_x)SiO₃ glasses: homogeneous (i.e., symmetric) peak broadening without a peak shift is observed for the NaAlSi₃O₈ + Fe₂O₃ glasses (Fe³⁺/ΣFe ~ 0.5). In contrast, preferential peak broadening of Q⁴_{Si}(*m*Al) with smaller *m*, with a peak shift toward higher frequency [corresponding to the Q⁴_{Si}(*m*Al) with a larger *m*], is observed for Fe³⁺-dominant Na(Al_{1-x}Fe_x)SiO₃ glasses (Fe³⁺/ΣFe ~ 0.8, see Section 5.3.2.1). This is likely due to the difference in the Fe³⁺/ΣFe ratio of the glasses. The symmetric peak broadening in NaAlSi₃O₈ + Fe₂O₃ glasses indicates that the relative fractions among the Q⁴_{Si}(*m*Al) species constituting the NaAlSi₃O₈ glasses may not change significantly as Fe₂O₃ increases. Therefore, both Fe²⁺ and Fe³⁺ in NaAlSi₃O₈ + Fe₂O₃ glasses tend to equally affect the Q⁴_{Si}(*m*Al) species regardless of *m* number. In contrast, Fe³⁺ in the Na(Al_{1-x}Fe_x)SiO₃ glasses interacts more strongly with Q⁴ species with a smaller number of Al as the second nearest neighbors. Therefore, Fe³⁺ in NaAlSi₃O₈ + Fe₂O₃ glasses interacts more strongly with Q⁴ species with a

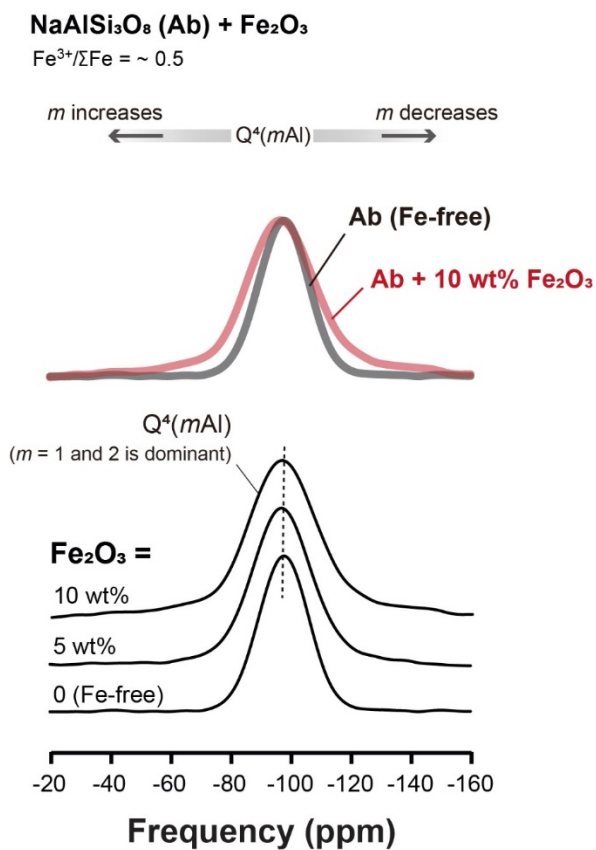


Figure 5-6. ²⁹Si MAS NMR spectra for NaAlSi₃O₈ glasses with varying additional Fe₂O₃ (0, 5, and 10 wt% Fe₂O₃). The spectra are plotted on a normalized vertical scale. A comparison of the ²⁹Si MAS NMR spectra for the iron-free (thick grey line) and iron-bearing (thick red line) is also shown.

smaller number of Al as the second nearest neighbors. In contrast, Fe²⁺ interacts more strongly Q⁴ species with a larger number of Al as the second nearest neighbors.

5.3.3.2. ²⁷Al NMR results

²⁷Al MAS NMR results. Figure 5-7 presents the ²⁷Al MAS NMR spectra for NaAlSi₃O₈ glasses with additional Fe₂O₃ (Fe³⁺/ΣFe ~ 0.5). The spectra show that the peak position of ⁴Al centered at ~50.4 ppm does not change with increasing Fe₂O₃, consistent with the Na(Al_{1-x}Fe_x)SiO₃ glasses. The trend of decreasing ²⁷Al MAS NMR signal intensity for NaAlSi₃O₈ + Fe₂O₃ glasses with increasing Fe₂O₃ is also similar with that for Na(Al_{1-x}Fe_x)SiO₃ glasses (see Section 5.4.5 below). However, the extent of ⁴Al peak broadening for NaAlSi₃O₈ + Fe₂O₃ glasses with increasing iron content is smaller than that for Na(Al_{1-x}Fe_x)Si₃O₈ glasses. The relatively larger broadening in Na(Al_{1-x}Fe_x)Si₃O₈ glasses with increasing X [=Fe/(Al+Fe)] may be due to the decrease in Al contents (by replacing Al with Fe).

²⁷Al 3QMAS NMR results. In the ²⁷Al 3QMAS NMR spectra for the NaAlSi₃O₈ glasses with varying Fe₂O₃ obtained at both fields [i.e., 9.4 T (17 kHz) and 14.1 T (35 kHz)], the ⁴Al is dominant (Figure 5-8A), consistent with the 1D NMR results. Note that ⁶Al signals in the spectra of the Fe-bearing glasses at 9.4 T due to the background from the empty rotor were subtracted (see Section 5A-5). Only the ⁴Al site is observed in the Fe-free and Fe-bearing NaAlSi₃O₈ glasses. We also collected 2D spectra at 14.1 T with a spinning speed of 35 kHz. The observed Al sites in the spectra at 14.1 T are consistent

NaAlSi₃O₈ (Ab) + Fe₂O₃

Fe³⁺/ΣFe = ~ 0.5

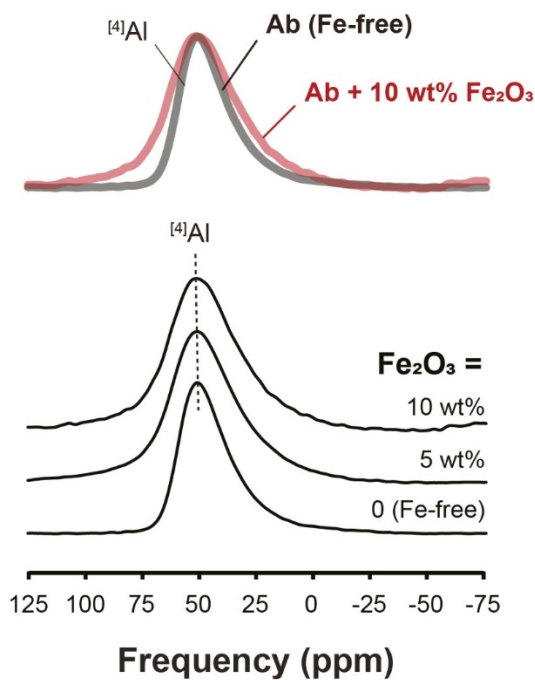


Figure 5-7. ²⁷Al MAS NMR spectra for NaAlSi₃O₈ glasses with varying additional Fe₂O₃ (0, 5, and 10 wt% Fe₂O₃) at 9.4 T. The spectra are plotted on a normalized vertical scale. The rotor backgrounds were subtracted from the spectra (see Section 5A-5). A comparison of the ²⁷Al MAS NMR spectra for the iron-free (thick grey line) and iron-bearing (thick red line) is also shown.

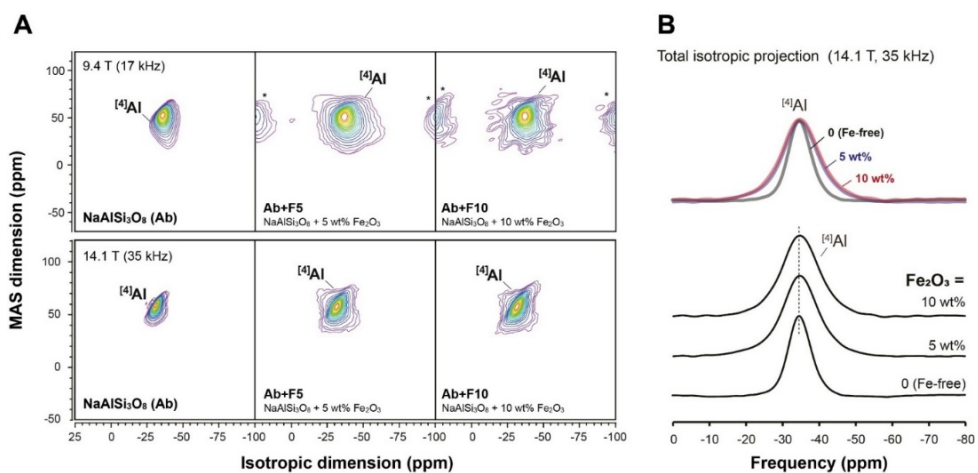


Figure 5-8. (A) 2D ^{27}Al 3QMAS NMR spectra for $\text{NaAlSi}_3\text{O}_8$ glasses with varying additional Fe_2O_3 (0, 5, and 10 wt% Fe_2O_3) at 9.4 T and 14.1 T, as labeled. Contour lines are drawn from 8% to 98% relative intensity with a 5% increment and an additional line at 6% levels. (B) Total isotropic projection of ^{27}Al 3QMAS NMR spectra. A comparison of spectrum for the iron-free (thick grey line) and iron-bearing (thick red line) is also shown.

with those at 9.4 T: only ^{41}Al is observed in the spectra at 14.1 T for the $\text{NaAlSi}_3\text{O}_8 + \text{Fe}_2\text{O}_3$ glasses.

Similar to the $\text{Na}(\text{Al}_{1-x}\text{Fe}_x)\text{Si}_3\text{O}_8$ glasses (Figure 5-5), ^{41}Al peak becomes broader along both the MAS and isotropic dimensions with increasing Fe_2O_3 content (at both 9.4 T and 14.1 T). Here, the ^{41}Al peak width in MAS dimension for the $\text{NaAlSi}_3\text{O}_8$ glasses does not seem to change with increasing Fe_2O_3 content from 5 wt% to 10 wt%. The similarity of the peak width along the MAS dimension implies that the ^{41}Al C_q of the glasses is not affected by the addition of Fe_2O_3 . Estimated the C_q of ^{41}Al of the $\text{NaAlSi}_3\text{O}_8$ glasses ($\sim 4.4 \pm 0.5$ MHz) with varying Fe_2O_3 at both 9.4 T and 14.1 T (see Section 5A-7) confirms that the ^{41}Al C_q values for both glasses do not change significantly with increasing Fe_2O_3 . Unlike the results of the $\text{Na}(\text{Al}_{1-x}\text{Fe}_x)\text{Si}_3\text{O}_8$ glasses (Figure 5-5B), the ^{41}Al peak position in isotropic projection (14.1 T) does not change with increasing Fe_2O_3 content in $\text{NaAlSi}_3\text{O}_8$ glasses (Figure 5-8B). The ^{41}Al peak width abruptly increases with increasing Fe_2O_3 content from 0 to 5 wt%, stemming from rapid T_2 relaxation due to paramagnetic interaction. However, the width does not change with a further increase in Fe_2O_3 content to 10 wt% for $\text{NaAlSi}_3\text{O}_8$ glasses. In the ^{27}Al 3QMAS NMR spectra (at both 9.4 T and 14.1 T) and total isotropic projections for $\text{NaAlSi}_3\text{O}_8 + \text{Fe}_2\text{O}_3$ glasses, the presence of highly coordinated Al (i.e., ^{51}Al) is not observed.

5.3.3.3. ^{17}O NMR results

Figure 5-9A presents the ^{17}O 3QMAS NMR spectra for the $\text{NaAlSi}_3\text{O}_8 + \text{Fe}_2\text{O}_3$ glasses with varying amount of Fe_2O_3 , showing a much improved resolution among peaks compared to the ^{17}O MAS NMR spectra (see Section

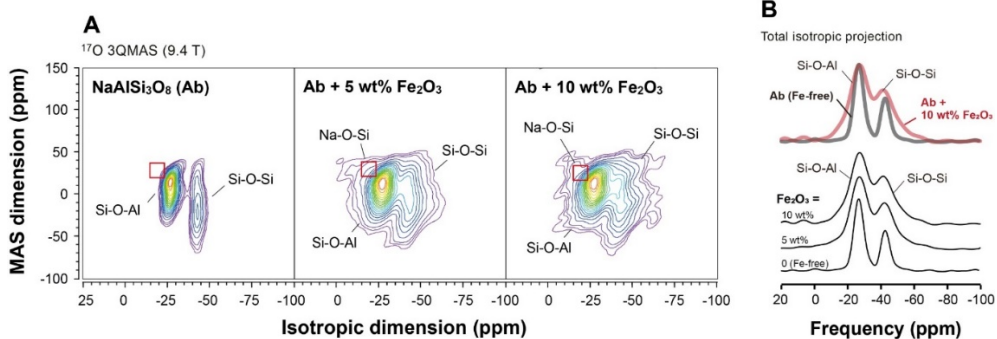


Figure 5-9. (A) ^{17}O 3QMAS NMR spectra for NaAlSi₃O₈ glasses with varying Fe₂O₃ contents (0, 5, and 10 wt% Fe₂O₃) at 9.4 T, as labeled. Contour lines are drawn from 13% to 93% relative intensity with a 5% increment and three additional lines at 5.5%, 7.5%, and 10% levels. The red square in the spectra refers to the expected position of Na-O-Si (Na-NBO). (B) Total isotropic projection of ^{17}O 3QMAS NMR spectra. A comparison of spectrum for the iron-free (thick grey line) and iron-bearing (thick red line) is also shown.

5A-8). In particular, $^{41}\text{Si-O-}^{41}\text{Al}$ (at ~ 27 ppm in isotropic dimension) and $^{41}\text{Si-O-}^{41}\text{Si}$ (at ~ 43 ppm in isotropic dimension) are completely resolved in the spectrum for iron-free $\text{NaAlSi}_3\text{O}_8$ glass; those are also well-resolved in the spectra of Fe-bearing $\text{NaAlSi}_3\text{O}_8$ glasses. The absence of Na-NBO indicates that Na^+ plays a role as a charge-balancing cation. As the Fe_2O_3 content increases, the peak widths for both sites in the 3QMAS NMR spectra are broadened along the isotropic dimension. Despite peak broadening, the ^{17}O 3QMAS NMR spectra provide clear evidence for the presence of Na-O-Si (i.e., Na-NBO) at ~ 20 ppm in the isotropic dimension for $\text{NaAlSi}_3\text{O}_8 + \text{Fe}_2\text{O}_3$ glasses. The presence of Na-NBO in $\text{NaAlSi}_3\text{O}_8 + \text{Fe}_2\text{O}_3$ glasses near a charge-balanced join suggests that the increase in the extent of structural disorder is due to the addition of high Z/r^2 cation (i.e., Fe^{2+}). Figure 5-9B shows the total isotropic projection of the ^{17}O 3QMAS NMR spectra for the $\text{NaAlSi}_3\text{O}_8 + \text{Fe}_2\text{O}_3$ glasses. Again, the Si-O-Al (~ 27 ppm) and Si-O-Si (~ 43 ppm) peaks are clearly resolved, manifesting the changes in peak width (along the isotropic dimension) and the relative fractions of each oxygen site with increasing Fe_2O_3 content. The small amount of Na-O-Si in the Fe_2O_3 -bearing $\text{NaAlSi}_3\text{O}_8$ glasses (which observed in 2D NMR spectra) is not fully resolved in the isotropic projection.

The fractions of Si-O-Si and Si-O-Al in the $\text{NaAlSi}_3\text{O}_8 + \text{Fe}_2\text{O}_3$ glasses do not change significantly with increasing Fe_2O_3 . The peak widths for both Si-O-Si and Si-O-Al increase significantly with increasing Fe_2O_3 contents, and there is no significant difference in their trends. Here, the $\text{Fe}^{3+}/\Sigma\text{Fe}$ of the $\text{NaAlSi}_3\text{O}_8 + \text{Fe}_2\text{O}_3$ glasses is ~ 0.5 , which indicates that similar fractions of Fe^{2+} and Fe^{3+} coexist. The fact that there is no obvious change in the apparent oxygen fractions with Fe_2O_3 stems from the simultaneous effect of Fe^{2+} and Fe^{3+} on each oxygen site. First, Fe^{3+} may interact more strongly with Si-O-Si,

resulting in a decrease in the actual Si-O-Si fraction. While there is a compositional difference between $\text{NaAlSi}_3\text{O}_8 + \text{Fe}_2\text{O}_3$ glasses and $\text{Na}(\text{Al}_{1-x}\text{Fe}_x)\text{Si}_3\text{O}_8$ glasses, the ^{29}Si NMR results showed that the Fe^{3+} has a preferential effect on the $\text{Q}^{4\text{Si}}(m\text{Al})$ species with smaller m (i.e., Si-rich framework). Second, the spatial proximity between Fe^{2+} and Al causes a selective decrease in the apparent fraction of the Si-O-Al site due to the paramagnetic effect. Thus, we expect that the dual effects are somewhat compensated. The changes in the oxygen fractions of $\text{NaAlSi}_3\text{O}_8 + \text{Fe}_2\text{O}_3$ glasses (with $\text{Fe}^{3+}/\Sigma\text{Fe} = 0.5$) have not been clearly observed. There is a possibility of the presence of Fe^{2+} -NBO (i.e., Fe^{2+} -O-Si and Fe^{2+} -O-Al) because Fe^{2+} could play a dual role as a charge-balancing and modifying cation, similar to Mg^{2+} and Ca^{2+} in aluminosilicate glasses (see discussion Section 5.4.2 below). Here, the oxygen sites directly bonded to iron, such as Fe^{3+} -BO and Fe^{2+} -NBO, cannot be observed in the ^{17}O NMR spectra.

5.3.4. The changes in the local configurations around framework cations and oxygen sites with increasing excess Fe_2O_3 in the $\text{CaAl}_2\text{Si}_2\text{O}_8$ glasses ($\text{CaAl}_2\text{Si}_2\text{O}_8 + \text{Fe}_2\text{O}_3$): ^{29}Si , ^{27}Al , and ^{17}O NMR results

5.3.4.1. ^{29}Si NMR results

Figure 5-10 presents the ^{29}Si MAS NMR spectra for the $\text{CaAl}_2\text{Si}_2\text{O}_8$ glasses with varying amount of Fe_2O_3 ($\text{CaAl}_2\text{Si}_2\text{O}_8 + \text{Fe}_2\text{O}_3$, $\text{Fe}^{3+}/\Sigma\text{Fe} \sim 0.3$). The spectra for $\text{CaAl}_2\text{Si}_2\text{O}_8 + \text{Fe}_2\text{O}_3$ glasses with varying Fe_2O_3 content show a single broad peak corresponding to $\text{Q}^{4\text{Si}}(m\text{Al})$ species centered at ~ 87 ppm. The peak position of $\text{CaAl}_2\text{Si}_2\text{O}_8$ glasses ($\text{Si}/\text{Al} = 1$) is located at a lower frequency than that of $\text{NaAlSi}_3\text{O}_8$ glasses ($\text{Si}/\text{Al} = 3$), which indicates that $\text{Q}^{4\text{Si}}(3\text{Al})$ and $\text{Q}^{4\text{Si}}(4\text{Al})$ are predominant in the series of $\text{CaAl}_2\text{Si}_2\text{O}_8$ glasses (Lee and Stebbins, 1999). The trend of decreasing ^{29}Si signal intensity with

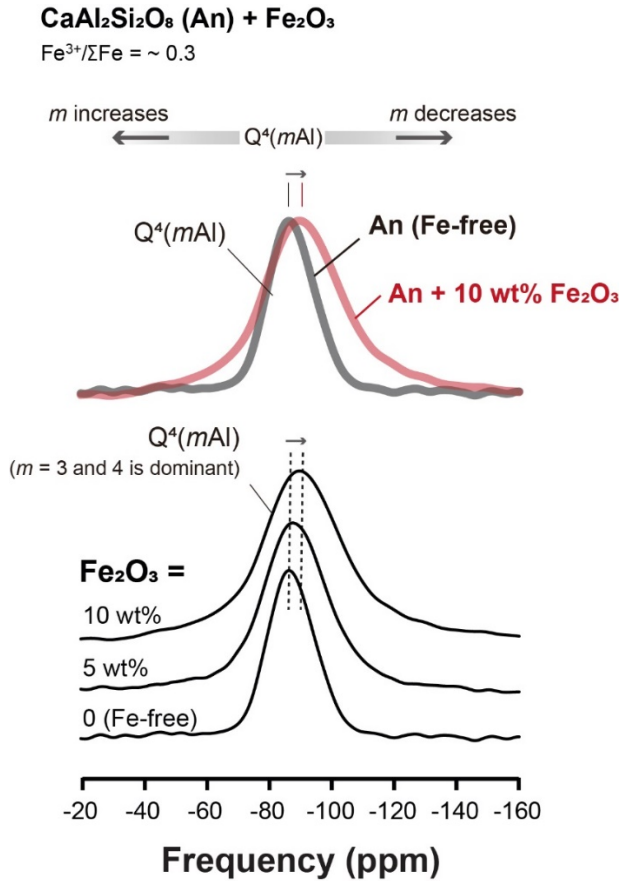


Figure 5-10. ²⁹Si MAS NMR spectra for CaAl₂Si₂O₈ glasses with varying additional Fe₂O₃ (0, 5, and 10 wt% Fe₂O₃). The spectra are plotted on a normalized vertical scale. A comparison of the ²⁹Si MAS NMR spectra for the iron-free (thick grey line) and iron-bearing (thick red line) is also shown.

increasing Fe₂O₃ in Fe²⁺-dominant CaAl₂Si₂O₈ + Fe₂O₃ glasses is similar to those in Fe³⁺-dominant Na(Al_{1-x}Fe_x)Si₃O₈ glasses and NaAlSi₃O₈ + Fe₂O₃ glasses (Fe³⁺/ΣFe ~0.5) (see Section 5.4.5 for detailed discussion).

As the Fe₂O₃ content increases, the peak position for CaAl₂Si₂O₈ systematically changes toward a lower frequency from -87.2 ppm (Fe-free), through -88.5 ppm (5 wt% Fe₂O₃), to -90.3 ppm (10 wt% Fe₂O₃). In addition, the fraction in the Q⁴_{Si}(*m*Al) species with lower *m* number (i.e., 1 and 2) apparently increases with increasing Fe₂O₃. Note that the changes in peak position and shape of ²⁹Si NMR spectra for the Fe²⁺-dominant CaAl₂Si₂O₈ + Fe₂O₃ glasses show opposite trends to those for the Fe³⁺-dominant Na(Al_{1-x}Fe_x)Si₃O₈ glasses.

Again, based on the premise of no preferential paramagnetic effect on each Q⁴_{Si}(*m*Al) species, these observations suggest that the average *m* of Q⁴_{Si}(*m*Al) may decrease and/or there is a relatively large increase in the degree of topological disorder of the Q⁴_{Si}(*m*Al) species with a larger *m* number (i.e., 3 and 4), compared to that with a smaller *m* number (i.e., 1 and 2) for the Fe²⁺-dominant CaAl₂Si₂O₈ glasses. Alternatively, if there are preferential paramagnetic effects in specific Q⁴_{Si}(*m*Al) species due to their proximity to Fe, the apparent increase in the fraction of Q⁴_{Si}(*m*Al) with a smaller *m* number with increasing Fe₂O₃ content for the Fe²⁺-dominant CaAl₂Si₂O₈ + Fe₂O₃ glasses suggests preferential proximity between Fe²⁺ and Q⁴_{Si}(*m*Al) with a larger *m* number. As mentioned in Section 5.3.2.1, both contributions (i.e., structural changes and paramagnetic effect) can lead to observed spectral changes. Thus, it is difficult to interpret changes in spectra considering each individual case. Nevertheless, in both cases, changes in the Q⁴_{Si}(*m*Al) with a larger *m* number appear to be more pronounced than in Q⁴_{Si}(*m*Al) with a smaller *m* number. This suggests that the local configurations of Al for the

Fe²⁺-dominant CaAl₂Si₂O₈ glasses would be perturbed by increasing Fe₂O₃ (see Section 5.3.4.2).

5.3.4.2. ²⁷Al NMR results

²⁷Al MAS NMR results. Figure 5-11 presents normalized ²⁷Al MAS NMR spectra for CaAl₂Si₂O₈ glasses with varying Fe₂O₃ (Fe³⁺/ΣFe ~0.3) where the broad peak is at ~49.2 ppm (corresponding to ⁴Al). The peak width of Fe-free CaAl₂Si₂O₈ glass (~51 ppm) is much greater than that of Fe-free NaAlSi₃O₈ glass (~25 ppm), suggesting that the degree of network distortion around Al and/or the configurational disorder is much larger for CaAl₂Si₂O₈ glasses than NaAlSi₃O₈ glasses. With increasing Fe₂O₃ content, the ²⁷Al signal intensities for CaAl₂Si₂O₈ glasses decrease (see Section 5A-4). Note that the trend of the decreasing ²⁷Al signal intensity with increasing Fe content is similar for all the series of samples, consistent with the ²⁹Si MAS NMR results (see Section 5.4.5).

The ⁴Al peak width of CaAl₂Si₂O₈ + Fe₂O₃ glasses increases significantly with increasing Fe₂O₃, and the peak shape also changes from asymmetrical (i.e., quadrupolar line shape) to symmetrical (i.e., Lorentzian broadening due to paramagnetic effect), similar to the ⁴Al peak for Na(Al_{1-x}Fe_x)Si₃O₈ and NaAlSi₃O₈ + Fe₂O₃ glasses. However, the ⁴Al peak maxima for the CaAl₂Si₂O₈ + Fe₂O₃ glasses apparently moves toward lower frequencies, from 49 ppm (Fe-free), through 47 ppm (5 wt% Fe₂O₃), to 46 ppm (10 wt% Fe₂O₃), unlike the ²⁷Al NMR results for Na(Al_{1-x}Fe_x)Si₃O₈ and NaAlSi₃O₈ + Fe₂O₃ glasses. Thus, the observed spectral changes (i.e., the paramagnetic broadening with systematic peak shifts) demonstrate iron-induced structural perturbation of the Al sites in the CaAl₂Si₂O₈ glasses. Note that the pronounced changes in Al peaks of CaAl₂Si₂O₈ with increasing Fe²⁺

$\text{CaAl}_2\text{Si}_2\text{O}_8$ (An) + Fe_2O_3

$\text{Fe}^{3+}/\Sigma\text{Fe} = \sim 0.3$

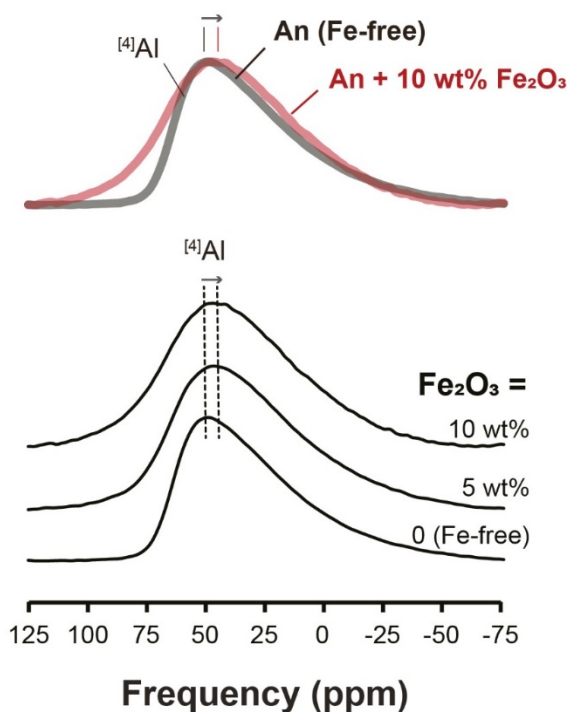


Figure 5-11. ^{27}Al MAS NMR spectra for $\text{CaAl}_2\text{Si}_2\text{O}_8$ glasses with varying additional Fe_2O_3 (0, 5, and 10 wt% Fe_2O_3) at 9.4 T. The spectra are plotted on a normalized vertical scale. The rotor backgrounds were subtracted from the spectra (see Section 5A-5). A comparison of the ^{27}Al MAS NMR spectra for the iron-free (thick grey line) and iron-bearing (thick red line) is also shown.

are also consistent with the trend shown in the ^{29}Si NMR results (Section 5.3.4.1). As shown in the ^{29}Si NMR results of $\text{CaAl}_2\text{Si}_2\text{O}_8 + \text{Fe}_2\text{O}_3$ glasses, the changes in Q^4 species with a larger number of Al as the second nearest neighbors are more pronounced, suggesting that the Fe^{2+} preferentially interacts with the Al-rich framework. These observed changes in ^{27}Al MAS NMR spectra imply spatial proximity between Al and Fe^{2+} . However, it is also necessary to discuss the possibility that the slight shift of peak maxima toward the direction of negative chemical shift may be due to changes in local configuration around the Al. If the peak shift stems from actual structural changes, the observed peak shift may be due to an increase in topological disorder around Al and/or the formation of highly coordinated Al (i.e., $^{[5]}\text{Al}$) with increasing Fe^{2+} content in $\text{CaAl}_2\text{Si}_2\text{O}_8$ glasses. For robust spectral analysis, ^{27}Al 3QMAS NMR experiments are necessary (see below).

^{27}Al 3QMAS NMR results. Figure 5-12A shows the ^{27}Al 3QMAS NMR spectra for the $\text{CaAl}_2\text{Si}_2\text{O}_8$ glasses with varying additional Fe_2O_3 at 9.4 T (17 kHz) and 14.1 T (35 kHz). For the iron-free $\text{CaAl}_2\text{Si}_2\text{O}_8$ glass, $^{[4]}\text{Al}$ is dominant and a minor but detectable amount of $^{[5]}\text{Al}$ is observed in the 2D NMR spectra, which is consistent with previous NMR studies (Neuville et al., 2004b, 2006; Stebbins et al., 2008; Xue and Kanzaki, 2008). The presence of $^{[5]}\text{Al}$ (~ -25 ppm in the isotropic projection) in the $\text{CaAl}_2\text{Si}_2\text{O}_8$ glass (i.e., fully-polymerized Ca-aluminosilicate glass) is associated with the NBO (i.e., Ca-NBO), which is observed in the current ^{17}O NMR results (see Section 5.3.4.3 below). For $\text{CaAl}_2\text{Si}_2\text{O}_8 + \text{Fe}_2\text{O}_3$ glasses, it is difficult to resolve a small amount of $^{[5]}\text{Al}$, even in the 2D spectra, because of severe peak broadening and overlap with the spinning sideband as the Fe_2O_3 content increases. The 2D ^{27}Al NMR spectra obtained at 14.1 T with 35 kHz of spinning speed show much enhan-

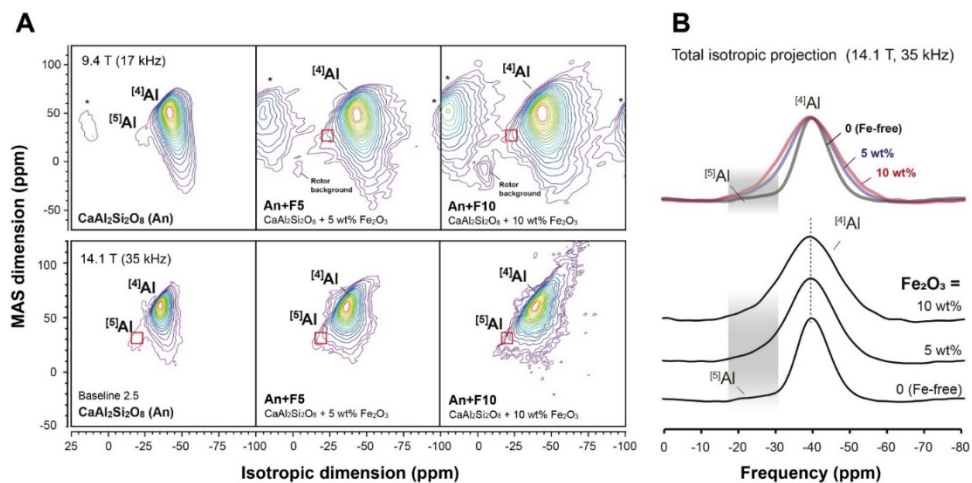


Figure 5-12. (A) 2D ^{27}Al 3QMAS NMR spectra for $\text{CaAl}_2\text{Si}_2\text{O}_8$ glasses with varying additional Fe_2O_3 (0, 5, and 10 wt% Fe_2O_3) at 9.4 T (top) and 14.1 T (bottom), as labeled. Contour lines are drawn from 8% to 93% relative intensity with a 5% increment and two additional lines at 4 and 6% levels. The red square in the spectra refers to the expected position of ^{51}Al . (B) Total isotropic projection of ^{27}Al 3QMAS NMR spectra. A comparison of spectrum for the iron-free (thick grey line) and iron-bearing (thick red line) is also shown.

ced resolution among the Al configurations. In addition, the tail of the ^{41}Al peak, extending in the diagonal direction in the 2D spectra obtained from 14.1 T NMR (Figure 5-12A, top) is shorter than that obtained from 9.4 T NMR (Figure 5-12A, bottom), indicating that the quadrupolar broadening is effectively reduced in the high-field NMR experiment. The spectra at 14.1 T for the $\text{CaAl}_2\text{Si}_2\text{O}_8$ glasses show the predominant ^{41}Al , and the non-negligible fraction of ^{51}Al is also clearly observed in the iron-free $\text{CaAl}_2\text{Si}_2\text{O}_8$ glass. While significant peak broadening makes it difficult to fully resolve and quantify the Al configurations, it can be seen that the signal intensity at the position where the ^{51}Al peak exists (red square in Figure 5-12A) apparently increases with increasing Fe_2O_3 content.

The total isotropic projections of the ^{27}Al 3QMAS NMR spectra for the $\text{CaAl}_2\text{Si}_2\text{O}_8$ glasses with varying Fe_2O_3 at 14.1 T are shown in Figure 5-12B. The ^{41}Al peak width for $\text{CaAl}_2\text{Si}_2\text{O}_8$ glasses abruptly increases as the Fe_2O_3 increases from 0 to 5 wt%, and then further increases as Fe_2O_3 increases from 5 wt% to 10 wt%. The additional increase in peak width with further Fe_2O_3 (to 10 wt%) for $\text{CaAl}_2\text{Si}_2\text{O}_8$ glasses suggests that the extent of topological disorder around ^{41}Al increases with increasing Fe_2O_3 . The increase in topological disorder stems from preferential interaction between Fe^{2+} and Al^{3+} . In addition, the apparent increase in the fraction of ^{51}Al (\sim -25 ppm) with increasing Fe_2O_3 from 0 to 10 wt% is more clearly observed in the total isotropic projection of ^{27}Al 3QMAS NMR spectra. This confirms that the addition of Fe^{2+} (i.e., cations with high field strength) in the $\text{CaAl}_2\text{Si}_2\text{O}_8$ glasses promotes the formation of ^{51}Al .

5.3.4.3. ^{17}O NMR results

While oxygen sites are not completely resolved in ^{17}O MAS NMR spectra (see Section 5A-8), the ^{17}O 3QMAS NMR spectra of the $\text{CaAl}_2\text{Si}_2\text{O}_8 + \text{Fe}_2\text{O}_3$ glasses show that Ca-NBO (at ~ -69 ppm in isotropic dimension) and three types of BOs (i.e., Si-O-Si, Si-O-Al, and minor fraction of Al-O-Al) are partially resolved (Figure 5-13A). The presence of Ca-NBO in the glasses of anorthite composition (i.e., charge-balanced join), which has also previously been reported (e.g., Stebbins and Xu, 1997; Xu et al., 1998), indicates that Ca^{2+} can play a dual roles as a charge-balancing and a network-modifying cation. The BO sites are not resolved even for the iron-free $\text{CaAl}_2\text{Si}_2\text{O}_8$ glass, making it difficult to observe changes in each BO site with increasing Fe_2O_3 . Further, peak broadening with increasing Fe_2O_3 also hampers the quantitative analysis. However, the Ca-NBO peak is effectively resolved in the 2D ^{17}O NMR spectra for the Fe-bearing $\text{CaAl}_2\text{Si}_2\text{O}_8$ glasses, providing the possibility for a qualitative description of changes in the peak widths and relative fractions of Ca-NBO and BOs with increasing Fe. In particular, preferential broadening in the Ca-NBO and BOs peaks is not observed, and the peak intensity of Ca-NBO does not tend to increase or decrease noticeably, despite an increase in Fe_2O_3 content up to 10 wt%.

The Ca-NBO (~ -68 ppm) and BOs (~ -43 ppm) peaks for $\text{CaAl}_2\text{Si}_2\text{O}_8 + \text{Fe}_2\text{O}_3$ glasses are also well-resolved in the total isotropic projection of the 3QMAS NMR spectra for $\text{CaAl}_2\text{Si}_2\text{O}_8 + \text{Fe}_2\text{O}_3$ glasses (Figure 5-13B). Qualitatively, the relative fractions of BOs (Si-O-Si + Si-O-Al + small fraction of Al-O-Al) and Ca-NBO are also consistent with increasing Fe_2O_3 . These observations may stem from the simultaneous decrease in the apparent fractions of BOs and Ca-NBO. This is because Fe^{2+} can play dual roles as a charge-balancing and a network-modifying cations, which is similar to Ca^{2+}

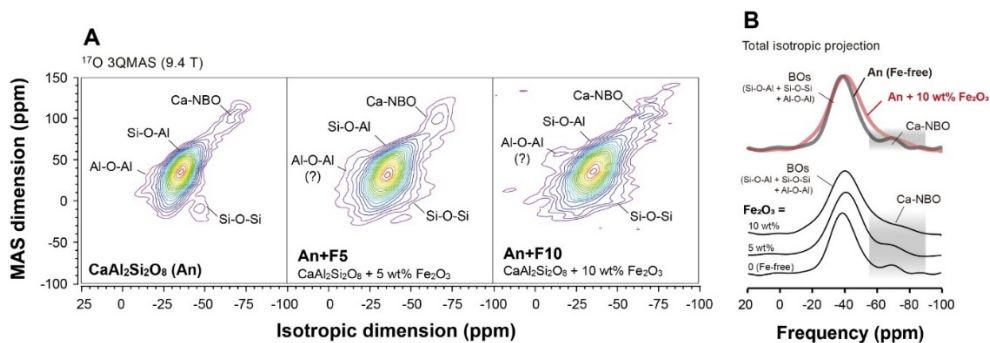


Figure 5-13. (A) ^{17}O 3QMAS NMR spectra for $\text{CaAl}_2\text{Si}_2\text{O}_8$ glasses with varying Fe_2O_3 contents (0, 5, and 10 wt% Fe_2O_3) at 9.4 T, as labeled. Contour lines are drawn from 13% to 98% relative intensity with a 5% increment and two additional lines at 5.5% and 9% levels. (B) Total isotropic projection of ^{17}O 3QMAS NMR spectra. A comparison of spectrum for the iron-free (thick grey line) and iron-bearing (thick red line) is also shown.

in the glasses. In particular, the formation of $[\text{Fe}^{2+}, \text{Ca}]\text{-NBO}$ is expected due to the network-modifying Fe^{2+} , resulting in a decrease in the apparent intensity of Ca-NBO. In addition, it is expected that the signal intensity of BOs would decrease due to the charge-balancing Fe^{2+} , which is preferentially located around oxygen sites related to Al, such as Si-O-Al and Al-O-Al. Note that changes in the signal intensity of specific BO sites could not be observed due to the severe overlap. Preferential interaction between Fe^{2+} and Al is also suggested in the results of ^{29}Si and ^{27}Al NMR (Section 5.3.4).

5.4. Discussion

Based on the predicted role of Fe^{3+} (network-forming cation) and Fe^{2+} (network-modifying cation), the anticipated changes in the Al and O environments with increasing Fe^{3+} and Fe^{2+} can be partly predicted: if network-forming Fe^{3+} is added to charge-balanced aluminosilicate glasses, the overall composition of the glasses would be peraluminous [$\text{M}^{n+}\text{O}_{n/2}/(\text{Al}_2\text{O}_3 + \text{Fe}_2\text{O}_3) < 1$] (Figure 5-1). So, the fraction of highly-coordinated framework cation (i.e., $^{[5]}\text{Al}^{3+}$ and $^{[5]}\text{Fe}^{3+}$) would increase. If the Fe^{2+} content increases in charge-balanced aluminosilicate glasses, the peralkalinity [i.e., $\text{M}^{n+}\text{O}_{n/2}/(\text{Al}_2\text{O}_3 + \text{Fe}_2\text{O}_3)$] would increase, which increases the NBO fraction. In such depolymerized melts and glasses, multiple NBO configurations including Na-NBO, Ca-NBO, Fe^{2+} -NBO, and/or mixed-NBO (i.e., $[\text{Na},\text{Fe}^{2+}]$ -NBO and $[\text{Ca},\text{Fe}^{2+}]$ -NBO) may form. If equal amounts of Fe^{2+} and Fe^{3+} are added in the glasses along the charge-balanced join, the degree of network polymerization is not expected to vary. Nevertheless, the detailed nature of structural disorder may vary. For example, the relative populations of oxygen sites (i.e., Si-O-Si, Si-O-Al, Si-O- Fe^{3+} , and Al-O- Fe^{3+}) in the iron-bearing aluminosilicate glasses depend on how the framework cations, such as Si, Al, and Fe^{3+} are intermixed. Alternatively, the addition of Fe^{2+} leads to an increase in the extent of overall disorder around Al, increasing the fractions of highly coordinated framework cations and/or NBO. Together with the spectral broadening due to the paramagnetic effect, these structural changes enable an explanation for the observed changes in NMR spectra with increasing iron content in the charge-balanced aluminosilicate glasses of three compositional series [i.e., $\text{Na}(\text{Al}_{1-x}\text{Fe}_x)\text{Si}_3\text{O}_8$, $\text{NaAlSi}_3\text{O}_8 + \text{Fe}_2\text{O}_3$, and $\text{CaAl}_2\text{Si}_2\text{O}_8 + \text{Fe}_2\text{O}_3$ glasses] with difference in iron redox states ($\text{Fe}^{3+}/\Sigma\text{Fe}$). Despite the paramagnetic effect and compositional complexity, the solid-state

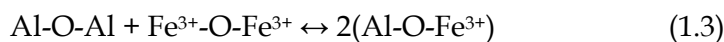
NMR can be successfully applied to provide details about the structure and disorder of iron-bearing Na- and Ca-aluminosilicate glasses. Particularly, the increase in the extent of overall structural disorder around Al and O can be directly probed using multi-nuclear NMR methods. In addition, the experimental data also confirm the spatial proximity between iron and specific Q⁴ species (e.g., Fe³⁺ ... Si-rich framework and Fe²⁺ ... Al-rich framework).

5.4.1. Effect of iron on the extent of structural disorder in iron-bearing albite and anorthite glasses

Effect of Fe³⁺ on the extent of disorder: Insights from the ²⁹Si and ²⁷Al NMR results for Na(Al_{1-x}Fe_x)Si₃O₈ glasses with Fe³⁺/ΣFe of 0.8. The peralkalinity of the Na(Al_{1-x}Fe_x)Si₃O₈ glasses slightly increases by replacing Al with Fe. The current Mössbauer results show that 4-coordinated Fe³⁺ is dominant in Na(Al_{0.5}Fe_{0.5})Si₃O₈ glass. The ²⁷Al 3QMAS NMR spectrum shows the presence of a small amount of ⁵Al, though the composition of Na(Al_{0.5}Fe_{0.5})Si₃O₈ glass is peralkaline. This suggests that the extent of disorder around Al increases by Al-Fe³⁺ substitution. Furthermore, the ²⁹Si NMR results for the Na(Al_{1-x}Fe_x)Si₃O₈ glasses show much larger structural changes in the Si-rich framework [i.e., Q⁴(0,1Al)] compared with the Al-rich framework [i.e., Q⁴(2,3Al)] with increasing Fe³⁺. The preferential interaction and proximity have also been shown in the ²⁷Al NMR. The observed preferential interaction between Fe³⁺ and Si-rich framework suggests an extensive mixing between ⁴Si and ⁴Fe³⁺.

Effect of iron on the Al coordination environments and O configurations of NaAlSi₃O₈ + Fe₂O₃ glasses with Fe³⁺/ΣFe = 0.5. We discuss the structural

changes around Al and O when the equal fraction of Fe³⁺ and Fe²⁺ is added to charge-balanced NaAlSi₃O₈ glass. Because identical fractions of Fe³⁺ (network-forming cation) and Fe²⁺ (network modifier) are added, the extent of polymerization is not expected to vary with Fe₂O₃ content. Nevertheless, the degree of structural disorder tends to increase because the addition of Fe³⁺ can change the way that Si and Al are inter-mixed in the glass networks. For example, the following schemes may describe the extent of mixing among framework cations as Fe³⁺ is incorporated into the aluminosilicate glasses:



The schemes in eqs 1.1 and 1.2 account for the current experimental observation regarding the preferential interaction between Fe³⁺ and Si-rich framework (see above), while the possibility of the presence of Al-O-Fe³⁺ cannot be excluded. Furthermore, because an increase in cation field strength of non-framework cations promotes the formation of ^{5,6}Al in iron-free aluminosilicate glasses (Kelsey et al., 2008b; Neuville et al., 2004b, 2006; Park and Lee, 2014; Schaller and Stebbins, 1998; Stebbins et al., 2008), the extent of disorder increases with an increasing fraction of Fe²⁺ (with Z/r^2 of ~3.56). The ¹⁷O NMR spectra for NaAlSi₃O₈ glasses with 5 wt% and 10 wt% Fe₂O₃ indeed show a non-negligible fraction of Na-NBO, despite signal loss and peak broadening (Figure 5-9). The existence of Na-NBO in Fe₂O₃-bearing NaAlSi₃O₈ glasses suggests Fe²⁺-induced structural disorder. The ²⁷Al NMR results for NaAlSi₃O₈ + Fe₂O₃ glasses show that the formation of ⁵Al is largely prohibited. The absence of ⁵Al in NaAlSi₃O₈ + Fe₂O₃ glasses indicates that Fe³⁺ is more likely to form a highly-coordinated framework (i.e., ⁵Fe³⁺)

when excess Fe³⁺ is added to charge-balanced glasses (in which all Al are polymerized). This is also suggested from the Mössbauer results where isomer shifts of Fe³⁺ ($\delta^{\text{Fe}^{3+}}$) for NaAlSi₃O₈ + 5 wt% and 10 wt% Fe₂O₃ glasses ($\delta^{\text{Fe}^{3+}}$ of ~0.32) are slightly larger than that of Na(Al_{0.5}Fe_{0.5})Si₃O₈ glass ($\delta^{\text{Fe}^{3+}}$ of ~0.27), suggesting a larger Fe³⁺ coordination number in NaAlSi₃O₈ + Fe₂O₃ glasses than that in Na(Al_{0.5}Fe_{0.5})Si₃O₈ glass.

Effect of Fe²⁺ on the extent of disorder around Al and O in CaAl₂Si₂O₈ + Fe₂O₃ glasses with Fe³⁺/ΣFe = 0.3. The addition of iron (with 0.3 of Fe³⁺/ΣFe) to CaAl₂Si₂O₈ glass would lead to an increase in peralkalinity and the NBO fraction. Additionally, the extent of structural disorder in CaAl₂Si₂O₈ glass is expected to increase with Fe₂O₃ due to the relatively high field strength of Fe²⁺. The ²⁷Al NMR showed the Fe₂O₃-induced increase in the ⁵Al fraction and confirmed that the overall degree of disorder increases with increasing Fe₂O₃ content. Furthermore, the ²⁹Si NMR results showed that network-modifying Fe²⁺ would contribute to an increase in topological disorder around the Al-rich framework.

The fraction of Ca-NBO does not change noticeably with increasing Fe₂O₃ content (up to 10 wt%) (Figure 5-13), while the NBO fraction is expected to increase. This may be attributed to the formation of ⁵Al. We propose the following structural schemes to describe Fe²⁺-induced increase in the structural disorder, consistent with the current experimental observations and suggestions:



where network-modifying Fe²⁺ may play a dual role as charge-balancing cation (*) near Al-bearing species and network-modifier, as supported by the

current ^{29}Si and ^{27}Al NMR results where the proximity between Fe^{2+} and Al-rich framework is demonstrated.

5.4.2. The mixing among non-framework cations and selective partitioning of Na^+ , Ca^{2+} , and Fe^{2+} into NBO and BOs

The previous ^{17}O NMR studies have reported the presence of mixed NBO environments in various silicate/aluminosilicate glasses consisting of more than two distinct types of non-framework cations and quantified the degree of mixing between these constituent non-framework cations (Allwardt and Stebbins, 2004; e.g., Dupree et al., 1990; Farnan et al., 1992; Florian et al., 1996; Lee and Sung, 2008; Park and Lee, 2012; Park and Lee, 2016, and references therein; Stebbins et al., 1997). These studies also confirmed that the partitioning of those cations into NBO and/or BOs is heavily dependent on the cation field strength of these cations. In particular, higher field strength cations tend to play a role as network-modifying cations (see, Mysen and Richet, 2018; Park and Lee, 2018 and references therein).

Similar quantification of the aforementioned bond preference is difficult to establish in the iron-bearing aluminosilicate glasses, as most of the iron-bearing species will not be shown in the current ^{17}O NMR spectra. Nevertheless, Na-O-Si and Ca-O-Si are observed in the current ^{17}O NMR spectra for $\text{NaAlSi}_3\text{O}_8 + \text{Fe}_2\text{O}_3$ glasses and those for $\text{CaAl}_2\text{Si}_2\text{O}_8 + \text{Fe}_2\text{O}_3$ glasses, respectively. Considering the similar Z/r^2 between Mg^{2+} (~ 3.86) and Fe^{2+} (~ 3.56), the nature of distribution of Fe^{2+} in iron-bearing glasses is likely to be similar with those of Mg-bearing aluminosilicate glasses. The previous ^{17}O NMR study of Na-Mg aluminosilicate glasses suggested a substantial mixing of Na^+ and Mg^{2+} around NBOs (Park and Lee, 2018). In addition, Mg^{2+} , a high Z/r^2 cation, preferentially acts as a network-modifier near the NBO, while

Na⁺ acts as a charge-balancing cation near BO sites. Considering similarity in the cation field strength of Fe²⁺ and Mg²⁺, the mixing of Na⁺ and Fe²⁺ would be prevalent. Furthermore, as also implied from Na-Mg aluminosilicate glasses, various types of NBO (including Na-NBO, Fe²⁺-NBO, and [Na,Fe²⁺]-NBO) are present in iron-bearing NaAlSi₃O₈ glasses. The previous ¹⁷O NMR study of CaO-MgO-Al₂O₃-SiO₂ glasses has suggested non-random distribution of Ca²⁺ and Mg²⁺ around NBO and BO (e.g., Si-O-Al) (Park and Lee, 2012). Again, considering a minor difference in cation field strengths of Mg²⁺ and Fe²⁺, the nonrandom distribution of Ca²⁺ and Fe²⁺ in the iron-bearing aluminosilicate glasses is also expected. Furthermore, the spatial proximity between Fe²⁺ and Al-bearing BO sites is also expected, as inferred from the ²⁹Si and ²⁷Al NMR spectra (Figures 5-10 and 5-11, see Section 5.4.1 above).

5.4.3. Iron-induced changes in NMR peak intensities

Figure 5-14 shows the variations in the ²⁹Si, ²⁷Al, and ¹⁷O NMR signal intensities of Na(Al_{1-x}Fe_x)Si₃O₈ (Fe³⁺/ΣFe = ~0.8), NaAlSi₃O₈ + Fe₂O₃ glasses (Fe³⁺/ΣFe = ~0.5), and CaAl₂Si₂O₈ + Fe₂O₃ glasses (Fe³⁺/ΣFe = ~0.3) with varying iron content (atom%). The peak intensities of the Fe-bearing glasses are normalized with respect to those of iron-free samples and the weight of each glass in the rotor. The ²⁹Si (Figure 5-14A) and ¹⁷O (Figure 5-14C) signal intensities decrease exponentially with increasing iron content. The similar trends have also been reported in the previous NMR studies for Na₂O-Fe₂O₃-SiO₂ and MgO-FeO-SiO₂ glasses (Kim and Lee, 2019; Kim et al., 2016b). The trends of the decreasing ²⁹Si and ¹⁷O signal intensity with increasing Fe content are similar regardless of the glass composition. This indicates that the spatial proximity between Fe-²⁹Si and Fe-¹⁷O within the *r_c* may not be heavily dependent on the iron redox ratio (Fe³⁺/ΣFe) and the type of non-framework cation (i.e., Na⁺ and Ca²⁺). The ²⁷Al NMR signal also exponentially decreases

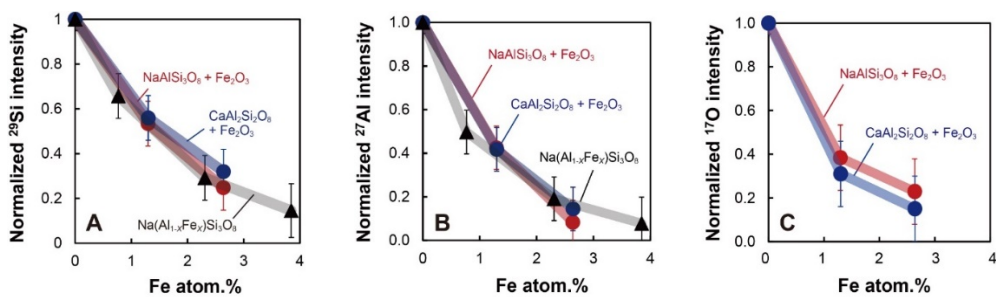


Figure 5-14. Variations in the (A) ^{29}Si , (B) ^{27}Al , and (C) ^{17}O MAS NMR signal intensities of $\text{Na}(\text{Al}_{1-x}\text{Fe}_x)\text{Si}_3\text{O}_8$ (red circles), $\text{NaAlSi}_3\text{O}_8 + \text{Fe}_2\text{O}_3$ glasses (black triangles), and $\text{CaAl}_2\text{Si}_2\text{O}_8 + \text{Fe}_2\text{O}_3$ glasses with varying iron content (atom%). The lines are to guide the eye.

(Figure 5-14B), consistent with ^{29}Si NMR results: the normalized ^{27}Al peak intensities for the $\text{Na}(\text{Al}_{1-x}\text{Fe}_x)\text{Si}_3\text{O}_8$ glasses (black line in Figure 5-14B) with varying X [$=\text{Fe}/(\text{Fe}+\text{Al})$] decrease from 1 (Fe-free), through 0.5 ($X = 0.1$) and 0.2 ($X = 0.3$), to 0.1 ($X = 0.5$). The signal intensity of the $\text{NaAlSi}_3\text{O}_8 + \text{Fe}_2\text{O}_3$ glasses (red line) decreases from 1 (Fe-free), through 0.4 (5 wt% Fe_2O_3 , 1.3 atom%), to 0.1 (10 wt% Fe_2O_3 , 2.6 atom%) with increasing Fe_2O_3 , and that for the $\text{CaAl}_2\text{Si}_2\text{O}_8 + \text{Fe}_2\text{O}_3$ glasses (blue line) also decreases from 1 (Fe-free), through 0.4 (5 wt% Fe_2O_3 , 1.3 atom%), to 0.1 (10 wt% Fe_2O_3 , 2.6 atom%). The similar trends for the signal loss, regardless of the compositional difference (i.e., Na^+ and Ca^{2+}), indicate that the spatial proximity between Fe and Al is similar within the r_c (i.e., removing spins near iron up to ~ 3.3 Å). The preferential broadening of the peak results from the interaction between nuclear spins and unpaired electron with a distance beyond 3.3 Å (Kim and Lee, 2019). The selective loss in NMR signal for distinct structural units thus

allowed us to infer the possibility of the heterogeneous distribution of iron in the glass network at nanoscale (beyond the r_c). As shown in the current ^{29}Si NMR results, the Fe^{3+} preferentially interacts with the Si-rich framework and Fe^{2+} is expected to be in proximity to BOs. The observed preferential broadening in specific $\text{Q}^4(m\text{Al})$ species suggests the preferential distribution of iron around Q^4 species.

Finally, we briefly address the limitations and uncertainties of the structural interpretations of the observed spectral changes. Despite the aforementioned progress, peak broadening of NMR peaks accompanied by the low signal-to-noise ratio of spectra makes it intrinsically difficult to fully resolve the specific atomic environments, such as Na-NBO and ^{51}Al : the changes in NBO fraction and the formation of highly coordinated Al are expected to prevail with a further increase in iron content. However, this also results in an enhanced peak broadening, which obscures the quantification of observed changes. Furthermore, NMR studies of iron-bearing glasses inevitably have inherent limitations: the oxygen species, such as Fe^{2+} -NBO and Fe^{3+} -BO cannot be shown in the current NMR spectra. Thus, discussion on the existence of mixed-NBO (i.e., $[\text{Na},\text{Fe}^{2+}]$ -NBO and $[\text{Ca},\text{Fe}^{2+}]$ -NBO) and $^{51}\text{Fe}^{3+}$ in charge-balanced glass is somewhat speculative. It is also difficult to quantify the degree of intermixing among framework cations (i.e., Si, Al, and Fe^{3+}) due to the presence of hidden species. In particular, it is expected that Al^{3+} -O- Fe^{3+} may exist when the configurational disorder among framework cations (Si^{4+} , Al^{3+} , and Fe^{3+}) increases, similar to the existence of Al-O-Al in the glasses (which indicates the violation of the Al-avoidance rule). However, direct observation of Al^{3+} -O- Fe^{3+} in the NMR spectra is not feasible. Additionally, while it is known that Al-NBO is energetically much less favorable (Allwardt et al., 2003; Lee et al., 2005; Lee and Stebbins, 2006), Al-

O-Fe²⁺ (i.e., Al-NBO) could be formed in Fe-bearing aluminosilicate glasses due to Fe²⁺- and Fe³⁺-induced structural disorder. Note that previous study of Si-rich and highly polymerized rare earth element (REE)-bearing aluminosilicate glasses has indicated that there is a noticeable fraction of Al-NBOs (Jaworski et al., 2015).

We also note that the experimental conditions for synthesizing ¹⁷O-enriched sample, unfortunately, result in a diversity of iron redox ratios for the glasses. Thus, further experimental studies, including experiments for aluminosilicate glasses with systematically constrained redox ratio, will help to quantitatively advance the current qualitative interpretation of the changes in NMR spectra with increasing iron content.

5.4.4. Implications

Effect of the structural disorder on the transport properties of iron-bearing silicates melts. The observed increase in the extent of structural disorder in charge-balanced Na- and Ca-aluminosilicate glasses with increasing Fe²⁺ and Fe³⁺ can account for the iron-induced changes in viscosity of the corresponding melts (such as rhyolitic and pantelleritic melts, which are nominally fully polymerized melts). The calculated activation enthalpy of viscous flow of natural rhyolitic melts decreases rapidly from ~180 to ~150 kJ/mol with a slight increase in NBO/T (Giordano and Dingwell, 2003; Giordano et al., 2004; Giordano et al., 2008; Mysen and Richet, 2018). While we could not directly quantify the fraction of NBO of the glasses in this study, the formation of NBO in glass with charge-balanced join with increasing iron content is observed. This suggests that the degree of polymerization decreases with increasing Fe²⁺ (thus, increasing peralkalinity). Thus, taking into consideration the relationship between viscosity (μ) and the NBO

fraction [i.e., $\mu \propto 1/\exp(A + X_{\text{NBO}})$, where A is constant depending on glass composition] (Giordano and Dingwell, 2003; Mazurin, 1983), the viscosity of aluminosilicate melts with charge-balanced join (at constant temperature) is expected to decrease with increasing iron contents. In addition, the melt viscosity is dependent on the configurational (S_{config}) and topological entropy (S_{topo}) (Adam and Gibbs, 1965; Lee, 2005; Neuville and Richet, 1991; Richet, 1984). In particular, the melt viscosity is expected to decrease with increasing configurational and topological disorder. The observed increase in the overall structural disorder may contribute to a decrease in the viscosity when iron content increases in charge-balanced aluminosilicate melts. Note that we investigated the structure of the glasses quenched from supercooled liquid at the glass-transition temperature not at the melting temperature. While the effect of the quench rate (and thus the fictive temperature) on the Q species, Al environments, and oxygen configurations on iron-bearing silicate glasses remains further investigation (e.g., Stebbins, 1995 for the review; 2008).

Formation of $^{51}\text{Fe}^{3+}$ in iron-bearing aluminosilicate melts at ambient and high pressure. The ^{51}Al in charge-balanced aluminosilicate glasses has been linked to the melt viscosity and the glass transition temperatures (Le Losq et al., 2014; Neuville et al., 2004b; Neuville et al., 2008; Stebbins et al., 2000). Recent study has suggested that an increasing proportion of ^{51}Al promotes a non-linear decrease in the activation energy for viscous flow, and thus increase the melt fragility (Le Losq et al., 2014). The current ^{27}Al NMR results show the presence of ^{51}Al in $\text{Na}(\text{Al}_{0.5}\text{Fe}_{0.5})\text{Si}_3\text{O}_8$ glass. Furthermore, the proportion of highly coordinated ^{51}Al in $\text{CaAl}_2\text{Si}_2\text{O}_8$ glasses increases with increasing Fe^{2+} content. Taking into consideration the role of highly coordinated framework cations on the melt properties, it is expected that the increase in iron content in charge-balanced aluminosilicate glasses also

promotes an increase in melt fragility. The increase in the fraction of $^{[5,6]}\text{Al}$ has precedence over that of $^{[5,6]}\text{Si}$ (e.g., Lee, 2010; Lee et al., 2012b). The ^{27}Al NMR results of $\text{NaAlSi}_3\text{O}_8 + \text{Fe}_2\text{O}_3$ glasses, showing the absence of $^{[5]}\text{Al}$, imply that the highly coordinated Fe^{3+} (i.e., $^{[5]}\text{Fe}^{3+}$) is formed when excess Fe^{3+} is added to charge-balanced aluminosilicate glasses, and Fe^{3+} is more likely to form highly-coordinated framework (i.e., $^{[5]}\text{Fe}^{3+}$ rather than $^{[5]}\text{Al}$). Further experimental effort is needed to reveal the proposed preferential formation of $^{[5]}\text{Fe}^{3+}$ or $^{[5]}\text{Al}$ under compression.

5.5. Conclusion

While the properties of iron-bearing aluminosilicate melts are expected to depend on the local structures around the framework cations (such as Al and Si) and the extent of network polymerization, there had been no direct experimental observations of changes in the local environments around cations and anions constituting aluminosilicate glasses (i.e., Al, O, and Si) with increasing iron content. This lack of information is mainly because the presence of paramagnetic cation (i.e., Fe) causes the loss of NMR signals and significant peak broadening, thereby obscuring structural information. Recent advances in high-resolution NMR, particularly, 3QMAS NMR techniques involving ^{17}O and ^{27}Al enable us to delve into the structural details of iron-bearing oxide glasses. In this study, we investigated the detailed local structures around Al, along with those around O and Si, in the charge-balanced aluminosilicate glasses of three compositional series [i.e., $\text{Na}(\text{Al}_{1-x}\text{Fe}_x)\text{Si}_3\text{O}_8$, $\text{NaAlSi}_3\text{O}_8 + \text{Fe}_2\text{O}_3$, and $\text{CaAl}_2\text{Si}_2\text{O}_8 + \text{Fe}_2\text{O}_3$ glasses] with difference in iron redox states ($\text{Fe}^{3+}/\Sigma\text{Fe}$) using high-resolution solid-state

NMR spectroscopy and provided atomistic insights into the macroscopic properties of aluminosilicate melts with varying iron content.

The NMR results for iron-bearing aluminosilicate glasses indicate that Fe^{3+} interacts more strongly with the Si-rich framework (e.g., Si-O-Si) than the Al-rich framework, while Fe^{2+} may have proximity toward oxygen clusters involving Al (e.g., Si-O-Al and Al-O-Al). The ^{17}O 3QMAS NMR spectra for $\text{NaAlSi}_3\text{O}_8 + \text{Fe}_2\text{O}_3$ glasses provide evidence for the presence of Na-O-Si. This suggests a decrease in the degree of polymerization with increasing Fe^{2+} , while the overall structural disorder increases due mainly to the addition of high Z/r^2 cation (i.e., Fe^{2+}). The absence of ^{51}Al in $\text{NaAlSi}_3\text{O}_8 + \text{Fe}_2\text{O}_3$ glasses implies that the highly coordinated Fe^{3+} (i.e., $^{51}\text{Fe}^{3+}$) is formed when excess Fe^{3+} is added to charge-balanced aluminosilicate glasses, and Fe^{3+} is more likely to form a highly-coordinated framework (i.e., $^{51}\text{Fe}^{3+}$ rather than ^{51}Al). In contrast, the apparent increase in the ^{51}Al fraction in the $\text{CaAl}_2\text{Si}_2\text{O}_8$ glasses with increasing Fe_2O_3 is observed, confirming that the addition of Fe^{2+} promotes the overall structural disorder.

While the NMR signal intensity for ^{29}Si , ^{17}O , as well as ^{27}Al decreases exponentially with increasing iron content regardless of the glass composition, the observed changes in NMR spectra with increasing iron content in the charge-balanced aluminosilicate glasses allowed us to reveal the effect of iron on the degree of network polymerization, iron-induced evolution of network topology around Al and Si. The results also confirmed that the degree of structural disorder in aluminosilicate glasses tends to increase with increasing Fe^{3+} and Fe^{2+} content. The observed increase in the overall extent of structural disorder in charge-balanced Na- and Ca-aluminosilicate glasses with increasing Fe^{2+} and Fe^{3+} may contribute to an observed decrease in the melt viscosity.

APPENDIX

5A-1. Local configurations around iron in iron-bearing *silicate* glasses

The Fe³⁺-O distance has been reported to decrease with increasing Fe³⁺ content in the (Na₂O)_{0.3}·(SiO₂)_{0.7} – (Na₂O)_{0.3}·(Fe₂O₃)_{0.7} join (Holland et al., 1999; Johnson et al., 1999). The decrease in the isomer shifts of the Na₂Si₂O₅-Fe₂O₃ join with increasing Fe³⁺ content obtained from Mössbauer spectroscopy also indicates that the Fe³⁺-O distance decreases with increasing Fe³⁺ (Dingwell and Virgo, 1988; Virgo et al., 1983). Earlier studies for Na₂O-Fe₂O₃-SiO₂ and CaO-FeO-SiO₂ glasses have shown that the average coordination number of iron is higher than 4, thereby suggesting the presence of highly-coordinated Fe (i.e., ^{5,6}Fe) (Drewitt et al., 2013; Farges et al., 2004; Farges et al., 2005; Henderson et al., 1995; Iwamoto et al., 1987; Rossano et al., 2000).

Earlier and recent Raman spectroscopy studies for Na₂SiO₃-NaFe³⁺Si₂O₆ glasses have suggested that the structural role of Fe³⁺ changes with varying Na/Fe ratio and the extent of network polymerization increases as Fe³⁺ content increases, which is primarily considered as a network-forming cation (similar with Al³⁺) (Cochain et al., 2012; Farges et al., 2004; Hannoyer et al., 1992; Holland et al., 1999; Mysen et al., 1980; Mysen and Virgo, 1985). By contrast, the addition of network-modifying Fe²⁺ (similar with Mg²⁺) has been known to depolymerize the silicate network (Mao et al., 1973; Mysen and Virgo, 1978; Nolet, 1980; Rossano et al., 2000). The coordination number of Fe³⁺ and Fe²⁺ varies from 4 to 6 depending on the composition of silicate glasses and melts (Alberto et al., 1996; Calas and Petiau, 1983; Farges et al., 2004; Farges et al., 2005; Jackson et al., 2005; Rossano et al., 2000; Waychunas et al., 1988).

5A-2. Changes in atomic structure of iron-free aluminosilicate glasses with degree of network polymerization

Figure 5-1 in the main text illustrates a ternary composition diagram with SiO_2 , $\text{M}^{n+}\text{O}_{n/2}$ (M refers to non-framework cations, such as Na^+ , Ca^{2+} , and Fe^{2+}), and Z_2O_3 [Z refers to framework cations (except SiO_2), such as Al^{3+} and Fe^{3+}] as the respective vertices. For *iron-free* peralkaline glasses ($\text{M}^{n+}\text{O}_{n/2}/\text{Al}_2\text{O}_3 > 1$), Al^{3+} is commonly 4-coordinated. A small amount of $^{[5,6]}\text{Al}$ can often be observed if the field strength (Z/r^2 , where Z refers to the charge and r refers to the ionic radius) of network-modifying M^{n+} is high (e.g., Mg^{2+}). A fraction of $^{[5,6]}\text{Al}$ tends to increase in peraluminous join (i.e., $\text{M}^{n+}\text{O}_{n/2}/\text{Al}_2\text{O}_3 < 1$). The non-framework cations in peraluminous glasses preferentially act as charge-balancing cations. Along the charge-balanced join ($\text{M}^{n+}\text{O}_{n/2}/\text{Al}_2\text{O}_3 = 1$), the Al coordination number and structural role of non-framework cations are dependent on the Z/r^2 of non-framework cations. In charge-balanced Na-aluminosilicate glasses, $^{[4]}\text{Al}$ is predominant and NBO is not observed. The glasses with high Z/r^2 cations (such as Ca^{2+} and Mg^{2+}), however, can contain a few percent of NBO fractions and $^{[5,6]}\text{Al}$ fractions, even though the nominal NBO/T (based on stoichiometry) is 0 (Lee and Stebbins, 2000a; Neuville et al., 2004b; Stebbins and Xu, 1997; Xu et al., 1998)).

5A-3. Detailed NMR experimental conditions used in this study

Detailed information on NMR experimental conditions including collection time in this study is summarized in Table 5A-1.

Table 5A-1(1). ^{27}Al NMR experimental conditions at 9.4 T used in this study.

Glass composition	^{27}Al (at 9.4 T, 17 kHz)						
	1D MAS			2D 3QMAS			
	Number of scans	Delay (s)	Time (h)	Number of scans	Delay (s)	FIDs	Time (h)
<i>Na(Al_{1-x}Fe_x)Si₃O₈ glasses</i>							
X = 0 (Ab)	1920	1	0.5	960	1	65	17.3
X = 0.1	19200	0.5	2.7	14400	0.25	40	40.0
X = 0.3	10000	0.5	1.4	194000	0.25	25	336.8
X = 0.5	20160	0.5	2.8	614400	0.25	20	853.3
<i>NaAlSi₃O₈ (Ab) + Fe₂O₃ glasses</i>							
Ab + 5 wt% Fe ₂ O ₃	19200	0.3	1.6	21120	0.25	25	36.7
Ab + 10 wt% Fe ₂ O ₃	19200	0.3	1.6	57600	0.25	25	100.0
<i>CaAl₂Si₂O₈ (An) + Fe₂O₃ glasses</i>							
CaAl ₂ Si ₂ O ₈ (An)	3200	1	0.9	14400	0.25	50	50.0
An + 5 wt% Fe ₂ O ₃	6400	0.5	0.9	9600	0.25	27	18.0
An + 10 wt% Fe ₂ O ₃	12800	0.5	1.8	72000	0.25	25	125.0

Table 5A-1(2). ^{27}Al NMR experimental conditions at 14.1 T used in this study.

^{27}Al (at 14.1 T, 35 kHz)				
2D 3QMAS				
Glass composition	Number of scans	Delay (s)	FIDs	Time (h)
<i>Na(Al_{1-x}Fe_x)Si₃O₈ glasses</i>				
X = 0 (Ab)	1056	1	80	23.5
X = 0.1	-	-	-	-
X = 0.3	-	-	-	-
X = 0.5	-	-	-	-
<i>NaAlSi₃O₈ (Ab) + Fe₂O₃ glasses</i>				
Ab + 5 wt% Fe ₂ O ₃	16800	0.5	54	126.0
Ab + 10 wt% Fe ₂ O ₃	28800	0.5	45	180.0
<i>CaAl₂Si₂O₈ (An) + Fe₂O₃ glasses</i>				
CaAl ₂ Si ₂ O ₈ (An)	2400	1	60	40.0
An + 5 wt% Fe ₂ O ₃	19200	0.5	48	128.0
An + 10 wt% Fe ₂ O ₃	38400	0.5	48	256.0

Table 5A-1(3). ^{17}O NMR experimental conditions at 9.4 T used in this study.

^{17}O (at 9.4 T, 14 kHz)							
Glass composition	1D MAS			2D 3QMAS			
	Number of scans	Delay (s)	Time (h)	Number of scans	Delay (s)	FIDs	Time (h)
<i>Na(Al_{1-x}Fe_x)Si₃O₈ glasses</i>							
X = 0 (Ab)	5000	1	1.4	2400	1	70	46.7
X = 0.1	-	-	-	-	-	-	-
X = 0.3	-	-	-	-	-	-	-
X = 0.5	-	-	-	-	-	-	-
<i>NaAlSi₃O₈ (Ab) + Fe₂O₃ glasses</i>							
Ab + 5 wt% Fe ₂ O ₃	5000	0.5	0.7	14400	1	43	172.0
Ab + 10 wt% Fe ₂ O ₃	20000	0.5	2.8	16800	1	41	191.3
<i>CaAl₂Si₂O₈ (An) + Fe₂O₃ glasses</i>							
CaAl ₂ Si ₂ O ₈ (An)	10000	1	2.8	6720	1	35	65.3
An + 5 wt% Fe ₂ O ₃	20000	0.5	2.8	16800	1	27	126.0
An + 10 wt% Fe ₂ O ₃	40000	0.5	5.6	24000	1	25	166.7

Table 5A-1(4). ^{29}Si NMR experimental conditions at 9.4 T used in this study.

Glass composition	^{29}Si (at 9.4 T, 14 kHz)		
	1D MAS		
	Number of scans	Delay (s)	Time (h)
<i>Na(Al_{1-x}Fe_x)Si₃O₈ glasses</i>			
X = 0 (Ab)	1056	60	17.6
X = 0.1	50592	1	14.1
X = 0.3	86400	1	24.0
X = 0.5	76704	1	21.3
<i>NaAlSi₃O₈ (Ab) + Fe₂O₃ glasses</i>			
Ab + 5 wt% Fe ₂ O ₃	21568	1	6.0
Ab + 10 wt% Fe ₂ O ₃	64032	1	17.8
<i>CaAl₂Si₂O₈ (An) + Fe₂O₃ glasses</i>			
CaAl ₂ Si ₂ O ₈ (An)	2880	60	48.0
An + 5 wt% Fe ₂ O ₃	24096	1	6.7
An + 10 wt% Fe ₂ O ₃	60000	1	16.7

5A-4. Effect of iron content on the ^{29}Si and ^{27}Al MAS NMR signal intensity of iron-bearing Na- and Ca-aluminosilicate glasses.

Figures 5A-1 and 5A-2 show the ^{29}Si and ^{27}Al MAS NMR spectra of $\text{Na}(\text{Al}_{1-x}\text{Fe}_x)\text{Si}_3\text{O}_8$, $\text{NaAlSi}_3\text{O}_8 + \text{Fe}_2\text{O}_3$, and $\text{CaAl}_2\text{Si}_2\text{O}_8 + \text{Fe}_2\text{O}_3$ glasses with varying iron content. The spectra are plotted on a vertical scale reflecting signal intensity reduction corresponding to iron content. The NMR signal intensities were further calibrated with the weight of each glass in the rotor. Note that the NMR spectra were acquired after full relaxation, which was ensured by a sufficient delay time. The NMR signal intensity decreases with increasing Fe_2O_3 content due to strong interaction between the unpaired electrons in the d-orbitals of iron and each nuclear spin. As shown in Figures

5A-1 and 5A-2, the trend of a decrease in signal intensity with increasing Fe_2O_3 content is not heavily dependent on the composition of the glasses. Quantitative trends of the decrease in ^{29}Si and ^{27}Al MAS NMR intensity with increasing Fe_2O_3 content are shown in Figure 5-14 of the manuscript.

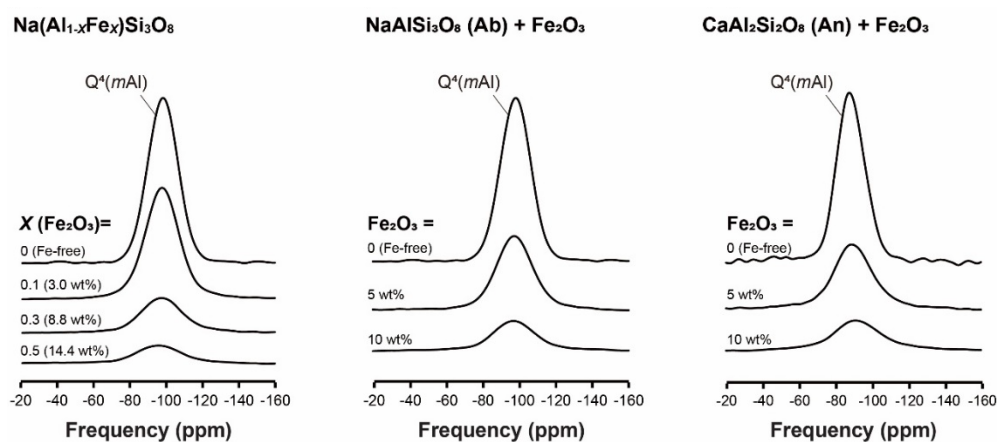


Figure 5A-1. ^{29}Si MAS NMR spectra of $\text{Na}(\text{Al}_{1-x}\text{Fe}_x)\text{Si}_3\text{O}_8$ (left), $\text{NaAlSi}_3\text{O}_8 + \text{Fe}_2\text{O}_3$ (middle), and $\text{CaAl}_2\text{Si}_2\text{O}_8 + \text{Fe}_2\text{O}_3$ (right) glasses with varying iron content, as labeled. The spectra are plotted on a vertical scale reflecting signal intensity reduction corresponding in iron content.

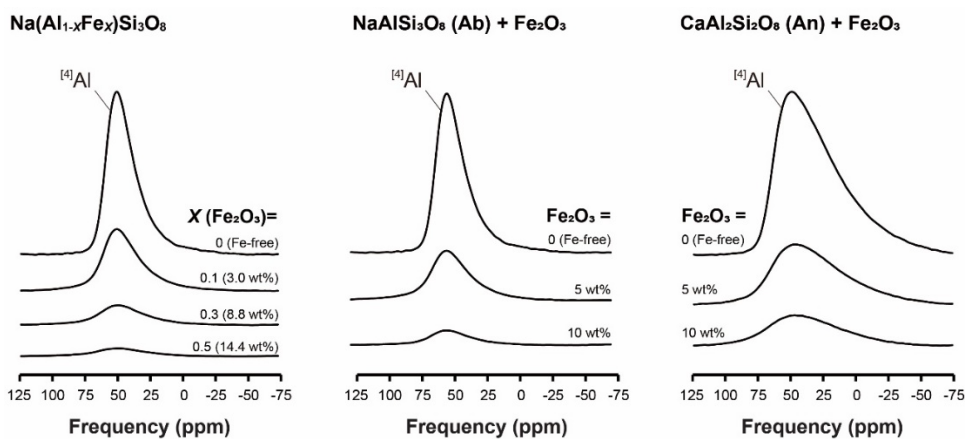


Figure 5A-2. ^{27}Al MAS NMR spectra (obtained at 9.4 T) of $\text{Na}(\text{Al}_{1-x}\text{Fe}_x)\text{Si}_3\text{O}_8$ (left), $\text{NaAlSi}_3\text{O}_8 + \text{Fe}_2\text{O}_3$ (middle), and $\text{CaAl}_2\text{Si}_2\text{O}_8 + \text{Fe}_2\text{O}_3$ (right) glasses with varying iron content, as labeled. The spectra are plotted on a vertical scale reflecting signal intensity reduction corresponding in iron content.

5A-5. Subtraction of rotor background from ^{27}Al MAS and 3QMAS NMR spectra obtained at 9.4 T.

Figure 5A-4 shows the background-subtracted ^{27}Al MAS NMR spectra (obtained at 9.4 T) of iron-bearing aluminosilicate glasses [i.e., $\text{Na}(\text{Al}_{0.5}\text{Fe}_{0.5})\text{Si}_3\text{O}_8$, $\text{NaAlSi}_3\text{O}_8 + 10 \text{ wt}\% \text{ Fe}_2\text{O}_3$, and $\text{CaAl}_2\text{Si}_2\text{O}_8 + 10 \text{ wt}\% \text{ Fe}_2\text{O}_3$ glasses] and rotor background. The Al rotor background consists mostly of ^{6}Al . Figures 5-4, 5-7, and 5-11 in the manuscript were obtained by subtracting the background signal from spectra.

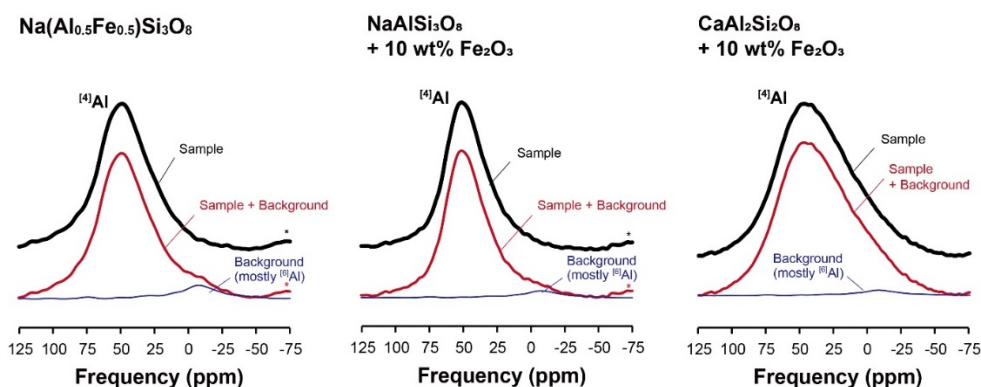


Figure 5A-3. The ^{27}Al MAS NMR spectra at 9.4 T with 17 kHz of spinning speed for background-subtracted iron-bearing aluminosilicate glasses [black, $\text{Na}(\text{Al}_{0.5}\text{Fe}_{0.5})\text{Si}_3\text{O}_8$ (left), $\text{NaAlSi}_3\text{O}_8 + 10 \text{ wt}\% \text{Fe}_2\text{O}_3$ (center), and $\text{CaAl}_2\text{Si}_2\text{O}_8 + \text{Fe}_2\text{O}_3$ (right) glasses] and rotor background (blue).

In the 2D ^{27}Al 3QMAS NMR spectra for $\text{Na}(\text{Al}_{1-x}\text{Fe}_x)\text{Si}_3\text{O}_8$ and $\text{NaAlSi}_3\text{O}_8 + 10 \text{ wt}\% \text{Fe}_2\text{O}_3$ glasses obtained at 9.4 T, the rotor background (mostly ^{61}Al) was observed as shown in Figures 5A-4(1) and 5A-4(2), showing that the rotor background is completely resolved from the NMR signal from glasses. Figures 5-5 and 5-8 in the manuscript show spectra that the rotor background is subtracted. The total isotropic projection of $\text{Na}(\text{Al}_{1-x}\text{Fe}_x)\text{Si}_3\text{O}_8$ glasses (Figure 5-5B in the manuscript) was obtained as the sum of the NMR signal from the sample alone. We note that no signal from the rotor background was observed in the spectra obtained at 14.1 T.

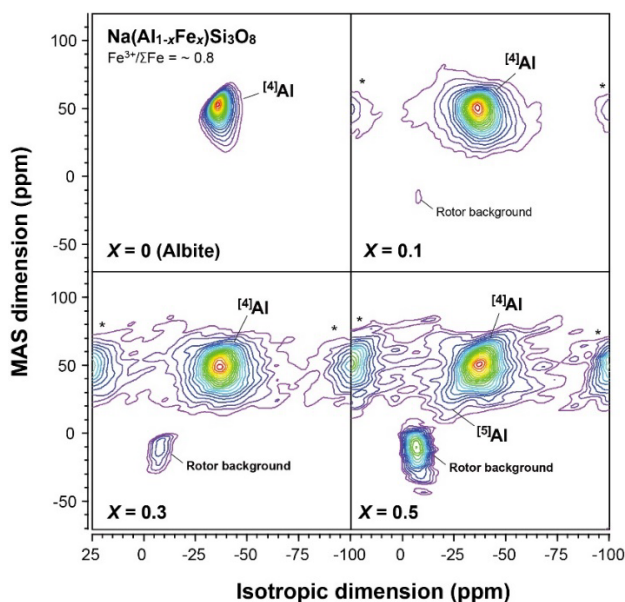


Figure 5A-4(1). ^{27}Al 3QMAS NMR spectra at 9.4 T for $\text{Na}(\text{Al}_{1-x}\text{Fe}_x)\text{Si}_3\text{O}_8$ glasses with varying iron content, showing the spinning side band (*). Contour lines are drawn from 8% to 98% relative intensity with a 5% increment and an additional line at 6% levels.

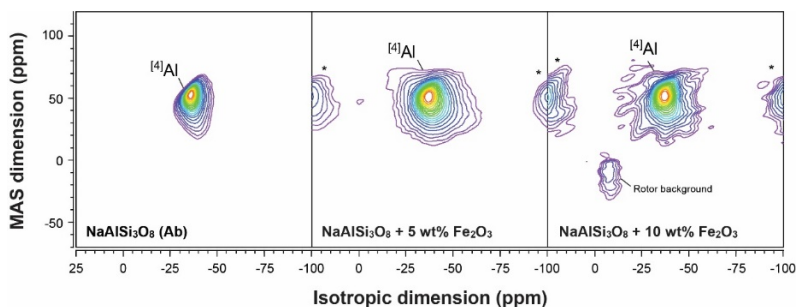


Figure 5A-4(2). ^{27}Al 3QMAS NMR spectra at 9.4 T for $\text{NaAlSi}_3\text{O}_8 + \text{Fe}_2\text{O}_3$ glasses with varying iron content, showing the spinning side band (*). Contour lines are drawn from 13% to 93% relative intensity with a 5% increment and three additional lines at 5.5%, 7.5%, and 10% levels.

5A-6. ^{27}Al MAS NMR spectra for iron-bearing Na- and Ca-aluminosilicate glasses

Figure 5A-5 shows the ^{27}Al MAS NMR spectra for $\text{Na}(\text{Al}_{1-x}\text{Fe}_x)\text{Si}_3\text{O}_8$, $\text{NaAlSi}_3\text{O}_8 + \text{Fe}_2\text{O}_3$, and $\text{CaAl}_2\text{Si}_2\text{O}_8 + \text{Fe}_2\text{O}_3$ glasses (obtained at 9.4 T with 17 kHz of spinning speed). Here, the frequency range of the spectra varies from -300 ppm to 300 ppm, allowing us to observe the spinning side band pattern (marked with *).

5A-7. ^{27}Al NMR parameters in iron-bearing Na-aluminosilicate glasses

As shown in Figures 5-5 and 5-8 of the manuscript, only ^{41}Al peak is observed in the ^{27}Al 3QMAS NMR spectra for $\text{Na}(\text{Al}_{1-x}\text{Fe}_x)\text{Si}_3\text{O}_8$ and $\text{NaAlSi}_3\text{O}_8 + \text{Fe}_2\text{O}_3$ glasses, except the spectrum of $\text{Na}(\text{Al}_{0.5}\text{Fe}_{0.5})\text{Si}_3\text{O}_8$ glass. We estimated the quadrupolar coupling constant (C_q) and isotropic chemical shifts (δ_{iso}) from the center of gravity of the ^{41}Al peak in the ^{27}Al 3QMAS NMR spectra. The asymmetry parameter (η) was assumed to be 0.5 to calculate C_q [$=P_q / (1 + \eta^2/3)^{1/2}$].

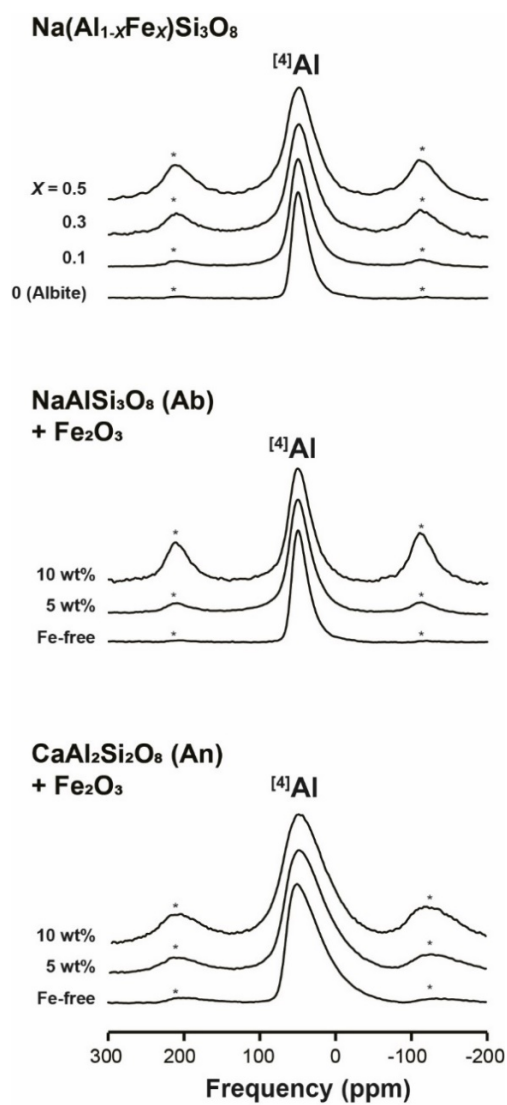


Figure 5A-5. ^{27}Al NMR spectra at 9.4 T with 17 kHz of spinning speed for $\text{Na}(\text{Al}_{1-x}\text{Fe}_x)\text{Si}_3\text{O}_8$ (top), $\text{NaAlSi}_3\text{O}_8 + \text{Fe}_2\text{O}_3$ (middle), and $\text{CaAl}_2\text{Si}_2\text{O}_8 + \text{Fe}_2\text{O}_3$ (bottom) glasses with varying iron content, showing the spinning side band (*).

Table 5A-2. The center of gravity (obtained from MAS and isotropic dimension) and NMR parameters for iron-bearing Na-aluminosilicate glasses (obtained at 9.4 T and 14.1 T)

B ₀	Glass composition	Center of gravity (ppm)		δ _{iso} (ppm)	C _q (MHz) (η = 0.5)	
		MAS dimension	Isotropic dimension			
9.4 T	<i>Na(Al_{1-x}Fe_x)Si₃O₈ glasses</i>					
	X = 0 (Ab)	45.8 ± 1.5	-35.1 ± 1.5	57.3 ± 1.0	4.4 ± 0.2	
	X = 0.1	46.8 ± 1.5	-35.3 ± 1.5	57.9 ± 1.0	4.3 ± 0.2	
	X = 0.3	48.4 ± 2.0	-35.6 ± 2.0	58.8 ± 1.5	4.2 ± 0.3	
	X = 0.5*	47.3 ± 2.5	-35.8 ± 2.5	58.6 ± 2.0	4.4 ± 0.5	
	<i>NaAlSi₃O₈ (Ab)+ Fe₂O₃ glasses</i>					
	Ab + 5 wt% Fe ₂ O ₃	46.8 ± 2.0	-34.9 ± 2.0	57.1 ± 1.5	4.3 ± 0.5	
	Ab + 10 wt% Fe ₂ O ₃	45.9 ± 2.0	-34.8 ± 2.0	57.0 ± 1.5	4.3 ± 0.5	
	14.1 T	Ab (iron-free)	54.9 ± 1.5	-34.4 ± 1.5	59.8 ± 1.0	4.3 ± 0.2
		Ab + 5 wt% Fe ₂ O ₃	54.7 ± 2.0	-34.5 ± 2.0	59.9 ± 1.5	4.4 ± 0.5
Ab + 10 wt% Fe ₂ O ₃		55.0 ± 2.0	-34.8 ± 2.0	60.3 ± 1.5	4.4 ± 0.5	

*Due to the overlap among ⁴Al and small amount of ⁵Al, the uncertainty of estimated NMR parameters for X = 0.5 is larger than other glasses.

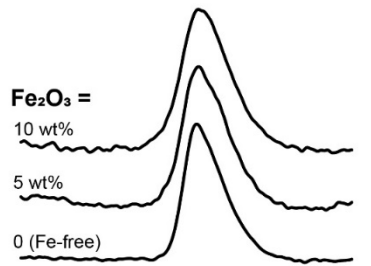
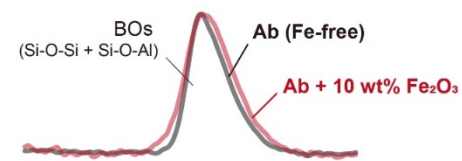
5A-8. ^{17}O MAS NMR spectra for $\text{NaAlSi}_3\text{O}_8 + \text{Fe}_2\text{O}_3$ and $\text{CaAl}_2\text{Si}_2\text{O}_8 + \text{Fe}_2\text{O}_3$ glasses obtained at 9.4 T

Figure 5A-6 presents the ^{17}O MAS NMR spectra for the $\text{NaAlSi}_3\text{O}_8$ and $\text{CaAl}_2\text{Si}_2\text{O}_8$ glasses with varying additional Fe_2O_3 contents (0, 5, and 10 wt% Fe_2O_3). The ^{17}O MAS NMR spectrum for the Fe-free $\text{NaAlSi}_3\text{O}_8$ glass is consistent with previous results (Lee and Stebbins, 2002; Stebbins and Xu, 1997; Xu et al., 1998). The spectrum for the $\text{NaAlSi}_3\text{O}_8$ glass shows a broad peak at ~ 13 ppm that results from overlapping Si-O-Al and Si-O-Si. The peak shapes of the iron-bearing glasses are not significantly different from those of the iron-free glasses for each compositional series. It is clear, however, that the ^{17}O peak widths increase with increasing Fe_2O_3 content, while the increase in the peak width is less than that of the ^{27}Al and ^{29}Si NMR peaks. The overlapped peaks are not fully resolved in the 1D MAS NMR spectra, but a better resolution can be achieved in 2D ^{17}O 3QMAS NMR spectra.

The spectrum for the $\text{CaAl}_2\text{Si}_2\text{O}_8$ glass exhibits partially resolved Ca-NBO at ~ 100 ppm and overlapped BOs (i.e., Si-O-Si, Si-O-Al, and a minor fraction of Al-O-Al) at ~ 32 ppm, consistent with the previous studies. The peak shapes of the iron-bearing glasses are not significantly different from those of the iron-free glasses for each compositional series. It is clear, however, that the ^{17}O peak widths increase with increasing Fe_2O_3 content, while the increase in the peak width is less than that of the ^{27}Al and ^{29}Si NMR peaks. The increase in the peak width with Fe_2O_3 content is slightly larger in the $\text{CaAl}_2\text{Si}_2\text{O}_8$ glasses than in the $\text{NaAlSi}_3\text{O}_8$ glasses. The overlapped peaks are not fully resolved in the 1D MAS NMR spectra, but a better resolution can be achieved in 2D ^{17}O 3QMAS NMR spectra.

NaAlSi₃O₈ (Ab) + Fe₂O₃

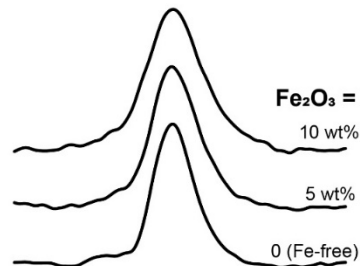
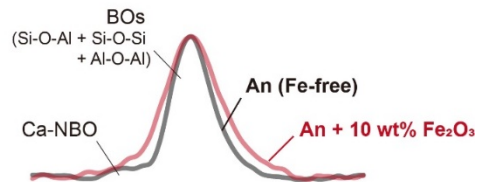
¹⁷O MAS



Frequency (ppm)

CaAl₂Si₂O₈ (An) + Fe₂O₃

¹⁷O MAS



Frequency (ppm)

Figure 5A-6. ¹⁷O MAS NMR spectra for NaAlSi₃O₈ + Fe₂O₃ (left) and CaAl₂Si₂O₈ + Fe₂O₃ (right) glasses with varying Fe₂O₃ (wt%) content, as labeled.

5A-9. Simulation of ^{29}Si MAS NMR spectra for iron-bearing Na- and Ca-aluminosilicate glasses at constant peak position and relative fraction of each $\text{Q}^4_{\text{Si}}(m\text{Al})$ species with increasing iron content

Figure 5A-7 shows the ^{29}Si MAS NMR spectra and simulation results for $\text{NaAlSi}_3\text{O}_8$ (top), $\text{Na}(\text{Al}_{0.5}\text{Fe}_{0.5})\text{Si}_3\text{O}_8$ (with $\text{Fe}^{3+}/\Sigma\text{Fe} \sim 0.8$), and $\text{NaAlSi}_3\text{O}_8 + 10 \text{ wt}\% \text{Fe}_2\text{O}_3$ (with $\text{Fe}^{3+}/\Sigma\text{Fe} \sim 0.5$) glasses. The ^{29}Si MAS NMR spectrum for iron-free $\text{NaAlSi}_3\text{O}_8$ glass was simulated with four Gaussian functions representing $\text{Q}^4_{\text{Si}}(m\text{Al})$ with 0 to 3. The peak positions and their relative fractions of the Q species are based on the results of a previous study (Lee and Stebbins, 1999). The peak positions of $\text{Q}^4_{\text{Si}}(m\text{Al})$ species are approximately -108 [$\text{Q}^4_{\text{Si}}(0\text{Al})$], -100 [$\text{Q}^4_{\text{Si}}(1\text{Al})$], -92 [$\text{Q}^4_{\text{Si}}(2\text{Al})$], and -88.5 ppm [$\text{Q}^4_{\text{Si}}(3\text{Al})$], respectively. The simulation of the ^{29}Si MAS NMR spectra for iron-bearing $\text{NaAlSi}_3\text{O}_8$ glasses was performed with the assumption that the peak position and relative fractions for $\text{Q}^4_{\text{Si}}(m\text{Al})$ species are constant. Each peak is modeled as a combination of the Gaussian and the Lorentzian functions, taking into consideration the paramagnetic effect. The ratio of the area under the Lorentzian part to that under the Gaussian part was assumed $\sim 50\%$. As shown in Figure 5A-7, the $\text{Q}^4_{\text{Si}}(m\text{Al})$ components are significantly broadened with increasing iron content, regardless of composition. For Fe^{3+} -dominant $\text{Na}(\text{Al}_{0.5}\text{Fe}_{0.5})\text{Si}_3\text{O}_8$ glass, the extent of peak broadening in $\text{Q}^4_{\text{Si}}(0\text{Al})$ [red component in Figure 5A-7 (middle)] is relatively larger than that in $\text{Q}^4_{\text{Si}}(3\text{Al})$ [blue component in Figure 5A-7 (middle)]. The simulation results for iron-bearing $\text{NaAlSi}_3\text{O}_8$ glasses suggest that the $\text{Na}(\text{Al}_{1-x}\text{Fe}_x)\text{Si}_3\text{O}_8$ glasses show much larger structural changes in the Si-rich framework [i.e., $\text{Q}^4(0,1\text{Al})$] compared with the Al-rich framework [i.e., $\text{Q}^4(2,3\text{Al})$] with increasing Fe^{3+} . On the other hand, the degree of an increase in peak width for both $\text{Q}^4_{\text{Si}}(0\text{Al})$ and $\text{Q}^4_{\text{Si}}(3\text{Al})$ species for $\text{NaAlSi}_3\text{O}_8 + \text{Fe}_2\text{O}_3$ glass ($\text{Fe}^{3+}/\Sigma\text{Fe} \sim 0.5$) is similar,

suggesting that both Fe^{2+} and Fe^{3+} in $\text{NaAlSi}_3\text{O}_8 + \text{Fe}_2\text{O}_3$ glasses tend to equally affect the $\text{Q}^{4_{\text{Si}}}(m\text{Al})$ species regardless of m number. Figure 5A-8 exhibits the ^{29}Si MAS NMR spectra and simulation results for $\text{CaAl}_2\text{Si}_2\text{O}_8$ (top) and $\text{CaAl}_2\text{Si}_2\text{O}_8 + 10 \text{ wt}\% \text{Fe}_2\text{O}_3$ (with $\text{Fe}^{3+}/\Sigma\text{Fe} \sim 0.3$, bottom) glasses. The simulation was also performed with the constant peak position and relative fractions for $\text{Q}^{4_{\text{Si}}}(m\text{Al})$ species. For iron-free $\text{CaAl}_2\text{Si}_2\text{O}_8$ glass, the spectrum was simulated with the 4-components corresponding $\text{Q}^{4_{\text{Si}}}(1\text{Al})$ (~ -102 ppm), $\text{Q}^{4_{\text{Si}}}(2\text{Al})$ (~ -94 ppm), $\text{Q}^{4_{\text{Si}}}(3\text{Al})$ (~ -89 ppm), and $\text{Q}^{4_{\text{Si}}}(4\text{Al})$ (-82 ppm). Note that the peak position and relative fractions were determined based on the previous study (Lee and Stebbins, 1999). For $\text{CaAl}_2\text{Si}_2\text{O}_8 + 10 \text{ wt}\% \text{Fe}_2\text{O}_3$ glass, each component was also modeled with the combination of Gaussian (50%) and Lorentzian (50%) part, consistent with the simulation of iron-bearing $\text{NaAlSi}_3\text{O}_8$ glasses. As shown in Figure 5A-8, the changes in the $\text{Q}^{4_{\text{Si}}}(m\text{Al})$ with a larger m number appear to be more pronounced than in $\text{Q}^{4_{\text{Si}}}(m\text{Al})$ with a smaller m number, suggesting that the local configurations of Al for the Fe^{2+} -dominant $\text{CaAl}_2\text{Si}_2\text{O}_8$ glasses would be perturbed by increasing Fe_2O_3 . We note that the fits and simulation results are largely non-unique. The simulations of ^{29}Si MAS NMR spectra for in the current study, hence, were performed to obtain *qualitative* trend.

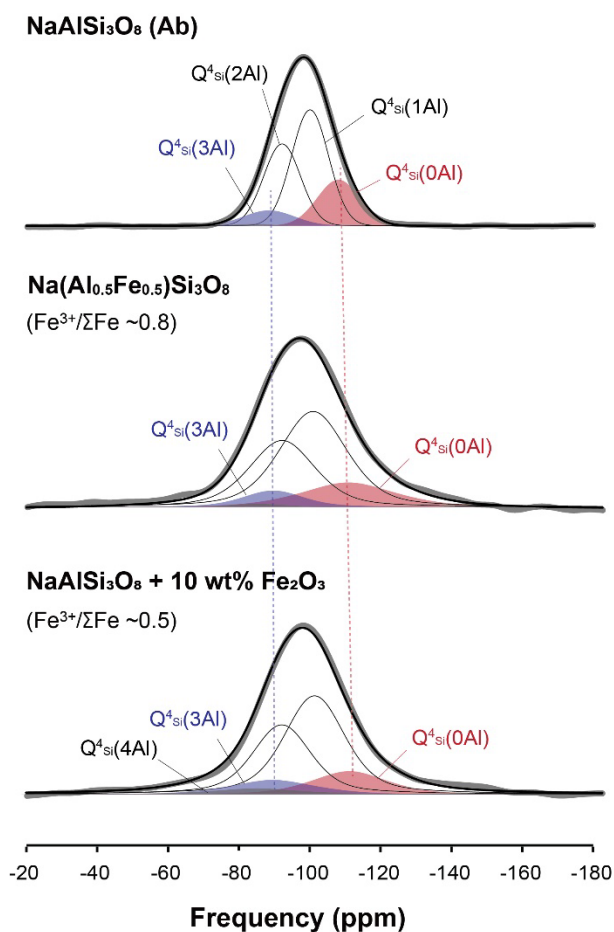


Figure 5A-7. ²⁹Si MAS NMR spectra and simulation results for NaAlSi₃O₈ (top), Na(Al_{0.5}Fe_{0.5})Si₃O₈ (with Fe³⁺/ΣFe ~0.8, middle), and NaAlSi₃O₈ + 10 wt% Fe₂O₃ (with Fe³⁺/ΣFe ~0.5, bottom) glasses. The simulation was performed with the constant peak position and relative fractions for Q⁴Si(*m*Al) species. The thick lines represent the observed spectra and thin lines refer to results fitted using the Gaussian functions for iron-free glass and combination of the Gaussian and Lorentzian functions for iron-bearing glasses.

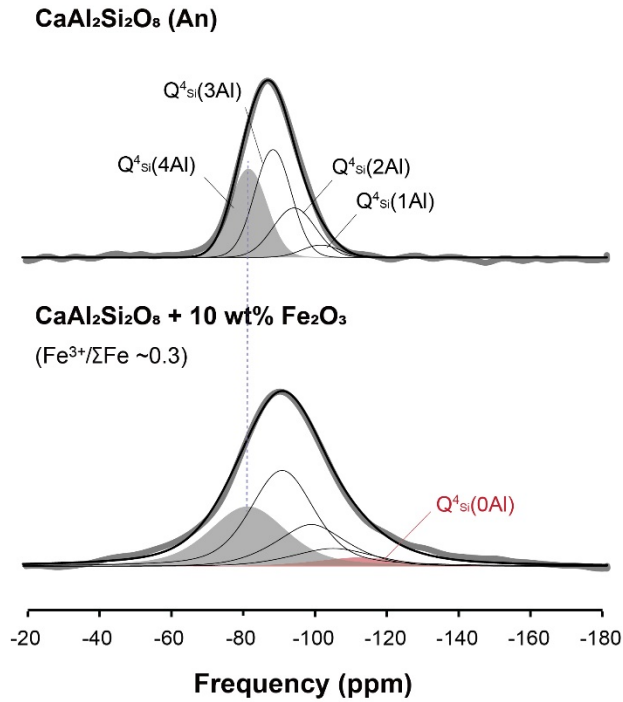


Figure 5A-8. ²⁹Si MAS NMR spectra and simulation results for CaAl₂Si₂O₈ (top) and CaAl₂Si₂O₈ + 10 wt% Fe₂O₃ (with Fe³⁺/ΣFe ~0.3, bottom) glasses. The simulation was performed with the constant peak position and relative fractions for Q⁴_{Si}(*m*Al) species. The thick lines represent the observed spectra and thin lines refer to results fitted using the Gaussian functions for iron-free glass and combination of the Gaussian and Lorentzian functions for iron-bearing glasses.

5A-10. Interpretation of the changes in ^{29}Si NMR spectra for $\text{CaAl}_2\text{Si}_2\text{O}_8 + \text{Fe}_2\text{O}_3$ glasses with varying Fe_2O_3

As described in the manuscript, the peak position for $\text{CaAl}_2\text{Si}_2\text{O}_8$ glass systematically moves toward a lower frequency, and the fraction in the $\text{Q}^{4_{\text{Si}}}(m\text{Al})$ species with smaller m (i.e., 1 and 2) apparently increases with increasing Fe_2O_3 . The observed changes in ^{29}Si NMR spectra with increasing Fe_2O_3 stem from both structural changes and paramagnetic effect. Assuming no preferential paramagnetic effect on each $\text{Q}^{4_{\text{Si}}}(m\text{Al})$ species, these observations suggest that the average m of $\text{Q}^{4_{\text{Si}}}(m\text{Al})$ may decrease and/or there is a relatively large increase in the degree of topological disorder of the $\text{Q}^{4_{\text{Si}}}(m\text{Al})$ species with a larger m number (i.e., 3 and 4), compared to that with a smaller m number (i.e., 1 and 2) for the Fe^{2+} -dominant $\text{CaAl}_2\text{Si}_2\text{O}_8$ glasses. Alternatively, if there are preferential paramagnetic effects in specific $\text{Q}^{4_{\text{Si}}}(m\text{Al})$ species due to their proximity to Fe, the apparent increase in the fraction of $\text{Q}^{4_{\text{Si}}}(m\text{Al})$ with a smaller m number with increasing Fe_2O_3 content for the Fe^{2+} -dominant $\text{CaAl}_2\text{Si}_2\text{O}_8 + \text{Fe}_2\text{O}_3$ glasses suggests preferential proximity between Fe^{2+} and $\text{Q}^{4_{\text{Si}}}(m\text{Al})$ with a larger m number. Thus, this indicates that the preferential interaction between Al and Fe^{2+} in the iron-bearing $\text{CaAl}_2\text{Si}_2\text{O}_8$.

REFERENCES

- Adam, G. and Gibbs, J.H. (1965) On temperature dependence of cooperative relaxation properties in glass-forming liquids. *J. Chem. Phys.* 43, 139-146.
- Alberto, H.V., daCunha, J.L.P., Mysen, B.O., Gil, J.M. and deCampos, N.A. (1996) Analysis of Mössbauer spectra of silicate glasses using a two-dimensional Gaussian distribution of hyperfine parameters. *J. Non-Cryst. Solids* 194, 48-57.
- Alderman, O.L.G., Lazareva, L., Wilding, M.C., Benmore, C.J., Heald, M., Johnson, C.E., Johnson, J.A., Hah, H.Y., Sendelbach, S., Tamalonis, A., Skinner, L.B., Parise, J.B. and Weber, J.K.R. (2017a) Local structural variation with oxygen fugacity in $\text{Fe}_2\text{SiO}_{4+x}$ fayalitic iron silicate melts. *Geochim. Cosmochim. Acta* 203, 15-36.
- Alderman, O.L.G., Wilding, M.C., Tamalonis, A., Sendelbach, S., Heald, S.M., Benmore, C.J., Johnson, C.E., Johnson, J.A., Hah, H.Y. and Weber, J.K.R. (2017b) Iron K-edge X-ray absorption near-edge structure spectroscopy of aerodynamically levitated silicate melts and glasses. *Chem. Geol.* 453, 169-185.
- Allwardt, J.R., Lee, S.K. and Stebbins, J.F. (2003) Bonding preferences of non-bridging O atoms: Evidence from ^{17}O MAS and 3QMAS NMR on calcium aluminate and low-silica Ca-aluminosilicate glasses. *Am. Mineral.* 88, 949-954.
- Allwardt, J.R., Poe, B.T. and Stebbins, J.F. (2005a) The effect of fictive temperature on Al coordination in high-pressure (10 GPa) sodium aluminosilicate glasses. *Am. Mineral.* 90, 1453-1457.
- Allwardt, J.R. and Stebbins, J.F. (2004) Ca-Mg and K-Mg mixing around non-bridging O atoms in silicate glasses: An investigation using ^{17}O MAS and 3QMAS NMR. *Am. Mineral.* 89, 777-784.
- Allwardt, J.R., Stebbins, J.F., Schmidt, B.C., Frost, D.J., Withers, A.C. and Hirschmann, M.M. (2005b) Aluminum coordination and the densification of high-pressure aluminosilicate glasses. *Am. Mineral.* 90, 1218-1222.
- Allwardt, J.R., Stebbins, J.F., Terasaki, H., Du, L.-S., Frost, D.J., Withers, A.C., Hirschmann, M.M., Suzuki, A. and Ohtani, E. (2007) Effect of structural transitions on properties of high-pressure silicate melts: ^{27}Al NMR, glass densities, and melt viscosities. *Am. Mineral.* 92, 1093-1104.

- Angeli, F., Delaye, J.M., Charpentier, T., Petit, J.C., Ghaleb, D. and Faucon, P. (2000) Investigation of Al-O-Si bond angle in glass by ^{27}Al 3Q-MAS NMR and molecular dynamics. *Chem. Phys. Lett.* 320, 681-687.
- Baltisberger, J.H., Xu, Z., Stebbins, J.F., Wang, S.H. and Pines, A. (1996) Triple-quantum two-dimensional ^{27}Al magic-angle spinning nuclear magnetic resonance spectroscopic study of aluminosilicate and aluminate crystals and glasses. *J. Am. Chem. Soc.* 118, 7209-7214.
- Bouhifd, M.A., Richet, P., Besson, P., Roskosz, M. and Ingrin, J. (2004) Redox state, microstructure and viscosity of a partially crystallized basalt melt. *Earth Planet. Sci. Lett.* 218, 31-44.
- Calas, G. and Petiau, J. (1983) Coordination of iron in oxide glasses through high-resolution K-edge spectra: Information from the pre-edge. *Solid State Commun.* 48, 625-629.
- Chevrel, M.O., Giordano, D., Potuzak, M., Courtial, P. and Dingwell, D.B. (2013) Physical properties of $\text{CaAl}_2\text{Si}_2\text{O}_8\text{-CaMgSi}_2\text{O}_6\text{-FeO-Fe}_2\text{O}_3$ melts: Analogues for extra-terrestrial basalt. *Chem. Geol.* 346, 93-105.
- Cochain, B., Neuville, D.R., Henderson, G.S., McCammon, C.A., Pinet, O. and Richet, P. (2012) Effects of the iron content and redox state on the structure of sodium borosilicate glasses: A raman, Mössbauer and boron k-edge XANES spectroscopy study. *J. Am. Ceram. Soc.* 95, 962-971.
- Coltorti, M., Beccaluva, L., Bonadiman, C., Salvini, L. and Siena, F. (2000) Glasses in mantle xenoliths as geochemical indicators of metasomatic agents. *Earth Planet. Sci. Lett.* 183, 303-320.
- Cormier, L., Ghaleb, D., Neuville, D.R., Delaye, J.M. and Calas, G. (2003) Chemical dependence of network topology of calcium aluminosilicate glasses: a computer simulation study. *J. Non-Cryst. Solids* 332, 255-270.
- Cukierman, M. and Uhlmann, D.R. (1974) Effects of iron oxidation-state on viscosity, lunar composition 15555. *J. Geophys. Res.* 79, 1594-1598.
- Di Genova, D., Vasseur, J., Hess, K.U., Neuville, D.R. and Dingwell, D.B. (2017) Effect of oxygen fugacity on the glass transition, viscosity and structure of silica- and iron-rich magmatic melts. *J. Non-Cryst. Solids* 470, 78-85.

- Dingwell, D.B. (1991) Redox viscometry of some Fe-bearing silicate melts. *Am. Mineral.* 76, 1560-1562.
- Dingwell, D.B., Brearley, M. and Dickinson, J.E. (1988) Melt densities in the Na_2O - FeO - Fe_2O_3 - SiO_2 system and the partial molar volume of tetrahedrally-coordinated ferric iron in silicate melts. *Geochim. Cosmochim. Acta* 52, 2467-2475.
- Dingwell, D.B. and Virgo, D. (1987) The effect of oxidation-state on the viscosity of melts in the system Na_2O - FeO - Fe_2O_3 - SiO_2 . *Geochim. Cosmochim. Acta* 51, 195-205.
- Dingwell, D.B. and Virgo, D. (1988) Viscosities of melts in the Na_2O - FeO - Fe_2O_3 - SiO_2 system and factors controlling relative viscosities of fully polymerized silicate melts. *Geochim. Cosmochim. Acta* 52, 395-403.
- Drewitt, J.W.E., Sanloup, C., Bytchkov, A., Brassamin, S. and Hennet, L. (2013) Structure of $(\text{Fe}_x\text{Ca}_{1-x}\text{O})_y(\text{SiO}_2)_{1-y}$ liquids and glasses from high-energy x-ray diffraction: Implications for the structure of natural basaltic magmas. *Phys. Rev. B* 87, 224201.
- Dupree, R., Holland, D. and Mortuza, M.G. (1990) A MAS-NMR investigation of lithium silicate-glasses and glass-ceramics. *J. Non-Cryst. Solids* 116, 148-160.
- Dyar, M.D., Agresti, D.G., Schaefer, M.W., Grant, C.A. and Sklute, E.C. (2006) Mössbauer spectroscopy of earth and planetary materials, *Annu. Rev. Earth Pl. Sc.*, pp. 83-125.
- Eckert, H. (1992) Structural characterization of noncrystalline solids and glasses using solid-state NMR. *Prog. Nucl. Magn. Reson. Spectrosc.* 24, 159-293.
- Engelhardt, G., Nofz, M., Forkel, K., Wihsmann, F.G., Magi, M., Samoson, A. and Lippmaa, E. (1985) Structural studies of calcium aluminosilicate glasses by high-resolution solid-state Si-29 and Al-27 magic angle spinning nuclear magnetic-resonance. *Phys. Chem. Glasses* 26, 157-165.
- Farges, F., Lefrere, Y., Rossano, S., Berthereau, A., Calas, G. and Brown, G.E. (2004) The effect of redox state on the local structural environment of iron in silicate glasses: a molecular dynamics, combined XAFS spectroscopy, and bond valence study. *J. Non-Cryst. Solids* 344, 176-188.

- Farges, F., Rossano, S., Lefrere, Y., Wilke, M. and Brown, G.E. (2005) Iron in silicate glasses: a systematic analysis of pre-edge, XANES and EXAFS features. *Phys. Scr.* T115, 957-959.
- Farnan, I., Grandinetti, P.J., Baltisberger, J.H., Stebbins, J.F., Werner, U., Eastman, M.A. and Pines, A. (1992) Quantification of the disorder in network-modified silicate glasses. *Nature* 358, 31-35.
- Fleet, M.E., Herzberg, C.T., Henderson, G.S., Crozier, E.D., Osborne, M.D. and Scarfe, C.M. (1984) Coordination of Fe, Ga and Ge in high-pressure glasses by Mössbauer, Raman and x-ray absorption-spectroscopy, and geological implications. *Geochim. Cosmochim. Acta* 48, 1455-1466.
- Florian, P., Sadiki, N., Massiot, D. and Coutures, J.P. (2007) Al-27 NMR study of the structure of lanthanum- and yttrium-based aluminosilicate glasses and melts. *J. Phys. Chem. B* 111, 9747-9757.
- Florian, P., Vermillion, K.E., Grandinetti, P.J., Farnan, I. and Stebbins, J.F. (1996) Cation distribution in mixed alkali disilicate glasses. *J. Am. Chem. Soc.* 118, 3493-3497.
- Giordano, D. and Dingwell, D.B. (2003) Non-Arrhenian multicomponent melt viscosity: A model. *Earth Planet. Sci. Lett.* 208, 337-349.
- Giordano, D., Romano, C., Papale, P. and Dingwell, D.B. (2004) The viscosity of trachytes, and comparison with basalts, phonolites, and rhyolites. *Chem. Geol.* 213, 49-61.
- Giordano, D., Russell, J.K. and Dingwell, D.B. (2008) Viscosity of magmatic liquids: A model. *Earth Planet. Sci. Lett.* 271, 123-134.
- Grey, C.P., Dobson, C.M., Cheetham, A.K. and Jakeman, R.J.B. (1989) Studies of rare-earth stannates by ¹¹⁹Sn MAS NMR: The use of paramagnetic shift probes in the solid-state. *J. Am. Chem. Soc.* 111, 505-511.
- Hannoyer, B., Lenglet, M., Durr, J. and Cortes, R. (1992) Spectroscopic evidence of octahedral iron(III) in soda-lime silicate glasses. *J. Non-Cryst. Solids* 151, 209-216.
- Henderson, C.M.B., Cressey, G. and Redfern, S.A.T. (1995) Geological applications of synchrotron-radiation. *Radiat. Phys. Chem.* 45, 459-481.

- Henderson, G.S., Fleet, M.E. and Bancroft, G.M. (1984) An x-ray-scattering study of vitreous KFeSi_3O_8 and $\text{NaFeSi}_3\text{O}_8$ and reinvestigation of vitreous SiO_2 using quasi-crystalline modeling. *J. Non-Cryst. Solids* 68, 333-349.
- Holland, D., Mekki, A., Gee, I.A., McConville, C.F., Johnson, J.A., Johnson, C.E., Appleyard, P. and Thomas, M. (1999) The structure of sodium iron silicate glass: A multi-technique approach. *J. Non-Cryst. Solids* 253, 192-202.
- Iwamoto, N., Umesaki, N. and Atsumi, T. (1987) EXAFS and x-ray-diffraction studies of iron ions in a $0.2(\text{Fe}_2\text{O}_3) \cdot 0.8(\text{Na}_2\text{O} \cdot 2\text{SiO}_2)$ glass. *J. Mater. Sci. Lett.* 6, 271-273.
- Jackson, W.E., Farges, F., Yeager, M., Mabrouk, P.A., Rossano, S., Waychunas, G.A., Solomon, E.I. and Brown, G.E. (2005) Multi-spectroscopic study of Fe(II) in silicate glasses: Implications for the coordination environment of Fe(II) in silicate melts. *Geochim. Cosmochim. Acta* 69, 4315-4332.
- Jaworski, A., Stevansson, B. and Eden, M. (2015) Direct O-17 NMR experimental evidence for Al-NBO bonds in Si-rich and highly polymerized aluminosilicate glasses. *Phys. Chem. Chem. Phys.* 17, 18269-18272.
- Johnson, J.A., Johnson, C.E., Holland, D., Mekki, A., Appleyard, P. and Thomas, M.F. (1999) Transition metal ions in ternary sodium silicate glasses: a Mössbauer and neutron study. *J. Non-Cryst. Solids* 246, 104-114.
- Kelly, P.J., Kyle, P.R., Dunbar, N.W. and Sims, K.W.W. (2008) Geochemistry and mineralogy of the phonolite lava lake, Erebus volcano, Antarctica: 1972-2004 and comparison with older lavas. *Journal of Volcanology and Geothermal Research* 177, 589-605.
- Kelsey, K.E., Allwardt, J.R. and Stebbins, J.F. (2008a) Ca-Mg mixing in aluminosilicate glasses: An investigation using ^{17}O MAS and 3QMAS and ^{37}Al MAS NMR. *J. Non-Cryst. Solids* 354, 4644-4653.
- Kelsey, K.E., Stebbins, J.F., Du, L.-S., Mosenfelder, J.L., Asimow, P.D. and Geiger, C.A. (2008b) Cation order/disorder behavior and crystal chemistry of pyrope-grossular garnets: An ^{17}O 3QMAS and ^{27}Al MAS NMR spectroscopic study. *Am. Mineral.* 93, 134-143.
- Kelsey, K.E., Stebbins, J.F., Singer, D.M., Brown, G.E., Mosenfelder, J.L. and Asimow, P.D. (2009) Cation field strength effects on high pressure aluminosilicate glass

- structure: Multinuclear NMR and La XAFS results. *Geochim. Cosmochim. Acta* 73, 3914-3933.
- Kim, E.J., Fei, Y. and Lee, S.K. (2018) Effect of pressure on the short-range structure and speciation of carbon in alkali silicate and aluminosilicate glasses and melts at high pressure up to 8 GPa: ^{13}C , ^{27}Al , ^{17}O and ^{29}Si solid-state NMR study. *Geochim. Cosmochim. Acta* 224, 327-343.
- Kim, E.J., Fei, Y.W. and Lee, S.K. (2016a) Probing carbon-bearing species and CO_2 inclusions in amorphous carbon-MgSiO₃ enstatite reaction products at 1.5 GPa: Insights from ^{13}C high-resolution solid-state NMR. *Am. Mineral.* 101, 1113-1124.
- Kim, H.-I. and Lee, S.K. (2019) Structure and disorder in (Mg,Fe)SiO₃ glasses and melts: Insights from high-resolution ^{29}Si and ^{17}O solid-state NMR. *Geochim. Cosmochim. Acta* 250, 268-291.
- Kim, H.-I., Sur, J.C. and Lee, S.K. (2016b) Effect of iron content on the structure and disorder of iron-bearing sodium silicate glasses: A high-resolution ^{29}Si and ^{17}O solid-state NMR study. *Geochim. Cosmochim. Acta* 173, 160-180.
- Kirkpatrick, R.J., Oestrike, R., Weiss, C.A., Smith, K.A. and Oldfield, E. (1986) High-resolution ^{27}Al and ^{29}Si NMR-spectroscopy of glasses and crystals along the join CaMgSi₂O₆-CaAl₂SiO₆. *Am. Mineral.* 71, 705-711.
- Kohn, S.C., Dupree, R. and Smith, M.E. (1989) A multinuclear magnetic-resonance study of the structure of hydrous albite glasses. *Geochim. Cosmochim. Acta* 53, 2925-2935.
- Kress, V.C. and Carmichael, I.S.E. (1991) The compressibility of silicate liquids containing Fe₂O₃ and the effect of composition, temperature, oxygen fugacity and pressure on their redox states. *Contrib. Mineral. Petrol.* 108, 82-92.
- Lange, R.A. and Carmichael, I.S.E. (1989) Ferric-ferrous equilibria in Na₂O-FeO-Fe₂O₃-SiO₂ melts: Effects of analytical techniques on derived partial molar volumes. *Geochim. Cosmochim. Acta* 53, 2195-2204.
- Le Losq, C., Neuville, D.R., Florian, P., Henderson, G.S. and Massiot, D. (2014) The role of Al³⁺ on rheology and structural changes in sodium silicate and aluminosilicate glasses and melts. *Geochim. Cosmochim. Acta* 126, 495-517.

- Lee, S.K. (2005) Microscopic origins of macroscopic properties of silicate melts and glasses at ambient and high pressure: Implications for melt generation and dynamics. *Geochim. Cosmochim. Acta* 69, 3695-3710.
- Lee, S.K. (2010) Effect of pressure on structure of oxide glasses at high pressure: Insights from solid-state NMR of quadrupolar nuclides. *Solid State Nucl. Magn. Reson.* 38, 45-57.
- Lee, S.K., Cody, G.D. and Mysen, B.O. (2005) Structure and the extent of disorder in quaternary (Ca-Mg and Ca-Na) aluminosilicate glasses and melts. *Am. Mineral.* 90, 1393-1401.
- Lee, S.K., Kim, H.-I., Kim, E.J., Mun, K.Y. and Ryu, S. (2016) Extent of disorder in magnesium aluminosilicate glasses: Insights from ^{27}Al and ^{17}O NMR. *J. Phys. Chem. C* 120, 737-749.
- Lee, S.K., Park, S.Y., Kim, H.-I., Tschauer, O., Asimow, P., Bai, L., Xiao, Y. and Chow, P. (2012a) Structure of shock compressed model basaltic glass: Insights from O K-edge X-ray Raman scattering and high-resolution ^{27}Al NMR spectroscopy. *Geophysical Research Letters* 39.
- Lee, S.K. and Ryu, S. (2018) Probing of triply coordinated oxygen in amorphous Al_2O_3 . *Journal of Physical Chemistry Letters* 9, 150-156.
- Lee, S.K. and Stebbins, J.F. (1999) The degree of aluminum avoidance in aluminosilicate glasses. *Am. Mineral.* 84, 937-945.
- Lee, S.K. and Stebbins, J.F. (2000a) Al-O-Al and Si-O-Si sites in framework aluminosilicate glasses with Si/Al=1: Quantification of framework disorder. *J. Non-Cryst. Solids* 270, 260-264.
- Lee, S.K. and Stebbins, J.F. (2000b) The structure of aluminosilicate glasses: High-resolution ^{17}O and ^{27}Al MAS and 3QMAS. *J. Phys. Chem. B* 104, 4091-4100.
- Lee, S.K. and Stebbins, J.F. (2002) Extent of intermixing among framework units in silicate glasses and melts. *Geochim. Cosmochim. Acta* 66, 303-309.
- Lee, S.K. and Stebbins, J.F. (2006) Disorder and the extent of polymerization in calcium silicate and aluminosilicate glasses: O-17 NMR results and quantum chemical molecular orbital calculations. *Geochim. Cosmochim. Acta* 70, 4275-4286.

- Lee, S.K. and Sung, S. (2008) The effect of network-modifying cations on the structure and disorder in peralkaline Ca-Na aluminosilicate glasses: O-17 $^3\text{QMAS}$ NMR study. *Chem. Geol.* 256, 326-333.
- Lee, S.K., Yi, Y.S., Cody, G.D., Mibe, K., Fei, Y. and Mysen, B.O. (2012b) Effect of network polymerization on the pressure-induced structural changes in sodium aluminosilicate glasses and melts: ^{27}Al and ^{17}O solid-state NMR study. *J. Phys. Chem. C* 116, 2183-2191.
- Lee, Y.J. and Grey, C.P. (2002) Determining the lithium local environments in the lithium manganates $\text{LiZn}_{0.5}\text{Mn}_{1.5}\text{O}_4$ and Li_2MnO_3 by analysis of the Li-6 MAS NMR spinning sideband manifolds. *J. Phys. Chem. B* 106, 3576-3582.
- Li, Q., Liu, Z.G., Zheng, F., Liu, R., Lee, J., Xu, G.L., Zhong, G.M., Hou, X., Fu, R.Q., Chen, Z.H., Amine, K., Mi, J.X., Wu, S.Q., Grey, C.P. and Yang, Y. (2018) Identifying the Structural Evolution of the Sodium Ion Battery $\text{Na}_2\text{FePO}_4\text{F}$ Cathode. *Angewandte Chemie-International Edition* 57, 11918-11923.
- Libourel, G., Geiger, C.A., Merwin, L. and Sebald, A. (1992) ^{29}Si and ^{27}Al MAS-NMR spectroscopy of glasses in the system $\text{CaSiO}_3\text{-MgSiO}_3\text{-Al}_2\text{O}_3$. *Chem. Geol.* 96, 387-397.
- Lippmaa, E., Samoson, A. and Magi, M. (1986) High-resolution ^{27}Al NMR of aluminosilicates. *J. Am. Chem. Soc.* 108, 1730-1735.
- Lussier, A.J., Aguiar, P.M., Michaelis, V.K., Kroeker, S. and Hawthorne, F.C. (2009) The occurrence of tetrahedrally coordinated Al and B in tourmaline: An ^{11}B and ^{27}Al MAS NMR study. *Am. Mineral.* 94, 785-792.
- Malfait, W.J., Verel, R., Ardia, P. and Sanchez-Valle, C. (2012) Aluminum coordination in rhyolite and andesite glasses and melts: Effect of temperature, pressure, composition and water content. *Geochim. Cosmochim. Acta* 77, 11-26.
- Mao, H.K., Virgo, D. and Bell, P.M. (1973) Analytical study of the orange lunar soil returned by the Apollo 17 astronauts, Year Book Charnegie Institution of Washington, pp. 631-638.
- Mazurin, O.V. (1983) Handbook of glass data: Silica glass and binary silicate glasses. Elsevier Science, Amsterdam.

- McCarty, R.J., Palke, A.C., Stebbins, J.F. and Hartman, J.S. (2015) Transition metal cation site preferences in forsterite (Mg_2SiO_4) determined from paramagnetically shifted NMR resonances. *Am. Mineral.* 100, 1265-1276.
- Merzbacher, C.I., Sherriff, B.L., Hartman, J.S. and White, W.B. (1990) A high-resolution ^{29}Si and ^{27}Al NMR-study of alkaline-earth aluminosilicate glasses. *J. Non-Cryst. Solids* 124, 194-206.
- Morizet, Y., Paris, M., Gaillard, F. and Scaillet, B. (2010) C-O-H fluid solubility in haplobasalt under reducing conditions: An experimental study. *Chem. Geol.* 279, 1-16.
- Murdoch, J.B., Stebbins, J.F. and Carmichael, I.S.E. (1985) High-resolution ^{29}Si NMR study of silicate and aluminosilicate glasses: The effect of network-modifying cations. *Am. Mineral.* 70, 332-343.
- Mysen, B. (2013) Structure-property relationships of COHN-saturated silicate melt coexisting with COHN fluid: A review of in-situ, high-temperature, high-pressure experiments. *Chem. Geol.* 346, 113-124.
- Mysen, B.O. (2006) The structural behavior of ferric and ferrous iron in aluminosilicate glass near meta-aluminosilicate joins. *Geochim. Cosmochim. Acta* 70, 2337-2353.
- Mysen, B.O. and Richet, P. (2018) *Silicate glasses and melts: Properties and structure*, 2nd ed. Elsevier, Amsterdam.
- Mysen, B.O., Seifert, F. and Virgo, D. (1980) Structure and redox equilibria of iron-bearing silicate melts. *Am. Mineral.* 65, 867-884.
- Mysen, B.O. and Toplis, M.J. (2007) Structural behavior of Al^{3+} in peralkaline, metaluminous, and peraluminous silicate melts and glasses at ambient pressure. *Am. Mineral.* 92, 933-946.
- Mysen, B.O. and Virgo, D. (1978) Influence of pressure, temperature, and bulk composition on melt structures in system $\text{NaAlSi}_2\text{O}_6$ - $\text{NaFe}^{3+}\text{Si}_2\text{O}_6$. *Am. J. Sci.* 278, 1307-1322.
- Mysen, B.O. and Virgo, D. (1985) Iron-bearing silicate melts: Relations between pressure and redox equilibria. *Phys. Chem. Miner.* 12, 191-200.
- Mysen, B.O. and Virgo, D. (1989) Redox equilibria, structure, and properties of Fe-bearing aluminosilicate melts: Relationships among temperature, composition,

- and oxygen fugacity in the system $\text{Na}_2\text{O}-\text{Al}_2\text{O}_3-\text{SiO}_2-\text{Fe}-\text{O}$. *Am. Mineral.* 74, 58-76.
- Mysen, B.O., Virgo, D. and Kushiro, I. (1981) The structural role of aluminum in silicate melts: A Raman-spectroscopic study at 1-atmosphere. *Am. Mineral.* 66, 678-701.
- Mysen, B.O., Virgo, D., Scarfe, C.M. and Cronin, D.J. (1985) Viscosity and structure of iron-bearing and aluminum-bearing calcium silicate melts at 1 atm. *Am. Mineral.* 70, 487-498.
- Mysen, B.O., Virgo, D. and Seifert, F.A. (1984) Redox equilibria of iron in alkaline-earth silicate melts: Relationships between melt structure, oxygen fugacity, temperature and properties of iron-bearing silicate liquids. *Am. Mineral.* 69, 834-847.
- Neuvill, D.R., Cormier, L., Flank, A.M., Briois, V. and Massiot, D. (2004a) Al speciation and Ca environment in calcium aluminosilicate glasses and crystals by Al and Ca K-edge X-ray absorption spectroscopy. *Chem. Geol.* 213, 153-163.
- Neuvill, D.R., Cormier, L. and Massiot, D. (2004b) Al environment in tectosilicate and peraluminous glasses: A Al-27 MQ-MAS NMR, Raman, and XANES investigation. *Geochim. Cosmochim. Acta* 68, 5071-5079.
- Neuvill, D.R., Cormier, L. and Massiot, D. (2006) Al coordination and speciation in calcium aluminosilicate glasses: Effects of composition determined by Al-27 MQ-MAS NMR and Raman spectroscopy. *Chem. Geol.* 229, 173-185.
- Neuvill, D.R., Cormier, L., Montouillout, V., Florian, P., Millot, F., Rifflet, J.-C. and Massiot, D. (2008) Structure of Mg- and Mg/Ca aluminosilicate glasses: ^{27}Al NMR and Raman spectroscopy investigations. *Am. Mineral.* 93, 1721-1731.
- Neuvill, D.R., Cormier, L., Montouillout, V. and Massiot, D. (2007) Local Al site distribution in aluminosilicate glasses by Al-27 MQMAS NMR. *J. Non-Cryst. Solids* 353, 180-184.
- Neuvill, D.R. and Richet, P. (1991) Viscosity and mixing in molten (Ca, Mg) pyroxenes and garnets. *Geochim. Cosmochim. Acta* 55, 1011-1019.
- Nielsen, U.G., Paik, Y., Julmis, K., Schoonen, M.A.A., Reeder, R.J. and Grey, C.P. (2005) Investigating sorption on iron-oxyhydroxide soil minerals by solid-state

- NMR spectroscopy: A ${}^6\text{Li}$ MAS NMR study of adsorption and absorption on goethite. *J. Phys. Chem. B* 109, 18310-18315.
- Nolet, D.A. (1980) Optical-absorption and Mössbauer-spectra of Fe, Ti silicate-glasses. *J. Non-Cryst. Solids* 37, 99-110.
- Oestrike, R., Yang, W.H., Kirkpatrick, R.J., Hervig, R.L., Navrotsky, A. and Montez, B. (1987) High-resolution ${}^{23}\text{Na}$, ${}^{27}\text{Al}$, and ${}^{29}\text{Si}$ NMR spectroscopy of framework aluminosilicate glasses. *Geochim. Cosmochim. Acta* 51, 2199-2209.
- Osugi, T., Sukenaga, S., Inatomi, Y., Gonda, Y., Saito, N. and Nakashima, K. (2013) Effect of oxidation state of iron ions on the viscosity of alkali silicate melts. *ISIJ Int.* 53, 185-190.
- Palke, A.C. and Stebbins, J.F. (2011) Variable-temperature ${}^{27}\text{Al}$ and ${}^{29}\text{Si}$ NMR studies of synthetic forsterite and Fe-bearing Dora Maira pyrope garnet: Temperature dependence and mechanisms of paramagnetically shifted peaks. *Am. Mineral.* 96, 1090-1099.
- Palke, A.C., Stebbins, J.F., Frost, D.J. and McCammon, C.A. (2012) Incorporation of Fe and Al in MgSiO_3 perovskite: An investigation by ${}^{27}\text{Al}$ and ${}^{29}\text{Si}$ NMR spectroscopy. *Am. Mineral.* 97, 1955-1964.
- Palke, A.C., Stebbins, J.F., Geiger, C.A. and Tippelt, G. (2015) Cation order-disorder in Fe-bearing pyrope and grossular garnets: A ${}^{27}\text{Al}$ and ${}^{29}\text{Si}$ MAS NMR and ${}^{57}\text{Fe}$ Mössbauer spectroscopy study. *Am. Mineral.* 100, 536-547.
- Park, S.Y. and Lee, S.K. (2012) Structure and disorder in basaltic glasses and melts: Insights from high-resolution solid-state NMR study of glasses in diopside–Ca-tschermakite join and diopside–anorthite eutectic composition. *Geochim. Cosmochim. Acta* 80, 125-142.
- Park, S.Y. and Lee, S.K. (2014) High-resolution solid-state NMR study of the effect of composition on network connectivity and structural disorder in multi-component glasses in the diopside and jadeite join: Implications for structure of andesitic melts. *Geochim. Cosmochim. Acta* 147, 26-42.
- Park, S.Y. and Lee, S.K. (2016) Effects of difference in ionic radii on chemical ordering in mixed-cation silicate glasses: Insights from solid-state ${}^{17}\text{O}$ and ${}^6\text{Li}$ NMR of Li-Ba silicate glasses. *J. Am. Ceram. Soc.* 99, 3948-3956.

- Park, S.Y. and Lee, S.K. (2018) Probing the structure of Fe-free model basaltic glasses: A view from a solid-state ^{27}Al and ^{17}O NMR study of Na-Mg silicate glasses, $\text{Na}_2\text{O-MgO-Al}_2\text{O}_3\text{-SiO}_2$ glasses, and synthetic Fe-free KLB-1 basaltic glasses. *Geochim. Cosmochim. Acta* 238, 563-579.
- Philpotts, A.R. (1982) Compositions of immiscible liquids in volcanic-rocks. *Contrib. Mineral. Petrol.* 80, 201-218.
- Philpotts, A.R. and Ague, J.J. (2009) Principles of igneous and metamorphic petrology. Cambridge University Press, Cambridge.
- Richet, P. (1984) Viscosity and configurational entropy of silicate melts. *Geochim. Cosmochim. Acta* 48, 471-483.
- Robinson, J.A.C., Wood, B.J. and Blundy, J.D. (1998) The beginning of melting of fertile and depleted peridotite at 1.5 GPa. *Earth Planet. Sci. Lett.* 155, 97-111.
- Rossano, S., Ramos, A., Delaye, J.M., Creux, S., Filipponi, A., Brouder, C. and Calas, G. (2000) EXAFS and Molecular Dynamics combined study of CaO-FeO-2SiO_2 glass: New insight into site significance in silicate glasses. *Europhys. Lett.* 49, 597-602.
- Schaller, T. and Stebbins, J.F. (1998) The structural role of lanthanum and yttrium in aluminosilicate glasses: A ^{27}Al and ^{17}O MAS NMR study. *J. Phys. Chem. B* 102, 10690-10697.
- Schramm, C.M., Dejong, B. and Parziale, V.E. (1984) ^{29}Si magic angle spinning NMR-study on local silicon environments in amorphous and crystalline lithium silicates. *J. Am. Chem. Soc.* 106, 4396-4402.
- Sehlke, A. and Whittington, A.G. (2016) The viscosity of planetary tholeiitic melts: A configurational entropy model. *Geochim. Cosmochim. Acta* 191, 277-299.
- Sen, S., Maekawa, H. and Papatheodorou, G.N. (2009) Short-range structure of invert glasses along the pseudo-binary join $\text{MgSiO}_3\text{-Mg}_2\text{SiO}_4$: Results from ^{29}Si and ^{25}Mg MAS NMR spectroscopy. *J. Phys. Chem. B* 113, 15243-15248.
- Spice, H., Sanloup, C., Cochain, B., de Grouchy, C. and Kono, Y. (2015) Viscosity of liquid fayalite up to 9 GPa. *Geochim. Cosmochim. Acta* 148, 219-227.
- Stebbins, J.F. (1995) Dynamics and structure of silicate and oxide melts: Nuclear magnetic resonance studies, in: Stebbins, J.F., McMillan, P.F., Dingwell, D.B.

- (Eds.), *Reviews in Mineralogy*. Mineralogical Society of America, Washington, D.C., pp. 191-246.
- Stebbins, J.F. (2008) Temperature effects on the network structure of oxide melts and their consequences for configurational heat capacity. *Chem. Geol.* 256, 80-91.
- Stebbins, J.F. (2017a) "Free" oxide ions in silicate melts: Thermodynamic considerations and probable effects of temperature. *Chem. Geol.* 461, 2-12.
- Stebbins, J.F. (2017b) Toward the wider application of ^{29}Si NMR spectroscopy to paramagnetic transition metal silicate minerals: Copper(II) silicates. *Am. Mineral.* 102, 2406-2414.
- Stebbins, J.F. (2017c) Toward the wider application of Si-29 NMR spectroscopy to paramagnetic transition metal silicate minerals: Copper(II) silicates. *Am. Mineral.* 102, 2406-2414.
- Stebbins, J.F., Dubinsky, E.V., Kanehashi, K. and Kelsey, K.E. (2008) Temperature effects on non-bridging oxygen and aluminum coordination number in calcium aluminosilicate glasses and melts. *Geochim. Cosmochim. Acta* 72, 910-925.
- Stebbins, J.F. and Kelsey, K.E. (2009) Anomalous resonances in ^{29}Si and ^{27}Al NMR spectra of pyrope ($[\text{Mg,Fe}]_3\text{Al}_2\text{Si}_3\text{O}_{12}$) garnets: Effects of paramagnetic cations. *Phys. Chem. Chem. Phys.* 11, 6906-6917.
- Stebbins, J.F., Kroeker, S., Lee, S.K. and Kiczinski, T.J. (2000) Quantification of five- and six-coordinated aluminum ions in aluminosilicate and fluoride-containing glasses by high-field, high-resolution Al-27 NMR. *J. Non-Cryst. Solids* 275, 1-6.
- Stebbins, J.F., Lee, S.K. and Oglesby, J.V. (1999) Al-O-Al oxygen sites in crystalline aluminates and aluminosilicate glasses: High-resolution oxygen-17 NMR results. *Am. Mineral.* 84, 983-986.
- Stebbins, J.F., Oglesby, J.V. and Xu, Z. (1997) Disorder among network-modifier cations in silicate glasses: New constraints from triple-quantum O-17 NMR. *Am. Mineral.* 82, 1116-1124.
- Stebbins, J.F. and Xu, Z. (1997) NMR evidence for excess non-bridging oxygen in an aluminosilicate glass. *Nature* 390, 60-62.
- Toplis, M.J., Dingwell, D.B. and Lenci, T. (1997) Peraluminous viscosity maxima in $\text{Na}_2\text{O}-\text{Al}_2\text{O}_3-\text{SiO}_2$ liquids: The role of triclusters in tectosilicate melts. *Geochim. Cosmochim. Acta* 61, 2605-2612.

- Toplis, M.J., Dingwell, D.B. and Libourel, G. (1994) The effect of phosphorus on the iron redox ratio, viscosity, and density of an evolved ferro-basalt. *Contrib. Mineral. Petrol.* 117, 293-304.
- Toplis, M.J., Kohn, S.C., Smith, M.E. and Poplett, I.J.F. (2000) Fivefold-coordinated aluminum in tectosilicate glasses observed by triple quantum MAS NMR. *Am. Mineral.* 85, 1556-1560.
- Virgo, D., Mysen, B.O. and Danckwerth, P.D. (1983) The coordination of Fe³⁺ in oxidized vs. reduced sodium aluminosilicate glasses: a ⁵⁷Fe Mossbauer study., *Carnegie Instn. Washington Year Book*, pp. 309-313.
- Waseda, Y. and Toguri, J.M. (1978) Structure of the molten FeO-SiO₂ system. *Metallurgical Transactions B-Process Metallurgy* 9, 595-601.
- Waychunas, G.A., Brown, G.E., Ponader, C.W. and Jackson, W.E. (1988) Evidence from X-ray absorption for network-forming Fe²⁺ in molten alkali silicates. *Nature* 332, 251-253.
- Weigel, C., Cormier, L., Calas, G., Galois, L. and Bowron, D.T. (2008) Nature and distribution of iron sites in a sodium silicate glass investigated by neutron diffraction and EPSR simulation. *J. Non-Cryst. Solids* 354, 5378-5385.
- Winter, J.D. (2009) *An introduction to igneous and metamorphic petrology*. Prentice Hall.
- Xu, Z., Maekawa, H., Oglesby, J.V. and Stebbins, J.F. (1998) Oxygen speciation in hydrous silicate glasses: An oxygen-17 NMR study. *J. Am. Chem. Soc.* 120, 9894-9901.
- Xue, X. (2009) Water speciation in hydrous silicate and aluminosilicate glasses: Direct evidence from ²⁹Si-¹H and ²⁷Al-¹H double-resonance NMR. *Am. Mineral.* 94, 395-398.
- Xue, X. and Kanzaki, M. (2008) Structure of hydrous aluminosilicate glasses along the diopside-anorthite join: A comprehensive one- and two-dimensional ¹H and ²⁷Al NMR study. *Geochim. Cosmochim. Acta* 72, 2331-2348.

APPENDIX I. The determination of iron redox ratios ($\text{Fe}^{3+}/\Sigma\text{Fe}$) of iron-bearing silicate and aluminosilicate glasses: Preliminary electron microprobe (EPMA) study

1. Importance and scope of this work

The oxidation state of silicate glasses is given by the ratio of Fe^{3+} and Fe^{2+} (expressed as $\text{Fe}^{3+}/\Sigma\text{Fe}$), and reflects the nature of the source and partial melting conditions. The $\text{Fe}^{3+}/\Sigma\text{Fe}$ ratio is dependent on the oxygen fugacity, temperature and melt compositions, and influences the physical and chemical properties of silicate melts and glasses. It also affects the speciation and amount of volatiles degassed during magmatic processes, particularly sulfur-bearing gases (e.g., SO_2) and O_2 , and thus global climate in early Earth. Thus, the determination of $\text{Fe}^{3+}/\Sigma\text{Fe}$ in the silicate glasses is essential to understand the redox conditions during rock formation and petrogenetic histories of magma in the Earth's interior.

To obtain the precise $\text{Fe}^{3+}/\Sigma\text{Fe}$ values in the crystalline and non-crystalline earth materials, various experimental techniques have been developed: wet-chemical analysis (Kilinc et al., 1983; Sack et al., 1980), Mössbauer spectroscopy (Mysen, 1987; Mysen et al., 1985), electron energy-loss spectroscopy (EELS) with a transmission electron microscope (Garvie and Buseck, 1998), X-ray absorption near-edge structure (XANES) spectroscopy (Berry et al., 2003; Wilke et al., 2007), resonant X-ray inelastic scattering (RIXS) (de Groot et al., 2005), and electron microprobe (EPMA) (Fialin et al., 2004; France et al., 2010; Hofer and Brey, 2007). However, several techniques have some disadvantage to determine $\text{Fe}^{3+}/\Sigma\text{Fe}$ of silicate glasses and melts in the geological sample. For example, although wet chemical

analysis and Mössbauer spectroscopy provide the relatively accurate $\text{Fe}^{3+}/\Sigma\text{Fe}$ values, these techniques are generally limited to bulk samples. EELS, which provides the superior spatial resolution ($\sim \text{nm}$), is unlikely to be suitable to the analysis of glass because the high electron beam fluxes cause the damage to the sample. Recently, XANES and RIXS techniques have been commonly used to determine the oxidation state of silicate glasses because they provide the spatial resolution of micrometer size and enable non-destructive experiments. However, these experiments require access to the synchrotron X-ray facilities with sufficient fluxes of hard X-ray.

EPMA is one of the most accessible equipment for chemical analysis of various geological samples, enabling *in-situ* analysis of minerals and glasses in thin section with a spatial resolution on the order of a few micrometers. Thus, various efforts have been made to determine the iron oxidation state ($\text{Fe}^{3+}/\Sigma\text{Fe}$) in the minerals and glasses using EPMA. These previous studies have shown that the $\text{Fe}^{3+}/\Sigma\text{Fe}$ can be related to the intensity and wavelength of the soft $\text{FeL}\alpha$ and $\text{FeL}\beta$ emission band. In previous studies, $\text{Fe}^{3+}/\Sigma\text{Fe}$ is measured with three different methods for processing of $\text{FeL}\alpha$ and $\text{FeL}\beta$ emission band: (1) measurement of the $\text{FeL}\alpha$ peak shift (Fialin et al., 2004; Fialin et al., 2001), (2) measurement of the changes in $\text{FeL}\alpha/\text{FeL}\beta$ intensity ratio, and (3) a combination of 1 and 2 (Hofer and Brey, 2007; Hofer et al., 1994). The previous study also reported that peak position of $\text{FeL}\alpha$ is not only dependent on the $\text{Fe}^{3+}/\Sigma\text{Fe}$, but it also depends on the total Fe content and other characteristics of the bulk matrix (Fialin et al., 2001). While further experimental and theoretical studies for measurement of $\text{Fe}^{3+}/\Sigma\text{Fe}$ are necessary to overcome several limitations related to the accuracy and precision, this study holds promise for $\text{Fe}^{3+}/\Sigma\text{Fe}$ measurements of silicate glasses at the micrometer scale.

2. Research in progress

In this study, I preliminarily have determined the $\text{Fe}^{3+}/\Sigma\text{Fe}$ of several silicate glasses with various composition (synthesized in an air) by the measurement of $\text{FeL}\alpha$ peak position as a function of Fe content using EPMA. Working curve, constructed by the measurement of $\text{FeL}\alpha$ peak position for Fe^{2+} -only (e.g., olivines, hedenbergite, orthopyroxene, and almandine) and Fe^{3+} -only (e.g., acmite, epidote, and andradite) silicate minerals, was used to calibrate the $\text{Fe}^{3+}/\Sigma\text{Fe}$ of glasses. Measurements were performed using JXA-8900R electron microprobe in NCIRF at Seoul National University, operating at 10 keV, using TAP monochromator crystals ($2d = 2.575 \text{ nm}$). The electron beam diameter was $15 \mu\text{m}$ and beam current was 100 nA. The energy scan range was from 674 to 740 eV. The FeO and Fe_2O_3 crystal were used to check the variation of $\text{FeL}\alpha$ peak position and compare the values in previous study. As shown in Figure A1-1, the peak positions of $\text{FeL}\alpha$ and $\text{FeL}\beta$ vary with the $\text{Fe}^{3+}/\Sigma\text{Fe}$. The $\text{FeL}\alpha$ positions ($\sin\theta$) of FeO and Fe_2O_3 are 0.6843 ± 0.002 and 0.6831 ± 0.002 , respectively, consistent with the values measured in the previous study with same operating conditions (Fialin et al., 2001).

Based on the previous study, the working curve is as follows:

$$\sin\theta_{\text{Fe}^{2+}} = -4\text{e-}06 x^2 + 0.0002x + 0.6823 \quad (\text{eq. A1-1})$$

$$\sin\theta_{\text{Fe}^{3+}} = 2\text{e-}05x + 0.6826 \quad (\text{eq. A1-2})$$

where x refers the total Fe concentration (wt%) in the samples. Using the above working curves and the measured $\text{FeL}\alpha$ peak positions, the $\text{Fe}^{3+}/\Sigma\text{Fe}$ for the glasses were calculated:

$$\text{Fe}^{3+}/\Sigma\text{Fe} = (\sin\theta_x - \sin\theta_{\text{Fe}^{2+}}) / (\sin\theta_{\text{Fe}^{3+}} - \sin\theta_{\text{Fe}^{2+}}) \quad (\text{eq. A1-3})$$

where $\sin\theta_x$ is the measured $\text{FeL}\alpha$ peak positions.

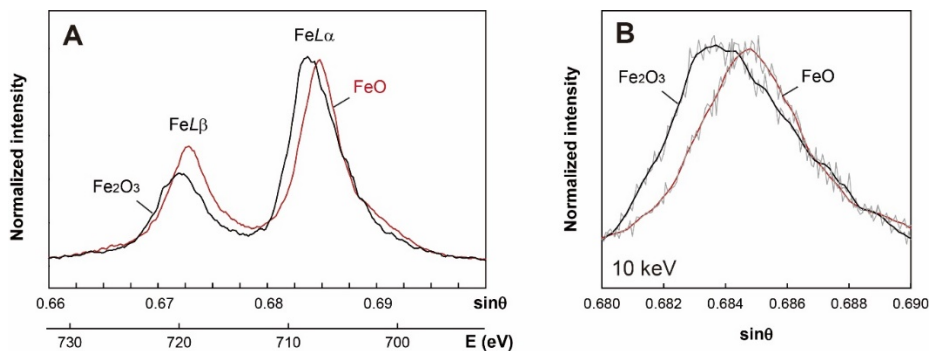
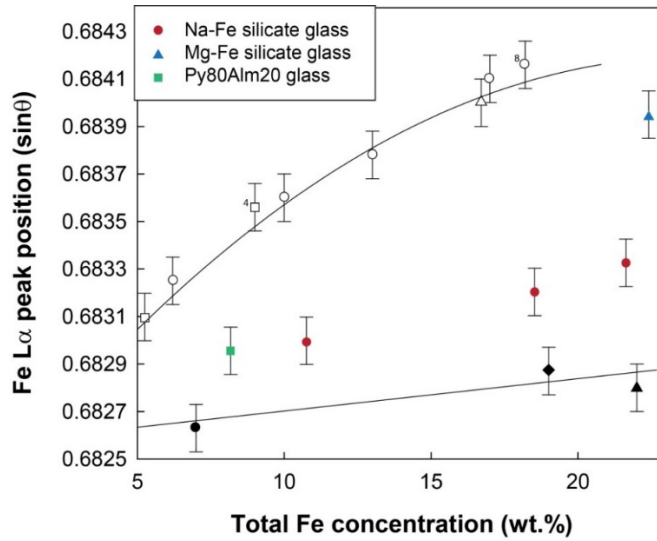


Figure A1-1. (A) Fe *L*-edge emission spectra (operating with 10 keV) of crystalline iron oxides (FeO and Fe₂O₃). The enlarged spectra (B) are also shown to manifest the FeL α peaks.

The preliminarily measured $\text{Fe}^{3+}/\Sigma\text{Fe}$ for various silicate glasses are shown in Figure A1-2 and Table A1-1. These results suggest that the iron-bearing sodium silicate glasses ($\text{Fe}^{3+}/\Sigma\text{Fe} \sim 0.9$) is much oxidized than (Mg,Fe)SiO₃ glasses ($\text{Fe}^{3+}/\Sigma\text{Fe} \sim 0.4$). The $\text{Fe}^{3+}/\Sigma\text{Fe}$ of iron-bearing Mg-aluminosilicate glass (pyrope-almandine join) is about ~ 0.7 . The preliminarily obtained $\text{Fe}^{3+}/\Sigma\text{Fe}$ of silicate glasses using EPMA techniques are consistent with Mössbauer results in the current studies (Table A1-1). Particularly, the $\text{Fe}^{3+}/\Sigma\text{Fe}$ values of Na₂O-Fe₂O₃-SiO₂ glasses (fused in an air, $\log f_{\text{O}_2} = \sim -0.68$) obtained from both EPMA and Mössbauer techniques are ~ 0.9 . The $\text{Fe}^{3+}/\Sigma\text{Fe}$ of MgO-FeO-SiO₂ glasses fused in an Ar environment ($\log f_{\text{O}_2} = \sim -2.13$) is measured as ~ 0.8 in Mössbauer experiment, and that fused in an air ($\log f_{\text{O}_2} = \sim -0.68$), which is obtained from EPMA, is relatively lower than the former (~ 0.6), consistent with the previous studies. While our preliminary EPMA study shows that EPMA technique can be an effective experimental

tool for determining iron oxidation states of silicate glasses, further extensive experiments are necessary to obtain more accurate values of $\text{Fe}^{3+}/\Sigma\text{Fe}$ for various compositions of silicate glasses. For example, it is essential to construct the calibration curve (regarding the relationship between Fe *L*-edge peak position and iron content) using standard samples which are similar to the composition of the analyzing material. We note again that the fitting curve used in this study (Figure A1-2) was previously constructed with data from silicate minerals (Fialin et al., 2004), thus the further confirmation using silicate glasses is necessary. In addition, the previous EPMA studies have shown that the measured $\text{Fe}^{3+}/\Sigma\text{Fe}$ values are significantly changed by the experimental conditions such as beam current and accumulation time (Fialin et al., 2004). This is mainly because the glass surface is oxidized and/or reduced by beam radiation. Particularly, the beam-induced Na^+ migration occurs, resulting an increase in $\text{Fe}^{3+}/\Sigma\text{Fe}$. Alternatively, $\text{Fe}^{3+}/\Sigma\text{Fe}$ may decrease during experiment due to the carbon contamination. Thus, the finding the optimized experimental condition should be accompanied in the future study.



modified from Fialin et al. (2001)

Figure A1-2. Variations of the FeL α peak positions as a function of the total Fe concentration for a series of pure Fe²⁺-bearing (black open symbols) and Fe³⁺-bearing (black closed symbols) minerals and iron-bearing silicate glasses in the current study (colored closed symbols).

Table A1-1. Measured FeL α peak positions and calculated Fe³⁺/ Σ Fe for various silicate glasses

Composition	Total Fe concentration (wt%)	Fe L α peak position* (sin θ)	Fe ³⁺ / Σ Fe (EPMA)	Fe ³⁺ / Σ Fe (Mössbauer)
Na ₂ O:Fe ₂ O ₃ :SiO ₂ =0.8:0.2:2	10.3	0.6830	0.8 \pm 0.1	0.89 \pm 0.05
Na ₂ O:Fe ₂ O ₃ :SiO ₂ =0.5:0.5:2	23.6	0.6833	0.9 \pm 0.1	
Na ₂ O:Fe ₂ O ₃ :SiO ₂ =1:1:6	18.7	0.6832	0.9 \pm 0.1	
MgO:FeO:SiO ₂ =0.4:0.6:1	31.8*	0.6841	0.3 \pm 0.1	
MgO:FeO:SiO ₂ =0.6:0.4:1	22.6	0.6840	0.5 \pm 0.1	
Py80Alm20	7.72	0.6830	0.7 \pm 0.1	0.78 \pm 0.05

REFERENCES

- Berry, A.J., O'Neill, H.S., Jayasuriya, K.D., Campbell, S.J. and Foran, G.J. (2003) XANES calibrations for the oxidation state of iron in a silicate glass. *Am. Mineral.* 88, 967-977.
- de Groot, F.M.F., Glatzel, P., Bergmann, U., van Aken, P.A., Barrea, R.A., Klemme, S., Havecker, M., Knop-Gericke, A., Heijboer, W.M. and Weckhuysen, B.M. (2005) 1s2p resonant inelastic X-ray scattering of iron oxides. *J. Phys. Chem. B* 109, 20751-20762.
- Fialin, M., Bezos, A., Wagner, C., Magnien, V. and Humler, E. (2004) Quantitative electron microprobe analysis of Fe³⁺/ΣFe: Basic concepts and experimental protocol for glasses. *Am. Mineral.* 89, 654-662.
- Fialin, M., Wagner, C., Metrich, N., Humler, E., Galoisy, L. and Bezos, A. (2001) Fe³⁺/ΣFe vs. FeLα peak energy for minerals and glasses: Recent advances with the electron microprobe. *Am. Mineral.* 86, 456-465.
- France, L., Ildefonse, B., Koepke, J. and Bech, F. (2010) A new method to estimate the oxidation state of basaltic series from microprobe analyses. *Journal of Volcanology and Geothermal Research* 189, 340-346.
- Garvie, L.A.J. and Buseck, P.R. (1998) Ratios of ferrous to ferric iron from nanometre-sized areas in minerals. *Nature* 396, 667-670.
- Hofer, H.E. and Brey, G.P. (2007) The iron oxidation state of garnet by electron microprobe: Its determination with the flank method combined with major-element analysis. *Am. Mineral.* 92, 873-885.
- Hofer, H.E., Brey, G.P., Schulzdobrick, B. and Oberhansli, R. (1994) The determination of the oxidation-state of iron by the electron-microprobe. *Eur. J. Mineral.* 6, 407-418.
- Kilinc, A., Carmichael, I.S.E., Rivers, M.L. and Sack, R.O. (1983) The ferric-ferrous ratio of natural silicate liquids equilibrated in air. *Contrib. Mineral. Petrol.* 83, 136-140.
- Mysen, B.O. (1987) Redox equilibria and coordination of Fe-2+ and Fe-3+ in silicate-glasses from Fe-57 mossbauer-spectroscopy. *J. Non-Cryst. Solids* 95-6, 247-254.

- Mysen, B.O., Carmichael, I.S.E. and Virgo, D. (1985) A comparison of iron redox ratios in silicate-glasses determined by wet-chemical and Fe-57 mossbauer resonant absorption methods. *Contrib. Mineral. Petrol.* 90, 101-106.
- Sack, R.O., Carmichael, I.S.E., Rivers, M. and Ghiorso, M.S. (1980) Ferric-ferrous equilibria in natural silicate liquids at 1 bar. *Contrib. Mineral. Petrol.* 75, 369-376.
- Wilke, M., Farges, F., Partzsch, G.M., Schmidt, C. and Behrens, H. (2007) Speciation of Fe in silicate glasses and melts by in-situ XANES spectroscopy. *Am. Mineral.* 92, 44-56.

APPENDIX II. Effect of spinning speed on ^{29}Si and ^{27}Al solid-state MAS NMR spectra for iron-bearing silicate glasses

Hyo-Im Kim and Sung Keun Lee*

Published in *Journal of Mineralogical Society of Korea* (2018) **31(4)** 295-306

ABSTRACT

Despite the utility of solid-state NMR, NMR studies of iron-bearing silicate glasses remain a challenge because the variations in the peak position and width with increasing iron content reflect both paramagnetic effect and iron-induced structural changes. Therefore, it is essential to elucidate the effect of temperature on the NMR signal for iron-bearing silicate glasses. Here, we report the ^{29}Si and ^{27}Al MAS NMR spectra for $(\text{Mg,Fe})\text{SiO}_3$ and Fe_2O_3 -bearing $\text{CaAl}_2\text{Si}_2\text{O}_8$ (anorthite) glasses with varying spinning speed to interpret the NMR spectra for iron-bearing silicate glasses. The increase in the spinning speed results an increase in the sample temperature. The current NMR results allow us to understand the origins of the changes in NMR signal with increasing iron content and to provide information on the dipolar interaction between nuclear spins. The ^{29}Si NMR spectra for $(\text{Mg}_{0.95}\text{Fe}_{0.05})\text{SiO}_3$ glass (Figure 2A-1) and ^{27}Al NMR spectra for Fe_2O_3 -bearing $\text{CaAl}_2\text{Si}_2\text{O}_8$ glasses (Figures 2A-2) show that the peak shape and position of iron-bearing glasses do not change with increasing spinning speed up to 30 kHz. These

$(\text{Mg}_{0.95}\text{Fe}_{0.05})\text{SiO}_3$

^{29}Si MAS (9.4 T)

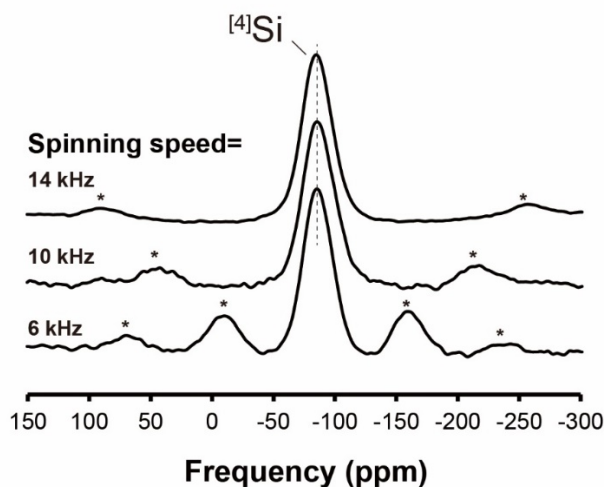


Figure A2-1. ^{29}Si MAS NMR spectra for $(\text{Mg}_{0.95}\text{Fe}_{0.05})\text{SiO}_3$ glass with varying spinning speed (6, 10, and 14 kHz) at 9.4 T. The asterisks (*) denote spinning side band.

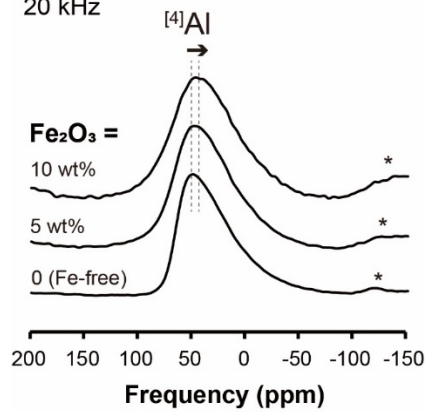
results suggest that the NMR signal in the Fe-bearing glasses may stem from the 'survived nuclear spins' beyond the cutoff radius from the Fe, not from paramagnetic shift. Based on the current results, the observed apparent shifts toward lower frequency of $^{[4]}\text{Al}$ peak for Fe_2O_3 -bearing $\text{CaAl}_2\text{Si}_2\text{O}_8$ glasses with increasing Fe_2O_3 at all spinning speed (15 kHz to 30 kHz, Figure 2A-3) indicate the increase in the fraction of $\text{Q}^4_{\text{Al}}(n\text{Si})$ with lower n (i.e., 1 or 2) with increasing Fe_2O_3 and the spatial proximity between Fe and $\text{Q}^4_{\text{Al}}(n\text{Si})$ with higher n (i.e., 3 or 4).

CaAl₂Si₂O₈ (An) + Fe₂O₃

²⁷Al MAS (9.4 T)

(A)

20 kHz



(B)

30 kHz

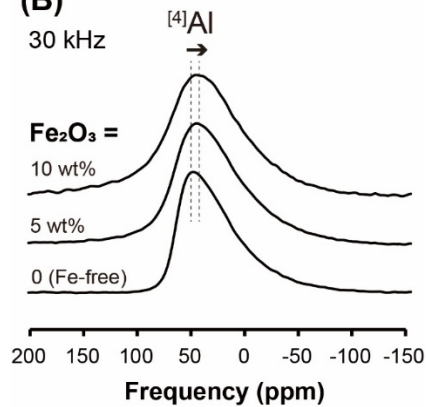


Figure A2-2. The normalized ²⁷Al MAS NMR spectra for Fe₂O₃-bearing CaAl₂Si₂O₈ glasses with varying Fe₂O₃ at spinning speed of (A) 20 kHz and (B) 30 kHz. The asterisks (*) refer the spinning side band.

We also quantify the NMR signal intensity of Fe₂O₃-bearing CaAl₂Si₂O₈ glasses with varying spinning speed up to 30 kHz. ²⁷Al signal intensity of iron-free CaAl₂Si₂O₈ glass does not significantly change with varying spinning speed (from 17 to 30 kHz), suggesting that the dipolar interaction of ²⁷Al spins in the iron-free CaAl₂Si₂O₈ glass was effectively reduced by magic angle spinning of < 17 kHz. In contrast, the ²⁷Al signal intensity for Fe₂O₃-bearing CaAl₂Si₂O₈ glass increases with increasing spinning speed from 17 kHz to 30 kHz. The trend of increasing signal intensity with increasing spinning speed (above 17 kHz) implies that the dipolar interaction is enhanced by addition of iron. Further experimental studies using ultra-fast MAS technique (~ 60 kHz) are needed to confirm the changes in extent of dipolar inter-action with increasing iron content.

The present results show that changes in the NMR signal for iron-bearing silicate glasses reflect the actual iron-induced structural changes. Thus, it is clear that the applications of solid-state NMR for Fe-bearing silicate glasses hold strong promise for unraveling the atomic structure of natural silicate glasses.

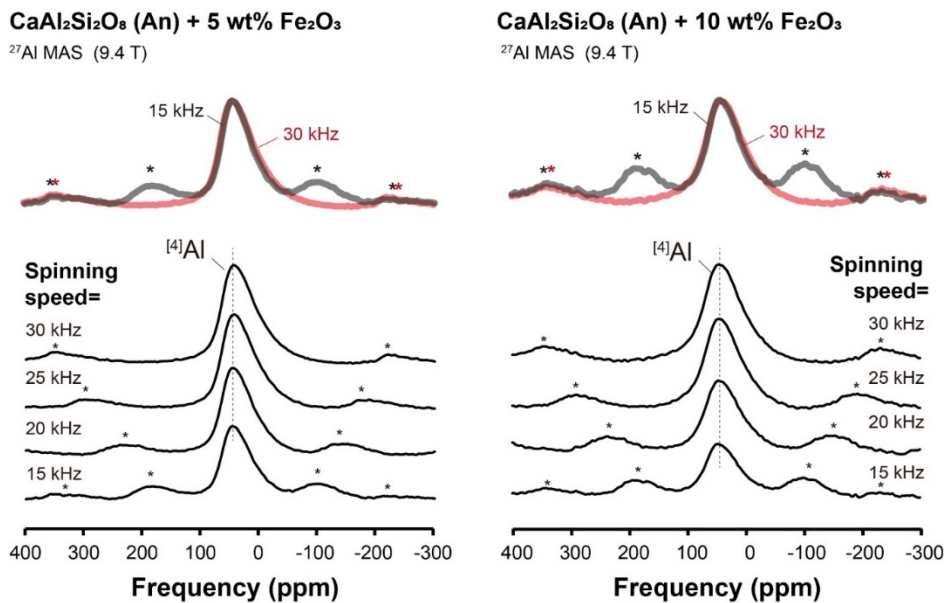


Figure A2-3. ²⁷Al MAS NMR spectra for CaAl₂Si₂O₈ glasses with 5 wt% Fe₂O₃ (left) and 10 wt% Fe₂O₃ (right) with varying spinning speed (15 to 30 kHz). The spectra are plotted on a vertical scale reflecting the variation of signal intensity with the changes in spinning speed.

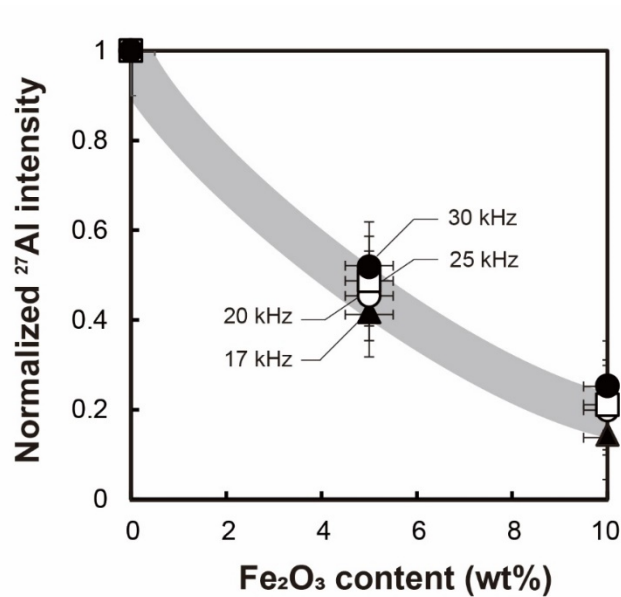


Figure A2-4. The normalized ²⁷Al NMR signal intensities of Fe₂O₃-bearing CaAl₂Si₂O₈ glasses with respect to the signal intensity of Fe-free glass with varying spinning speed. Closed circles, open squares, open circles, and closed triangles refer the 17, 20, 25, and 30 kHz of spinning speed, respectively. Grey line is guide to eye.

APPENDIX III. Publication list

A1. Publication list

- Kim, H.-I.** and Lee, S. K., Extent of disorder in iron-bearing sodium and calcium aluminosilicate glasses: Insights from Mössbauer and multi-nuclear (^{29}Si , ^{27}Al , and ^{17}O) solid-state NMR study, *submitted to Chemical Geology*
- Kim, H.-I.** and Lee, S. K., The degree of polymerization and structural disorder in (Mg,Fe)SiO₃ glasses and melts: Insights from high-resolution ^{29}Si and ^{17}O solid-state NMR, *Geochimica et Cosmochimica Acta*, **250** 269-291 (2019)
- Kim, H.-I.** and Lee, S. K., Effect of spinning speed on ^{29}Si and ^{27}Al solid-state MAS NMR spectra for iron-bearing silicate glasses, *Journal of Mineralogical Society of Korea*, **31(4)** 295-306 (2018)
- Fu, S., Yang, J., Zhang, Y., Okuchi, T., McCammon, C., Iiu, J., **Kim, H.-I.**, Lee, S. K., and Lin, J.-F., Abnormal elasticity of Fe-bearing bridgmanite in the Earth's lower mantle, *Geophysical Research Letters*, **45** 4725-4732 (2018)
- Kim, H.-I.**, Sur, J. C., and Lee, S. K., Effect of iron content on the structure and disorder of iron-bearing sodium silicate glasses: A high-resolution ^{29}Si and ^{17}O solid-state NMR study, *Geochimica et Cosmochim Acta*, **173** 160-180 (2016)
- Lee, S. K., **Kim, H.-I.**, Kim, E. J., Mun, K. Y., and Ryu, S. B., Extent of disorder in magnesium aluminosilicate glasses: Insights from ^{27}Al and ^{17}O NMR, *Journal of Physical Chemistry C*, **120** 737-749 (2016)
- Lee, S. K., Park, S. Y., **Kim, H.-I.**, Tschauner, O., Asimow, P., Bai, L., Xiao, Y., and Chow, P., Structure of shock compressed model basaltic glass: Insights from O K-edge X-ray Raman scattering and high-resolution ^{27}Al NMR spectroscopy, *Geophysical Research Letters*, **39** 5306 (2012)
- Kim, H.-I.**, and Lee, S. K., The effect of iron content on the atomic structure of alkali silicate glasses using solid-state NMR spectroscopy, *Journal of the Mineralogical Society of Korea*, **24(4)** 301-312 (2011)
- Lee, S. K., Kim, H. N., Lee, B. H., **Kim, H.-I.**, and Kim, E. J., Nature of chemical and topological disorder in borogermanate glasses: Insights from B-11 and O-17 solid-

state NMR and quantum chemical calculations, *Journal of Physical Chemistry B*, **114** 412 (2010)

A2. Conference List

International Conferences

- Mun, K. Y.*, **Kim, H.-I.**, and Lee, S., K., Probing the degree of polymerization in iron-bearing calcium silicate glasses: A view from high-resolution solid-state Nuclear Magnetic Resonance, 15th International Conference on the Physics of Non-Crystalline Solids & 14th European Society of Glass Conference, July 2018 (Poster)
- Kim, H.-I.*** and Lee, S. K., Effect of iron content on the structure and disorder of iron-bearing sodium silicate glasses: Insights from high-resolution solid-state NMR study, Madison, May 2016 (Poster)
- Kim, H.-I.*** and Lee, S. K., Structure and disorder of iron-bearing silicate melts: A view from high-resolution solid-state NMR, 2nd Paris (IPGP) – SNU Workshop on Glasses, Melts, and Earth Materials, Seoul, May 2016 (Oral)
- Kim, H.-I.*** and Lee, S. K., Structure and disorder in iron-bearing sodium silicate glasses and melts: High-resolution ^{29}Si and ^{17}O solid-state NMR study, 2012 American Geophysical Union Fall Meeting, San Francisco, December 2012 (Poster)
- Lee, S., K.*, Mosenfelder, J., Tschauner, O., Asimow, P., Park., S. Y., and **Kim, H.-I.**, Structure of Multi-component Basaltic Glasses under Static and Dynamic Compression: Implications for Mantle Melting and Impact Processes on Planetary Surfaces, 2012 American Geophysical Union Fall Meeting, San Francisco, December 2012 (Poster)

Domestic Conferences

- Kim, H.-I.***, and Lee, S. K., Effect of iron content on the structure and disorder in iron-bearing sodium and calcium aluminosilicate glasses: Insights from Mössbauer and multi-nuclear (^{29}Si , ^{27}Al , and ^{17}O) solid-state NMR study, 2019 Proceedings of the Joint Annual Conference, the Petrological Society of Korea and Mineralogical Society of Korea, May 2019 (Oral)
- Kim, H.-I.***, and Lee, S. K., Effect of iron content on the structure and disorder of iron-bearing silicate glasses: A high-resolution solid-state NMR study, Workshop on Solid-state NMR of Condensed & Soft Matters, November 2018 (Oral)
- Kim, H.-I.***, and Lee, S. K., Atomistic origins of iron-induced changes in volcanic eruption style and lava flow: Insights from multi-nuclear solid-state NMR, 2018 The Geological Society of Korea Meeting, October 2018 (Oral)
- Kim, H.-I.***, and Lee, S. K., Multi-nuclear solid-state NMR study of the effect of iron content on the atomic structure of fully-polymerized Na- and Ca-aluminosilicate glasses: Implication for the structural role of iron in framework aluminosilicate glasses, 2018 Proceedings of the Joint Annual Conference, the Petrological Society of Korea and Mineralogical Society of Korea, May 2018 (Poster)
- Kim, H.-I.***, and Lee, S. K., Microscopic origin of the dynamics and morphology of iron-bearing silicate melts: Insights from high-resolution solid-state NMR, 2017 The Geological Society of Korea Meeting, October 2017 (Oral)
- Mun, K. Y.*, **Kim, H.-I.**, and Lee, S., K., Understanding of the iron partitioning in silicate melts using phase separation in the silicate glasses: Implication to formation processes of the Earth's core, 2017 The Geological Society of Korea Meeting, October 2017 (Poster)
- Mun, K. Y.*, **Kim, H.-I.**, and Lee, S., K., Quantifying the paramagnetic effect of iron ion within melt structure in calcium silicate system: Insight from solid-state nuclear magnetic resonance (solid-state NMR), 2015 Proceedings of the Joint Annual Conference, the Petrological Society of Korea and Mineralogical Society of Korea, May 2017 (Oral)

- Kim, H.-I.***, and Lee, S. K., High-resolution ^{29}Si and ^{17}O solid-state NMR study of the structure and disorder in iron-bearing albite melts and glasses, 2015 The Geological Society of Korea Meeting, October 2015 (Oral)
- Mun, K. Y.*, **Kim, H.-I.**, Kim, E. J., and Lee, S. K., Probing of atomic structure and disorder with Mg-aluminosilicate ($\text{MgSiO}_3\text{-Mg}_3\text{Al}_2\text{Si}_3\text{O}_{12}$) glasses to analyze the mafic mantle melts: A high-resolution solid-state multi-nuclear (^{27}Al , ^{17}O , and ^{29}Si) NMR study, 2015 The Geological Society of Korea Meeting, October 2015 (Poster)
- Kim, H.-I.***, and Lee, S. K., The structural role of iron in iron-bearing albite melts and glasses: Insights from ^{29}Si and ^{27}Al solid-state NMR, 2015 Proceedings of the Joint Annual Conference, the Petrological Society of Korea and Mineralogical Society of Korea, May 2015 (Poster)
- Kim, H.-I.***, and Lee, S. K., Effect of iron concentration on the structure and disorder in $\text{Na}_2\text{O-Fe}_2\text{O}_3\text{-SiO}_2$ and MgO-FeO-SiO_2 glasses: High-resolution ^{29}Si and ^{17}O NMR study, Proceedings of the Joint Annual Conference, 2014 Proceedings of the Joint Annual Conference, the Petrological Society of Korea and Mineralogical Society of Korea, May 2014 (Poster)
- Kim, H.-I.***, and Lee, S. K., Solid-state high-resolution Si-29 and O-17 NMR study of $(\text{Mg,Fe})\text{SiO}_3$ glasses: Implications for iron-bearing silicate melts in Earth's interior, 2013 Proceedings of the Joint Annual Conference, the Petrological Society of Korea and Mineralogical Society of Korea, May 2013 (Oral)
- Kim, H.-I.***, Yi, K., and Lee, S. K., Effects of iron contents and oxidation state on structure and disorder in iron-bearing Earth materials: EPMA and O-17 NMR study, 2012 Proceedings of the Joint Annual Conference, the Petrological Society of Korea and Mineralogical Society of Korea, May 2012 (Oral)
- Kim, H.-I.***, and Lee, S. K., Effect of iron content on structure and disorder in iron-bearing silicate glasses and melts: Insights from high-resolution solid-state NMR, 2011 The Geological Society of Korea Meeting, October 2011 (Oral)

요약 (국문초록)

철은 지구 및 지구형 행성에서 생성되는 규산염 용융체와 지표의 비정질을 구성하고 있는 가장 풍부한 전이금속 원소로서, 물질 내 철의 함량과 산화상태의 변화는 점성도 등의 물질의 성질에 변동을 야기하며, 나아가 화산 분출 양상 등의 다양한 지질학적 과정에 영향을 준다. 이러한 변화를 근본적으로 이해하기 위해서는 철이 포함되어 있는 용융체와 비정질의 원자 단위에서의 구조적 연결도, 화학적 배열, 그리고 위상학적 무질서도를 규명하는 연구가 필수적이다. 이러한 중요성에도 불구하고, 합철 비정질 및 용융체의 원자구조와 무질서도를 규명하는 것은 적합한 실험 방법론의 부재로 인하여 지질학 분야뿐만 아니라 자연과학 전반에 걸친 난제로 남아있었다. 특히, 고상 핵자기공명 분광분석(NMR)은 비정질의 구조적 정보를 직접적으로 체계적으로 제공하는 높은 이론적/기술적 성숙도를 갖는 실험방법론임에도 불구하고, 합철 물질의 NMR 연구는 상자성 효과로 인한 신호의 감소 및 분해능의 저하로 인해 극히 제한적으로만 수행되어 왔다. 이 학위논문에서는 상기 언급한 실험적 난점들을 극복하고 고상 NMR 방법론을 이용하여 획득한 다양한 조성의 합철 규산염 및 알루미늄규산염 비정질의 원자구조와 무질서도 정보를 제시하였다. 또한, 획득된 구조적 정보를 기반으로 철 함량 및 산화상태의 변화에 따른 합철 용융체의 물성 변동의 미시적 메커니즘을 규명하였다.

먼저, 최고 23 wt%까지의 다양한 함량의 산화철($\text{Fe}^{3+}/\Sigma\text{Fe} = 0.89$)이 포함된 $\text{Na}_2\text{O}-\text{Fe}_2\text{O}_3-\text{SiO}_2$ 비정질의 규소 및 산소 주변의 원자 환경에 관한 정량적 정보를 획득하였다. Fe^{3+} 의 함량이 증가할수록 구조의 중합도가 증가하고 비연결산소의 비율이 감소하는 양상을 관찰하였고, 이를 통해 Fe^{3+} 가 네트워크 형성이온으로서의 역할을 한다는 것을 확인하였다. 또한 Fe^{3+} 의 함량에 따라 연결산소의 무질서도 증가가 우세함을 규명하였

고, 이는 Fe^{3+} 과 연결산소가 공간적 근접성을 가지고 있음을 제시한다. 이와 더불어, 지구 맨틀 물질의 조성인 $(\text{Mg,Fe})\text{SiO}_3$ 비정질($\text{Fe}^{3+}/\Sigma\text{Fe} = 0.2$)의 철 함량 증가에 따른 구조 및 무질서도의 변화를 관찰하였다. 이 연구 결과를 통하여 Fe^{2+} 가 증가함에 따라 중합도가 낮은 규소 환경과 비연결 산소 주변의 화학적 및 위상학적 무질서도가 증가됨을 확인하였다. 마지막으로, 이 연구에서는 다양한 함량의 철이 포함된 자연계 유문암질의 모델시스템인 함철 엘바이트 및 아노르사이트 비정질의 알루미늄, 규소, 그리고 산소 주변의 원자 환경을 규명하였다. 해당 연구에서는 현재까지 보고되지 않았던 함철 비정질의 알루미늄 환경을 관찰한 결과를 제시함으로써, 규소와 Fe^{3+} 간의 혼합, 알루미늄과 Fe^{2+} 간의 우세한 상호작용, 철 함량 증가에 따른 고배위수의 알루미늄과 철의 형성 등의 철 진입에 따른 구조적 무질서도의 변화를 확인하였다.

본 학위 논문의 연구 결과는 다양한 조성의 규산염과 알루미늄규산염 비정질 내 철 함량의 증가가 화학적 및 위상학적 무질서도를 증가시키는 등의 구조적 변동을 야기한다는 사실을 보여주었다. 이와 같은 무질서도의 증가는 철 함량 증가에 따른 용융체의 점성도의 감소를 근본적으로 설명할 수 있는 미시적 원인이 된다. 본 연구는 고상 NMR 을 이용하여 함철 비정질의 중합도 및 무질서도에 관한 유의미한 정보를 획득한 최초의 실험적 연구이다. 이에, 이 학위 논문의 결과들은 자연계에 존재하는 각종 함철 유리질과 용융체의 구조와 물성의 관계를 이해하는 것에 있어 중요한 역할을 할 수 있을 것으로 기대된다.

주요어: 함철 규산염 용융체, 원자구조와 무질서도, 고상 핵자기공명 분광분석, 상자성 효과

학 번: 2011-30916